UNIVERSIDADE FEDERAL DO RIO GRANDE DO SUL
INSTITUTO DE FÍSICA
DEPARTAMENTO DE ASTRONOMIA
TESE DE DOUTORADO

Um estudo pancromático espacialmente resolvido dos 500 pc centrais da galáxia NGC 1052

A panchromatic spatially resolved study of the inner 500pc of NGC1052

Luis Gabriel Dahmer Hahn

Tese de doutorado realizada sob orientação do Prof. Dr. Rogério Riffel e apresentada ao Programa de Pós-Graduação em Física da Universidade Federal do Rio Grande do Sul, como requisito parcial para a obtenção do título de Doutor em Física.

Porto Alegre, Agosto de 2019

* Trabalho financiado pelo CNPq, CAPES e FAPERGS

Agradecimentos

⋆ Agradeço primeiramente à minha esposa, por estar sempre ao meu lado nestes mais de 6 anos de casamento. Na alegria e na tristeza, na saúde e na doença, na pobreza e na pobreza. Te amo e te amarei até o último dia. Esta tese não teria sido possível sem você.

⋆ Agradeço muito à minha mãe, por ter me criado e me ensinado grande parte do que sei. A senhora é um exemplo para mim, obrigado por todas as lições que me ensinou.

⋆ Agradeço muito ao meu orientador, professor e grande amigo Rogério Riffel por ter me guiado nestes 4 anos.

⋆ Agradeço também ao meu orientador de mestrado, Alberto Ardila por ter sido quem me ensinou o básico da astronomia. Tu és um eterno amigo.

⋆ Um agradecimento especial para o meu professor de matemática do ensino médio Rogério Gonçalves por ter me incentivado a ser um físico. Tu és, até hoje, um grande exemplo para mim.

⋆ Meu grande irmão Henrique (maninhooo) por ter me aguentado por tanto tempo (e eu nem te obriguei). Te levo no coração para onde for.

⋆ Meu mais antigo amigo Fernando, tu é meu amigo desde antes de eu saber falar a palavra amigo. Obrigado por estes mais de 20 anos de amizade

⋆ Dhyandra Maria Dias do Nascimento, minha amiga super normal. Saudades de nossos papos sobre como a mecânica quântica afeta os gnomos que orbitam os

buracos negros das florestas. Um dia a gente se reencontra.

⋆ Agradeço à CAPES, ao CNPq, à FAPERGS e ao Departamento de Astronomia da Universidade Federal do Rio Grande do Sul pelo suporte financeiro e estrutural para a realização desta pesquisa

Resumo

Com o objetivo de entender as limitações de modelos de população estelar no infravermelho próximo (NIR), realizamos na presente tese um teste extensivo de bibliotecas de modelos de populações estelares simples no NIR em comparação com o óptico. Tal estudo foi feito ajustando o espectro inteiro com o programa STARLIGHT e através da comparação de índices espectrais. Os principais resultados obtidos foram *(i)* bibliotecas de modelos NIR com baixa resolução espectral produzem resultados que dependem da escolha da biblioteca estelar e não produzem resultados consistentes entre si *(ii)* de maneira geral, bibliotecas no NIR com baixa resolução espectral tendem a superestimar a extinção por poeira e a quantidade de população estelar jovem e *(iii)* para bibliotecas com alta resolução espectral, este cenário é consideravelmente melhor, com as duas bibliotecas testadas produzindo resultados mais compatíveis com os resultados encontrados no óptico. Com a metodologia consolidada, utilizamos cubos de dados no óptico e no NIR, ambos obtidos com o telescópio Gemini, para mapearmos a população estelar da galáxia elíptica NGC 1052. A partir dos dados ópticos, a galáxia NGC 1052 apresenta população estelar velha em todos os pontos do cubo de dados. No entanto, a partir de dados no NIR, os mesmos pontos apresentam uma contribuição de população estelar de idade intermediária. Afim de detectar populações sensíveis aos dois intervalos de comprimento de onda, combinamos os dois conjuntos de dados em um único cubo de dados, analisando assim simultaneamente o óptico e o NIR. Os resultados obtidos nesta análise pancromática mostram que a população estelar que domina a luz desta galáxia é predominantemente velha. Argumentamos que a divergência entre os resultados ópticos e NIR pode ser explicada pela baixa razão sinal-ruído da banda J e a ausência de dados na banda H, a qual contém grande parte das absorções estelares no NIR. Também mapeamos as propriedades do gás desta galáxia, encontrando 5 componentes cinemáticas nas linhas de emissão: (1 e 2) Duas componentes espacialmente não resolvidas, sendo uma componente larga em Hα, com um FWHM de $\sim$3200 km s^{-1} e uma componente intermediária-larga no dubleto [OIII]$\lambda\lambda$4959,5007; (3) uma componente estendida de largura intermediária com 280<FWHM<450 km s^{-1} e velocidade central de até 400 km s^{-1}, e que domina o fluxo em nossos dados; (4 e 5) duas componentes estreitas (FWHM<150 km s^{-1}), uma em [OIII], e uma visível nas demais linhas de emissão, a qual se estende além de nossos dados. Nossos resultados também sugerem que a ionização em nosso campo de visão não pode ser explicada por apenas um mecanismo, de modo que fotoionização domina no núcleo com as demais regiões sendo ionizadas por uma combinação de choques e fotoionização.

Abstract

Aimed at understanding the limitations of stellar population models in the near-infrared (NIR), we performed in the present thesis an extensive test of simple stellar population model libraries in the NIR compared to the optical. This study has been made by fitting the spectra with STARLIGHT program and also comparing spectral indexes. The main results obtained were *(i)* NIR libraries with low spectral resolution produce results that depend on the choice of library and also do not produce consistent results *(ii)* generally, NIR libraries with low spectral resolution tend to overestimate dust extinction and the amount of young star population and *(iii)* for libraries with high spectral resolution, this scenario is considerably better, with the two libraries tested producing results more compatible with results found in the optical. With the methodology consolidated, we used optical and NIR data cubes, both obtained with the Gemini telescope, in order to map the stellar population of the elliptical galaxy NGC 1052. From the optical data, the galaxy NGC 1052 has an old stellar population at all points of the data cube. However, from NIR data, the same points present a contribution of intermediate age stellar population. In order to detect populations sensitive to both wavelength ranges, we combine the two sets of data in a single datacube, analyzing optical and NIR simultaneously. The obtained results from this panchromatic analysis show that the stellar population that dominates the light of this galaxy is predominantly old. We argue that the divergence between the optical and NIR results can be explained by the low signal-to-noise ratio of the J band and the absence of data in the H band, which contains a large part of the stellar absorptions in the NIR. We also mapped the gas properties of this galaxy, detecting five kinematic components: (1 and 2) Two spatially unresolved components, being a broad line region visible in Hα, with a FWHM of $\sim$3200 km s^{-1} and an intermediate-broad component seen in the [OIII]$\lambda\lambda$4959,5007 doublet; (3) an extended intermediate-width component with 280<FWHM<450 km s^{-1} and centroid velocities up to 400 km s^{-1}, which dominates the flux in our data; (4 and 5) two narrow (FWHM<150 km s^{-1}) components, one visible in [OIII], and one visible in the other emission lines, extending beyond the field-of-view of our data. Our results also suggest that the ionization within the observed field of view cannot be explained by a single mechanism, with photoionization being the dominant mechanism in the nucleus with a combination of shocks and photoionization responsible for the extended ionization.

Conteúdo

Conteúdo **V**

Lista de Figuras **2**

1 Introdução **3**
1.1 Núcleos ativos de galáxias 3
1.2 A relação entre o buraco negro e a galáxia hospedeira 5
1.3 Regiões de linhas de emissão nucleares de baixa ionização 7
1.4 O caso de NGC 1052 9
1.5 Motivação 11
1.6 Objetivos específicos da tese 12

2 Metodologia **14**
2.1 Síntese de População estelar 14
2.1.1 Modelos utilizados neste estudo 15
2.1.2 O código STARLIGHT 18
2.2 Análise do gás em emissão 19
2.2.1 Medidas de densidade eletrônica 19
2.2.2 Medidas de temperatura eletrônica 19

3 Testando Modelos no NIR a partir de galáxias *early-type* **22**

4 NGC 1052: análise da população estelar **46**

5 NGC 1052: excitação e cinemática do gás **59**

6 Sumário e perspectivas **76**
6.1 Perspectivas 78

Referências Bibliográficas **79**

Apêndices **92**

A.1 Levantamento NIFS de galáxias ativas próximas: I - Cinemática estelar 92

A.2 Levantamento NIFS de galáxias ativas próximas: II - Amostra e perfis de densidade de massa superficial 119

A.3 Absorções estelares e índices de linhas de emissão no óptico e NIR . . 138

Lista de Figuras

1.1 Representação do modelo unificado dos AGNs. 4
1.2 Imagem óptica da galáxia NGC 1052. 9
1.3 Exemplo de um cubo de dados. 13

2.1 Diagrama dos níveis de energia da configuração $3p^3$ do enxofre ionizado. 20
2.2 Diagrama dos níveis de energia do oxigênio duas vezes ionizado 21

Capítulo 1

Introdução

1.1 Núcleos ativos de galáxias

Um núcleo ativo de galáxia (AGN) é uma estrutura localizada no centro de algumas galáxias, que emite uma grande quantidade de energia se comparado com o restante da galáxia hospedeira, sob a forma de processos que não podem ser atribuídos à fusão nuclear, como ocorre nas estrelas. AGNs são encontrados em uma fração significativa das galáxias, podendo chegar à 50% dos objetos (Ho, 2008). Segundo o paradigma atual, o AGN é composto por um buraco negro supermassivo (Supermassive Black Hole, SMBH) com um disco de gás ($\sim 10^{-3}$ pc) que é acretado pelo SMBH, e um conjunto de nuvens de gás e poeira distribuídas em formato toroidal e que envolvem as duas outras estruturas, se estendendo desde $\sim 10^{-3}$ pc até ~ 10 pc (Antonucci, 1993, Urry & Padovani, 1995, Ramos Almeida & Ricci, 2017). A similaridade de características observadas em diferentes galáxias e diferenças pontuais como a quantidade de radiação e a presença ou não de componentes largas nas linhas de transição permitidas (e.g. H e He) fizeram com que os astrônomos propusessem um modelo unificado para descrever os AGNs (veja Figura 1.1).

Esta estrutura extremamente compacta (Figura 1.1) possui luminosidades que podem atingir $10^{47}\,\mathrm{ergs\,s^{-1}}$ (Koratkar & Blaes, 1999), sendo que em alguns casos a luminosidade do AGN é maior que a luminosidade integrada emitida por todas as estrelas da galáxia. Para gerar tamanha emissão em uma região tão compacta, é necessário que a fonte desta energia seja gravitacional (Schneider, 2015), com partículas de matéria situadas em regiões mais afastadas perdendo momento angular e caindo em direção ao centro da estrutura.

Próximo ao SMBH, está a região onde são produzidas as linhas de emissão mais

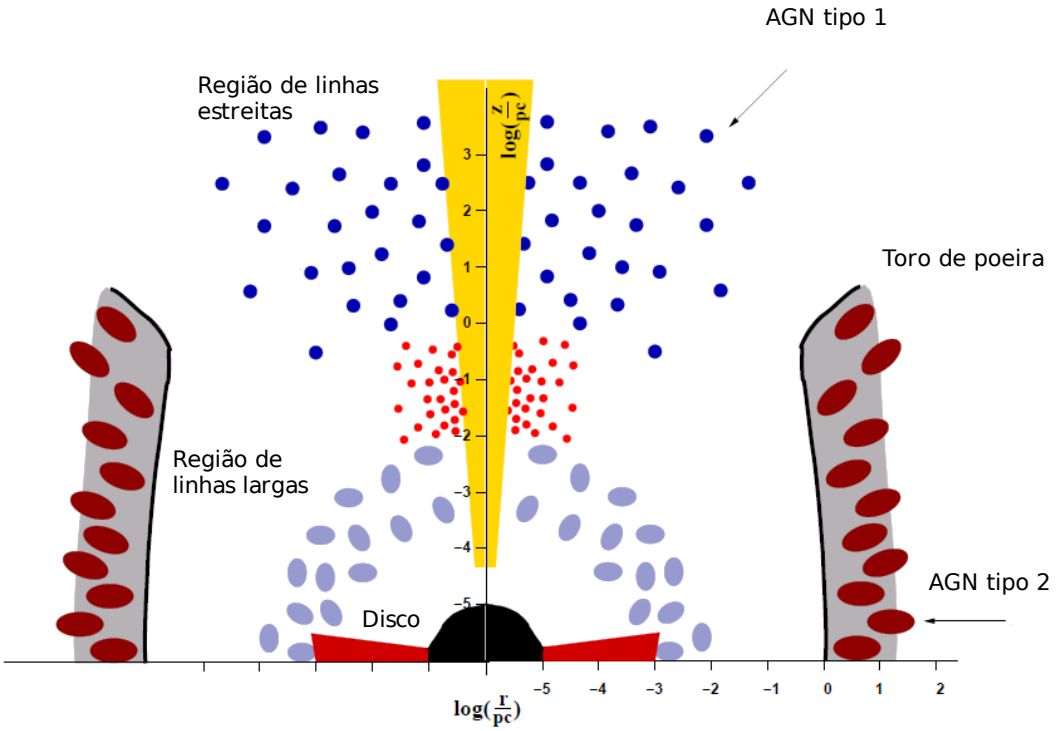

Figura 1.1: Representação do modelo unificado dos AGNs. Nesta figura, estão representados o buraco negro central, o disco de acreção, o toro de poeira, e as regiões onde são produzidas as linhas estreitas e as linhas largas. Devido à diferença de tamanho entre as estruturas, a escala de representação é logarítmica. Figura adaptada de Zier & Biermann (2002).

largas, com largura à meia altura (FWHM) maiores que 2000 km s^{-1}. Esta estrutura recebe o nome de região de linhas largas (BLR). Em uma região mais distante (∼10-1000 pc), são produzidas linhas de emissão com FWHM<1000 km s^{-1}, recebendo assim o nome de região de linhas estreitas (NLR). Uma boa revisão sobre a física de AGNs pode ser encontrada em Peterson (1997) e Beckmann & Shrader (2012).

Dependendo da distribuição espacial das nuvens que compõem o toro, o observador identifica regiões diferenciadas advindas do AGN. Nos casos onde nuvens de gás e poeira obscurecem a BLR, são visíveis apenas as linhas de emissão estreitas, recebendo assim a classificação de AGN tipo 2. Por outro lado, quando visualizamos a BLR diretamente, somos capazes de enxergar a região próxima ao SMBH, recebendo assim a classificação de AGN tipo 1 (ver o *review* de Ramos Almeida & Ricci, 2017).

1.2 A relação entre o buraco negro e a galáxia hospedeira

O paradigma atual indica que a grande maioria das galáxias possui um SMBH em seu centro (Kormendy & Richstone, 1995, Magorrian et al., 1998, Kormendy & Ho, 2013), portanto, é de suma importância o estudo da relação entre esta estrutura compacta e a galáxia hospedeira. Uma correlação bastante conhecida é a relação M-σ, descrita pela primeira vez por Ferrarese & Merritt (2000) e Gebhardt et al. (2000). Segundo esta relação empírica, a dispersão de velocidade do bojo de uma galáxia (σ) e a massa do SMBH (M) apresentam uma correlação logarítmica. Além disto, a comparação da massa do SMBH derivada a partir da luminosidade do AGN e a partir da luminosidade do bojo sugere que o crescimento do SMBH se dá, principalmente, por acreção de matéria durante períodos nos quais o AGN encontra-se ativo (Soltan, 1982, Marconi et al., 2004, Shankar et al., 2004, Merloni & Heinz, 2008). Além de sugerir uma correlação entre o buraco negro e a galáxia hospedeira, estas descobertas mostraram que a grande maioria dos SMBHs passam por períodos de intensa atividade.

No entanto, ainda é questão de debate se todas as galáxias possuem um SMBH em seu centro. Para galáxias com bojo clássico, a relação M-σ é consistente para todas as galáxias em que tem sido testada, o que sugere que todas estas galáxias hospedam um SMBH em seu centro. No entanto, para galáxias com pseudo-bojos, a massa do SMBH não se correlaciona fortemente com a dispersão de velocidades do bojo (Hu, 2009, Greene et al., 2010, Kormendy et al., 2011), o que sugere que algumas destas galáxias podem nem ter um SMBH. Para explicar este cenário, é necessário que os mecanismos que geram a correlação em bojos clássicos não ocorra nesta classe de galáxias (Kormendy & Ho, 2013). Greene et al. (2008) e Kormendy et al. (2011) sugeriram, independentemente, que bojos clássicos são criados em galáxias que experienciaram episódios intensos de fusão, os quais geraram AGNs de alta intensidade. Por outro lado, pseudo-bojos estariam presentes em galáxias que possuíram apenas AGNs de baixa intensidade, os quais teriam apenas uma influência local, não sendo capazes de afetar toda a galáxia. Esta hipótese é consistente com a descoberta feita por Greene & Ho (2004), de que as massas dos buracos negros em galáxias Seyferts de baixa luminosidade são mais baixas que as preditas pela relação M-σ.

Além de se correlacionar com a massa do bojo, AGNs são necessários na maioria dos modelos de formação de galáxias para reproduzir dados observados, tanto de

população estelar quanto de material intergaláctico (Harrison, 2017, e referências internas). Alguns dos observáveis são a correlação entre luminosidade em raios-X e a temperatura em raios-X observada para o gás no meio intra-cluster para grupos de galáxias; a baixa taxa de esfriamento do gás em *clusters*; a ineficiência de formação estelar na maioria dos halos massivos de galáxias; a formação de galáxias vermelhas massivas dominadas por bojo, as quais não possuem taxas de formação estelar (*Star Formation Rate*, SFR) significativa (Harrison, 2017).

Ao longo dos anos, vários estudos têm sido feitos relacionando o AGN à galáxia hospedeira. Segundo Kauffmann et al. (2003), os quais analisaram mais de 22 mil galáxias do *Sloan Digital Sky Survey* (SDSS), AGNs tendem a povoar galáxias mais massivas. No entanto, eles também reportaram ausência de uma correlação entre a luminosidade do AGN e a massa da galáxia hospedeira. Outra descoberta importante, é que tanto a formação estelar média por volume do espaço quanto a luminosidade dos AGNs apresentam um pico em torno de z$\sim$2 (Silverman et al., 2008). Rembold et al. (2017) e Mallmann et al. (2018), utilizando 62 AGNs com dados ópticos, encontraram que nas regiões internas (R$\leq$0.5 R_e), AGNs mais luminosos são mais jovens que galáxias controle, enquanto AGNs menos luminosos apresentam frações muito similares de populações jovens se comparado à amostra de controle, o que sugere uma conexão entre o crescimento do bojo da galáxia e o crescimento do SMBH.

Em vista destas descobertas, fica clara uma possível relação entre o buraco negro central e a galáxia hospedeira. No entanto, muitas são as questões em aberto dentro deste cenário. Uma das mais debatidas é a respeito da população estelar que habita a região próxima ao AGN. Alguns autores (e.g. Storchi-Bergmann et al., 2000, Kauffmann et al., 2003, Lutz et al., 2010) argumentam que a perda de momento angular do gás causaria um aumento na densidade próxima ao AGN, o que desencadearia um surto de formação estelar, fazendo com que a população estelar fosse mais jovem nesta região. Outros autores (e.g. Leslie et al., 2016, Ellison et al., 2016), no entanto, argumentam que os *outflows* de gás causados pelo núcleo ativo varreriam o gás da região próxima à fonte central, de modo que AGNs impediriam a formação estelar enquanto estivessem ativos. Ainda, há os que argumentam que a presença ou ausência de atividade nuclear não influenciaria a população estelar nas redondezas do buraco negro (e.g. Stanley et al., 2017). Este último cenário pode ocorrer por dois motivos: a) tanto a perda de momento angular quanto os *outflows* se contrabalanceariam, de modo que a população circumnuclear não seria afetada ou b) os efeitos do AGN (perda de momento angular e *outflows*) não seriam intensos

o suficiente para afetar esta população.

Mais recentemente, Zubovas & Bourne (2017) encontraram, a partir de simulações, que a interação entre o AGN e a galáxia hospedeira é mais complexa, de modo que diferentes galáxias podem se comportar diferentemente. Eles encontraram que, enquanto ativos, os AGNs tendem a remover o gás da região central, cessando assim a formação estelar. Após o fim do ciclo de atividade do AGN, a formação estelar sofreria um surto de formação estelar, graças à compressão do gás causada pelo AGN. No entanto, segundo os autores, estes efeitos dependem da luminosidade do AGN, havendo um valor no qual estes efeitos são máximos, de modo que para AGNs muito mais ou muito menos luminosos que este valor crítico, este efeito seria pequeno.

Segundo Harrison (2017), estas diferenças nas conclusões a respeito do impacto do AGN na população estelar circumnuclear podem ser atribuídas às diferenças nas amostras e nos métodos utilizados.

Para galáxias mais massivas, no entanto, mesmo os modelos empíricos mais simples precisam de algum processo físico para cessar a formação estelar (Peng et al., 2010). Para estas galáxias, efeitos de AGNs são consequentemente associados com esta cessação. Este cenário é interessante, pois ∼50-70% das galáxias elípticas e lenticulares (dominadas por bojo) hospedam AGNs em seus centros, enquanto em galáxias espirais, mais de 80% possuem núcleos dominados por formação estelar (Ho, 2008). Pelo exposto acima, fica evidente que para compreender melhor essa possível relação entre AGN e a galáxia hospedeira faz-se necessário mapear espacialmente as populações estelares nas dezenas de pc da região central das galáxias, comparando-as com as propriedades física e químicas do gás ionizado na região próxima do AGN.

1.3 Regiões de linhas de emissão nucleares de baixa ionização

Um tipo especial de galáxias em atividade é a classe de regiões de linhas de emissão nucleares de baixa ionização (LINER Heckman, 1980). A principal característica desta classe de objetos é a presença de emissões muito intensas nas linhas espectrais de baixa ionização, como [OI] e [NI], mas com emissões menos intensas nas linhas de alta ionização, como [OIII], se comparadas à galáxias Seyfert e quasares (Heckman, 1980, Kauffmann et al., 2003). O fato de as absorções estelares não estarem completamente diluídas pelo AGN faz com que estes objetos sejam objetos chave no estudo de populações estelares na região nuclear de galáxias ativas.

A discussão destes objetos estava inicialmente restrita a regiões mais internas das galáxias, de modo que a ionização deles era fortemente associada à AGNs de baixa luminosidade (LLAGN). No entanto, estudos posteriores mostraram que a emissão LINER não está restrita à região nuclear, de modo que mecanismos adicionais além de AGNs são necessários para explicar estas galáxias, como por exemplo choques (Heckman, 1980), estrelas pAGB (post-asymptotic giant branch, Binette et al., 1994, Stasińska et al., 2008, Cid Fernandes et al., 2011, Yan & Blanton, 2012) e *starbursts* com idades entre 3 e 5 Myr, dominadas por estrelas Wolf-Rayet (Barth & Shields, 2000).

Observações de LINERs no ultravioleta sugerem que esta classe é extremamente inomogênea, com algumas fontes possuindo fortes linhas em emissão e outras com um espectro UV causado apenas por estrelas velhas (Maoz et al., 1998), podendo apresentar as duas características simultaneamente.

Com observações utilizando unidades de campo integral (IFU), é possível isolar os diferentes componentes de cada galáxia. Por exemplo, a partir da amostra SAURON (Sarzi et al., 2010), foi encontrada uma forte correlação entre o brilho estelar superficial e o fluxo da emissão de Hβ. Os autores também reportaram que estrelas pAGB são o melhor candidato para explicar a ionização do gás. Por outro lado, Loubser & Soechting (2013) encontraram em sua amostra de galáxias centrais de aglomerados de galáxias (CCG) com emissão LINER, que modelos de fotoionização por AGN com metalicidade sobre-solar são capazes de reproduzir as razões de linha observadas, embora não fosse possível descartar ionização por choques ou estrelas pAGB. Em uma série de artigos, Ricci et al. (2014b,a, 2015) estudaram uma amostra de 10 LINERs e encontraram que a maioria apresenta ionização compatível com um AGN, embora três galáxias apresentam uma estrutura circumnuclear em formato de disco compatível com fotoionização por estrelas pAGB e uma galáxia com ionização compatível com choques. Já Belfiore et al. (2015), a partir de uma amostra de 14 galáxias Seyfert/LINER, reportou que a emissão estendida é consistente com ionização causada por estrelas em estágios finais de evolução. Outra sequência de artigos (Kehrig et al., 2012, Papaderos et al., 2013, Gomes et al., 2016), realizada com dados do levantamento Calar Alto Legacy Integral Field Area (CALIFA), encontrou evidência de dois tipos de galáxias *early-type* (ETG), classificadas como tipo i e tipo ii. ETGs tipo i possuem largura equivalente de Hα praticamente constante fora do núcleo, as quais são compatíveis com a hipótese de fotoionização por estrelas pAGB, enquanto a largura equivalente de Hα cresce radialmente para fora em ETGs tipo ii, de modo que ainda há debates sobre a ionização nestas fontes.

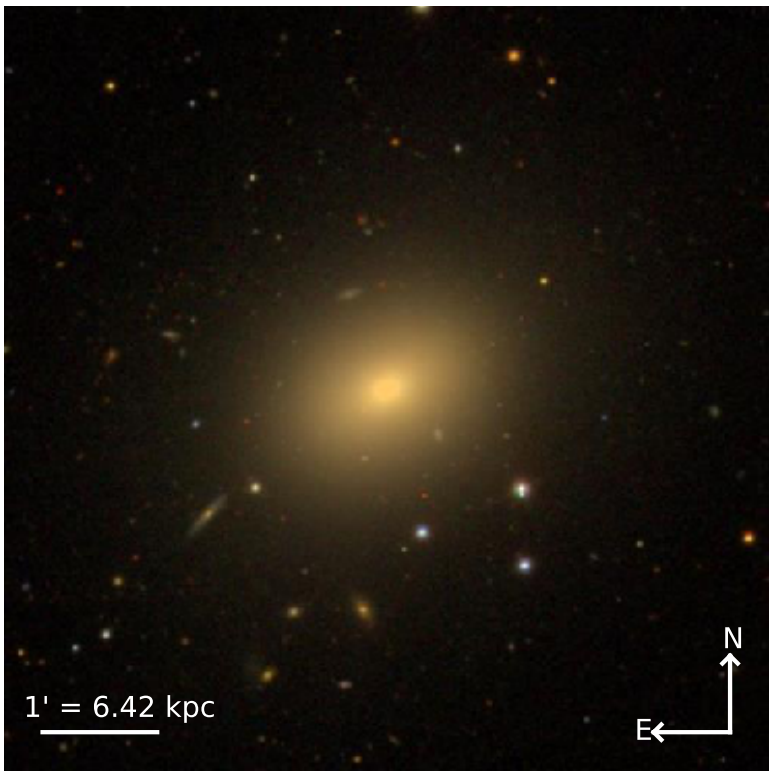

Figura 1.2: Imagem óptica da galáxia NGC 1052 obtida com o Sloan Digital Sky Survey.

Como os resultados são controversos, para ter um entendimento completo é necessário estudar as propriedades físicas do gás e populações estelares em um amplo intervalo de comprimentos de onda, de modo a provar assim diferentes estágios das populações estelares e diferentes espécies atômicas e moleculares do gás.

1.4 O caso de NGC 1052

Com o intuito de estudar a relação entre o SMBH e a galáxia hospedeira, assim como os mecanismos de ionização em LINERs, nós realizamos um estudo piloto da galáxia NGC 1052, com um tipo morfológico E4 e que está localizada à uma distância de 19.1±1.4 Mpc. Este objeto apresenta uma classificação ambígua de Seyfert/LINER, e é fruto de um longo debate acerca de sua ionização. Na Figura 1.2 apresentamos uma imagem da galáxia.

Vários autores têm proposto choques como o mecanismo principal por trás da

ionização deste objeto. Por exemplo, Koski & Osterbrock (1976) estudaram uma região de 2,7×4,0 arcsec e sugeriram que a ionização desta região seria causada por choques, de modo que Fosbury et al. (1978) mais tarde apresentou um modelo detalhado de choques para explicar esta ionização. Outro estudo foi conduzido por Sugai & Malkan (2000), os quais utilizaram espectros no infravermelho médio e encontraram evidências de que choques respondem por ∼80% da excitação da fonte. Mais tarde, Dopita et al. (2015) analisou dados IFU obtidos com o Wide Field Spectrograph do telescópio de 2.3m do Siding Spring Observatory e reportou que um modelo com choques é capaz de explicar melhor os dados.

Por outro lado, outros autores têm defendido fotoionização pelo SMBH como o principal ionizador de NGC 1052. Diaz et al. (1985) reportou que a intensidade das linhas de [SIII]λ9069,λ9532 favoreciam fotoionização. Também, Gabel et al. (2000) estudou este objeto e concluiu que os fluxos das linhas de emissão obtidos com o Faint Object Spectrograph do telescópio espacial Hubble Space Telescope podem ser simulados com simples modelos de fotoionização usando uma lei de potência com α = -1.2. Eles também encontraram que nenhum modelo simples com uma densidade constante é capaz de reproduzir as linhas de emissão de NGC 1052, requerendo ao menos duas densidades

Dois estudos anteriores encontraram linhas largas de hidrogênio ionizado neste objeto. Barth et al. (1999) utilizou luz polarizada e confirmou a presença de uma componente larga em Hα. Mais tarde, Sugai et al. (2005) observou esta galáxia com o instrumento Kyoto 3DII do telescópio Subaru e reportou detecção direta de uma componente larga em Hβ.

NGC 1052 também apresenta propriedades em outros comprimentos de onda, além do óptico. Em rádio, ela possui dois jatos com diferentes orientações, um em escala de parsec e outro em escala de kiloparsec (Wrobel, 1984, Fey & Charlot, 1997). Em raios-X, ela apresenta um núcleo compacto, além de várias emissões relacionadas aos jatos rádio e uma região estendida alinhada com uma emissão synchrotron (Kadler et al., 2004).

Estudos passados também focaram na população estelar deste objeto. Raimann et al. (2001) concluiu, a partir de espectros longslit, que o 1 kpc interno é dominado por uma população velha (∼10 Gyr) e bastante metálica, enquanto que a medida que os dados se afastam do núcleo uma população de 1 Gyr se torna importante. Milone et al. (2007) também estudaram este objeto, e a partir de índices de Lick encontraram que o bojo da galáxia possui uma idade de 12-15 Gyr e uma metalicidade maior que no restante da galáxia, sugerindo que a formação estelar ocorreu

primeiro no bojo em um período de tempo bastante curto, mas que no eixo maior, uma população mais jovem é responsável por ∼30% da luminosidade a 1.5 kpc. Eles não encontraram a mesma população ao longo do eixo menor da galáxia. Por outro lado, a partir de espectros Keck, Pierce et al. (2005) encontraram uma idade central de ∼2 Gyr, quando medida pela luminosidade. Segundo eles, isto é consistente com o processo de fusão sofrido por esta galáxia há ∼1 Gyr (van Gorkom et al., 1986). Eles também estudaram 16 aglomerados globulares, e encontraram uma idade média de ∼13 Gyr, com alguns destes apresentando fortes ramos horizontais azuis que não podem ser completamente explicados a partir de modelos de população estelar. Um resultado compatível foi reportado por Fernández-Ontiveros et al. (2011), que encontrou 15 fontes compactas exibindo luminosidade Hα uma ordem de magnitude acima do estimado para uma população evoluída, consistente com uma população com <7 Myr. Segundo eles, esta descoberta está praticamente ligada ao evento de fusão sofrido por esta galáxia

1.5 Motivação

Um importante avanço na compreensão do papel das populações estelares nas vizinhanças do AGN e seus efeitos na atividade nuclear pode ser alcançado através de uma investigação simples, mas completa, na investigação da presença ou não de estrelas de idade jovens ou intermediárias nas poucas centenas de pc em torno do AGN. Neste contexto, se estrelas jovens dominam a luz, a alimentação do AGN e a formação estelar ocorrem concomitantemente. Se, em vez disso, estrelas de idade intermediárias dominarem a população estelar, a alimentação do AGN seria resultado da massa ejetada pelas estrelas evoluídas, de modo que a fase de AGN seria posterior a fase de formação estelar (fase *post-starburt*). Finalmente, se apenas encontrarmos populações estelares velhas, o *inflow* de gás para o AGN é eficiente e a formação estelar não ocorre. Questões fundamentais ainda permanecem sem respostas, tais como: a formação estelar desempenha um papel decisivo em disparar a atividade nuclear? a formação estelar cessa a atividade nuclear? ou a atividade nuclear pára a formação estelar? são estes dois fenômenos correlacionados?

No caso de galáxias ativas, que geralmente são obscurecidas por poeira ou têm as assinaturas espectrais associadas às estrelas completamente diluídas na região do óptico, a região do infravermelho próximo é a mais adequada para o estudo das populações estelares. Também, neste intervalo de comprimento de onda é muito difícil identificar populações dominadas por estrelas TP-AGB, já que tanto suas principais

absorções quanto seu pico de emissão ocorrem no NIR (Maraston, 2005, Riffel et al., 2009, 2015). Além destas dificuldade, espectrógrafos de campo integral no óptico não dispõem de resoluções espaciais tão altas quanto espectrógrafos NIR, que podem ser utilizados em conjunto com módulos de optica adaptativa. Deste modo, estudos coletados no óptico têm dificuldade em separar espacialmente a emissão do AGN do restante da galáxia.

Já projetos que se baseiem no NIR, além da falta de bibliotecas de modelos adequadas, caso não possuam emissão de poeira quente suficientemente pronunciada, ela não é detectada na banda K. Desta maneira, é necessário o óptico para quantificar o AGN (contínuo em forma de lei de potência, com $f_\nu \sim \nu^{-1.5}$). Além disto, o NIR é pouco sensível à luminosidade advinda de estrelas jovens, cujo pico de emissão ocorre em comprimentos de onda mais azuis.

Desta maneira, pesquisas de populações estelares que utilizem o óptico e o NIR concomitantemente, tendem a se ser mais sensíveis a todas as classes de populações estelares. Portanto, estes estudos teriam uma maior facilidade em separar as diferentes populações, além de separar a emissão do AGN do contínuo estelar.

O grupo AGNIFS[1] vem se dedicando nos últimos anos a entender as populações estelares e propriedades físicas do gás ionizado em regiões circumnucleares em AGNs, contudo focadas em análises da região espectral do NIR (Riffel et al., 2009, 2017, 2018, Schönell et al., 2019). Nos Apêndices A.1 e A.2 apresentamos dois artigos publicados por este grupo apresentando a amostra e discutindo a cinemática estelar e os perfis de densidade de massa superficial.

1.6 Objetivos específicos da tese

A fim de jogar alguma luz nas questões acima, pretendemos inicialmente testar os modelos de populações estelares disponíveis na literatura e que cobrem a faixa do optico ao NIR para saber quais as suas limitações. Posteriormente, aplicaremos estes modelos a cubos de dados de AGNs para estudar o conteúdo estelar circumnuclear destes objetos, traçando uma comparação entre estas populações e a ionização do gás causada pela atividade nuclear. Um cubo de dados é composto por um conjunto de imagens em diferentes comprimentos de ondas. Deste modo, cada píxel da imagem final é composto por um espectro, e recebe o nome de spaxel. Este formato de dados é importante pois, através dele, é possível extrair informações espectrais de maneira espacialmente resolvida, de modo a produzir mapas de fluxos e cinemáticas.

[1] do qual faço parte

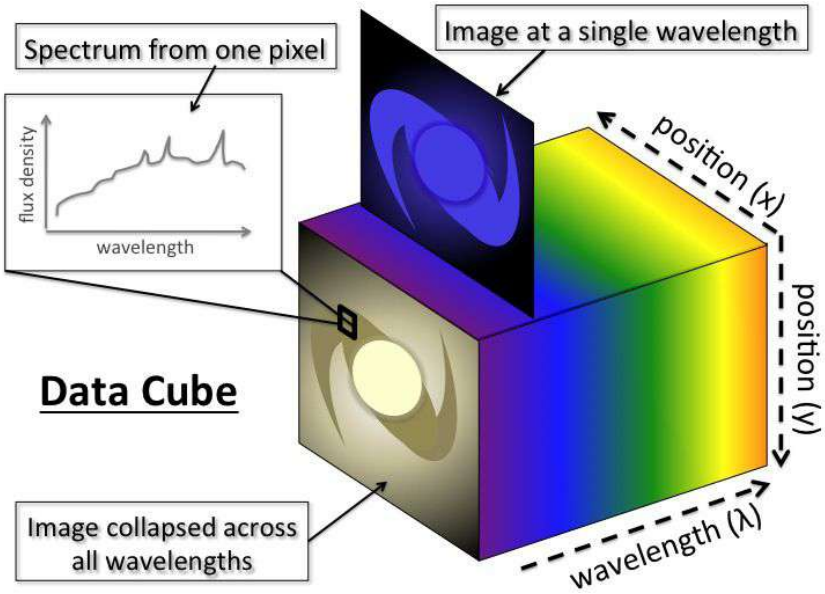

Figura 1.3: Exemplo de um cubo de dados, ilustrando várias imagens em comprimentos de onda diferentes.

A Figura 1.3 ilustra um cubo de dados[2].

Para alcançarmos estes objetivos, inicialmente realizamos um estudo comparativo (Capítulo 3), onde mostramos que bibliotecas de modelos de síntese de população estelar no NIR precisam de uma resolução espectral adequada para realizar o ajuste das linhas e bandas de absorção corretamente. Caso contrário, as bandas de absorção são diluídas no contínuo, de modo que peso excessivo é dado ao formato e inclinação do contínuo.

No entanto, como ainda não existem bibliotecas com alta resolução espectral e que incluam populações jovens, torna-se difícil realizar uma correta caracterização da população estelar jovem, limitando assim os testes propostos acima ao uso de modelos de mais baixa resolução espectral. Além do mais, demonstramos em Riffel et al. (2019, Apêndice A.3) que, de uma maneira geral, os indices das linhas de absorção no NIR são capazes de predizer os valores observados em galáxias do tipo *early-type*, embora falhem em predizer os índices de galáxias *late-type*.

Desta maneira, afim de iniciar a segunda etapa, mapeamos as populações estelares, cinemática estelar e do gás e excitação do gás de NGC 1052. Os resultados destes estudos se encontram nos Capítulos 4 e 5. No Capitulo 6, resumimos nossas conclusões e fazemos uma discussão geral dos resultados.

[2]Retirado de https://astro3d.org.au/research/

Capítulo 2

Metodologia

O espectro de uma galáxia pode ser dividido em informação de contínuo e de linhas de emissão. Enquanto o contínuo contém majoritariamente informação acerca das estrelas que compõem uma galáxia, as linhas de emissão revelam principalmente informação a respeito do gás presente em cada objeto.

Dentre os diversos meios disponíveis para se analisar a população estelar de galáxias, focamos nossos estudos majoritariamente no método de síntese de população estelar, por ser capaz de utilizar grande parte da informação espectral disponível simultaneamente (Cid Fernandes et al., 2004, 2005).

Já para a análise do gás em emissão, focamos na determinação de temperatura e densidade, assim como em diagramas de diagnóstico por razões de linhas. O principal motivo para esta escolha é que a combinação destas informações é capaz de fornecer dados importantes a respeito dos mecanismos de ionização por trás das diferentes regiões de galáxias.

2.1 Síntese de População estelar

Quando analisa-se o espectro de uma estrela, é possível estimar valores para idade, massa, temperatura efetiva, raio, gravidade superficial e composição química. Para tal, compara-se o espectro da estrela com espectros de estrelas conhecidas e, a partir destes, identifica-se a qual classe a estrela pertence.

Quando observamos uma imagem ou espectro de uma galáxia, salvo para algumas fontes extremamente próximas, não é possível separar estrelas para estudá-las individualmente, e o que observamos é, na verdade, a soma da luz de todos os es-

pectros estelares, gás, poeira, e em alguns casos, de um AGN, integrados ao longo da linha de visada. Ao estudar o contínuo deste espectro integrado, seja através da cinemática ou de uma análise de suas características espectrais, buscamos recuperar estas informações.

Sendo assim, estuda-se a luz integrada de todas as estrelas, mais gás e poeira, comparando o espectro observado a vários modelos de populações estelares simples de diferentes idades e metalicidades, buscando identificar qual a fração de cada uma destas populações jovens ao espectro, ou seja, determinamos o histórico de formação estelar (SFH) da galáxia.

2.1.1 Modelos utilizados neste estudo

O elemento mais importante em uma síntese de população estelar é a biblioteca de modelos (Riffel et al., 2009) a ser utilizada para representar o espectro da galáxia. Uma biblioteca ideal deve cobrir as propriedades de idade e metalicidade da galáxia em estudo com resolução em idade e metalicidade suficiente para que suas propriedades sejam resolvidas (Schmidt et al., 1991, Cid Fernandes et al., 2005).

Como reportado por Chen et al. (2010) para o óptico, diferentes bibliotecas de modelos podem resultar em populações levemente diferentes. Embora para o óptico eles tenham encontrado que as populações dominantes se mantém inalteradas, no NIR esta discussão é mais recente. Baldwin et al. (2018) encontraram, a partir de espectros NIR e utilizando 4 bibliotecas de modelos, que a escolha da biblioteca de SSPs no NIR gera variações maiores que no óptico, e que os resultados estão fortemente associados à forma do contínuo.

Por este motivo, decidimos testar diferentes bibliotecas de modelos e comparar suas predições aos valores encontrados para o óptico. Estas mesmas informações, assim como as idades e metalicidades de cada biblioteca, são sumarizadas na Tabela 2 da Seção 3.

Um fator importante a se considerar na comparação entre os diferentes modelos é como cada um integra a contribuição de cada estrela após a saída da sequência principal. Existem dois métodos principais que são utilizados: um deles é através de isócronas (e.g. Bruzual & Charlot, 2003), as quais são modelos teóricos calculados através da teoria de evolução estelar. O segundo método é a chamada teoria do consumo de combustível (e.g. Maraston, 2005), onde a variável de integração é a quantidade de combustível consumida através da queima nuclear além da sequência principal. Para o óptico, a diferença entre estas duas formas não é tão evidente, de

modo que modelos que utilizam diferentes métodos são compatíveis (Chen et al., 2010). No entanto, para o NIR a diferença é significativa, de modo que modelos baseados na teoria de consumo de combustível produzem modelos cuja contribuição de estrelas TP-AGB pode chegar a 50%, enquanto modelos que utilizam isócronas possuem contribuições muito mais baixas, e em alguns casos até desprezíveis, advindas destas mesmas estrelas (Bruzual & Charlot, 2003, Maraston, 2005, Röck et al., 2016).

Algumas das bibliotecas aqui selecionadas oferecem mais de um conjunto de isócronas ou IMFs. No entanto, dentre as bibliotecas de modelos publicadas por cada um dos artigos, escolhemos aquele que cobrisse propriedades diferentes daquelas cobertas por outras bibliotecas, de modo a se testar a influência de cada um dos ingredientes na biblioteca final.

Bruzual & Charlot (2003)

A primeira biblioteca escolhida para este trabalho foi desenvolvida por Bruzual & Charlot (2003, daqui em diante BC03). Ela foi criada a partir das bibliotecas estelares de Le Borgne et al. (2003) e Lejeune et al. (1997, 1998), as quais possuem uma resolução espectral de R=2000 no óptico e 300 no NIR. A contribuição de cada estrela foi obtida usando as isócronas Padova (Marigo et al., 2008,e referências internas). Espectros empíricos de estrelas TP-AGB foram incluídos, a partir das observações de Le Sidaner & Le Bertre (1996), Le Bertre (1997), as quais possuem uma resolução similar aos demais espectros. Esta biblioteca possui uma baixa contribuição de estrelas TP-AGB, sendo classificada como *TP-AGB light*.

Maraston (2005)

A segunda biblioteca que escolhemos foi a publicada por Maraston (2005, daqui em diante M05). As contribuições de estrelas além da sequência principal foram calculadas a partir da teoria de consumo de combustível. As bibliotecas de estrelas utilizadas para estrelas não TP-AGB foram as publicadas por Lejeune et al. (1997, 1998), de modo que os modelos também possuem uma resolução espectral de 300 tanto no óptico quanto no NIR. Os espectros das estrelas TP-AGBs foram retirados de Lançon & Mouhcine (2002), as quais possuem no NIR uma resolução espectral melhor que os espectros das demais estrelas, de modo que, para SSPs com uma maior dependência desta classe de estrelas ($0.5<t<2.0\,\mathrm{Gyr}$), a resolução espectral é maior. Esta biblioteca possui uma alta contribuição de estrelas TP-AGB, sendo classificada como *TP-AGB heavy*.

Flexible Stellar Population Synthesis

O código FSPS (*Flexible Stellar Population Synthesis*) desenvolvido por Conroy et al. (2009, daqui em diante C09) permite que o usuário escolha a biblioteca estelar, a função de massa inicial (*Initial Mass Function*, IMF), as isócronas, assim como diversos parâmetros relacionados às estrelas gigantes, tais como a duração da fase TP-AGB e a quantidade de estrelas *blue stragglers*. A biblioteca que usamos foi gerada a partir da biblioteca estelar de Lejeune et al. (1997, 1998) com espectros de estrelas TP-AGB de Lançon & Mouhcine (2002), com uma resolução espectral final de 300. Para integrar a contribuição de cada estrela, foram utilizadas isócronas Padova. Relacionado à contribuição de estrelas TP-AGB, ela encontra-se entre M05 e BC03.

Meneses-Goytia et al. (2015)

A primeira biblioteca de modelos com mais alta resolução espectral no NIR (R$\sim$2000) que usamos é a de Meneses-Goytia et al. (2015, daqui em diante MG15). Ela foi gerada a partir da biblioteca estelar do Infrared Telescope Facility (IRTF, Cushing et al., 2005, Rayner et al., 2009), e isócronas Padova (Marigo et al., 2008). Como a biblioteca IRTF possui estrelas TP-AGB, não foram necessários outros espectros de estrelas deste tipo. No entanto, a biblioteca IRTF não inclui estrelas quentes, que são fundamentais para a construção de SSPs mais jovens. Por este motivo, esta biblioteca apenas inclui SSPs com t>1 Gyr. Em relação à contribuição de estrelas TP-AGB, ela é considerada TP-AGB heavy, embora as contribuições desta classe de estrelas sejam menos intensas que na biblioteca de M05. A desvantagem desta biblioteca é a ausência de dados ópticos, estando disponível apenas para o NIR ($9350 \lesssim \lambda \lesssim 24100 \mathring{A}$).

E-MILES

Essa biblioteca é uma expansão para a região do infravermelho da biblioteca de Vazdekis et al. (2010). Semelhantemente à biblioteca de modelos MG15, a biblioteca E-MILES (Vazdekis et al., 2016) possui mais alta resolução no NIR (R$\sim$2000), mas diferentemente da biblioteca MG15, esta inclui espectros ópticos. Os dados NIR também foram criados a partir da biblioteca de estrelas IRTF. Do mesmo modo,

ela não inclui SSPs jovens, estando limitada a modelos com idade t>0.5 Gyr. Outra característica que diferencia esta biblioteca da biblioteca MG15 é o fato de ter usado as isócronas de Pietrinferni et al. (2004). Esta biblioteca é considerada TP-AGB light.

2.1.2 O código STARLIGHT

O segundo passo para a síntese, após uma escolha adequada de uma base, é a escolha de um código que realize o processo do ajuste do espectro em questão através da combinação de elementos da base. Para nossa síntese, utilizamos o código STARLIGHT (Cid Fernandes et al., 2004, 2005, Cid Fernandes, 2018). Este código ajusta um espectro observado com uma combinação em diferentes proporções de SSPs. Este código também procura pelo avermelhamento que melhor descreve o espectro observado, através de uma lei de extinção fornecida pelo usuário. Basicamente, o código STARLIGHT encontra o melhor modelo M_λ dado por

$$M_\lambda = M_{\lambda 0}\left[\sum_{j=1}^{N_\star} x_j b_{j,\lambda} r_\lambda\right] \otimes G(v_\star, \sigma_\star)$$

onde $\mathrm{M}_{\lambda 0}$ é o fluxo no ponto normalizado $\lambda 0$, N é o número de SSPs usados para compor o modelo, $\vec{x}$ é o vetor de população, de modo que x_j indica a contribuição do j-ésimo espectro normalizado em $\lambda 0$, $\mathrm{b}_{j,\lambda}$ é o espectro do j-ésimo modelo, r_λ é o fator de avermelhamento ($r_\lambda = 10^{-0.4(A_\lambda - A_{\lambda 0})}$), e a convolução pela gaussiana $G(v_\star, \sigma_\star)$ leva em conta a dispersão e a velocidade de grupo estelar. Este melhor modelo é encontrado através da minimização de χ^2 na equação

$$\chi^2 = \sum_\lambda [(O_\lambda = M_\lambda) w_\lambda]^2$$

onde O_λ é o espectro observado e w_λ é o peso dado a cada ponto ajustado, usado para mascarar linhas de emissão e pontos com defeitos no espectro, para os quais $w_\lambda = 0$, além de poder ser utilizada para diminuir o peso de pontos com baixo S/N ou aumentar o peso de pontos com características importantes e determinantes dos espectros.

O STARLIGHT permite, ainda, adicionar componentes do contínuo para representar uma possível contribuição de poeira quente e uma lei de potência. Nas sínteses realizadas no NIR, seguimos Riffel et al. (2009) e adicionamos uma lei de potência com $f_\nu \sim \nu^{-1.5}$ para reproduzir a emissão proveniente do AGN e emissões de corpo negro entre 700 e 1400 K para reproduzir a emissão térmica advinda de poeira quente.

Para os ajustes no óptico, adicionamos apenas uma lei de potência, já que a emissão advinda de poeira quente é desprezível neste intervalo de comprimento de onda.

2.2 Análise do gás em emissão

Medidas de densidade e temperatura eletrônica são muito importantes no estudo do gás em emissão. Isto porque, através destas medidas, é possível identificar cenários de ionização compatíveis com as medidas. Por exemplo, segundo Osterbrock & Ferland (2006), regiões com temperatura maior que 14×10^3 K não são compatíveis com fotoionização, de modo que outros mecanismos dominam a ionização do gás. Nesta seção, discutimos os métodos que serão utilizados para medir estes valores.

2.2.1 Medidas de densidade eletrônica

Efetuamos a determinação da densidade eletrônica a partir das linhas de enxofre ionizado em 6716 e 6731 Å. Como elas se referem ao mesmo íon e possuem energia de excitação semelhante, são ideais para se determinar a densidade, já que elas não estão sujeitas a efeitos significativos de densidade e abundância. Como estes dois níveis têm taxas de desexcitação diferentes, assim como diferentes probabilidades de transição radioativa, a razão das linhas de emissão correspondentes é altamente dependente da densidade. A Figura 2.1 mostra os níveis da configuração $3p^3$ do [SII].

2.2.2 Medidas de temperatura eletrônica

Para se determinar a temperatura eletrônica de uma região de uma galáxia, vários métodos distintos podem ser aplicados, dependendo do intervalo de comprimento de onda observado. Entre estes métodos, destacam-se as razões de intensidades de pares de linhas advindos do mesmo íon mas com energias de excitação distintas e razão da intensidade de linhas de recombinação pela intensidade do contínuo de recombinação. Como o contínuo óptico e NIR de NGC 1052 é dominado por população estelar, focamos nossa análise em razões de linhas de emissão.

Os íons [OIII] e [NII] são capazes de fornecer uma estimativa acurada da temperatura (Osterbrock & Ferland, 2006). Isto acontece pois ambos os íons pertencem à configuração p^2, com as linhas aurorais sendo emitidas a partir dos níveis superiores

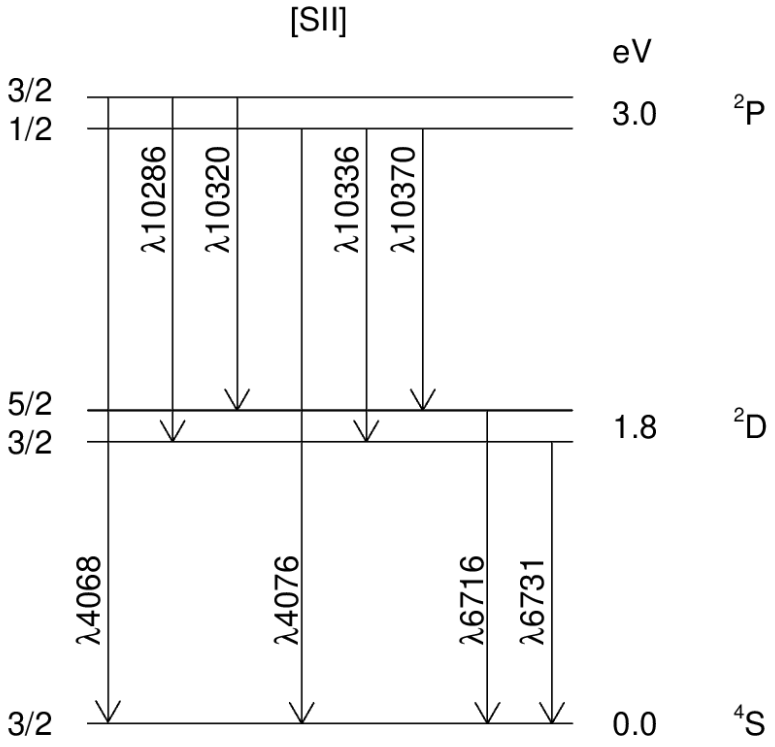

Figura 2.1: Diagrama dos níveis de energia da configuração $3p^3$ do [SII] (retirado de Riffel, 2004).

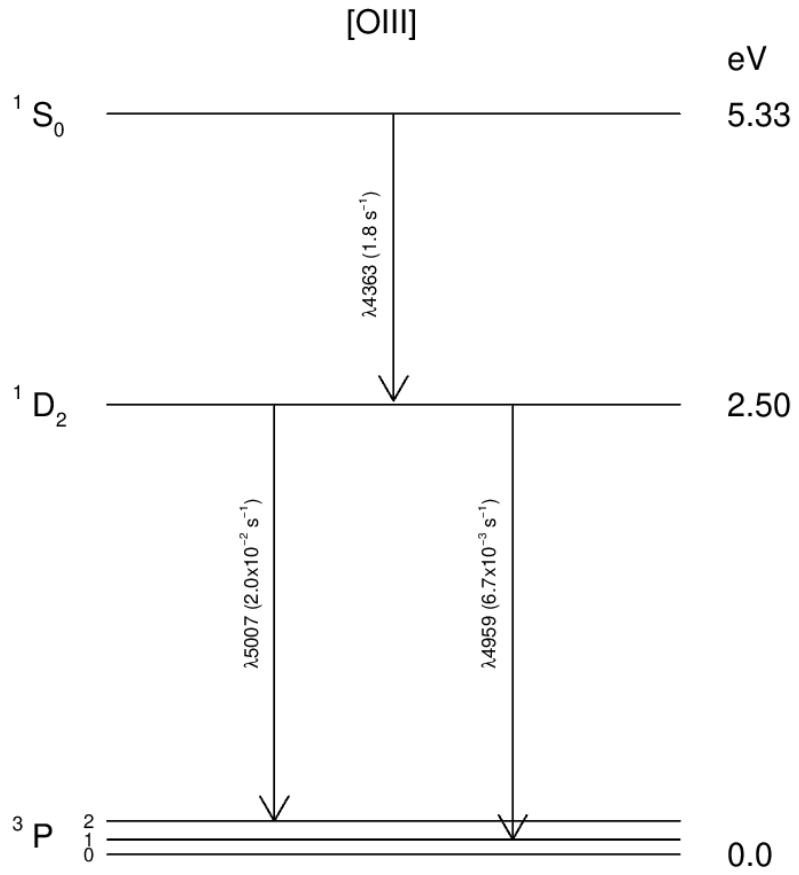

Figura 2.2: Diagrama dos níveis de energia do íon [OIII] (retirado de Riffel, 2004).

(^{1}S), apresentando maior potencial de ionização, enquanto as linhas nebulares são emitidas do nível intermediário (^{1}D), com mais baixo potencial de ionização. Desta maneira, a razão entre as linhas aurorais [OIII]λ4363 e [NII]λ5755 e as linhas nebulares [OIII]$\lambda\lambda 4959, 5007$ e [NII]$\lambda\lambda 6548, 6583$ se relaciona com a temperatura. A Figura 2.2 mostra os níveis da configuração do íon [OIII].

É importante frisar que o íon [NII] possui menor potencial de ionização que o [OIII], de modo que valores obtidos pela razão do nitrogênio fornecem uma estimativa de temperatura em regiões de mais baixa ionização se comparados aos valores determinados a partir do oxigênio.

Capítulo 3

Testando Modelos de Síntese de População Estelar no NIR a partir de galáxias *early-type*

Aqui apresentamos os resultados obtidos na primeira parte do trabalho da tese. Estes resultados, bem como uma discussão destes, se encontram na forma de um artigo que foi publicado na revista *Monthly Notices of the Royal Astronomical Society* (MNRAS) em Junho de 2018, intitulado *Probing Evolutionary Population Synthesis Models in the Near Infrared with Early Type Galaxies*. Uma análise complementar a respeito da qualidade dos modelos de populações estelares simples foi feita através da analise de indices espectrais e foi publicada no artigo intitulado *Optical/NIR stellar absorption and emission-line indices from luminous infrared galaxies* que pode ser encontrado no Apêndice A.3

MNRAS **000**, 1–23 (2015) Preprint 9 October 2018 Compiled using MNRAS LATEX style file v3.0

Probing Evolutionary Population Synthesis Models in the Near Infrared with Early Type Galaxies

Luis Gabriel Dahmer-Hahn[1,2]★, Rogério Riffel[1], Alberto Rodríguez-Ardila[3], Lucimara P. Martins[4], Carolina Kehrig[5], Timothy M. Heckman[6], Miriani G. Pastoriza[1], Natacha Z. Dametto[1].

[1] *Departamento de Astronomia, Universidade Federal do Rio Grande do Sul. Av. Bento Goncalves 9500, Porto Alegre, RS, Brazil.*
[2] *Instituto de Física e Química, Universidade Federal de Itajubá, Brasil.*
[3] *Laboratório Nacional de Astrofísica - Rua dos Estados Unidos 154, Bairro das Nações. CEP 37504-364, Itajubá, MG, Brazil.*
[4] *NAT - Universidade Cruzeiro do Sul, Rua Galvão Bueno, 868, São Paulo, SP, Brazil.*
[5] *Instituto de Astrofísica de Andalucía, CSIC, Apartado de correos 3004, 18080 Granada, Spain.*
[6] *Center for Astrophysical Sciences, Department of Physics and Astronomy, The Johns Hopkins University, Baltimore, MD 21218, USA.*

Accepted XXX. Received YYY; in original form ZZZ

ABSTRACT

We performed a near-infrared (NIR, ∼1.0μm-2.4μm) stellar population study in a sample of early type galaxies. The synthesis was performed using five different evolutionary population synthesis libraries of models. Our main results can be summarized as follows: low spectral resolution libraries are not able to produce reliable results when applied to the NIR alone, with each library finding a different dominant population. The two newest higher resolution models, on the other hand, perform considerably better, finding consistent results to each other and to literature values. We also found that optical results are consistent with each other even for lower resolution models. We also compared optical and NIR results, and found out that lower resolution models tend to disagree in the optical and in the NIR, with higher fraction of young populations in the NIR and dust extinction ∼1 magnitude higher than optical values. For higher resolution models, optical and NIR results tend do aggree much better, suggesting that a higher spectral resolution is fundamental to improve the quality of the results.

Key words: galaxies: stellar content – stars: AGB and post-AGB – infrared: galaxies

1 INTRODUCTION

Understanding the processes involved in galaxy evolution is one of the main topics of modern astrophysics. These processes are mainly driven by the star formation history (SFH) of the galaxies. One of the main methods to access the unresolved stellar content of galaxies is by comparing their observed spectra with combinations of simple stellar population (SSPs) libraries. These libraries can be empirical (in this case being limited by the properties of nearby stellar clusters) or can be constructed by using knowledge about stellar evolution, a technique called evolutionary population synthesis (EPS, e.g. Bruzual & Charlot 2003; Maraston 2005; Conroy et al. 2009; Meneses-Goytia et al. 2015; Röck et al. 2016, herefater BC03, M05, C09, MG15 and MIUSCAT, respectively).

The SSPs are usually constructed using one of the two alternatives: isochrone synthesis or "fuel consumption based" algorithms. With the first approach, SSPs are calculated by integrating the stellar contributions to the flux in the various pass-bands of all mass-bins along one isochrone, after assuming an Initial Mass Function (IMF, e.g. BC03). In the second approach, after leaving the main sequence, the duration of each subsequent phase in stellar evolution is calculated by using the fuel consumption theory (e.g. M05).

The big problem is that both approaches result in very different luminosities for short evolutionary stages, especially the crucial TP-AGB phase, whose underlying physics is still poorly known (M05, Marigo et al. 2008; Conroy & Gunn 2010; Conroy 2013; Kriek et al. 2010; Zibetti et al. 2013; Noël et al. 2013; Riffel et al. 2015). This happens be-

★ E-mail: dahmer.hahn@ufrgs.br

cause some processes of stellar evolution (mass-loss, changing opacities, dredge-up events, etc.) are not well understood, and receive a different treatment in each model flavour (e.g. BC03, M05, C09, MG15 and MIUSCAT). Models based on the fuel consumption theory tend to overpredict TP-AGB features while those based on isochrone synthesis generally underestimate them (Zibetti et al. 2013, and references therein), although a few models based on isochrone synthesis also contain large amounts of these stars (e.g. Marigo et al. 2008). Currently, there is no consensus regarding what TP-AGB contribution best reproduces the observed spectra of galaxies. Many stellar absorption features predicted by TP-AGB heavy models have been found, like the 1.1 μm CN band (Riffel et al. 2007), the 1.4 μm CN band (Martins et al. 2013) and the ZrO features at 0.8-1.0 μm (Martins et al. 2013). On the other hand, Zibetti et al. (2013) did not detect the TP-AGB spectral features predicted by M05 in their spectra of post-starburst galaxies at z~0.2. Riffel et al. (2015) found that models based on empirical libraries that predict relatively strong near infrared (NIR) features provide a more accurate description of the data. However, none of the models tested by them successfully reproduces all of the features observed in the spectra. Also, Riffel et al. (2015) claimed that stars in other evolutionary phases like RGB may be crucial to describe the absorption features detected in galaxies and that empirical spectra of these kind of stars should be included in the EPS models.

The libraries of SSPs are then used by a computing code (e.g. STARLIGHT, Cid Fernandes et al. 2005) to determine parameters such as ages, element abundances, stellar masses and stellar mass functions by searching for the combination of SSPs that best reproduces the observed spectrum.

A major issue when characterizing the stellar population of a galaxy is atributed to the dependence of results in the model set used when fitting the underlying stellar features (Chen et al. 2010). This happens because of all the uncertainties related to the construction of the SSPs. Summed to these effects, there is the well known age-metallicity degeneracy, which difficults to distinguish between an old stellar population and a reddened or more metallic younger one (Worthey 1994).

Here we aim to compare, for the first time in the literature, the stellar population predictions derived using NIR spectra of different sets of EPS models for the central region of 6 local early-type galaxies (ETGs) and one spiral galaxy. The former morphologycal type was chosen because it contains a relatively homogeneous old stellar population. We are aware, though, that current day interpretation is that these objects experienced moderately different star formation histories, with the present-day stellar populations slightly differing in metallicity and/or age (Rickes et al. 2009, and references therein).

This paper is structured as follows: The data and reduction process are presented in Section 2. The Stellar Population Synthesis method used in the analysis is presented in Section 3. In Section 4, we present the main results from the synthesis using the different sets of SSPs. A discussion of these results is in Section 5. The final remarks are given in section 6.

2 DATA AND REDUCTION

From the 6 ETGs, 5 are from the Calar Alto Legacy Integral Field Area Survey (CALIFA Sánchez et al. 2012; Walcher et al. 2014; Sánchez et al. 2016). These objects were selected for being the ETGs in the CALIFA data release 1 and accesible to the night sky during the observing run. Also, the CALIFA papers confirmed the presence of warm gas for these 5 galaxies. The final 7 targets were selected on the basis of surface brightness to offer a good compromise between S/N and exposure time. We also observed NGC 4636, a typical LINER, and NGC 5905, classified as SB(r)b, for comparison. The infrared data were obtained at the Astrophysical Research Consortium (ARC) telescope. The TripleSpec (Wilson et al. 2004) instrument was used to obtain cross-dispersed spectra in the range $0.95 - 2.46 \mu m$. We used the 1.1 $''$ slit, resulting in a spectral resolution of R~2000. After each target, we observed an A0V, A1V or A2V star at a similar airmass for flux calibration and telluric correction. Both the science objects and the telluric stars were observed following the dithering pattern object-sky-object. Internal flat-field and arc lamp exposures were also acquired for pixel response and wavelength calibration, respectively. The reduction of the data was done using Triplespectool, a modified version of Spextool (Vacca et al. 2004; Cushing et al. 2004) using standard settings. These spectra are available for download at the MNRAS website.

Table 1 shows the basic properties for the sample. Also, in order to compare NIR results with optical ones, for the five CALIFA objects, we extracted optical spectra using apertures of size similar to that of the NIR slit. For NGC 4636, which is not within the CALIFA targets, we used optical spectra from SDSS. Figure 1 shows Two Micron All Sky survey (2MASS) JHK imaging of the sample with the slit orientation. The individual description of the objects of the sample is presented in the Appendix A. Optical and NIR spectra are shown in Figure 2 and Figure 3, respectively.

3 STELLAR POPULATION SYNTHESIS

The stellar population synthesis technique consists basically of comparing the observed spectrum of a galaxy with a combination of SSPs with different ages and metallicities (this set of SSPs is known as a base of elements, Cid Fernandes et al. 2005), searching for a combination of SSPs that suitably fits the observed spectrum.

For a proper fitting of a galaxy's stellar population, the library of models must cover the range of possible observed spectral properties (e.g. ages and metallicities). It is also fundamental to choose an adequate number of elements for such library in order to have non-degenerate solutions (Schmidt et al. 1991; Cid Fernandes et al. 2005; Dametto et al. 2014). Chen et al. (2010), presented a study in the optical region showing that different models may result in quite different SFHs for the same observed spectrum. Studying six different types of galaxies (star-forming galaxies, composite galaxies, Seyfert 2s, LINERs, E+A, and early-type galaxies) using 6 different EPS models, they found that the differences found are significant, but the dominant populations are unaltered. Also, they found that using the same models, the results depend on the selected ages. In the NIR, this scenario seems

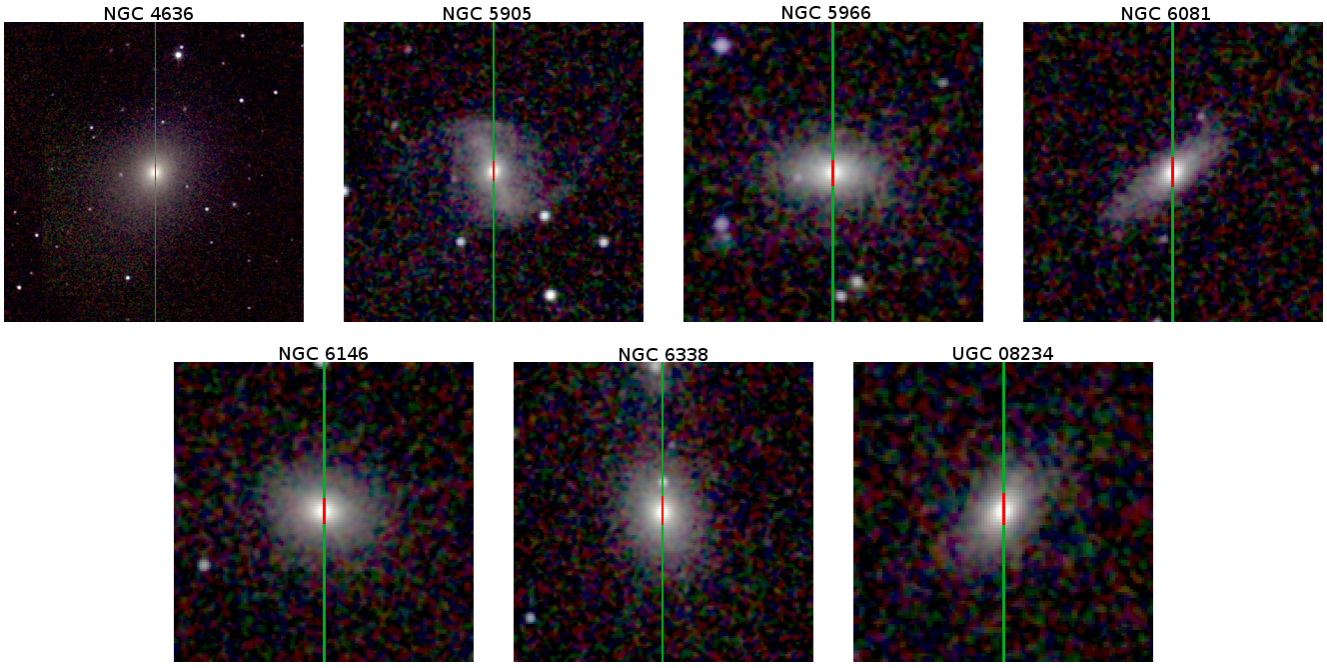

Figure 1. Combined 2MASS JHKs imaging for the galaxy sample. The vertical green line shows the slit orientation while the red segment indicates the aperture used to extract the spectra.

Table 1. Basic properties for the sample.

Object	Morphology [1]	K magnitude [2]	Absolute K magnitude [3]	z [4]	Aperture Radius (arcsec)	Exposure Time (min)	S/N[5]	Optical[6] spectrum
NGC 4636	E0-1	9.0	-21.6	0.003129	10.0	27.0	54	SDSS
NGC 5905	SB(r)b	11.0	-22.4	0.011308	7.0	24.0	30	—
NGC 5966	E	10.7	-23.3	0.014924	6.0	24.0	24	CALIFA
NGC 6081	S0	10.5	-23.8	0.017265	6.0	36.0	45	CALIFA
NGC 6146	E?	10.3	-25.2	0.029420	3.0	36.0	56	CALIFA
NGC 6338	S0	10.6	-24.7	0.027427	4.0	36.0	30	CALIFA
UGC 08234	S0/a	10.7	-24.6	0.027025	6.0	36.0	32	CALIFA

Table Notes: [1] de Vaucouleurs et al. (1991) [2] Two Micron All Sky survey team, 2003, 2MASS extended objects, final release [3] Calculated based in the apparent magnitude and the redshift and assuming H=70 km s^{-1} Mpc^{-1} [4] NED [5] K-band Signal-to-Noise ratio before smoothing the spectra. [6] Presence or absence of SDSS spectra.

to be more dramatic, since the inclusion of the TP-AGB phase in the models is still very uncertain and is a matter of debate (M05, Marigo et al. 2008; Conroy & Gunn 2010; Conroy 2013; Kriek et al. 2010; Zibetti et al. 2013; Noël et al. 2013; Riffel et al. 2015). To properly address this issue we decided to build eight different libraries of models using five different EPS models flavours, as follows:

i. Bruzual & Charlot (2003, BC03)
ii. Maraston (2005, M05)
iii. Conroy et al. (2009, C09)
iv. Meneses-Goytia et al. (2015, MG15)
v. Röck et al. (2016, MIUSCAT)

Details of the EPS models, as well as the choosen ages, metallicities and evolutionary tracks of the SSPs used in the fitting are listed in Table 2. Since MG15 and MIUSCAT have only SSPs with ages t≥1Gyr, in order to allow for a suitable comparison of the results from the different EPS models, we created 3 additional libraries of models by removing the SSPs with ages t<1 Gyr from BC03, M05 and C09 models. These libraries do not include SSPs younger than 1Gyr because of the lack of hot stars in the IRTF library (Cushing et al. 2005; Rayner et al. 2009), which was used to build the models.

It is worth mentioning that in the NIR, the spectral resolution of BC03, M05 and C09 is lower than that of the observed spectra. We then rebinned the data in order to match the spectral resolution of the models. Considering that MG15 and MIUSCAT have a spectral resolution similar to that of the observed spectra, this procedure was not necessary when these later libraries were employed.

Regarding TP-AGB teatment, BC03 uses low-resolution stellar templates from Höfner et al. (2000), while M05 and C09 use higher resolution TP-AGB spectra from

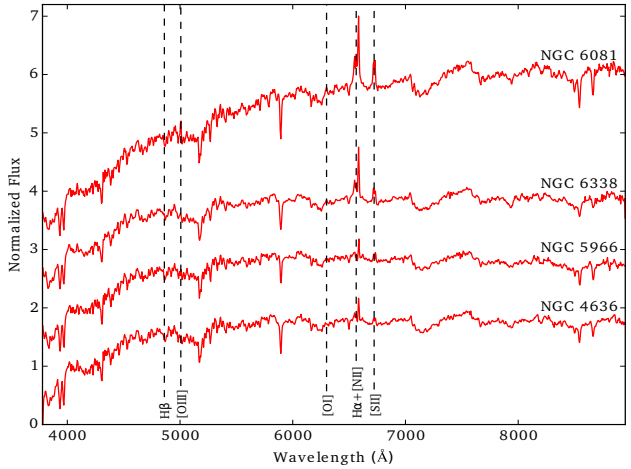

Figure 2. Red curves represent SDSS spectra, which are available for four galaxies of the sample. Rest-frame wavelengths of the main optical emission-lines are indicated.

Lançon & Mouhcine (2002), degrading them to match the rest of the spectra. MG15 and MIUSCAT use the IRTF library, which also contains TP-AGB stars (Riffel et al. 2015).

Since our objects may host a low-luminosity AGN (LLAGN), we followed Riffel et al. (2009, and references therein). In addition, we added to the base set a power law with $F_\nu \propto \nu^{-1.5}$ to represent the featureless continuum (FC) emission from the AGN. Moreover, in the NIR, 8 planck distributions with temperatures from 700 to 1400 K were also added, in steps of 100 K. They represent hot dust continuum heated by the AGN (see Riffel et al. 2009).

3.1 Fitting Procedures

In order to fit the stellar populations, we used the STARLIGHT code, which is described in Cid Fernandes et al. (2004, 2005). In summary, the code fits the observed spectrum with a combination of SSPs in different proportions. It also searches for the internal extinction that best describes the observed spectrum. To this aim, we used the Cardelli et al. (1989) reddening law. Basically, by using a χ^2 minimization approach, STARLIGHT fits an observed spectrum O_λ with a combination of $N_\star$ SSPs solving the equation:

$$M_\lambda = M_{\lambda 0}[\sum_{j=1}^{N\star} x_j b_{j,\lambda} r_\lambda] \otimes G(v_\star, \sigma_\star)$$

where M_λ is a model spectrum, M_{λ_0} is the flux at the normalized point λ_0, $N_\star$ is the number of SSPs used to compose the model, $\vec{x}$ is the population vector so that x_j indicates the contribution from the j-esim SSP normalized at λ_0, $b_{j,\lambda}$ is the j-esim model spectrum, r_λ is the reddening factor $r_\lambda = 10^{-0.4(A\lambda - A\lambda_0)}$, which is parameterized by the dust extinction, Av. The stellar velocity dispersions and group velocities are modelled by a gaussian function $G(v_\star, \sigma_\star)$.

4 RESULTS

The upper pannels of figs. 4 to 10 show, for each galaxy of the sample, the observed (black) and modeled (red) spectra for each of the 8 libraries of models employed. Areas with high atmospheric absortion were shaded in the Figures. The bottom pannels show in blue the luminosity contributions (metallicities summed) for every age of the best model fitted by STARLIGHT.

Since small differences in the ages of the stellar populations are washed away by the noise present in real data, a more consistent and robust way to present the results is in the form of condensed population vectors (Cid Fernandes et al. 2004, 2005). With this in mind, we followed Riffel et al. (2009) and defined the light fraction population vectors as follows: xy (t $\leqslant$ 50Myr), xi (50Myr < t $\leqslant$ 2Gyr) and xo(t > 2Gyr) to represent the young, intermediate and old stellar population vectors, respectively. The same age bins were used for the mass fraction population vectors. Besides, we defined cold and hot dust emission vectors, BB_c for T $\leqslant$ 1000K and BB_h for T > 1000K. The results for these binned population vectors for each galaxy are presented in Table 3.

We also followed Cid Fernandes et al. (2005), who proposed two additional parameters to describe the SP mixture of a galaxy. These parameters are the mean stellar age ($<t>$) and mean metallicity ($<Z>$), which are defined by the following equations

$$< t >_L = \sum_{j=1}^{N\star} x_j log(t_j)$$

$$< Z >_L = \sum_{j=1}^{N\star} x_j Z_j$$

where t_j and Z_j are the age and metallicity of the j-esim SSP. The x_j percentage contribution can be weighted by light (L) and mass (M) fractions. These parameters, together with the Adev, are also listed in Table 3 (Adev is a value that measures the fit quality, according to the relation $|O_\lambda - M_\lambda|/O_\lambda$). For a better visualization of the trends on each library of models, we summed the percentage contribution of the 7 objects and presented them on Fig 11.

Fits performed with the BC03 library of models display higher contribution from young populations, a mild contribution from old populations, no contribution of intermediate-age populations and a higher Av when compared with the other models. With M05, the sample shows a dominance of intermediate age populations, with significant ammounts of young and old populations. When using C09 library, STARLIGHT finds a dominance of old stellar populations, with mild contribution from young populations. When using low resolution models that do not include young populations, BC03io and C09io models result in a ~97% contribution from old populations for all the objects, with the other 3% due to the FC+BB. When using M05io models, on the other hand, 3 objects (NGC 4636, NGC 5905 and NGC 6081) appear dominated by intermediate age populations, with old populations dominating the rest of the sample. With high spectral resolution libraries of models, a dominance of old populations was found, with higher contributions from FC and BB when compared with lower resolution ones. However, results obtained using MIUSCAT library display a trend to-

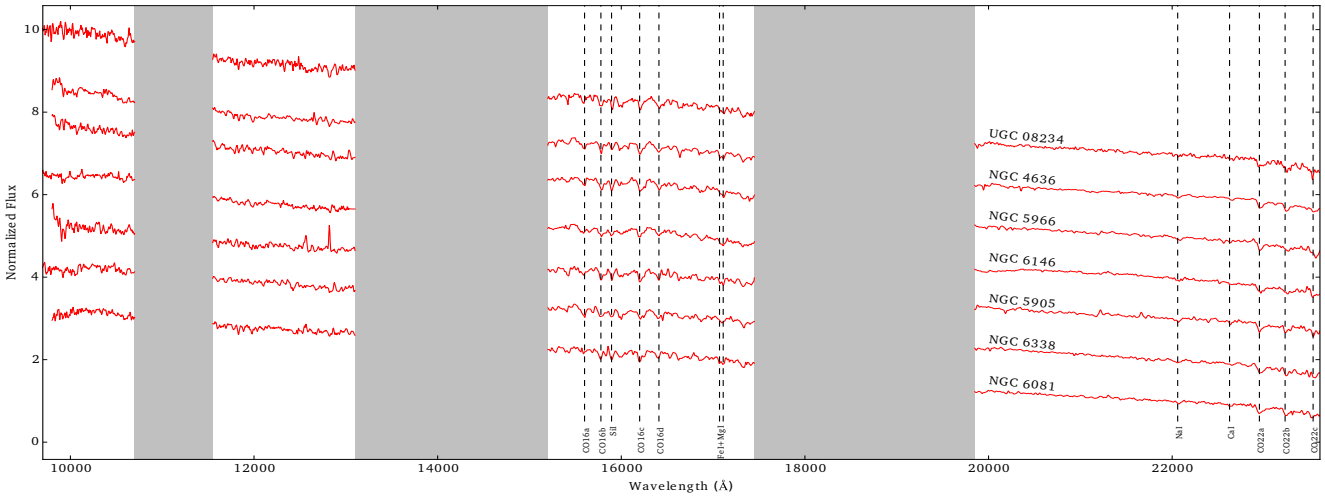

Figure 3. NIR spectra for the sample. The main absorption bands are indicated by dashed lines. High telluric absorption regions are shaded.

Table 2. Basic properties for the EPS models and informations on the used SSPs.

SSP	Ages (Gyr)	Metallicities (Z⊙)	Spectral resolution (Optical/NIR)	Stellar Library	IMF	Evolutionary Track
BC03	0.001, 0.0031, 0.0050, 0.0066, 0.0087, 0.01, 0.014, 0.025, 0.04, 0.055, 0.1, 0.16, 0.28, 0.50, 0.9, 1.27, 1.43, 2.5, 4.25, 6.25, 7.5, 10, 13 and 15	0.005, 0.02, 0.2, 0.4, 1, 2.5	2000/300	STELIB[1] / BaSeL 3.1[2]	Salpeter[3]	Padova[4]
BC03io	1.27, 1.43, 2.5, 4.25, 6.25, 7.5, 10, 13 and 15	0.005, 0.02, 0.2, 0.4, 1, 2.5	2000/300	STELIB/ BaSeL 3.1	Salpeter	Padova
M05	0.001, 0.003, 0.0035, 0.004, 0.005, 0.0055, 0.006, 0.0065, 0.007, 0.0075, 0.008, 0.0085, 0.009, 0.01, 0.015, 0.02, 0.025, 0.03, 0.05, 0.08, 0.2, 0.03, 0.04, 0.05, 0.07, 0.08, 1.0, 1.5, 2.0, 3.0 and 13	0.02, 0.5, 1 and 2	300/300	BaSeL 2.2[2]	Salpeter	Cassisi[5] + Geneva[6]
M05io	1.0, 1.5, 2.0, 3.0 and 13	0.02, 0.5, 1 and 2	300/300	BaSeL 2.2	Salpeter	Cassisi + Geneva
C09	0.00032, 0.00075, 0.0025, 0.0035, 0.004, 0.0044, 0.005, 0.0056, 0.0063, 0.0075, 0.0079, 0.0084, 0.0089, 0.016, 0.032, 0.038, 0.045, 0.063, 0.071, 0.089, 0.21, 0.32, 0.42, 0.53, 0.89, 2.11, 5.31, 6.31, 8.91 and 12.59	0.02, 0.3, 0.95 and 1.5	300/300	BaSeL 3.1	Salpeter	Padova
C09io	2.11, 5.31, 6.31, 8.91 and 12.59	0.02, 0.3, 0.95 and 1.5	300/300	BaSeL 3.1	Salpeter	Padova
MG15	1.0, 1.12, 1.26, 1.41, 1.58, 1.78, 2.0, 2.24, 2.51, 2.82, 3.16, 3.55, 3.98, 4.47, 5, 5.62, 6.31, 7, 7.94, 8.91, 10, 11.2, 12.6 and 14.1	0.0038, 0.0076, 0.019 and 0.03	—/2000	IRTF[7]	Salpeter	Padova
MIUSCAT	1.0, 1.25, 1.5, 1.75, 2.0, 2.25, 2.5, 2.75, 3.0, 3.25, 3.5, 3.75, 4.0, 4.5, 5.0, 5.5, 6.0, 6.5, 7.0, 7.5, 8.0, 8.5, 9.0, 9.5, 10.0, 10.5, 11.0, 11.5, 12.0, 12.5, 13.0, 13.5 and 14.0	0.0085, 0.01, 0.022, 0.027	—/2000	IRTF	Revised Kroupa[8]	BaSTI[9]

Table Notes: (1) Le Borgne et al. (2003) (2) Lejeune et al. (1997, 1998); Westera et al. (2002) (3) Salpeter (1955) (4) Marigo et al. (2008) and references therein (5) Cassisi et al. (1997b,a) (6) Schaller et al. (1992) (7) Cushing et al. (2005); Rayner et al. (2009) (8) Kroupa (2001) (9) Pietrinferni et al. (2004)

ward intermediate-age SSPs whereas results obtained using MG15 library display a trend toward old SSPs. For NGC 6338 and UGC 08234, STARLIGHT found intermediate-age populations dominating the emission (70% and 54 % respectively) when using MIUSCAT library, while no contribution was found when using MG15. For NGC 5905, a contribution of 31% from an intermediate population was found when using MIUSCAT library, while no contribution was found for this age when using MG15. For a better visualization of these differences, we plotted the average contribution from young, intermediate and old populations plus the summed contributions of the FC and BB on Figure 11

The stellar synthesis using low spectral resolution libraries of models did not fit properly the 2.3μm CO bands on NGC 5966, NGC 6146, NGC 6338 and UGC 08234 regardless of the low resolution library of models used. The NaI and CaI lines in the K-band and the absorptions in the J and H band were not fitted with any low resolution library. A similar result was reported by Riffel et al. (2015), who found that none of the models tested by them (BC03, M05 and Maraston & Strömbäck 2011) accurately repro-

Table 3. Results for the NIR synthesis.

Library	FC1.50	BB_c	BB_h	xy	xi	xo	my	mi	mo	Av	$< t >_L$	$< Z >_L$	Adev
							NGC 4636						
BC03	0.0	0.0	0.0	56.8	2.0	41.0	5.7	0.8	93.4	1.52	8.49	0.01796	1.34
M05	0.0	0.0	0.0	26.1	57.1	16.7	1.4	51.1	47.3	1.12	8.58	0.02362	1.05
C09	0.0	0.0	0.0	30.1	0.0	69.9	—	—	—	1.33	8.91	0.01439	1.27
BC03io	0.0	0.0	0.0	0.0	0.0	100.0	0.0	0.0	100.0	1.23	9.90	0.01679	1.86
M05io	0.0	0.0	0.0	0.0	60.2	39.7	0.0	40.0	59.9	1.02	9.36	0.02579	1.08
C09io	0.0	0.0	0.0	0.0	0.0	100.0	—	—	—	1.11	9.84	0.009632	1.54
MG15	0.0	0.0	6.4	0.0	0.0	93.5	—	—	—	0.27	9.82	0.02089	1.50
MIUSCAT	0.0	0.0	6.7	0.0	0.0	93.2	—	—	—	0.57	9.91	0.01624	1.85
							NGC 5905						
BC03	4.2	0.0	0.0	59.4	6.6	29.7	4.4	3.0	92.5	2.12	8.16	0.02282	1.28
M05	3.6	0.0	0.0	43.7	43.7	8.8	3.3	39.9	56.7	1.96	8.18	0.02438	1.02
C09	0.0	0.0	0.0	53.4	16.1	30.4	—	—	—	2.38	8.11	0.02211	1.08
BC03io	8.2	0.0	0.0	0.0	0.3	91.3	0.0	0.4	99.5	1.43	9.44	0.02104	1.85
M05io	5.6	0.0	0.0	0.0	51.5	42.8	0.0	34.9	65.0	1.58	9.38	0.02081	1.21
C09io	7.7	0.0	0.0	0.0	0.0	92.2	—	—	—	1.74	9.75	0.006616	1.56
MG15	13.3	0.0	0.0	0.0	0.0	86.6	—	—	—	0.93	10.06	0.005964	1.59
MIUSCAT	4.5	4.0	0.0	0.0	31.0	60.3	—	—	—	1.10	9.76	0.01444	1.63
							NGC 5966						
BC03	0.0	0.0	0.0	72.5	0.0	27.4	12.5	0.0	87.5	1.70	8.31	0.0146	1.85
M05	0.0	0.0	0.0	25.4	23.3	51.2	0.8	4.5	94.6	1.54	8.70	0.01968	2.12
C09	0.0	0.0	0.0	0.0	0.0	100.0	—	—	—	1.41	10.01	0.002981	2.02
BC03io	0.0	0.0	0.0	0.0	0.0	100.0	0.0	0.0	100.0	1.29	9.78	0.01137	2.54
M05io	0.0	0.0	0.0	0.0	21.6	78.3	0.0	6.2	93.7	1.41	9.71	0.0157	2.20
C09io	0.0	0.0	0.0	0.0	0.0	100.0	—	—	—	1.42	10.02	0.003037	2.01
MG15	0.0	0.0	0.0	0.0	0.0	100.0	—	—	—	0.77	10.15	0.006124	2.11
MIUSCAT	0.0	0.0	0.0	0.0	0.0	100.0	—	—	—	0.53	10.12	0.02184	2.01
							NGC 6081						
BC03	0.0	0.0	0.0	50.2	0.0	49.7	4.3	0.0	95.6	1.85	8.76	0.02432	0.94
M05	0.0	0.0	0.0	8.2	48.1	43.6	0.2	19.2	80.5	1.66	9.28	0.02499	0.97
C09	0.0	0.0	0.0	25.0	0.0	74.9	—	—	—	1.87	9.13	0.01255	1.04
BC03io	0.0	0.0	0.0	0.0	0.0	100.0	0.0	0.0	100.0	1.62	9.85	0.02028	1.28
M05io	0.0	0.0	0.0	0.0	52.9	47.0	0.0	23.8	76.2	1.61	9.52	0.02437	1.00
C09io	0.0	0.0	0.0	0.0	0.0	100.0	—	—	—	1.80	9.92	0.01291	1.06
MG15	0.0	2.3	0.0	0.0	0.0	97.6	—	—	—	1.04	10.07	0.0131	1.31
MIUSCAT	0.0	3.6	0.0	0.0	0.0	96.3	—	—	—	0.90	10.11	0.02622	1.34
							NGC 6146						
BC03	0.0	0.0	0.0	48.7	0.0	51.2	1.1	0.0	98.8	1.28	8.61	0.01962	1.88
M05	0.0	0.0	0.0	32.6	41.1	26.2	0.7	20.5	78.7	1.00	8.64	0.03	1.73
C09	0.0	0.0	0.0	55.3	9.9	34.7	—	—	—	1.42	8.17	0.02094	1.72
BC03io	7.0	0.0	0.1	0.0	0.0	92.8	0.0	0.0	100.0	0.75	9.77	0.01976	2.15
M05io	0.0	0.0	3.9	0.0	40.8	55.2	0.0	13.9	86.0	0.77	9.34	0.03544	1.77
C09io	0.0	0.0	5.5	0.0	0.0	94.4	—	—	—	0.88	10.03	0.01448	2.30
MG15	0.0	0.0	8.4	0.0	18.1	73.4	—	—	—	0.14	9.44	0.006848	2.00
MIUSCAT	0.0	0.0	12.4	0.0	17.8	69.7	—	—	—	0.22	9.51	0.02177	2.34
							NGC 6338						
BC03	0.00	0.00	0.00	72.3	0.00	27. 6	10.2	0.0	89.7	1.49	8.21	0.02373	1.86
M05	0.00	0.00	0.00	54.8	39.4	5.7	6.4	35.2	58.2	1.79	7.82	0.02323	2.12
C09	0.00	0.00	0.00	6.83	13.3	79.7	—	—	—	1.70	9.65	0.003544	2.16
BC03io	0.00	0.00	0.00	0.00	0.00	100.0	0.0	0.0	100.0	1.18	9.50	0.0243	2.23
M05io	0.00	0.00	0.00	0.00	45.7	54.2	0.0	22.4	77.5	1.56	9.37	0.01852	2.25
C09io	0.00	0.00	0.00	0.00	0.00	100.0	—	—	—	1.57	9.96	0.0004	2.09
MG15	1.8	0.00	0.00	0.00	0.00	98.1	—	—	—	0.88	10.13	0.005994	1.76
MIUSCAT	0.7	0.00	0.00	0.00	18.2	81.0	—	—	—	0.97	9.93	0.0119	1.75
							UGC 08234						
BC03	0.0	0.0	0.0	67.8	0.0	32.1	6.5	0.0	93.4	0.89	8.22	0.02292	1.48
M05	0.0	0.0	0.0	46.3	43.0	10.6	4.1	32.2	63.5	0.83	7.95	0.02678	1.41
C09	0.0	0.0	0.0	27.1	0.0	72.8	—	—	—	0.91	9.06	0.01242	1.68
BC03io	0.0	0.0	0.0	0.0	0.0	100.0	0.0	0.0	100.0	0.64	9.90	0.01971	1.74
M05io	0.0	0.0	0.0	0.0	47.7	52.2	0.0	21.6	78.3	0.62	9.42	0.02828	1.59
C09io	0.0	0.0	0.0	0.0	0.0	100.0	—	—	—	0.75	9.89	0.01307	1.77
MG15	0.0	0.0	0.0	0.0	0.0	100.0	—	—	—	0.17	9.88	0.01127	1.94
MIUSCAT	0.0	0.0	0.0	0.0	54.4	45.5	—	—	—	0.21	9.61	0.01744	2.11

duces all of the stellar features observed in the spectra. In all cases, the fits improved when young populations were included. When using high resolution libraries, the absorption features in H and K bands were fitted with a much better agreement between models and observations. However, in the J band, because of the low signal-to-noise ratio, the fits are not as good. Note that this is not a big issue because this band is mostly used for fitting the continuum inclination.

5 DISCUSSION

5.1 NIR models with low spectral resolution

Our sample is composed mainly of ETGs (NGC 4636, NGC 5966, NGC 6081 NGC 6146, NGC 6338 and UGC 08234), which are mainly constituted of old populations (Rickes et al. 2009, and references therein). Analysing Table 3, it is clear that for libraries of models with low spectral resolution (BC03, M05 and C09), the results are linked to the library used rather than to the galaxy properties themselves. This result is different from the optical result reported by Chen et al. (2010). They found that changing the library would result in a change of the percentage contributing light fractions, even though the dominant populations are unaltered. They also compared high and low resolution libraries, and the dominant populations still remained unchanged. This is not the case for the NIR. We found from figs. 4 to 10 (see also Table 3) that for the NIR spectral range, the dominant population is highly dependent on the chosen models.

According to our results, BC03 models give the highest contribution from young populations in the whole sample. The higher young SP contributions are also linked to a higher reddening value, as we can see from Table 3. This result is in agreement with those found by Riffel et al. (2015). However, they are in contrast with the ones reported by Capozzi et al. (e.g. 2016), who found that the inclusion of TP-AGB stars tend to produce results with older ages. This difference might be connected to the fact that they used panchromatic Spectral Energy Distributions, while we used only NIR spectra to make the comparison.

Indeed, for models with low spectral resolution, the large variation in age when young populations are not included implies that the synthesis is unable to distinguish between an old population and a reddened younger one or a more metallic one, since in all cases, the younger populations are followed by a higher extinction or a higher metallicity. This result was first discussed by Worthey (1994) and seems to still hold in the NIR.

Regarding the metallicity, when young populations are present in the fitting process, both BC03 and M05 find values close to solar. C09, on the other hand, tends to find subsolar values of metallicity. When young ages are removed, the same results still hold. Concerning the high resolution libraries, MIUSCAT also finds values close to $Z_{\odot}$ whereas MG15, tends to find subsolar values.

Also, all model sets with low spectral resolution found high ($A_V \gtrsim 1.0$mag) values of extinction. These results are uncompatible with literature results who show that ETGs have negligible amounts of dust (Padilla & Strauss 2008).

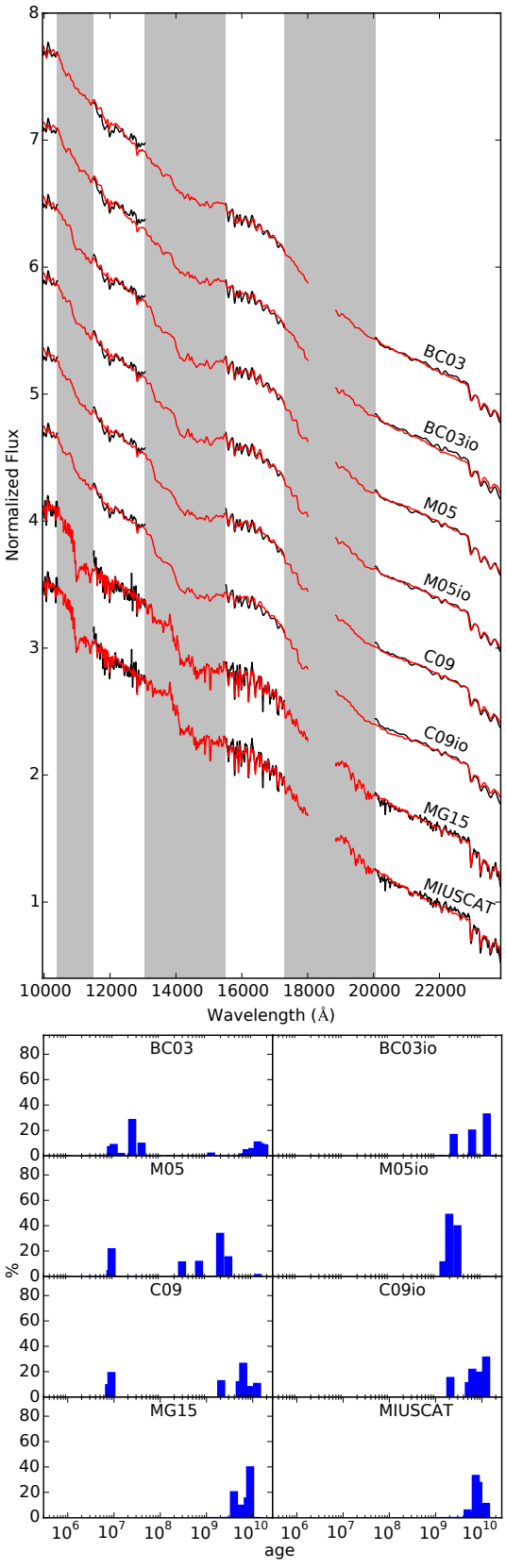

Figure 4. NIR results for NGC 4636 using the 8 libraries of models. On the upper pannel, observed spectrum is shown in black and modelled spectrum is shown in red. Masked areas are shaded. On the bottom pannel, we show in blue the percentage luminosity contribution for every age.

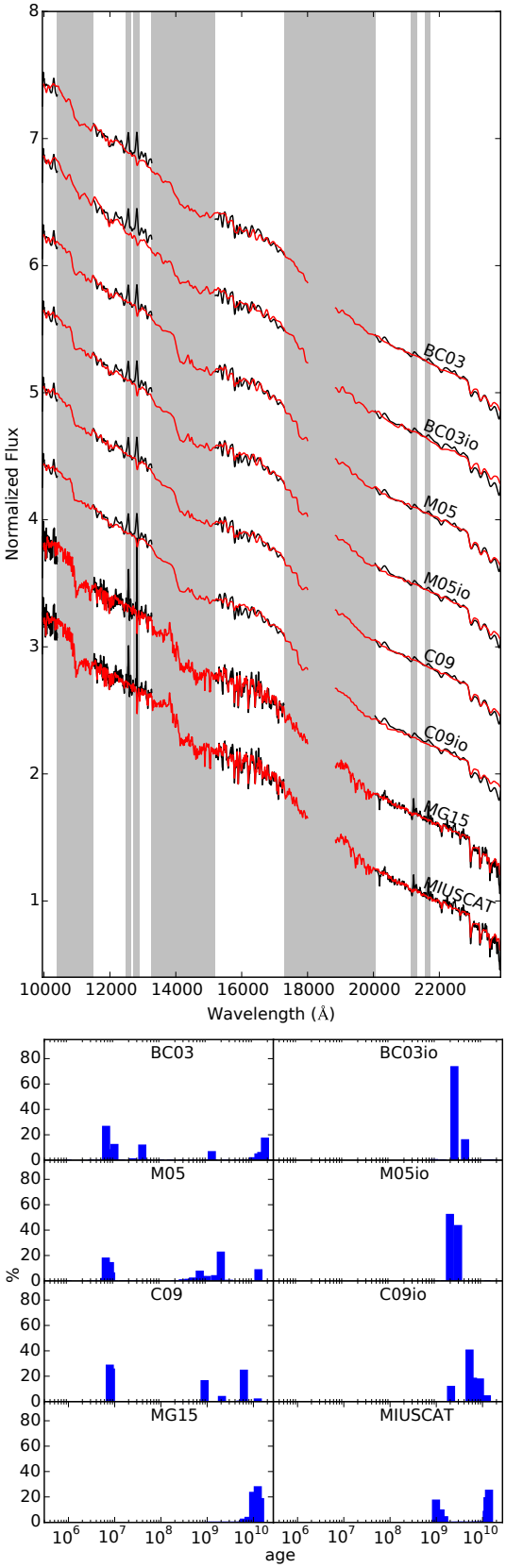

Figure 5. Same as Figure 4 for NGC 5905. Emission lines are also shaded on the upper panel.

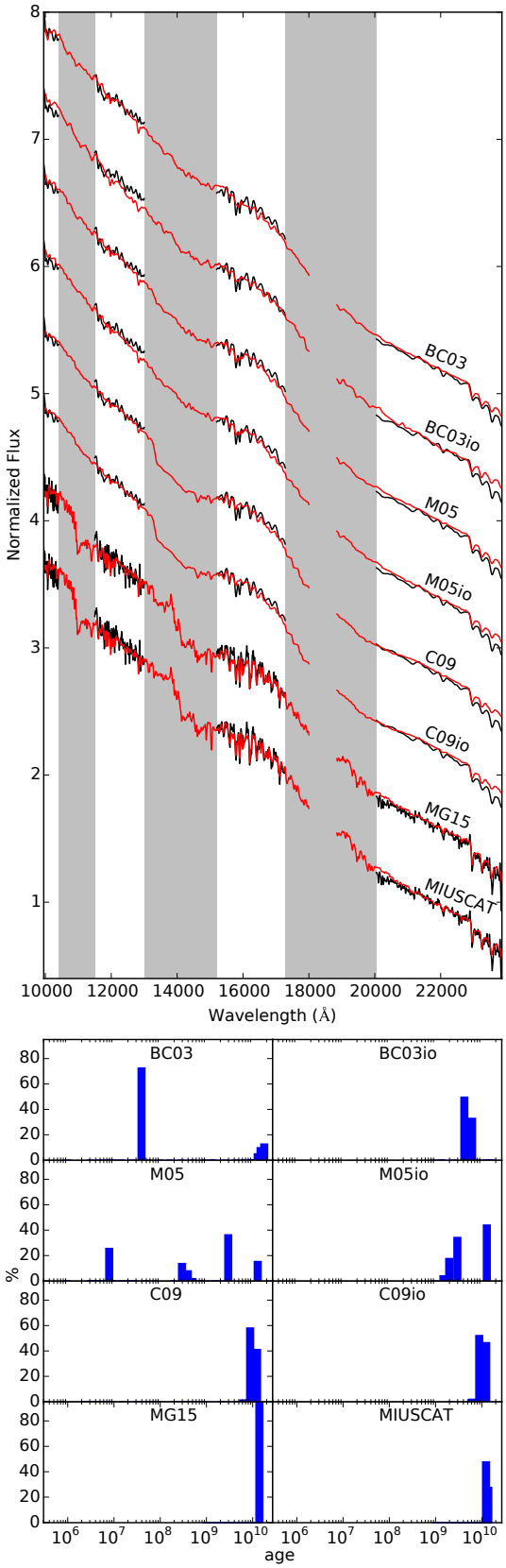

Figure 6. Same as Figure 4 but for NGC 5966

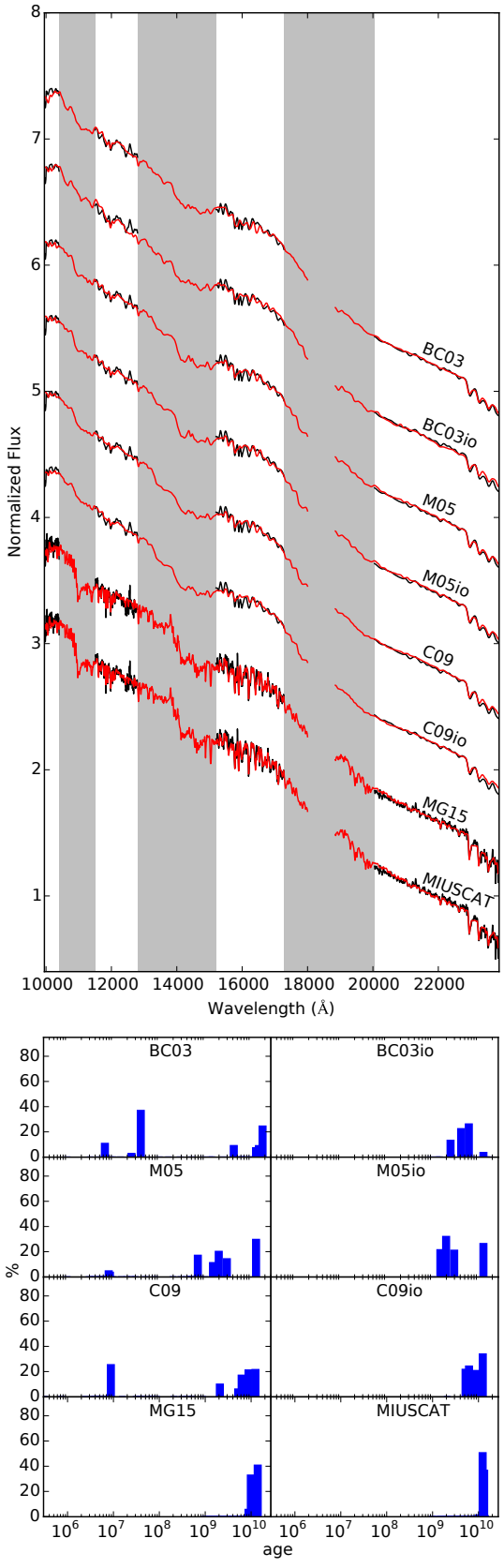

Figure 7. Same as Figure 4 but for NGC 6081

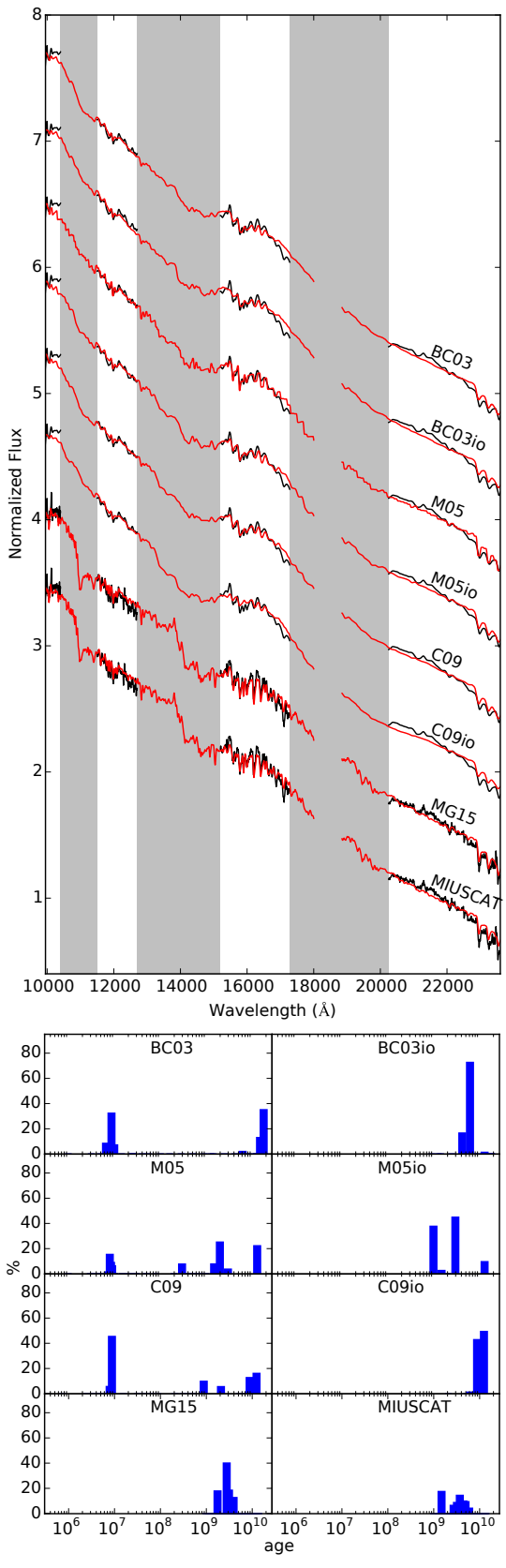

Figure 8. Same as Figure 4 but for NGC 6146

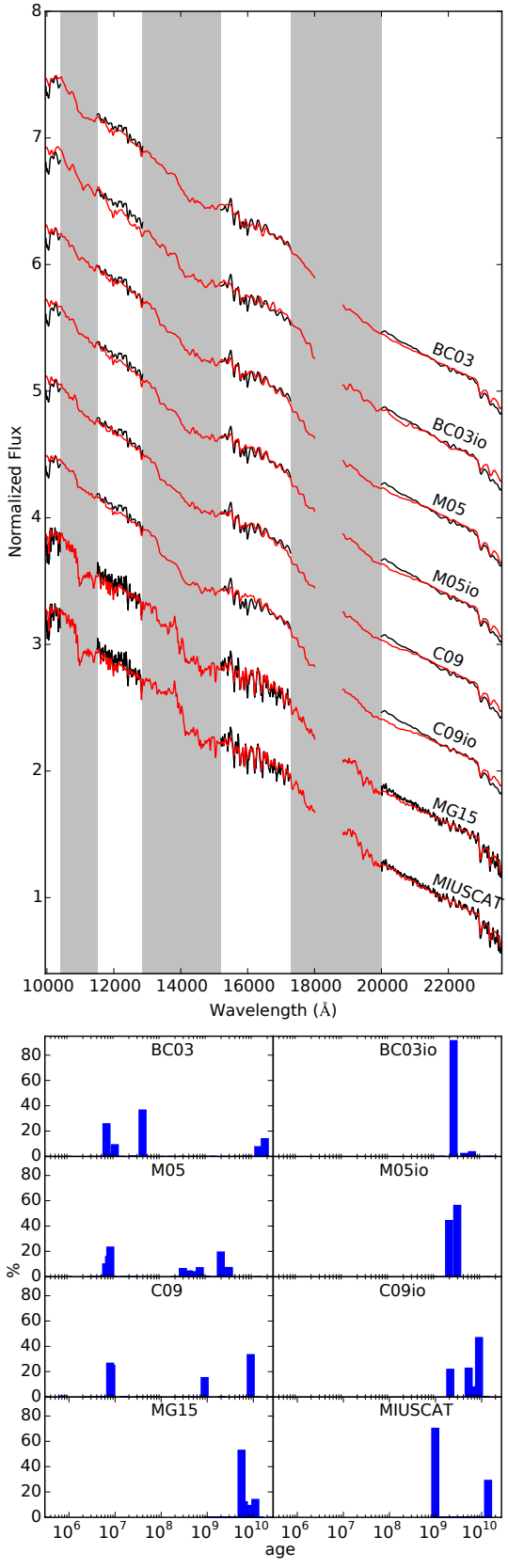

Figure 9. Same as Figure 4 but for NGC 6338

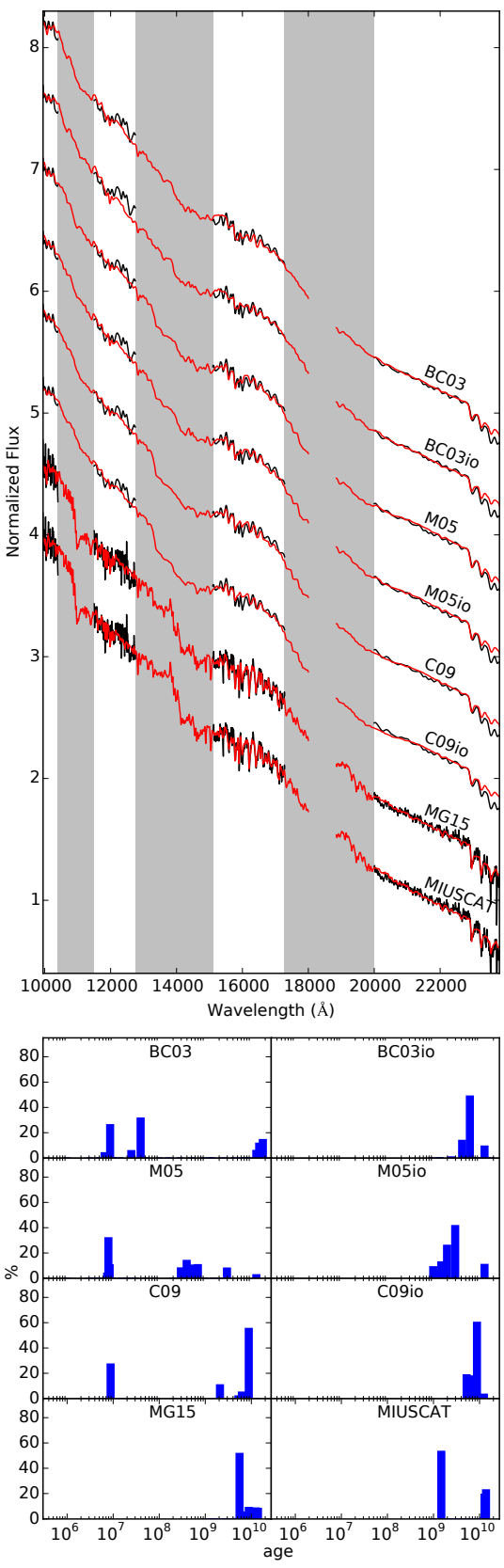

Figure 10. Same as Figure 4 but for UGC 08234

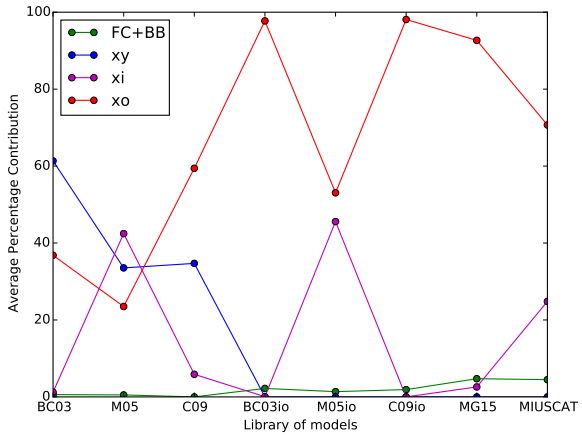

Figure 11. Average percentage contribution for each library of models. Young populations are displayed in blue, intermediate-aged populations in magenta and old stellar populations in red. In green, the summed contributions from featureless continuums and black bodies.

5.2 NIR models with high spectral resolution

For EPS models with high spectral resolution (MG15 and MIUSCAT), the above scenario improved considerably. For three objects (NGC 4636, NGC 5966 and NGC 6081), besides the small (<10%) contribution from dust, only old SSPs were found using both libraries of models. For NGC 6146, both libraries predict a contribution of intermediate populations of ~18%. For NGC 5905, the only spiral galaxy in our sample, a contribution of 31% from intermediate-age stars was obtained with MIUSCAT, but this same percentage was not detected when using MG15. Lastly, for UGC 08234, the fit with MG15 SSPs appear dominated by old populations. However, when MIUSCAT models are employed, the fits become dominated by intermediate-age stellar populations.

Note that it is not possible to fully test libraries with high spectral resolution, because MG15 and MIUSCAT are only composed of SSPs older than 1 Gyr. However, the results we obtained point toward an improvement when using libraries with high resolution. Also, the dust extinction values found with high spectral resolution libraries are much more consistent with literature results that showed that ETGs have very low amounts of dust.

5.3 Comparison with optical results

For the optical region, we also fit the data using the different libraries of models. Since MG15 models are only available in the NIR, we performed the synthesis using only BC03, M05, C09 and MIUSCAT libraries. Also, for a fair comparison between optical and NIR results, we performed the fits using the libraries without the young ages, *i.e.* BC03io, M05io and C09io. Figure 12 and Figure 13 present the optical synthesis results for the 6 galaxies with optical spectra. For each galaxy, we show the observed spectra in black and the model spectrum in red. On Figure 14 and Figure 15, we show the light fraction for each age in blue. The binned light and mass contribution, along with the Av, $<t>_L$, $<Z>_L$ and the Adev for each galaxy are shown in Table 4.

In the optical synthesis, the different libraries of models produced results that are more similar among each other than those derived from the NIR. The only exception were the fits with M05 and M05io models, that also in the optical found a high fraction of intermediate populations. For the other libraries, in the optical region, the synthesis found a dominant contribution of old populations to the light of NGC 4636, NGC 5966, NGC 6081, NGC 6146 and NGC 6338 and a dominance of intermediate-age populations for UGC 08234. Using M05, on the other hand, the synthesis found similar results for all the objects, with small ($\lesssim$5%) contributions of young populations and higher fractions of intermediate age (25%$\lesssim$xi$\lesssim$55%) and old (40%$\lesssim$xi$\lesssim$75%) populations. It is worth mentioning that when using BC03 to fit the optical spectra, a larger contribution from young stellar populations is found compared to the other libraries. However, the dominant old population (or intermediate for UGC 08234) still remains the same found with the other libraries (see Table 4), while in the NIR spectral range, the dominant population contributing to the galaxy emission was different (see Table 3). Removing the SSPs with t<1Gyr from BC03 did not change the results.

For a proper comparison between optical and NIR results, we present in figs. 16 to 23 the values of xy, xi, xo, A_V, $< t >_L$ and $< Z >_L$ found by STARLIGHT both for the optical and NIR ranges. The x axis displays the optical results and the y axis displays the NIR results found by STARLIGHT for the 8 different libraries of models used. For MG15 library, since it only has the NIR range of the spectra, we compared it to the optical results obtained with MIUSCAT. Over the 6 panels of each picture, we plotted a solid line, representing a perfect correlation between optical and NIR. Over the xy, xi and xo panels, we also plotted two dashed lines showing the 10% error margin and two dotted lines showing the 30% error margin. Over the A_V panel, we plotted two dashed lines showing the 0.1 magnitude error margin and two dotted lines showing the 0.3 magnitude error margin. For the $< t >_L$ and $< Z >_L$ panels, since they are logarithmic scales, we did not display error margins.

From figs. 16 to 23, it is possible to see that libraries with low spectral resolution and with young populations usually disagrees in the optical and the NIR about the fractions of each stellar populations that contributes to the galaxy integrated light. It is clear that the fits using BC03, BC03io, C09 and C09io overestimate the amount of younger stellar populations in the NIR when compared to the fits in the optical. On the other hand, the fits with M05 and M05io are more self consistent when comparing optical and NIR results, where in both cases sizable amounts of intermediate age stars are found. All the tests with the lower spectral resolution models displayed a tendency to find extinctions ~1 magnitude higher when fitting the NIR spectral range, compared to optical one. Regarding the metallicity, fits with C09 find lower metallicities in the NIR compared to the optical, whereas BC03 and M05 fits using NIR or optical data converge to nearly the same metallicities.

When SSPs with t≤1Gyr were removed from the libraries, the stellar populations found in the optical and NIR were much closer to each other. From the three libraries with low resolution and without young SSPs, M05io was the

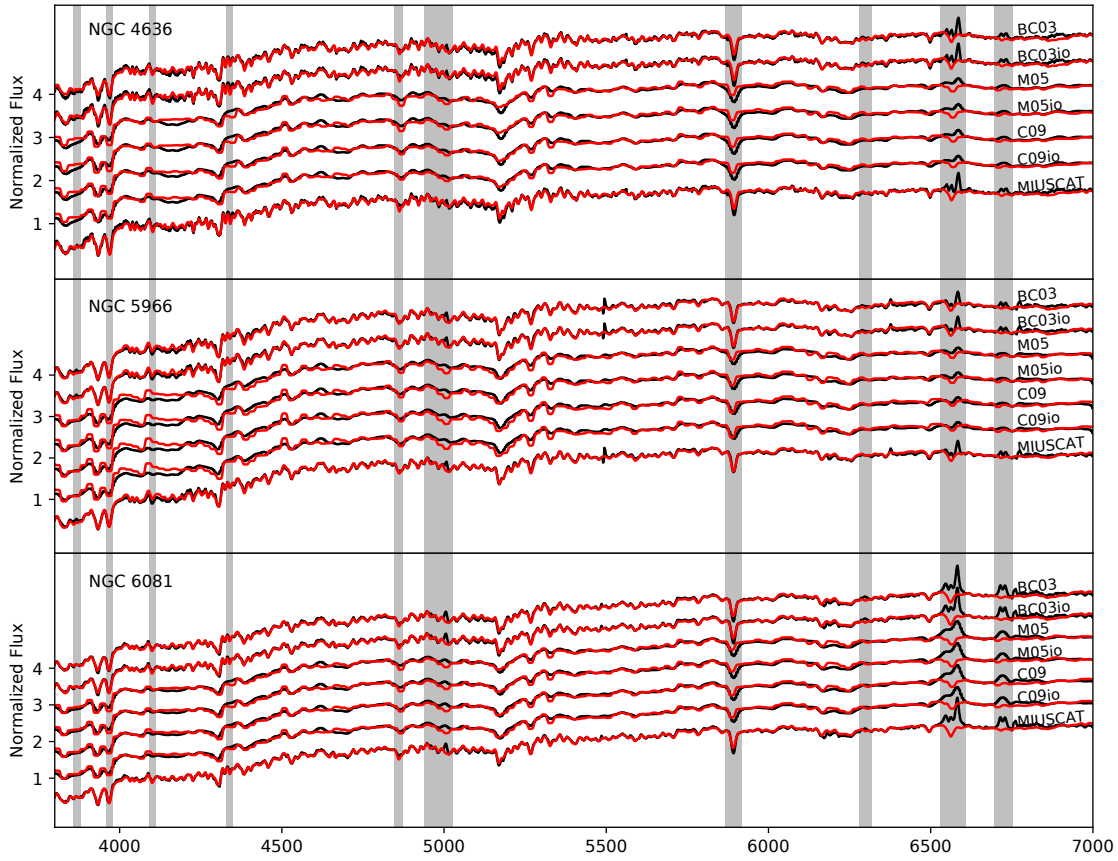

Figure 12. Optical fits for NGC 4636, NGC 5966 and NGC 6081. For each galaxy we present the observed (black) and modeled spectra (red) for the 4 libraries used.

one that found the most consistent results between the two wavelength ranges, with all the points in the xi and xo panels inside the 30% error margin. However, since the amounts of intermediate-age SSPs found with this library are close to ~50% and the sample is mainly composed of ETGs, these results suggest that both wavelength ranges tend equally to overestimate the amount of intermediate-age SSPs.

For BC03io, we found larger amounts of intermediate age stars in the optical than in the NIR, where only old SSPs contributed to the fits. For the tests with C09io, we found a dominant contribution from old SSPs in both spectral ranges. The only exception was UGC 08234, that a contribution of 85% of intermediate-age SSPs was required in the optical but only old SSPs where used in the NIR. When dealing with the reddening, these libraries also tend to overestimate the value of A_V by ~1 magnitude.

The high resolution models, on the other hand, perform considerably better, producing self consistent fits from NIR and optical fits. The reddening found with MG15 models is almost the same for the two wavelength ranges for the whole sample, while MIUSCAT fits required an A_V 0.3mag larger for two objects. From the two last panels of figs. 22 and 23, it is possible to see that for both libraries, optical and NIR tend to find similar values of $< t >_L$ and MG15 tends to find lower values of $< Z >_L$ in the NIR when compared to the optical.

Unfortunately, there are no libraries of high resolution models that include SSPs younger than 1Gyr, meaning that the full scenario cannot be tested. However, our results suggest that high resolution models are essencial to correctly disentangle the stellar population of a galaxy in the NIR, allowing in addition reliable reddening values. Otherwise, it is not possible to fit the absorptions and too much weight is given to the featureless continuum.

Baldwin et al. (2017) found that the impact of age variation in the near-infrared is largely dependent on the shape of the continuum. Our results show that the scenario is more complex, where the shape of the continuum is dependent on a combination of age and extinction, while the depth, shape and width of the absorption features are crucially shaped

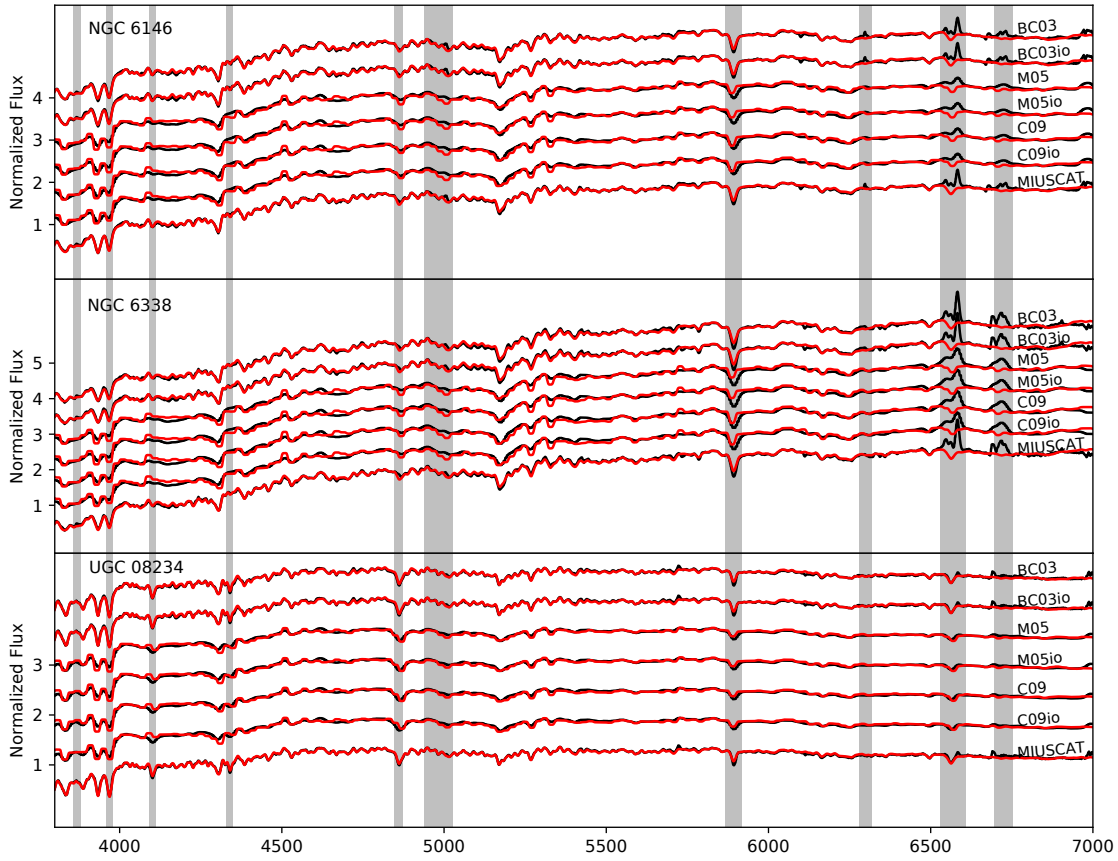

Figure 13. Same of Figure 12 but for NGC 6146, NGC 6338 and UGC 08234.

by the age of the population. For low resolution SSPs these features will be diluted. As a result, STARLIGHT will have more difficulties to differentiate among the individual SSPs. Therefore, we reinforce the need of adequate NIR stellar libraries for hotter stars, allowing thus the production of models with ages younger than 1 Gyr. This is specially important to properly fit the stellar content of active starforming galaxies.

5.4 Absorption Band Measurements

For comparison with future NIR SP studies, we computed the equivalent widths (W_λ) of the NIR absorption features measured with a python version of pacce code (Riffel & Borges Vale 2011). The values of W_λ are presented on Table 5. They were calculated based on the line limits and continuum bandpasses of Table 6. Mild correlations were found between CO16a and MgI, CO16b and SII, CO16c and NaI, CO16d and NaI, FeI and CaI, and the CO22 bands. Since the sample is small, these correlations should be seen with caution.

6 FINAL REMARKS

In this work we compared the stellar population of a sample of 6 ETGs and one spiral galaxy, both in the optical and NIR spectral ranges. We chose for the NIR 8 different bases of SSPs with different spectral resolutions and using different sets of isochrones to separately discuss their effects on the synthesis results. For 4 of the ETGs, we performed spectral synthesis in the optical using SDSS spectra and compared the results with those of the NIR. The approach followed here is based on the STARLIGHT code, which considers the whole observed spectrum, both the continuum and absorption features.

The main results can be sumarized as follows: for spectral synthesis using bases with low spectral resolution, the results are more linked to the library of models used rather than than to the object properties themselves. While BC03 models display a trend toward higher contributions of young populations, M05 usually finds more contributions from intermediate age populations whereas C09 tend to find higher contributions from old stellar populations. On all the cases,

Table 4. Results for the optical synthesis.

Library	xy	xi	xo	my	mi	mo	Av	$< t >_L$	$< Z >_L$	Adev
					NGC 4636					
BC03	17.1	4.3	78.4	0.0	0.1	99.8	-0.01	9.51	0.02398	1.93
M05	2.8	55.6	41.4	0.0	7.3	92.6	0.40	9.31	0.03275	2.50
C09	0.0	2.4	97.5	—	—	—	0.25	9.86	0.01811	2.37
BC03io	0.0	33.7	66.2	0.0	1.2	98.8	0.02	9.82	0.02305	2.02
M05io	0.0	60.7	39.2	0.0	14.2	85.7	0.37	9.39	0.0296	2.59
C09io	0.0	5.4	94.5	—	—	—	0.25	9.86	0.01895	2.38
MIUSCATIR	0.0	22.6	77.3	—	—	—	0.28	9.88	0.02315	1.95
					NGC 5966					
BC03	0.0	11.0	88.4	0.0	1.0	98.9	-0.01	10.11	0.02526	1.84
M05	0.0	26.8	73.2	0.0	2.5	97.4	0.26	9.77	0.02563	3.61
C09	0.0	0.0	100.0	—	—	—	0.16	9.90	0.02232	3.89
BC03io	0.0	15.1	84.8	0.0	1.4	98.5	-0.00	10.08	0.0265	1.83
M05io	0.0	40.5	59.5	0.0	9.9	90.0	0.23	9.73	0.02708	3.65
C09io	0.0	0.0	100.0	—	—	—	0.16	9.88	0.02289	3.89
MIUSCATIR	0.0	0.0	100.0	—	—	—	0.18	10.09	0.02663	1.74
					NGC 6081					
BC03	5.0	23.9	71.0	0.0	1.1	98.8	0.69	9.75	0.01817	1.60
M05	0.0	49.8	50.1	0.0	6.5	93.4	0.91	9.53	0.02232	2.48
C09	0.0	0.0	100.0	—	—	—	0.85	9.87	0.01503	2.60
BC03io	0.0	34.6	65.3	0.0	1.6	98.3	0.71	9.82	0.01778	1.69
M05io	0.0	47.7	52.2	0.0	6.1	93.8	0.88	9.59	0.0181	2.51
C09io	0.0	0.0	100.0	—	—	—	0.84	9.92	0.01447	2.59
MIUSCATIR	0.0	16.7	83.2	—	—	—	0.92	9.83	0.02177	1.49
					NGC 6146					
BC03	6.6	9.6	83.0	0.0	0.3	99.6	-0.03	9.84	0.0213	1.29
M05	0.0	38.6	61.4	0.0	4.4	95.5	0.28	9.60	0.02732	2.65
C09	0.0	0.0	100.0	—	—	—	0.16	9.89	0.02022	2.72
BC03io	0.0	13.3	86.6	0.0	0.5	99.5	-0.02	10.04	0.01982	1.33
M05io	0.0	33.3	66.6	0.0	4.5	95.4	0.26	9.71	0.02072	2.70
C09io	0.0	0.0	100.0	—	—	—	0.16	9.88	0.02289	3.89
MIUSCATIR	0.0	13.0	86.9	—	—	—	0.22	9.91	0.02246	1.13
					NGC 6338					
BC03	1.3	1.0	94.0	0.0	0.0	99.9	0.33	10.16	0.02569	1.77
M05	0.0	25.2	74.8	0.0	2.3	97.6	0.67	9.79	0.02561	3.17
C09	0.0	0.0	100.0	—	—	—	0.53	10.05	0.01783	3.36
BC03io	0.0	0.9	99.0	0.0	0.0	99.9	0.33	10.22	0.02434	1.78
M05io	0.0	21.5	78.4	0.0	2.0	97.9	0.65	9.87	0.02038	3.22
C09io	0.0	0.0	100.0	—	—	—	0.53	10.03	0.01938	3.34
MIUSCATIR	0.0	3.7	96.2	—	—	—	0.59	10.10	0.02628	1.63
					UGC 08234					
BC03	0.0	86.5	13.4	0.0	26.2	73.7	-0.07	9.15	0.04017	1.18
M05	0.0	40.0	60.0	0.0	8.5	91.4	0.03	9.28	0.02446	2.12
C09	0.0	65.5	34.4	—	—	—	0.23	9.28	0.02118	2.32
BC03io	0.0	85.0	14.9	0.0	25.9	74.1	-0.07	9.21	0.0368	1.18
M05io	0.0	42.7	57.2	0.0	14.0	85.9	-0.05	9.34	0.01896	2.20
C09io	0.0	61.5	38.4	—	—	—	0.21	9.29	0.01998	2.32
MIUSCATIR	0.0	67.1	32.8	—	—	—	0.07	9.40	0.02134	1.00

Table 5. Equivalent widths for the NIR absorption bands measured in Å.

Galaxy/Line Average Error	CO16a 0.10	CO16b 0.12	SiI 0.13	CO16c 0.32	CO16d 0.22	FeI 0.12	MgI 0.8	NaI 0.21	CaI 0.21	CO22a 0.86	CO22b 1.24	CO22c 1.58
NGC4636	2.06	3.08	1.97	6.41	4.71	0.42	2.47	4.55	2.86	16.42	18.81	18.01
NGC5905	1.69	3.69	3.03	7.61	5.03	0.47	2.03	5.79	4.08	17.50	6.78	8.94
NGC5966	1.74	4.29	3.72	7.17	3.89	0.37	2.41	4.68	2.23	7.79	4.73	6.68
NGC6081	0.23	3.18	2.77	6.53	3.40	0.53	1.95	3.68	3.26	19.77	24.23	27.59
NGC6146	2.38	4.23	4.07	5.89	3.72	0.39	2.55	2.50	1.65	34.72	46.77	50.05
NGC6338	2.31	3.13	2.90	5.53	4.34	0.47	2.10	3.57	3.76	13.79	13.60	8.64
UGC08234	1.29	3.36	3.36	5.24	3.91	–	1.82	2.20	3.69	17.77	25.97	35.33

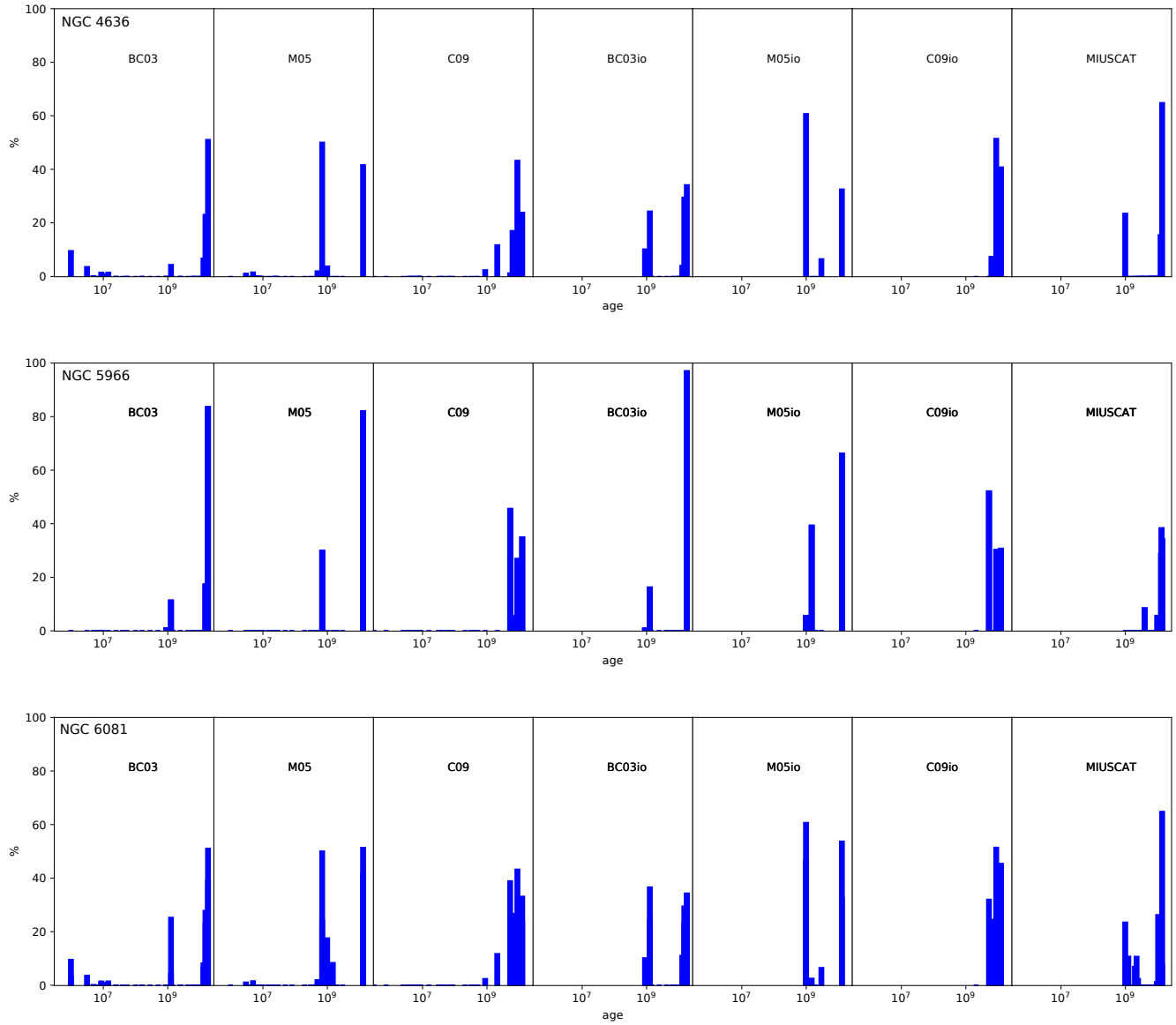

Figure 14. Optical star formation histories for NGC 4636, NGC 5966 and NGC 6081, metallicities summed.

the values of Adev are compatible, meaning that none of these bases offer a more reliable result. When using bases with high spectral resolution, MG15 and MIUSCAT produced more consistent results if compared to low spectral resolution libraries. Out of the 7 galaxies, the two libraries fitted consistent results for six of them.

The optical synthesis for the elliptical galaxies revealed a dominance of old stellar populations. The only exception was M05 library, which still found a high fraction of intermediate age populations. This may indicate that the TP-AGB treatment plays an important role, even in the optical region.

When comparing optical and NIR results, we found that NIR fits using low spectral resolution libraries tend to overestimate the amount of young SSPs and the reddening. The only exception were the M05 models, wich produced self consistent fits, but predicted sizable ammounts of intermediate age stars for the galaxies. For libraries with high spectral resolution, since they do not include young SSPs, this scenario cannot be fully tested. However, the reddening found was compatible with literature. Also, high spectral resolution libraries produced results much more consistent if compared to models with low spectral resolution.

We tabulated the equivalent widths (W_λ) of the NIR absorption features and the optical emission line fluxes to be used in future studies. Lastly, from the emission line ratios, we classified, for the first time in the literature, NGC 6081 and NGC 6338 as LINERs.

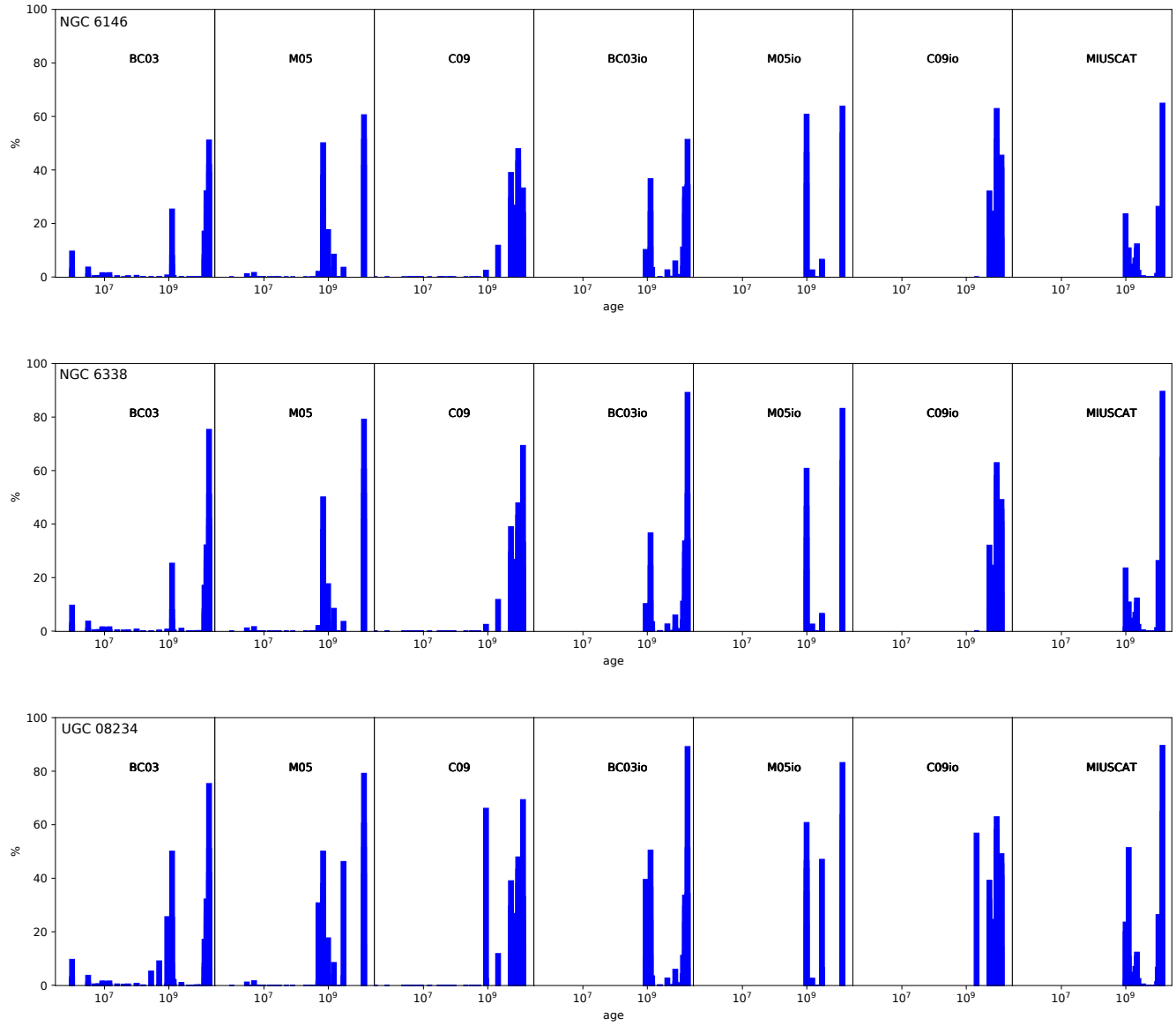

Figure 15. Same as Figure 14 but for NGC 6146, NGC 6338 and UGC 08234.

ACKNOWLEDGEMENTS

LGDH thanks CAPES and CNPq. RR thanks CNPq and FAPERGS for partial funding this project. ARA thanks CNPq for partial support to this work. LPM thanks CNPQ and FAPESP for partial funding of this project. CK acknowledges support through the research project AYA2017-79724-C4-4-P from the Spanish PNAYA. This research made use of the NASA/IPAC Extragalactic Database (NED), which is operated by the Jet Propulsion Laboratory, California Institute of Technology, under contract with the National Aeronautics and Space Administration. This study uses data provided by the Calar Alto Legacy Integral Field Area (CALIFA) survey (http://califa.caha.es/). Based on observations collected at the Centro Astronómico Hispano Alemán (CAHA) at Calar Alto, operated jointly by the Max-Planck-Institut für Astronomie and the Instituto de Astrofísica de Andalucía (CSIC). We thank the referee Reynier Peletier for carefully reading our paper and for giving such constructive comments which substantially helped improving the quality of the paper.

REFERENCES

Baldwin J. A., Phillips M. M., Terlevich R., 1981, PASP, 93, 5
Baldwin C. M., McDermid R. M., Kuntschner H., Maraston C., Conroy C., 2017, preprint, (arXiv:1709.09300)
Bamford S. P., Rojas A. L., Nichol R. C., Miller C. J., Wasserman L., Genovese C. R., Freeman P. E., 2008, MNRAS, 391, 607
Bruzual G., Charlot S., 2003, MNRAS, 344, 1000
Caccianiga A., Marchã M. J., Antón S., Mack K.-H., Neeser M. J., 2002, MNRAS, 329, 877

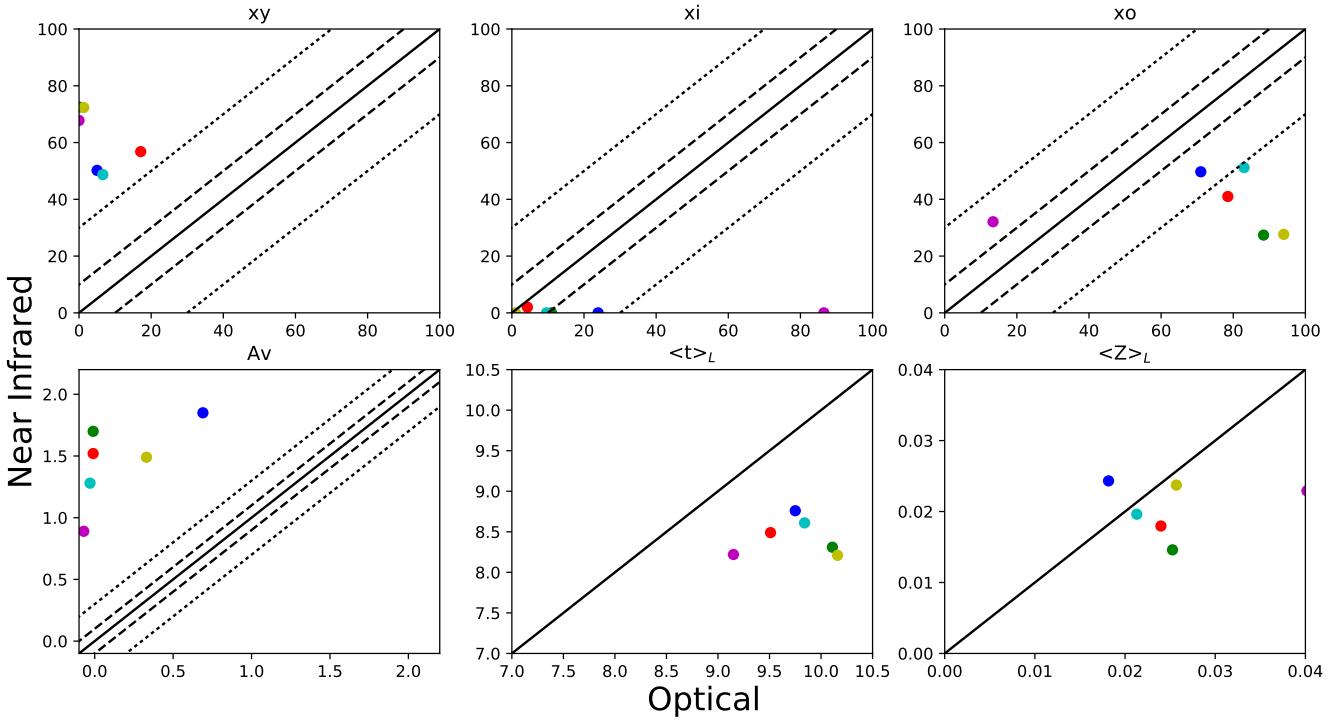

Figure 16. Comparison between optical and NIR results found using BC03 library of models. In the upper panels, we present from left to right the xy, xi and xo results. In the bottom panels, we show the A_V, $< t >_L$ and $< Z >_L$ results. Over all panels, we plotted a solid line, representing a perfect correlation between optical and NIR. Also, we plotted dashed and dotted lines representing error margins of 10 and 30% in the xy, xi and xo panel and error margins of 0.1 and 0.3 magnitudes in the A_V panel. Each galaxy was plotted in a different color: NGC 4636 - red, NGC 5966 - green, NGC 6081 - blue, NGC 6146 - cyan, NGC 6338 - yellow, UGC 08234 - magenta.

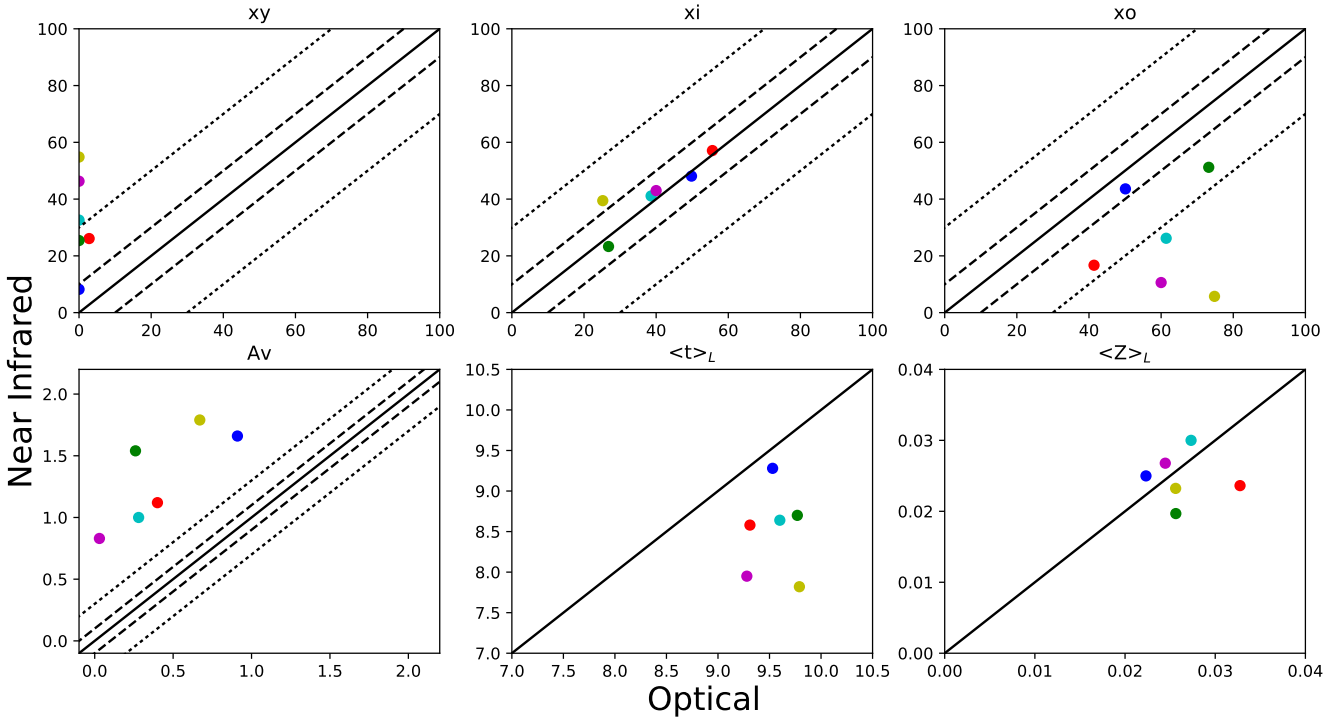

Figure 17. Same of Figure 16, but for M05 library of models.

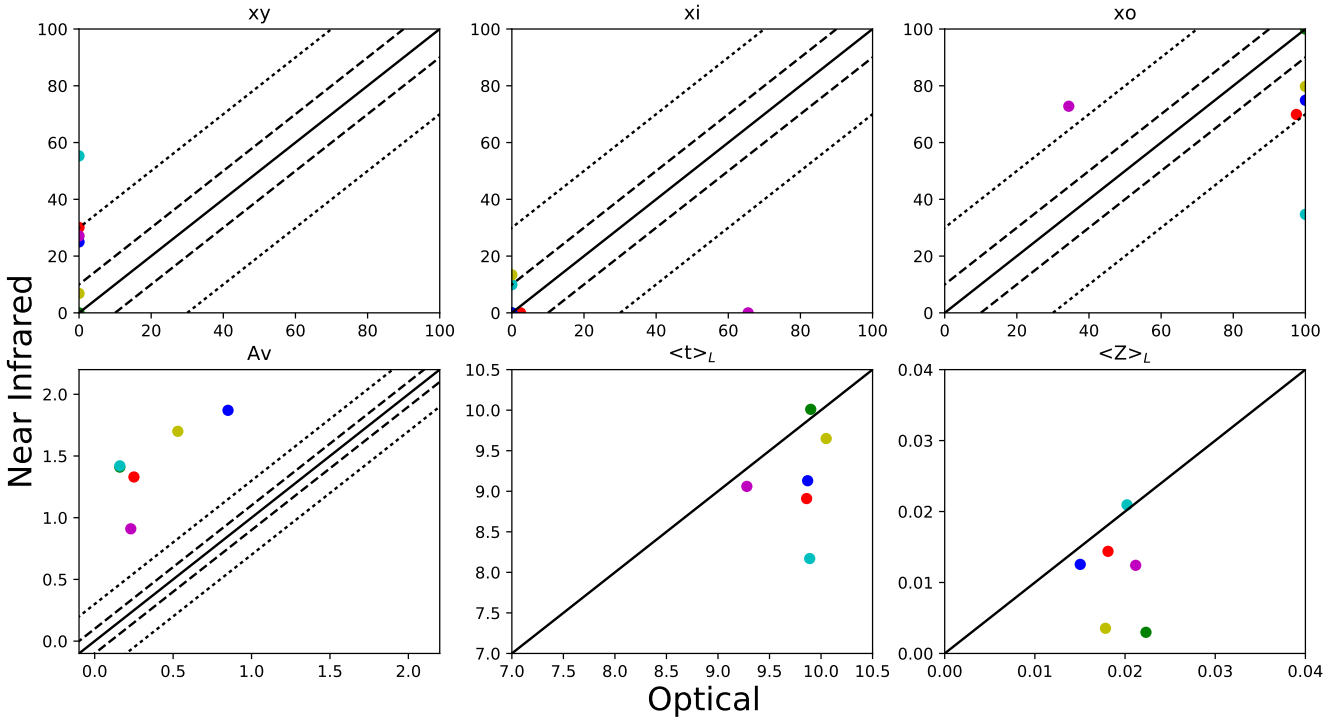

Figure 18. Same of Figure 16, but for C09 library of models.

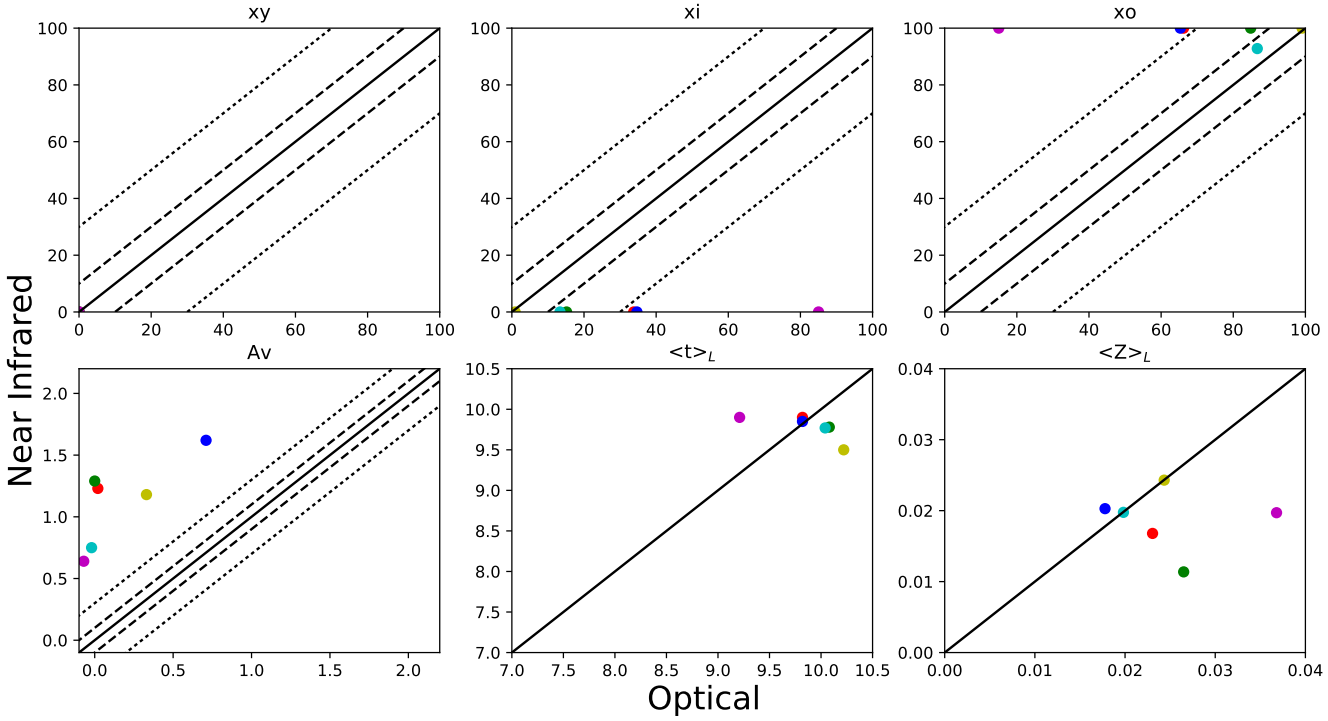

Figure 19. Same of Figure 16, but for BC03io library of models.

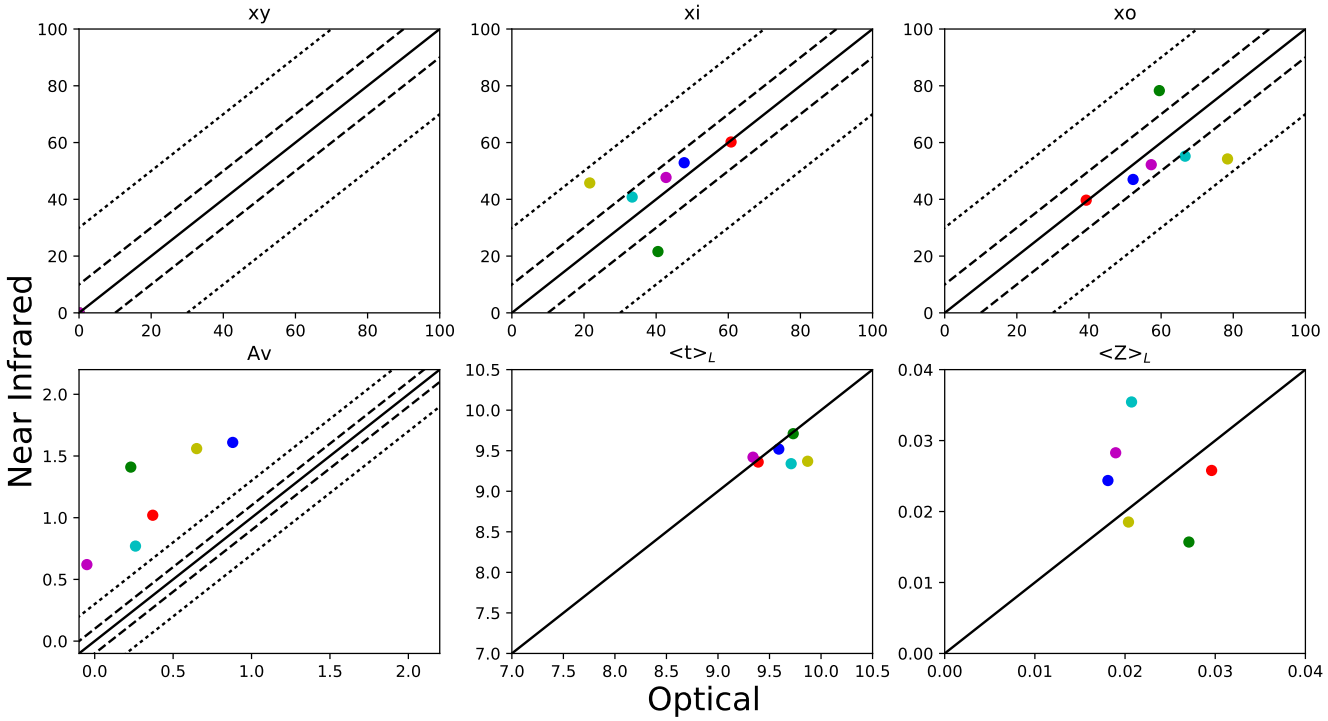

Figure 20. Same of Figure 16, but for M05io library of models.

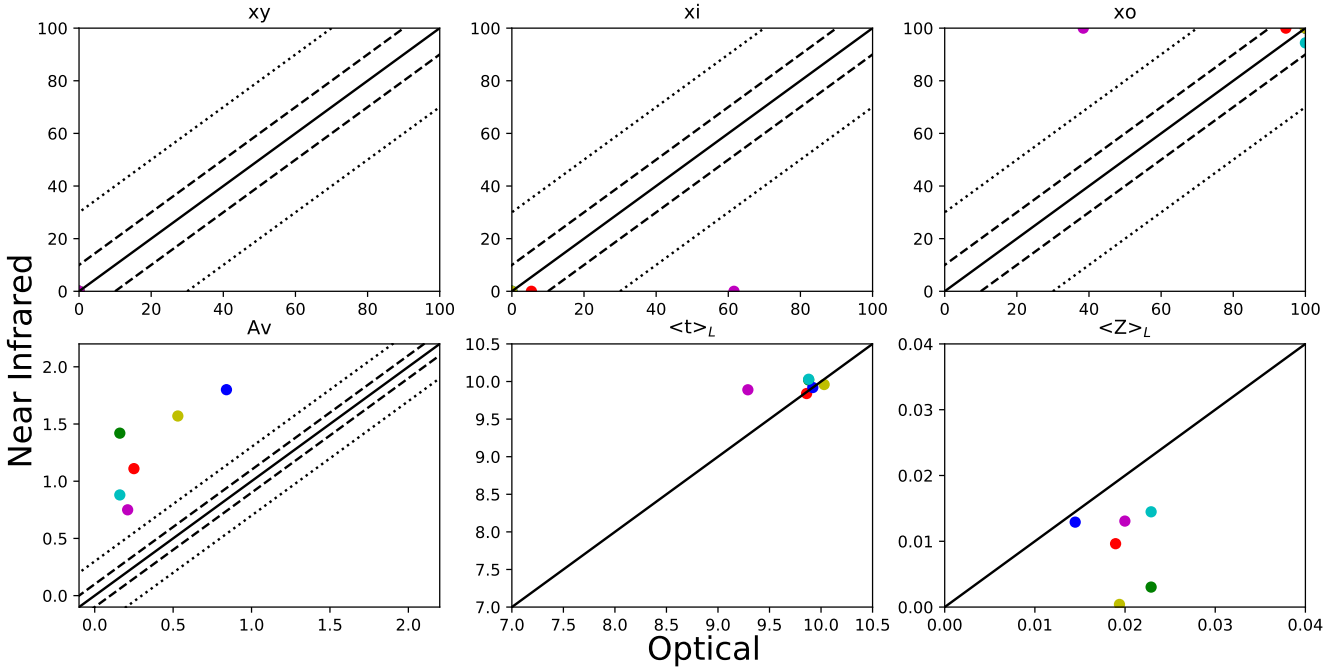

Figure 21. Same of Figure 16, but for C09io library of models.

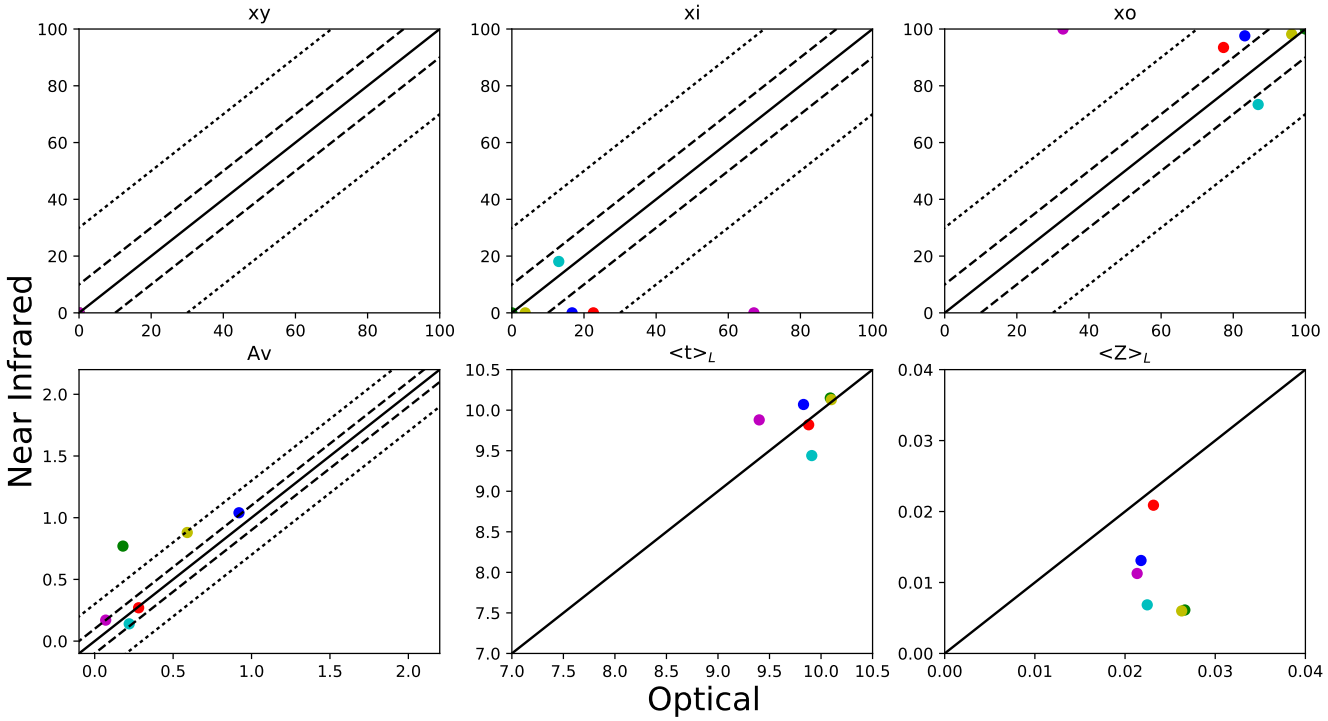

Figure 22. Same of Figure 16, but for MG15 library of models.

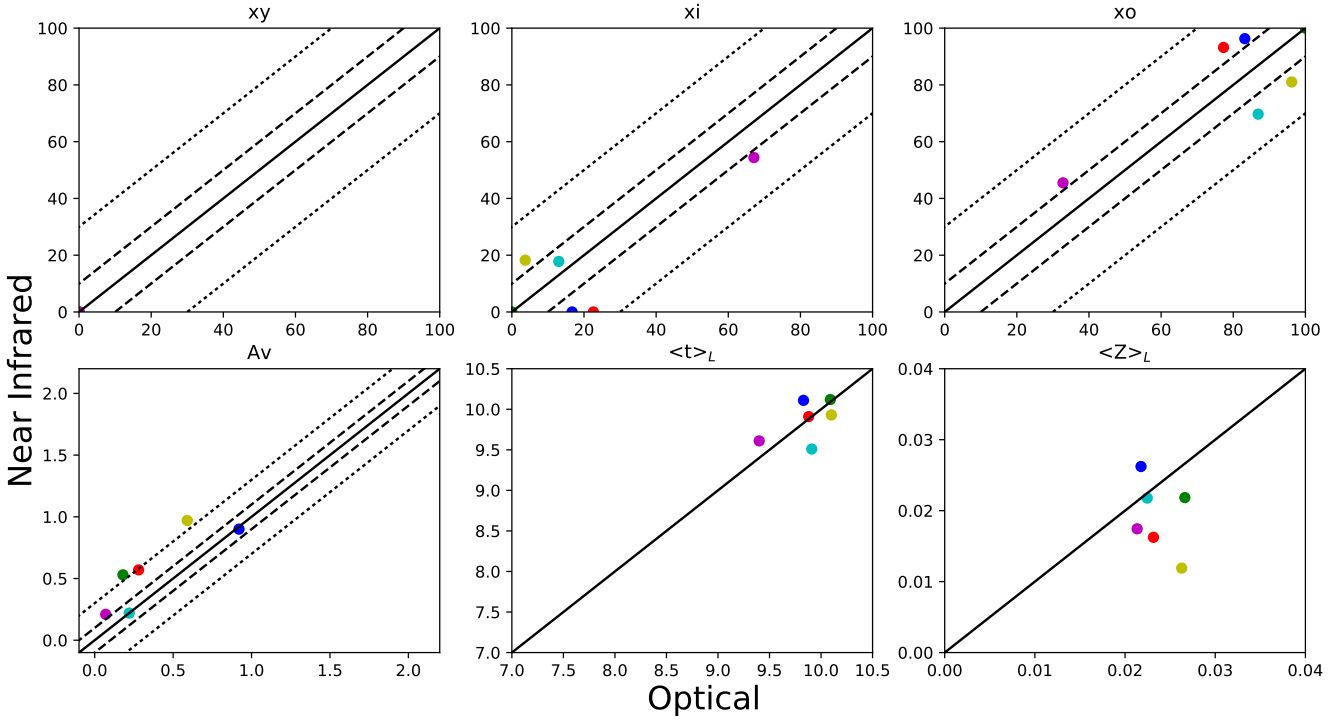

Figure 23. Same of Figure 16, but for MIUSCAT library of models.

Table 6. Line limits and continuum bandpasses.

Centre (Å)	Main Absorber	line limits (Å)	continuum bandpass (Å)
15587	CO	15555-15620	15110-15170, 15390-15410,16270-16310,16570-16580
15772	CO	15735-15810	15110-15170, 15390-15410,16270-16310,16570-16580
15890	SiI	15850-15930	15110-15170, 15390-15410,16270-16310,16570-16580
16215	CO	16145-16285	15110-15170, 15390-15410,16270-16310,16570-16580
16385	CO	16340-16430	15110-15170, 15390-15410,16270-16310,16570-16580
17054	FeI	17025-17083	16970-17083, 17140-17200
17106	MgI	17083-17130	16970-17083, 17140-17200
22025	NaI	21950-22100	21700-21930,22150-22200
22620	CaI	22570-22670	22450-22550,22680-22730
23015	CO	22870-23160	22690-22790, 23655-23680,23890-23920
23290	CO	23160-23420	22690-22790, 23655-23680,23890-23920
23535	CO	23420-23650	22690-22790, 23655-23680,23890-23920

Table Notes: The NIR indexes are based on Riffel et al. (2008, 2009, 2011, 2015).

Capozzi D., Maraston C., Daddi E., Renzini A., Strazzullo V., Gobat R., 2016, MNRAS, 456, 790
Cardelli J. A., Clayton G. C., Mathis J. S., 1989, ApJ, 345, 245
Cassisi S., degl'Innocenti S., Salaris M., 1997a, MNRAS, 290, 515
Cassisi S., Castellani M., Castellani V., 1997b, A&A, 317, 108
Chen X. Y., Liang Y. C., Hammer F., Prugniel P., Zhong G. H., Rodrigues M., Zhao Y. H., Flores H., 2010, A&A, 515, A101
Cid Fernandes R., Gu Q., Melnick J., Terlevich E., Terlevich R., Kunth D., Rodrigues Lacerda R., Joguet B., 2004, MNRAS, 355, 273
Cid Fernandes R., Mateus A., Sodré L., Stasińska G., Gomes J. M., 2005, MNRAS, 358, 363
Conroy C., 2013, ARA&A, 51, 393
Conroy C., Gunn J. E., 2010, ApJ, 712, 833
Conroy C., Gunn J. E., White M., 2009, ApJ, 699, 486
Cushing M. C., Vacca W. D., Rayner J. T., 2004, PASP, 116, 362
Cushing M. C., Rayner J. T., Vacca W. D., 2005, ApJ, 623, 1115
Dametto N. Z., Riffel R., Pastoriza M. G., Rodríguez-Ardila A., Hernandez-Jimenez J. A., Carvalho E. A., 2014, MNRAS, 443, 1754
Dressel L. L., Condon J. J., 1978, ApJS, 36, 53
Forman W., Jones C., Tucker W., 1985, ApJ, 293, 102
Gomes J. M., et al., 2016, A&A, 588, A68
Höfner S., Loidl R., Aringer B., Jørgensen U. G., Hron J., 2000, in Salama A., Kessler M. F., Leech K., Schulz B., eds, ESA Special Publication Vol. 456, ISO Beyond the Peaks: The 2nd ISO Workshop on Analytical Spectroscopy. p. 299
Jones C., Forman W., Vikhlinin A., Markevitch M., David L., Warmflash A., Murray S., Nulsen P. E. J., 2002, ApJ, 567, L115
Kehrig C., et al., 2012, A&A, 540, A11
Kriek M., et al., 2010, ApJ, 722, L64
Kroupa P., 2001, MNRAS, 322, 231
Lançon A., Mouhcine M., 2002, A&A, 393, 167
Le Borgne J.-F., et al., 2003, A&A, 402, 433
Lejeune T., Cuisinier F., Buser R., 1997, A&AS, 125
Lejeune T., Cuisinier F., Buser R., 1998, A&AS, 130, 65
Maraston C., 2005, MNRAS, 362, 799
Maraston C., Strömbäck G., 2011, MNRAS, 418, 2785
Marigo P., Girardi L., Bressan A., Groenewegen M. A. T., Silva L., Granato G. L., 2008, A&A, 482, 883
Martel A. R., et al., 2004, AJ, 128, 2758
Martins L. P., Lanfranchi G., Gonçalves D. R., Magrini L., Teodorescu A. M., Quireza C., 2012, MNRAS, 419, 3159
Martins L. P., Rodríguez-Ardila A., Diniz S., Gruenwald R., de Souza R., 2013, MNRAS, 431, 1823
Meneses-Goytia S., Peletier R. F., Trager S. C., Vazdekis A., 2015, A&A, 582, A97
Nilson P., 1973, Uppsala general catalogue of galaxies
Noël N. E. D., Greggio L., Renzini A., Carollo C. M., Maraston C., 2013, ApJ, 772, 58
Padilla N. D., Strauss M. A., 2008, MNRAS, 388, 1321
Pandge M. B., Vagshette N. D., David L. P., Patil M. K., 2012, MNRAS, 421, 808
Pietrinferni A., Cassisi S., Salaris M., Castelli F., 2004, ApJ, 612, 168
Raichur H., Das M., Herrero A. A., Shastri P., Kantharia N. G., 2015, Ap&SS, 357, 32
Rayner J. T., Cushing M. C., Vacca W. D., 2009, ApJS, 185, 289
Rickes M. G., Pastoriza M. G., Bonatto C., 2009, A&A, 505, 73
Riffel R., Borges Vale T., 2011, Ap&SS, 334, 351
Riffel R., Pastoriza M. G., Rodríguez-Ardila A., Maraston C., 2007, ApJ, 659, L103
Riffel R., Pastoriza M. G., Rodríguez-Ardila A., Maraston C., 2008, MNRAS, 388, 803
Riffel R., Pastoriza M. G., Rodríguez-Ardila A., Bonatto C., 2009, MNRAS, 400, 273
Riffel R., Riffel R. A., Ferrari F., Storchi-Bergmann T., 2011, MNRAS, 416, 493
Riffel R., et al., 2015, MNRAS, 450, 3069
Röck B., Vazdekis A., Ricciardelli E., Peletier R. F., Knapen J. H., Falcón-Barroso J., 2016, A&A, 589, A73
Salpeter E. E., 1955, ApJ, 121, 161
Sánchez S. F., et al., 2012, A&A, 538, A8
Sánchez S. F., et al., 2016, A&A, 594, A36
Schaller G., Schaerer D., Meynet G., Maeder A., 1992, A&AS, 96, 269
Schmidt A. A., Copetti M. V. F., Alloin D., Jablonka P., 1991, MNRAS, 249, 766
Stanger V. J., Warwick R. S., 1986, MNRAS, 220, 363
Vacca W. D., Cushing M. C., Rayner J. T., 2004, PASP, 116, 352
Véron-Cetty M.-P., Véron P., 2006, A&A, 455, 773
Walcher C. J., et al., 2014, A&A, 569, A1
Westera P., Lejeune T., Buser R., Cuisinier F., Bruzual G., 2002, A&A, 381, 524
Wilson J. C., et al., 2004, in Moorwood A. F. M., Iye M., eds, Proc. SPIEVol. 5492, Ground-based Instrumentation for Astronomy. pp 1295–1305, doi:10.1117/12.550925
Worthey G., 1994, ApJS, 95, 107
Wrobel J. M., 1984, ApJ, 284, 531
Zibetti S., Gallazzi A., Charlot S., Pierini D., Pasquali A., 2013, MNRAS, 428, 1479

de Vaucouleurs G., de Vaucouleurs A., Corwin Jr. H. G., Buta R. J., Paturel G., Fouqué P., 1991, Third Reference Catalogue of Bright Galaxies. Volume I: Explanations and references. Volume II: Data for galaxies between 0^h and 12^h. Volume III: Data for galaxies between 12^h and 24^h.

APPENDIX A: INDIVIDUAL DESCRIPTION OF THE SAMPLE

A1 NGC 4636

NGC 4636 is a giant elliptical galaxy with LINER emission. Is one of the nearest and more X-ray luminous ellipticals, with L_X $2x10^41$ ergs/s (Jones et al. 2002). It is surrounded by an extended corona of hot gas (Forman et al. 1985), and has an asymmetric gas distribution, probably the result of irregular flows (Stanger & Warwick 1986).

A2 NGC 5905

This galaxy is one of a few that did not have a previously evidence of an AGN but that had X-ray eruptions observed, what happened in 1991 and 1992 with Chandra telescope. Later, X-ray flux started to decrease in a rate consistent with the expected for a Tidal Disruption Event (TDE). Recent observations showed that the infrared flux is dominated by star formation, what suggests that the radio emission is caused by circumnuclear star formation. Besides, no radio emission consistent with the TDE event was detected (Raichur et al. 2015). Among the galaxies of our sample, it is the only that has clearly visible NIR emission lines an the only non-ETG.

A3 NGC 5966

NGC 5966 is an elliptical galaxy with a faint bar-like feature centered at the nucleus. Stars and gas are decoupled, with the gas showing an elongated emission feature, in such a way that an ionization cone or a decoupled rotational disk are two possible interpretations (Kehrig et al. 2012). According to these authors, the diagnostic diagrams indicate the presence of a LINER nucleus and a LINER-like gas emission extending ~5 kpc outward from the nucleus, also LINER-like. The presence of a nuclear ionizing source seems to be required to shape the elongated gas emission feature in the ionization cone" scenario, although ionization by pAGB stars cannot be ruled out. On the other hand, Gomes et al. (2016) classified this object as type i ETG, also reporting that the absence of ongoing star formation throughout the galaxy lends support to the idea that its gas outflow is powered by an AGN hosted in its LINER nucleus. According to Gomes et al. (2016), a Type i ETG is a system with a nearly constant EW(Hα) in their extranuclear component, compatible with the hypothesis of photoionization by pAGB as the main driver of extended warm interstellar medium (WIM) emission.

A4 NGC 6081

It is a galaxy with radio emission (Dressel & Condon 1978). Also, Gomes et al. (2016) classified it as a type i ETG, reporting that sources other than pAGB stars dominate in less than 7% of the area of the galaxy. Its SDSS spectra is dominated by stellar population, with strong absorption bands and [OIII], [NI], $H\alpha$ and [SII] typical of LINERs. It's APO spectrum shows a stellar continuum dominated source with strong CO bands and absence of emission lines.

Table B1. NIR emission line fluxes measured for NGC 5905.

Line	Flux ($\times10^{-15}$ ergs/s/cm^2)	FWHM (km/s)
[FeII] λ12570	9.33	806
Paβ	6.72	315
H_2 λ21218	2.68	385
Brγ	3.5	462

A5 NGC 6146

NGC 6146 is an elliptical galaxy with a radio jet (Wrobel 1984). Caccianiga et al. (2002) reported the detection of CaII H and K, G, Mg Ib and Na Id absorption bands and a weak $H\alpha$ emission line. Gomes et al. (2016) classified this galaxy as type i ETG, also reporting that the absence of star formation and the suggestion of an outflow are compatible with the idea of a low luminosity AGN powering the nucleus. Its APO spectra shows a stellar continuum dominated source with strong CO bands and absence of emission lines.

A6 NGC 6338

This galaxy is the brightest on Draco constellation. It posesses diffuse and ionized gas and dust filaments on kiloparsec scales (Martel et al. 2004). X-ray observations indicate two or possibly three emission cavities of ellipsoidal shape with lower X-ray surface flux. They also found cold filamentary structures matching the $H\alpha$ emission and with high extinction regions seen on the optical extinction maps. This indicates a cooling mechanism generated by dust (Pandge et al. 2012). On the same work, they reported that a harder ionizing source is required to maintain such a high degree of ionization and that most of the jet power is mechanical. Gomes et al. (2016), using CALIFA datacubes, classified this object as type ii ETG.

A7 UGC 08234

This galaxy is part of a galaxy group and posesses a spiral companion, UGC 08237 (Nilson 1973). Gomes et al. (2016) classified this object as type ii ETG. There are no X-ray or radio properties reported in the literature. Its APO spectrum is dominated by stellar population, characterized by intense absorption bands and absence of emission lines.

APPENDIX B: EMISSION LINE FLUXES

In the optical region, according to Baldwin et al. (1981, BPT), the line ratios [O III]λ5007 Å/Hβ and [N II]λ6583Å/Hα can be used to classify the excitation mechanism that powers the optical lines based on the position of the points in the diagram. After running the stellar population synthesis for the SDSS spectra, we subtracted the

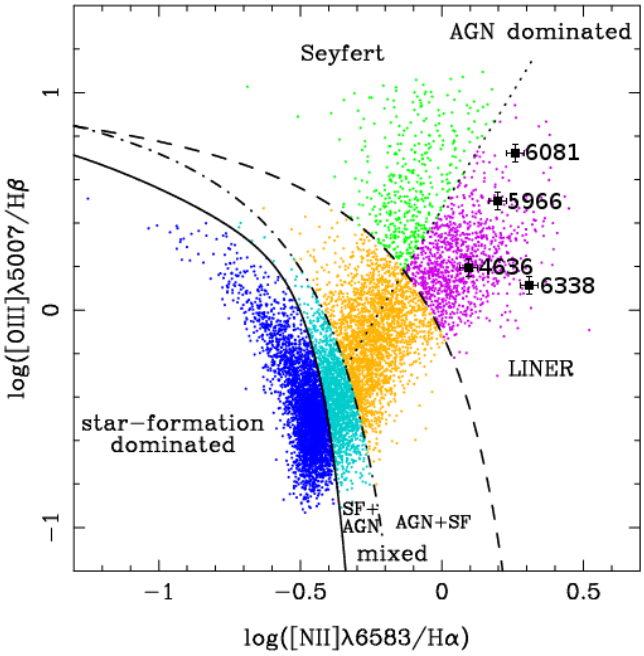

Figure B1. BPT diagram for the galaxies with optical spectra. The number of the NGC catalog is shown on the right side of each point. The points were plotted over the diagram from Bamford et al. (2008)

Table B2. Optical emission line fluxes in units of 10^{-15} ergs/s/cm^2/.

Object	Hβ 4861	[OIII] 5007	[NII] 6549	Hα 6563	[NII] 6585	[SII] 6718	[SII] 6732
NGC 4636	1.9	2.7	3.43	6.84	8.77	3.48	3.10
NGC 5966	0.87	2.26	1.75	2.69	3.92	2.79	2.00
NGC 6081	1.05	3.7	7.26	6.73	13.5	5.61	3.71
NGC 6338	1.82	2.38	4.37	5.43	11.5	3.99	2.87

stellar component and measured the emission line fluxes by fitting gaussians to the emission lines. Although there are still controversies on individual objects (e.g. Martins et al. 2012, who found a galaxy with no signs of activity but whose line ratios put it as a Seyfert galaxy), these diagrams can be used with great confidence to study the nature of the central source that powers the observed emission lines.

The emission line fluxes measured in the galaxy sample are listed in Table B2 and their ratios are plotted in Figure B1. From the locus of points occupied by our targets, we confirm the LINER nature of the galaxies. Only NGC 4636 and NGC 5966 had already been previously classified as LINER (Véron-Cetty & Véron 2006; Kehrig et al. 2012). The results obtained allow us to state that our sample is composed of 5 ETGs with LINER emission, 1 spiral galaxy and 1 ETG with no data about its emission lines.

This paper has been typeset from a TEX/LATEX file prepared by the author.

Capítulo 4

Um estudo pancromático espacialmente resolvido dos 500 pc centrais de NGC 1052: análise da população estelar

Agora conhecendo melhor as limitações dos modelos, aplicamos a síntese de população estelar ao caso da galáxia NGC 1052. A escolha deste objeto se deu pelo fato de ser uma galáxia elíptica (com emissão LINER) e por termos cubos de dados no óptico (GMOS) e no NIR (NIFS). A união dos dois intervalos espectrais torna possível uma análise mais robusta das componentes que contribuem para a distribuição espectral de energia deste objeto, conforme discutido na introdução. Os resultados e discussão encontram-se em forma de artigo científico publicado na revista MNRAS em Fevereiro de 2019 com o título *A panchromatic spatially resolved study of the inner 500 pc of NGC 1052 - I. Stellar population.*

MNRAS 000, 1–12 (2015) Preprint 9 November 2018 Compiled using MNRAS LATEX style file v3.0

A panchromatic spatially resolved study of the inner 500 pc of NGC 1052 - I: Stellar population

L. G. Dahmer-Hahn [1⋆], R. Riffel[1], J. E. Steiner[2], R. A. Riffel[3], R. B. Menezes[4], T.V. Ricci[5], N.Z. Dametto[1], T. Storchi-Bergmann[1], M. R. Diniz[3]

[1] *Departamento de Astronomia, Universidade Federal do Rio Grande do Sul. Av. Bento Goncalves 9500, 91501-970, Porto Alegre, RS, Brazil.*
[2] *Instituto de Astronomia, Geofísica e Ciências Atmosféricas, Universidade de São Paulo, 05508-900, São Paulo, Brazil*
[3] *Universidade Federal de Santa Maria, Departamento de Física, Centro de Ciências Naturais e Exatas, 97105-900, Santa Maria, RS, Brazil*
[4] *Centro de Ciências Naturais e Humanas, Universidade Federal do ABC, 09210-580, SP, Brazil*
[5] *Universidade Federal da Fronteira Sul, Campus Cerro Largo, RS 97900-000, Brazil*

Accepted XXX. Received YYY; in original form ZZZ

ABSTRACT

We map optical and near-infrared (NIR) stellar population properties of the inner 320×535 pc^2 of the elliptical galaxy NGC 1052. The optical and NIR spectra were obtained using the Gemini Integral Field Units of the GMOS instrument and NIFS, respectively. By performing stellar population synthesis in the optical alone, we find that this region of the galaxy is dominated by old (t>10 Gyr) stellar populations. Using the NIR, we find the nucleus to be dominated by old stellar populations, and a circumnuclear ring with younger (∼2.5 Gyr) stars. We also combined the optical and NIR datacubes and performed a panchromatic spatially resolved stellar population synthesis, which resulted in a dominance of older stellar populations, in agreement with optical results. We argue that the technique of combining optical and NIR data might be useful to isolate the contribution of stellar population ages with strong NIR absorption bands. We also derive the stellar kinematics and find that the stellar motions are dominated by a high (∼240km·s^{-1}) velocity dispersion in the nucleus, with stars also rotating around the center. Lastly, we measure the absorption bands, both in the optical and in the NIR, and find a nuclear drop in their equivalent widths. The favored explanation for this drop is a featureless continuum emission from the low luminosity active galactic nucleus.

Key words: galaxies: stellar content – galaxies: active – galaxies: elliptical and lenticular, cD

1 INTRODUCTION

In order to access the stellar population content in galaxies, the technique of stellar population synthesis (e.g. Bica 1988; Cid Fernandes et al. 2004, 2005; Wilkinson et al. 2017) has been widely used over the years, with many key results in galaxy evolution being obtained (Cid Fernandes et al. 2004, 2005; Rembold et al. 2017; Zheng et al. 2017; Goddard et al. 2017a,b; de Amorim et al. 2017; Mallmann et al. 2018). This stellar population synthesis technique has been employed mostly in the optical spectral region. However, with the development of new telescopes focused in other wavelength ranges, it became clear that new evolutionary population synthesis (EPS) models which cover wavelength ranges beyond the optical would have to be developed in order to explore the full potential these telescopes have to offer (Maraston 2005; Riffel et al. 2008; Noël et al. 2013; Zibetti et al. 2013; Meneses-Goytia et al. 2015; Baldwin et al. 2018; Dahmer-Hahn et al. 2018).

Although the use of near infrared (NIR) fingerprints on the study of stellar populations started nearly 40 years ago (Rieke et al. 1980; Origlia et al. 1993; Oliva et al. 1995; Engelbracht et al. 1998; Lançon et al. 2001), only in the last decade there was an improvement on the usage of the whole spectral range (Riffel et al. 2008, 2009; Cesetti et al. 2009; Riffel & Storchi-Bergmann 2011; Storchi-Bergmann et al. 2012; Kotilainen et al. 2012; Dametto et al. 2014; Diniz et al. 2017; Riffel et al. 2017). Part of this usage has been due to the lower effect of dust reddening in the NIR, meaning that it is possible to access populations in dustier regions, which in the optical and ultraviolet would be obscured. Also, the most prominent spectral features of stars beyond the

⋆ E-mail: dahmer.hahn@ufrgs.br

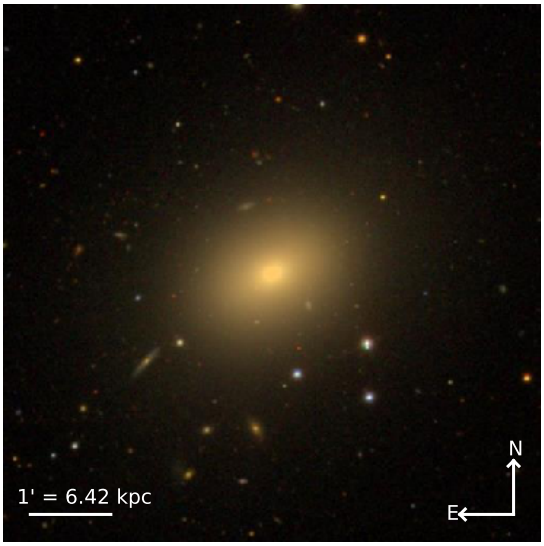

Figure 1. Optical image of NGC 1052 taken with Sloan Digital Sky Survey (Adelman-McCarthy et al. 2006; Baillard et al. 2011).

main sequence (especially thermally pulsing asymptotic giant branch stars, hereafter TP-AGB stars) are located in the NIR (Maraston 2005; Riffel et al. 2009; Noël et al. 2013; Zibetti et al. 2013; Riffel et al. 2015). Thus, the NIR is crucial in order to identify stellar populations which are dominated by these stars.

Two recent papers studied the ability to identify the stellar populations in the NIR compared to the optical region. Baldwin et al. (2018), by studying 12 early-type galaxies (ETG), found that the derived star formation histories vary dramatically in the NIR, if compared to the optical, depending on the chosen stellar spectral library. Also, they found that models based on high-quality spectral libraries fit NIR data better and also produce more consistent results when compared to optical ones, with the ages being imprinted on the shape of the continuum in the case of low spectral resolution models. Also, according to Dahmer-Hahn et al. (2018), NIR models with low ($\lesssim$300) spectral resolution have limitations to distinguish between the different stellar populations, since with these models too much weight is given to the shape of the continuum, when deriving the ages of the stellar populations. Combined, these results show that newer models with higher spectral resolution (e.g. Meneses-Goytia et al. 2015; Röck et al. 2016; Conroy et al. 2018) are essential in order to produce more consistent results in the NIR.

In this work, by using the new library of models of Vazdekis et al. (2016), which has high (~2000) spectral resolution both in the optical and in the NIR, we present a study of the stellar population of the nuclear region of NGC 1052 (Figure 1).

This galaxy is a giant elliptical classified as E4 (Forbes et al. 2001; Xilouris et al. 2004) and with a redshift of 0.005037, harboring one of the nearest radio-loud active galactic nuclei (AGN). On radio wavelengths, it displays two jets with slightly different orientations (Wrobel 1984; Fey & Charlot 1997). In X-rays, it shows a compact core, best fitted by an absorbed power law and various jet-related emissions and an extended region (Kadler et al. 2004).

In the optical, its nucleus is classified as low-ionization nuclear emission-line region (LINER, Heckman 1980; Ho et al. 1997). Barth et al. (1999) used polarized light, and confirmed a hidden BLR emission in the Hα line, making NGC 1052 the first LINER to have a broad emission component detected in polarized light. Later, Sugai et al. (2005), using integral field spectroscopic data obtained with the Subaru Telescope at a spatial resolution of ~0.4", reported the detection of weaker features at the nucleus, including the [Fe III] and He II emission lines, as well as an unresolved broad component of the Hβ emission. They also found that the spatial structure and velocity field of this source requires the existence of three main components: i) a high-velocity bipolar outflow, ii) low-velocity disk rotation, and iii) a spatially unresolved nuclear component.

Regarding the stellar content of NGC 1052, Raimann et al. (2001) used long slit spectra and found that the inner 1 kpc is dominated by an older and more metallic stellar population (~10 Gyr) whereas a younger, 1 Gyr population becomes increasingly more important outwards. Also, Milone et al. (2007) found, by measuring Lick indices, that the bulge of NGC 1052 is older (12-15 Gyr) and more metallic than the rest of the galaxy, suggesting this galaxy was formed by processes in which the star formation occurred first at the bulge on short timescales. They also found that, along the major axis, a younger population is responsible for ~30% of the light fraction at 1.5 kpc, whereas along the minor axis this stellar population is not important. On the other hand, Pierce et al. (2005) used Keck spectra of 16 globular clusters (GC) and a long-slit spectrum of the whole galaxy, finding that its nucleus has a luminosity-weighted central age of ~2 Gyr and [Fe/H]~+0.6 dex, which is consistent with the merger event that occurred ~1 Gyr ago (van Gorkom et al. 1986). They also found that the GCs of NGC 1052 are dominated by a ~13 Gyr stellar population, with a few of these GCs having strong blue horizontal branches which can not be fully accounted for using stellar population models. Based on the age of the GCs, they argued that, despite the recent merger event, little recent star formation occurred.

Also, Fernández-Ontiveros et al. (2011) found 15 compact sources exhibiting Hα luminosities an order of magnitude above the estimated for an evolved population of extreme horizontal branch stars. Their Hα equivalent widths and optical-to-NIR spectral energy distributions are consistent with them being young stellar clusters with ages <7 Myr. According to the authors, this is probably related with the merger event experienced by the galaxy.

Regarding the stellar kinematics, Dopita et al. (2015) found that the stars rotate smoothly around the photometric minor axis and are characterized by a velocity dispersion of ~200km·s^{-1}. They also found that there is a sharp cusp in the velocity dispersion close to the nucleus, presumably within the zone of influence of the central black hole. These results were later confirmed by Riffel et al. (2017) using NIR data, which also found a centrally peaked σ distribution and a rotation around the photometric minor axis. Besides that, they found an anti-correlation between the h_3 momentum and the velocity field, which they interpreted as due do the

contribution of stars rotating slower than those in the galaxy disk, probably due to motion in the galaxy bulge.

Most modern libraries of simple stellar populations (SSPs) still lack models younger than 1.0 Gyr in the NIR. This is caused by the low amount of observed hot stars with adequate signal-to-noise ratio and moderate (R>1000) spectral resolution in the NIR. The only library that includes models younger than 1 Gyr is the E-MILES (Vazdekis et al. 2016) library. However, as pointed out by the authors, models younger than 0.5 Gyr are unsafe.

The previous stellar population studies of NGC 1052, which showed that the inner 1 kpc is dominated by stellar populations older than 2 Gyr, make this galaxy an adequate object to have its stellar population properties studied with these modern NIR libraries. Also, while the optical range is more sensitive to bluer stars, the NIR is dominated by the red and cold stars (including the TP-AGB). Combining these two wavelength ranges provides a unique opportunity to test modern stellar population models simultaneously in the optical and in the NIR. Lastly, because the ionization source of the LINER-like emission in NGC 1052 is still under debate (Fosbury et al. 1978, 1981; Diaz et al. 1985; Sugai & Malkan 2000; Gabel et al. 2000; Dopita et al. 2015), combining these two wavelength ranges provides a unique opportunity to search for any contributions of an AGN, since hot dust emission peaks in the NIR and the featureless contribution from the AGN is stronger in bluer wavelengths.

In this work, we aim to study the stellar population properties of NGC 1052, in the optical and NIR separately, and also combining both wavelength ranges in a single fit. This paper is structured as follows: the data and reduction processes are presented in Section 2. In Section 3 , we present the method of spectral synthesis used throughout the paper. The results are presented in Section 4, and are discussed in Section 5. Lastly, the conclusions are drawn in Section 6.

2 DATA AND REDUCTION

In order to fully explore the inner region of NGC 1052, we used two sets of datacubes, one in the optical and the other in the NIR. The optical datacube was obtained with Gemini Multi-Object Spectrograph (hereafter GMOS, Hook et al. 2004; Allington-Smith et al. 2002) and the NIR one was obtained with the Near-infrared Integral Field Spectrograph (hereafter NIFS, McGregor et al. 2003), both instruments attached to the Gemini telescopes. Below we describe the observations and data reduction process.

2.1 Optical data

The optical data were obtained on September 30th 2013 as part of GS-2013B-Q-20 Gemini South project using GMOS on Integral Field Unit (IFU) mode. The original Field of View (FoV) is 3.″5×5.″0 (320×535 pc^2), with a natural seeing of 0.″88, estimated from stars present in the acquisition image, which was taken immediately before the datacube observation. One 30 min exposure was taken, using the B600-G5323 grating, with a central wavelength of 5620 Å. The FWHM is equal to 1.8 Å throughout the spectra.

The data were reduced using the Gemini/IRAF package and included: trimming, bias subtraction, bad pixel removal, cosmic ray removal (using the L. A. Cosmic routine van Dokkum 2001), extraction of the spectra, GCAL/twilight flat correction, wavelength calibration, sky subtraction and flux calibration (taking into account the atmospheric extinction). Finally, the datacube was constructed, with square spatial pixels (spaxels) of 0.″05 width.

In order to improve the quality of the data cube, we also applied the following treatment procedures to the data cube: correction of the differential atmospheric refraction, high spatial-frequency components removal with the Butterworth spatial filtering, "instrumental fingerprint" removal and Richardson-Lucy deconvolution. The final spatial resolution after the data treatment is 0.″79, estimated from a spatial profile obtained along the red wing of the broad Hα emission, and the spectral coverage is 4317-6775Å(Menezes et al. 2014, 2015). The optical continuum of the treated datacube is shown on the left panel of Fig. 2.

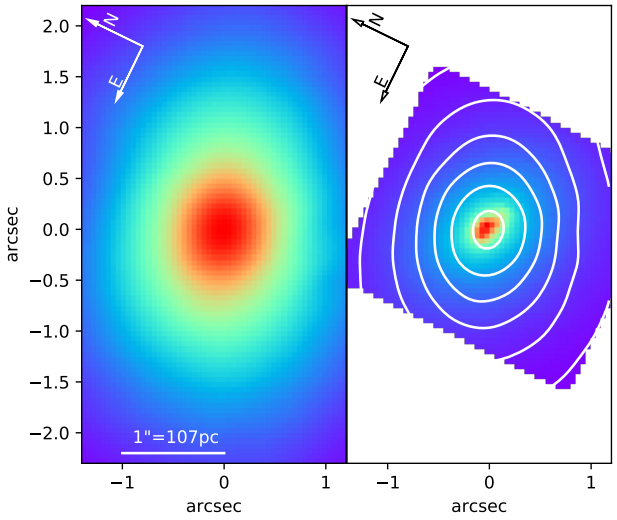

Figure 2. Left: optical continuum of NGC 1052 obtained with GMOS. Right: NIR k-band continuum of NGC 1052 obtained with NIFS. In white are shown optical continuum contours.

2.2 Near-Infrared data

The NIR data were obtained on October 2011 as part of GN-2010B-Q-25 Gemini North project using NIFS with ALTAIR adaptive optics system. Six 610 s on target exposures were taken in the J band and four 600 s exposures were taken in the K band. The spatial resolution is 0.″1 and the spectral resolution is 6040 for the J band and 5290 for the K band.

The data were reduced using the standard reduction scripts offered by the Gemini team, using tasks from the Gemini/IRAF package. The reduction included trimming of the images, flat fielding, sky subtraction, wavelength and s-distortion calibrations and telluric absorption removal. The flux calibration was performed by interpolating a blackbody function to the spectrum of the telluric standard star. The reduced datacubes were constructed with square spaxels of 0.″05×0.″05. After the differential atmospheric refraction correction, the individual datacubes in each band were median combined to a single datacube. The combined dat-

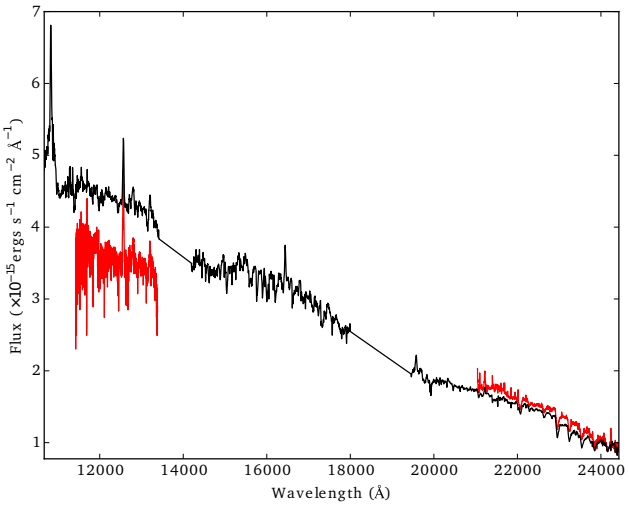

Figure 3. In black, GNIRS longslit spectra of NGC 1052, as published by Mason et al. (2015). In red, we show the extracted NIFS spectra corresponding to the GNIRS aperture, both in J and K bands.

acubes were spatially re-sampled, in order to obtain spaxels of 0.″021. This spaxel size was chosen because it is a sub-multiple value of the original NIFS spaxel dimensions (0.″103×0.″043). Such spatial re-sampling provides a better visualization of the contours of the structures. The Butterworth spatial filtering and the instrumental fingerprint removal were then applied. The final spectral coverage of the NIR data is 11472-13461 Å for the J band and 21060-24018 Å for the K band.

In addition, the original NIFS field of view is 3.″0 x 3.″0 (320×320 pc^2), but due to low signal-to-noise ratio (S/N) on the borders of the FoV, we have shorten it to 2.″5×2.″5. Since J and K bands were observed on different days, they may present some relative flux calibration problems. In order to minimize these effects, we have compared our data with a cross-dispersed spectrum of NGC 1052 observed with Gemini near-infrared spectrometer (GNIRS) by Mason et al. (2015). This comparison was made using an extraction emulating the GNIRS aperture (slit oriented 90° east of north, with an aperture of 26×155pc^2) in our datacubes. After that, we scaled the emulated NIFS long slit data with the GNIRS ones applying the obtained relation to all single spaxels of our data-cube. The GNIRS longslit spectra, together with the corresponding NIFS extracted spectra of the J and K bands are shown on Figure 3. The average correlation of the J band was ~80%, whereas for the K band was ~88%. The NIR image of the k-band continuum is shown on right panel of Figure 2.

2.3 Panchromatic datacube

For an improved characterization of the stellar population of the galaxy, we combined optical and NIR datacubes into a single panchromatic spatially resolved datacube. To do this, we followed the steps below:

(i) First, since the NIR datacube has a higher spatial resolution, we degraded it to match the optical data by convolving it with a gaussian of FWHM=0.7".

(ii) Considering that optical and NIR data were observed on different nights and using different instruments, in order to correct the spectra for scale factors, we extracted an optical spectrum with the same spatial area of the Mason et al. (2015) NIR longslit spectrum. The spectral separation between the end of the optical datacube and the beginning of the NIR longslit spectrum is small (<1700Å), so that we searched for the scale factor that yielded the best agreement between the stellar population models and the combined optical+NIR spectrum. We did this by performing spectral synthesis on combined spectra with different scale factors. We found for this step an error $\leqslant$5%. Lastly, we applied the scale factor to the NIR datacube.

(iii) Assuming that the photometric center of NGC 1052 in both NIR and optical observations are located at the same position, we sliced each NIR datacube spaxel in 900 subspaxels (30x30) and added their fluxes to the optical spaxel that matched the central position of the NIR subspaxel. This is illustrated in Figure 4. The combined spectrum of the central spaxel and the spectrum modeled by STARLIGHT are presented in Figure 5.

This approach of combining optical and NIR data might be useful to identify SSPs which are characterized by bluer colors, such as young populations, as well as stellar populations that are redder, such as intermediate-age ones. Also, since many important stellar features are located in the NIR (like the 1.1μm CN band, the 1.4μm CN band and the ZrO features at 0.8-1.0μm, which are strong indicatives of TP-AGB stars and populations between 0.5 and 2 Gyr Riffel et al. 2007; Martins et al. 2013; Riffel et al. 2015; Hennig et al. 2018), adding this wavelength range to optical studies can further help to identify the stellar mixture of the galaxy.

3 SPECTRAL SYNTHESIS

To study the stellar population of NGC 1052, we used the STARLIGHT code (Cid Fernandes et al. 2004, 2005, 2013). Basically, the code fits the observed spectrum by a combination of SSPs in different proportions, considering reddening and line of sight velocity corrections. The final fit is carried out by STARLIGHT searching for the M_λ model that better describes the data. The model is given by

$$M_\lambda = M_{\lambda 0}[\sum_{j=1}^{N\star} x_j b_{j,\lambda} r_\lambda] \otimes G(v_\star, \sigma_\star), \quad (1)$$

where $M_{\lambda 0}$ is the flux at the normalization wavelength $\lambda 0$, $N_\star$ is the number of SSPs used to compose the model, $\vec{x}$ is the population vector so that x_j indicates the contribution from the j-th SSP normalized at $\lambda 0$, $b_{j,\lambda}$ is the j-th model spectrum, r_λ is the reddening term $r_\lambda = 10^{-0.4(A_\lambda - A_{\lambda 0})}$, which is parameterized by the A_V. The stellar velocity dispersions ($\sigma_\star$) and line-of-sight velocities ($v_\star$) are modeled by a Gaussian function $G(v_\star, \sigma_\star)$.a

The best fit is carried out by minimizing the equation

$$\chi^2 = \sum_\lambda [(O_\lambda - M_\lambda) w_\lambda]^2, \quad (2)$$

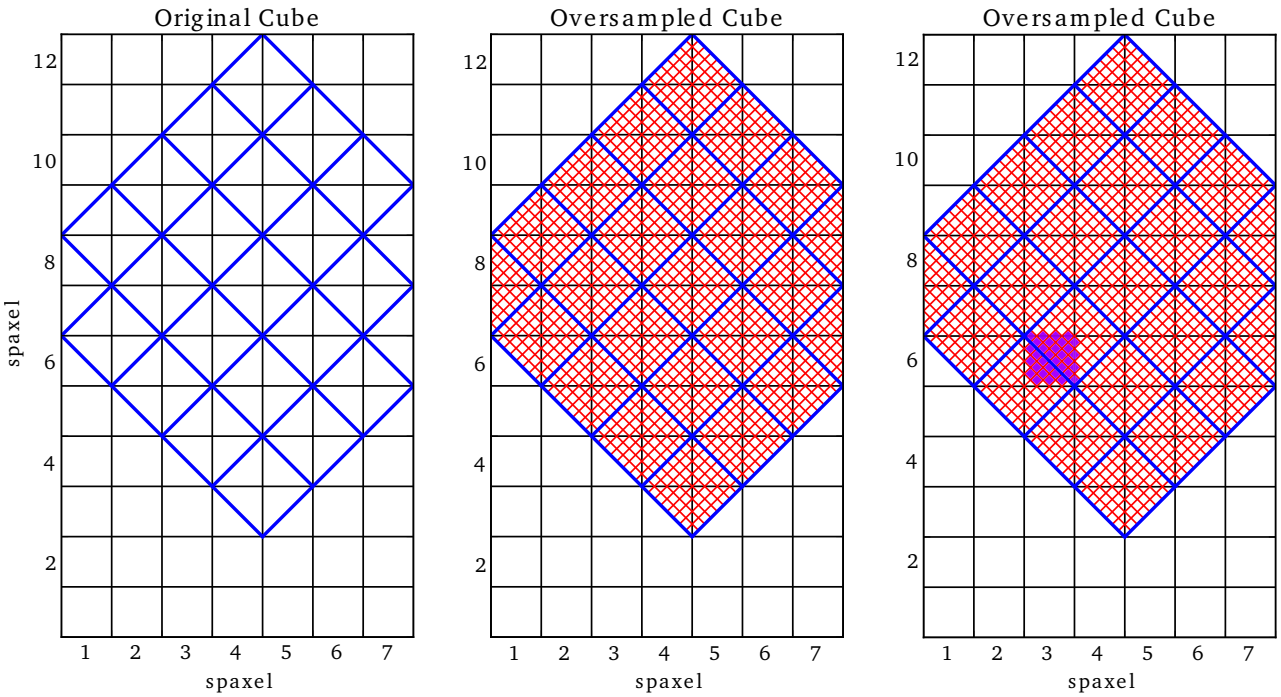

Figure 4. Combination of optical and NIR datacubes. In the left panel, optical data is represented by the black grid and NIR data is represented by the blue grid. In the middle panel, each NIR spaxel was sliced in 64 subspaxels (8×8), represented by the red grid. In our data treatment, we sliced each spaxel in 900 subspaxels (30×30) for better accuracy, rather than the 64 shown in the figure. In the right panel, all subspaxels marked in magenta were added to the optical (3,6) spaxel.

where O_λ is the observed spectrum. Emission lines and spurious features are masked out by setting $w_\lambda = 0$. Also, because of the lower S/N of the J band, we set $w_\lambda = 0.2$ to the whole wavelength range, both in the NIR and panchromatic synthesis. For the remaining spectral regions, we used $w_\lambda = 1.0$.

To fit the spectra, we used the EPS models developed by Vazdekis et al. (2016, hereafter E-MILES). These models are available with two possible evolutionary tracks and three possible initial mass functions (IMF). We chose the tracks of Girardi et al. (2000) and the Kroupa (2001) IMF, since in the NIR these models are based on the ones published by Röck et al. (2016), which we tested previously (Dahmer-Hahn et al. 2018) and found that they produce self-consistent results.

These models were chosen because they cover the full spectral range of our data (3500 to 25000 Å), offering a higher NIR spectral resolution when compared to other stellar population libraries (e.g. Bruzual & Charlot 2003; Maraston 2005; Conroy et al. 2009). This higher resolution is essential in order to produce better fits of the stellar absorptions.

The only drawback of the E-MILES library is that it used the IRTF library, which does not include hot stars. As a consequence, in the NIR, only SSPs older than 500 Myr are marked as safe by the authors. In the optical region, on the other hand, it includes SSPs as young as 30 Myr. We were then able to test if there are no significant amounts of SSPs younger than 500 Myr.

Also, since NGC 1052 is an elliptical galaxy, we used the reddening law from Cardelli et al. (1989) to reproduce dust extinction (A_V), which is best suited for objects without active star formation.

In order to remove the noise effects present in real data, a more consistent and robust way to present the stellar population is in the form of condensed population vectors (Cid Fernandes et al. 2004, 2005). Following Riffel et al. (2009), and considering that the library of SSPs only includes models older than 1 Gyr, we defined the light fraction population vectors as follows: xi(1 Gyr < t ⩽ 2 Gyr) and xo(t > 2 Gyr) to represent the intermediate-age and old stellar population vectors, respectively.

Also, to search for a possible emission from the AGN, we followed Riffel et al. (2009) and added to the library of models a featureless continuum with $f_\nu \sim \nu^{-1.5}$. We also added to the NIR library Planck functions with temperatures between 700 and 1400 K in order to reproduce the possible contribution from hot dust.

Lastly, in order to better identify the stellar population mixture of the inner region of the galaxy, we followed Cid Fernandes et al. (2005) and calculated the mean stellar age ($<t>$) and mean metallicity ($<Z>$). They are defined by the following equations:

$$< t >_L = \sum_{j=1}^{N\star} x_j log(t_j), \quad (3)$$

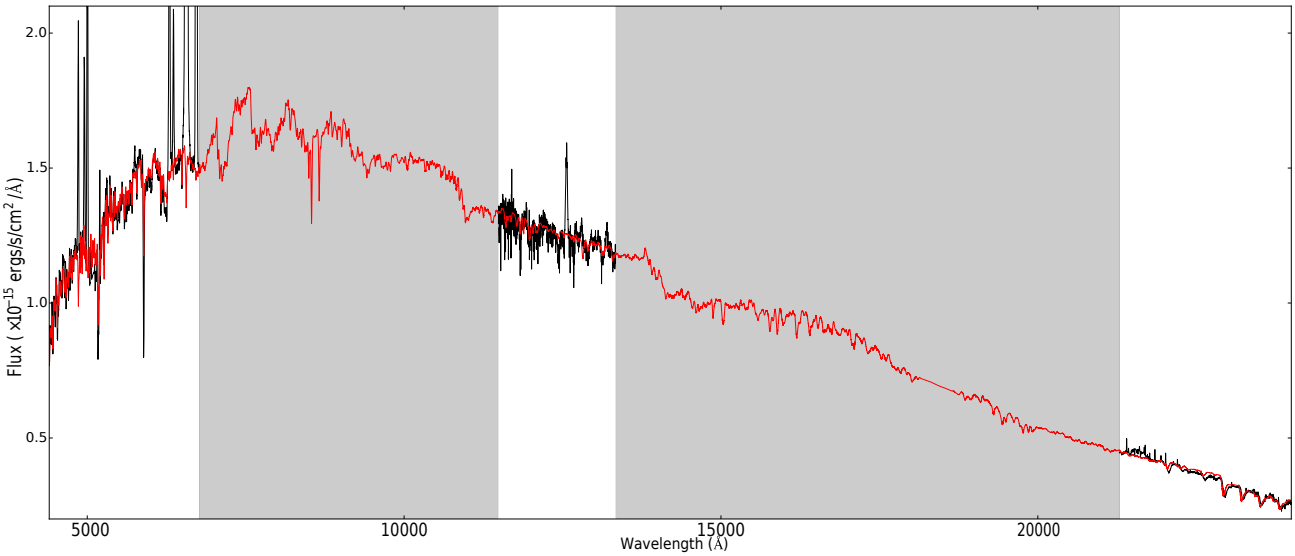

Figure 5. In black, we show the optical and NIR spectra of the combined datacube. Regions where we do not have data are grayed. In red, we present the corresponding spectrum modeled by STARLIGHT with $<t>_L$=10.15 and $<Z>_L$=0.014.

$$< Z >_L = \sum_{j=1}^{N\star} x_j Z_j, \quad (4)$$

where t_j and Z_j are the age and metallicity of the j-th SSP. The x_j percentage contribution can be weighted by light (L) and mass (M) fractions. We normalized optical and panchromatic data at 4500Å, and NIR data at 21910Å. We also used these values to calculate the luminosity contribution. These values were chosen because they contain relatively few stellar absorptions and good S/N.

4 RESULTS

4.1 Stellar Synthesis

By fitting the optical datacube with E-MILES library, we found only old stellar content in the entire datacube. Looking at the $<t>_L$, it is possible to see that the cube is dominated by a stellar population of ~12 Gyr, with some locations displaying a slightly younger (t~10 Gyr) stellar population. Also, no contribution from a featureless continuum was found. The A_V throughout the cube was very low (~0.2 mag), with the nucleus peaking at A_V=0.5 mag. We found metallicity values close to solar ($Z_\odot$=0.019, Girardi et al. 2000) in the entire cube. We show in the top panels of Figure 6 the spatial distribution of intermediate-age and old stellar populations, as well as the A_V, $< t >_L$ and Z_L for the optical results.

When fitting the NIR datacube, we found the same results in the nucleus of the galaxy, with a dominance of very old (t>10 Gyr) stellar populations, a higher dust reddening (~0.8 mag) and solar metallicity. Because of the better spatial resolution of NIR data, the reddening peak is much more concentrated and intense compared to the optical one. Also, no contribution from Planck functions nor from a featureless continuum were found.

However, according to the NIR data, the circumnuclear population is dominated by a ~2.5 Gyr population, which contributes to $\gtrsim$80 % of the light. Although this population is classified as old (t>2 Gyr) after binning the results, there is a clear circumnuclear drop in the $<t>_L$ values. The reddening in this region is much lower than the nucleus (<0.2 mag), and there is no significant difference in the metallicity if compared to the nucleus. We present these results in the middle panels of Figure 6.

By performing the synthesis using the panchromatic datacube, we found again a dominance of old stellar populations. No difference in the stellar population can be seen in the $<t>_L$ panel, with the whole panchromatic region displaying a ~10 Gyr stellar population. Also, we found a reddening contribution compatible with both optical and NIR results, as well as a metallicity slightly lower (Z~0.010) than solar throughout the datacube. The only exceptions were the borders of the cube, which are affected by a low S/N. As in optical and NIR results, we did not detect contributions from either Planck functions or a featureless continuum. The results for the combined datacube are presented in the bottom panels of Figure 6.

Since the panchromatic synthesis favored optical results, we performed the synthesis again, increasing the NIR weight. By setting w_{NIR} = 2, the results from STARLIGHT are the same, with a dominance of old stellar populations throughout the cube. When setting w_{NIR} = 4, the results found lie in between optical and NIR ones, with a dominance of old stellar populations in the datacube but with $<t>_L$ ~8 Gyr at the borders of the FoV. However, for all fits with $w_{NIR} > 2$, the fits are not able to match the optical spectral region.

4.2 Absorption Band Measurements

In order to avoid contamination due to stellar kinematics when measuring the equivalent widths (EW) of the ab-

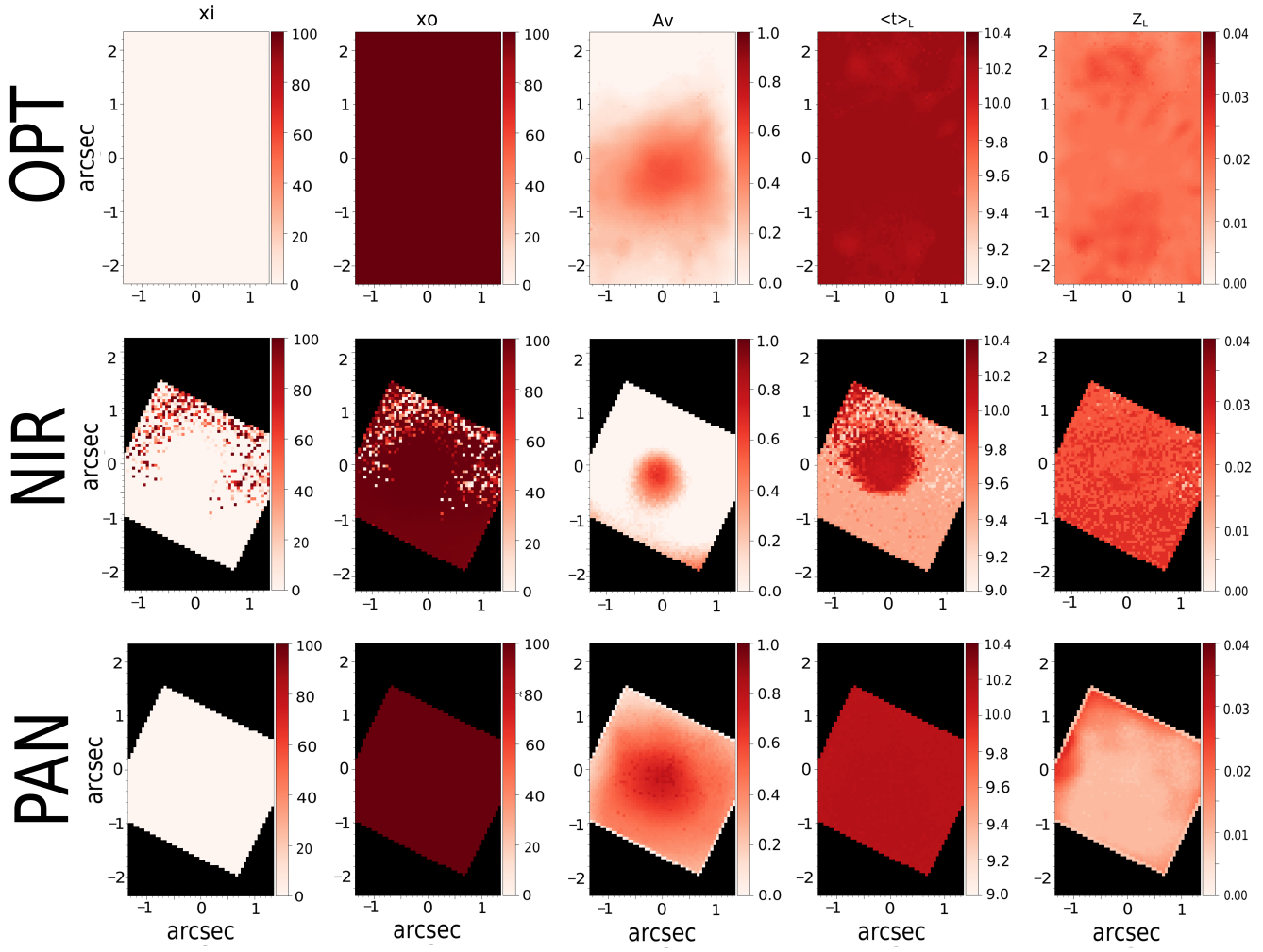

Figure 6. Synthesis results for NGC 1052. From left to right, we present the spatial distribution of intermediate-age and old stellar populations, the A_V, $< t >_L$ and lastly the Z_L. The top five panels show the optical results, the middle panels present the NIR results and the bottom panels show the results obtained with the combination of optical and NIR data.

sorption bands, we first corrected the spectra for Doppler shift, using the line-of-sight velocities derived in Section 4.3. We then applied a python version of the pacce code (Riffel & Borges Vale 2011) for each spaxel and measured the EWs based on the line limits and continuum bandpasses of Worthey et al. (1994) for the optical region and of Riffel et al. (in prep.) for the NIR, which are presented in Table 1.

From the optical bands, only Feλ5270Å was not contaminated by emission from the gas and with enough S/N. The NaDλ5895Å absorption band, although being the strongest in the optical region, was contaminated by the HeIλ5875Å emission line, as well as by the interstellar sodium. Also, the $Mg_2\lambda$5175Å band was contaminated by the [NII]λ5198Å emission line. In the NIR, on the other hand, the three CO bands near 23000Å were isolated and with a good S/N ratio (~100 for the nucleus). The EW maps for the optical Feλ5270Å and the three CO bands in the NIR are shown in Figure 7.

The Fe5270 map shows a constant 2.76±0.17Å EW throughout the cube, with lower (~1.8 Å) values closer to the nucleus with a 0.″6 FWHM. The three CO absorptions located in the end of the K band present the exact same spatial distribution, with a constant (~18 Å) EW throughout the cube and a lower (~10 Å) EW in the center. Because of the higher spatial resolution, the EW drop as seen in the NIR is much more concentrated, with a FWHM of 0.26. These results suggest that the component that causes this drop is emitted very close to the nucleus of the galaxy.

4.3 Stellar Kinematics

To derive the stellar kinematics, we used the penalized pixel-fitting (pPXF) code, described in Cappellari & Emsellem (2004). Like STARLIGHT, this code also searches for the combination of spectra from a user-provided library to fit the model that better reproduces the observed spectrum. We chose to perform the fitting of the stellar kinematics with pPXF because it allows the user to remove continuum information with a high-order polynomial, so that more weight is given to the stellar features.

In the optical region, we used the Vazdekis et al. (2016) stellar library, since it has an adequate spectral resolution

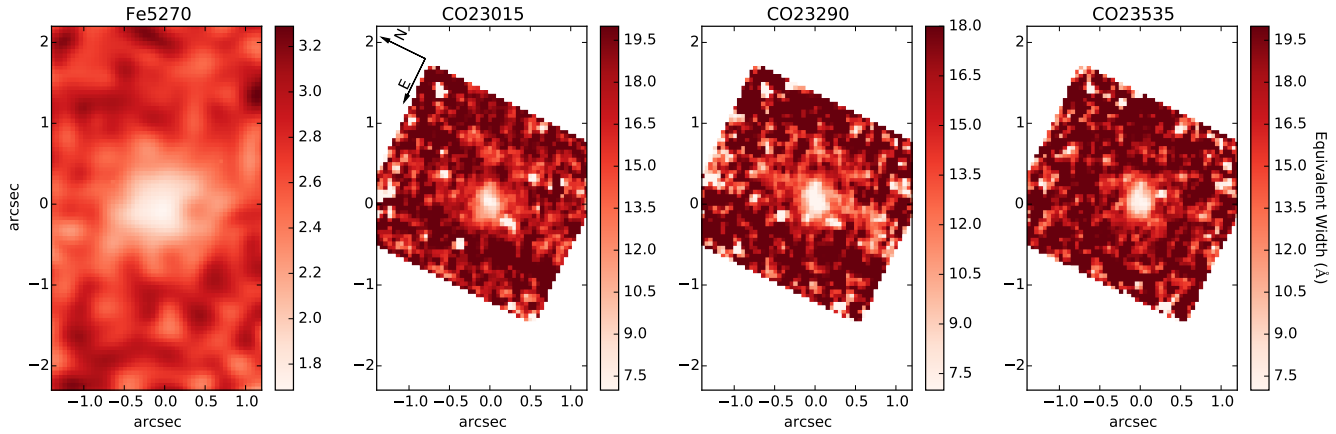

Figure 7. Equivalent width spatial distribution of the optical Feλ5265Åand the NIR CO bands.

Table 1. Line limits and continuum bandpasses.

Centre (Å)	Main Absorber	line limits (Å)	continuum bandpass (Å)
5265.65	Fe	5245.650-5285.650	5233.150-5248.150, 5285.650-5318.150
23015.0	CO	22870.000-23160.000	22700.000-22790.000, 23655.000-23680.000
23290.0	CO	23160.000-23420.000	22700.000-22790.000, 23655.000-23680.000
23535.0	CO	23420.000-23650.000	22700.000-22790.000, 23655.000-23680.000

Table Notes: The optical indices are based on Worthey et al. (1994) and the NIR indexes are based on Riffel et al. (in prep).

and coverage. For this wavelength range, we fitted the whole cube, masking only the emission lines. For the NIR stellar templates, on the other hand, we used the Winge et al. (2009) library of late spectral type stellar templates, which was observed with GNIRS, and provides a better spectral resolution (R>5000) and S/N, being limited to the end of the K-band (21500<λ<24200 Å). Since NIR data has a smaller (S/N), especially the K-band, we limited the fitting region to 22830-24025 Å, where the CO bands are present.

The pPXF code returns as output values for the radial velocity (v_c) and stellar velocity dispersion (σ) for each spatial position. The results are presented in Figure 8.

In order to search for deviations from circular motions, we followed Bertola et al. (1991) and assumed that the stars are on circular orbits in a plane with a rotation curve given by

$$v_c = \frac{Ar}{(r^2 + c_0^2)^{p/2}}, \quad (5)$$

where A, c_0 and p are parameters to be found and r is the radius. Then, the observed radial velocity at a position (R,Ψ) on the plane of the sky is given by:

$$v(R,\Psi) = v_{sys} + \frac{ARcos(\Psi-\Psi_0)sin\theta cos^p\theta}{\{R^2[sin^2(\Psi-\Psi_0)+cos^2\Theta cos^2(\Psi-\Psi_0)]+c_0^2cos^2\Theta\}^{p/2}}, \quad (6)$$

where Θ is the disk inclination (Θ=0 being is a face-on disk), Ψ_0 is the position angle of the line of nodes and v_{sys} is systematic velocity of the galaxy. We then developed a script that automatically searches for the center, inclination and velocity amplitude by performing a Levenberg-Marquardt χ^2 minimization.

Because of the lower S/N of the NIR data, we fitted only the rotation obtained with with optical data. In Figure 9, we present the stellar velocity field, the best fit model, and the residual map, obtained by the subtraction of the model from the observed velocities. The residual is, in all locations, below |16| km·s^{-1}.

These results show that the stellar motions in the central ~500 pc of NGC 1052 are dominated by two components: random orbits in the bulge with σ ~240 km s^{-1} and circular orbits in the galaxy plane with speeds up to 100 km s^{-1}.

5 DISCUSSION

5.1 Divergence in optical and NIR results

The optical results for the stellar population synthesis, revealing that this galaxy is dominated by old stellar content in the nuclear region, are in agreement with past results, which showed that NGC 1052 is dominated by stellar populations older than 2 Gyr (Raimann et al. 2001; Milone et al. 2007; Pierce et al. 2005). Even though one previous paper about this galaxy found spots suggesting younger globular clusters (t~7 Myr Fernández-Ontiveros et al. 2011), these regions are located outside the FoV of both the optical and NIR datacubes.

On the other hand, NIR results revealed a circumnuclear ring of ~2.5 Gyr (contributing up to 100% of the light in some regions). This stellar population can be real, in

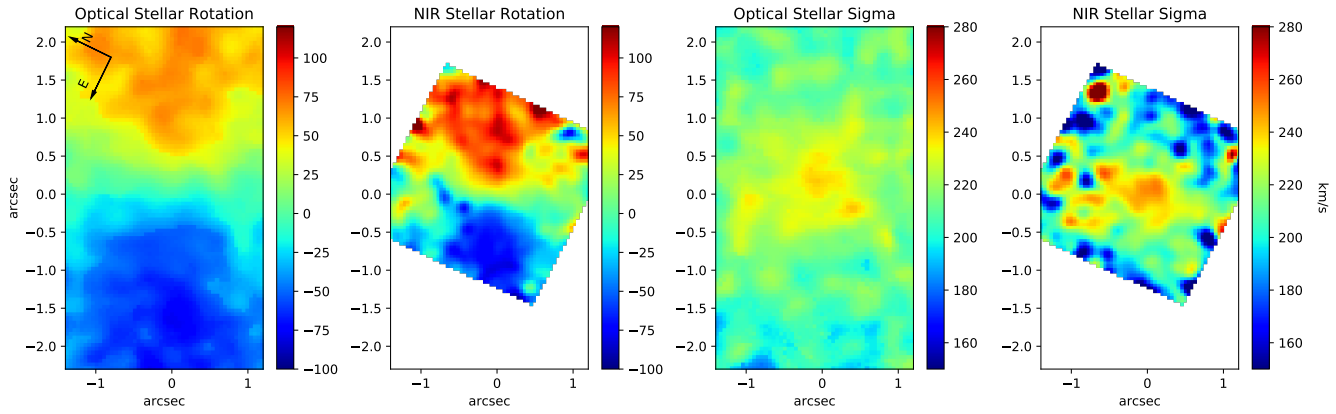

Figure 8. Optical and NIR stellar kinematics derived by pPXF

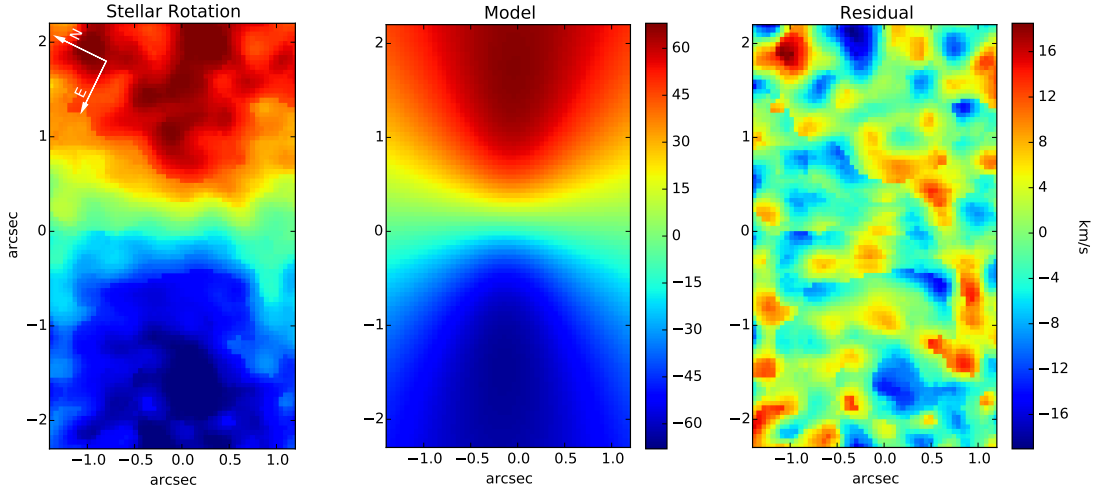

Figure 9. Stellar rotation, model and residual for the optical data.

which case NIR data was able to access stellar populations which were not found through optical data. By using NIR data, similar circumnuclear rings of intermediate-age populations were already reported before (Riffel et al. 2010, 2011; Storchi-Bergmann et al. 2012; Diniz et al. 2017), suggesting that this population can be real. However, the lack of any contribution from stellar populations younger than 10 Gyr in the optical spectra suggests a different explanation, in which these populations are being mistakenly identified by STARLIGHT as a consequence of other factors, discussed below.

5.2 Panchromatic synthesis

The results obtained by combining optical and NIR data favor optical results, with a dominance of old (~10 Gyr) stellar populations in the entire FoV. Also, NIR data is well reproduced by the panchromatic fit, suggesting that the result is degenerated. Lastly, our NIR results are in contrast with literature results, which show that elliptical galaxies are dominated by old stellar populations (e.g. Padilla & Strauss 2008; Zhu et al. 2010).

Knowing that the intermediate-age circumnuclear ring found in the NIR completely vanished after combining optical and NIR data (which added information allowing the identification of a broader range of stellar populations), our panchromatic results suggest that other factors might me playing an important role in the determination of the stellar population of the NIR data, besides the stellar properties of the galaxy itself. First, we do not have H-band data, which contains more stellar absorptions when compared to J and K-bands. Second, the low signal-to-noise ratio of the J precludes the presence of enough constraints to STARLIGHT, besides the shape of the continuum. As reported in the literature, the fit of the absorption bands is crucial to the correct determination of the stellar population of the galaxy using NIR data (Baldwin et al. 2018; Dahmer-Hahn et al. 2018). These results combined suggest that the circumnuclear ring found in the NIR might be biased towards younger ages.

Since optical results detected a dominance of old stel-

lar populations, and considering the elliptical nature of NGC 1052, we did not expect to detect a different stellar population by adding NIR data. However, for galaxies dominated by intermediate-age stellar populations (which display unique NIR features, Maraston 2005; Riffel et al. 2007, 2009), this technique of adding NIR data to optical studies might be useful in order to unambiguously determine their stellar populations. This technique might also be useful to study the contents of more luminous AGNs, such as Seyfert galaxies, due to the usual presence of a strong featureless continuum, emitted by the AGN, which peaks in the optical or even bluer wavelengths. The NIR also allows the constraint of the contribution of the AGN hot nuclear torus.

5.3 Equivalent Width Drop

For the optical Fe5270 index, we compared the EW values with the ones available online for the E-MILES library. For SSPs younger than 1 Gyr, their derived values for this absorption are much smaller than ours, with values close to zero for the younger models and subsolar metallicity. Our off-center measurements have an average value of 2.76±0.17Å, and are compatible with a wide range of values. For solar metallicity, the compatible ages range from 2.5 to 6.5 Gyr, whereas for subsolar metallicity the range goes from 1.0 to 4.0 Gyr and for supersolar metallicities range from 6.5 Gyr up to the older models with 14.0 Gyr.

In order to compare NIR absorptions, due to the lack of measurements in the literature, we employed our technique to the E-MILES models and measured their equivalent widths. For the safe models available (t>0.5 Gyr), the EW values range from 14.0 to 18.5 Å for the first CO absorption, 14.4 to 18.8 Å for the second, and 15.4 to 21.1 Å for the third. These measurements are compatible with all our extranuclear measurements for these bands within the standard error of the data (average EW of 17.5±1.2, 17.8±1.0, 20.4±1.1 for the three CO bands respectively). However, no valuable information can be extracted from these absorptions concerning the stellar population of the galaxy, since nearly all SSPs from 0.5 Gyr to 14 Gyr match our data properly.

The spatial distribution of the stellar absorptions shows a nuclear EW drop in the nuclear region, both in the optical and in the NIR, with the same spatial profile of the PSF of the data. These results suggest that the region in which the EW drop is produced is not spatially resolved, being confined to the region dominated by the LLAGN.

Since the spectral synthesis did not detect any contribution from a featureless continuum or a nuclear variation in the stellar populations, these results indicate that a stellar population synthesis is unable to detect all components that contribute to the emission of this galaxy. It is worth noting that, even the optical synthesis, which was performed with E-MILES library and included both young SSPs and a featureless continuum, did not detect such components.

There are two possible explanations for these EW drops. First, this can be caused by a difference in the stellar population in the central region, such as a young stellar population in which only the hydrogen absorptions are present, and thus could dilute the EWs of the other absorption lines. A second explanation is a featureless continuum caused by the AGN, which can dilute the stellar population features.

Since this galaxy is elliptical, suggesting that high contributions from young populations are not likely to occur, and since it hosts a LLAGN (Wrobel 1984; Fey & Charlot 1997; Kadler et al. 2004; Barth et al. 1999; Sugai et al. 2005), this nuclear EW drop points toward a featureless continuum associated with the LLAGN.

A similar result was already reported by Burtscher et al. (2015), which analyzed 51 local AGNs, with NGC 1052 as part of the sample, and found the same EW nuclear drop. They also associated this drop with the contribution from a featureless continuum from the AGN hosted by this galaxy.

5.4 Stellar Kinematics

The kinematic results, showing that this galaxy displays a circular rotation and a broadened nuclear dispersion, are in agreement with the ones derived by Dopita et al. (2015) and Riffel et al. (2017). The stellar kinematics of this galaxy is characterized by a rotation with a major axis oriented along the East-West direction (slightly inclined toward Southeast-Northwest) with blueshifted velocities in the eastern region and redshifted velocities in the western region. Also, the stellar sigma peaks at ~240 km·s^{-1} in the nucleus, with lower (~200 km·s^{-1}) values closer to the borders. In the NIR, even with a lower S/N, it is possible to see that the rotation pattern agrees with that seen in the optical. The dispersion derived from the NIR data, on the other hand, is ~20km·s^{-1} higher if compared to optical values, which is probably a feature caused by the lower S/N of the NIR data.

The stellar sigma peak is cospatial with the EW drop in the absorption lines, suggesting that these two phenomena might be related. The most probable explanation is that both of them are related to the nuclear region, with the sigma peak being also caused by the sphere of influence of the SMBH.

6 CONCLUSIONS

In this work, we studied the spatial distribution of the stellar spectral properties of the inner 320×535 pc^2 of NGC 1052, both in the optical and in the NIR. Our results can be summarized as follows:

The stellar population in the optical is dominated by old (t>10 Gyr) components, with low (~0.5) nuclear dust extinction and solar metallicity throughout the galaxy. When performing the synthesis in the NIR, on the other hand, a circumnuclear ring of stellar populations with ages ~2.5 Gyr was found, also with low (~0.8) nuclear dust extinction and solar metallicity throughout the galaxy.

When performing the synthesis in the combined optical and NIR datacube, we found results compatible with the ones found in the optical, with a dominance of old (t>10 Gyr) stellar populations with low (~0.5) nuclear dust extinction and solar metallicity in the entire FoV.

The absorption bands, both in the optical and in the NIR, display a drop in the equivalent widths in the nucleus. This drop was not detected in the stellar population synthesis, indicating that a stellar population synthesis is unable to identify all components that contribute to the emission of this galaxy. We find that the presence of a featureless contin-

uum emitted by the LLAGN is the most plausible scenario to explain these drops.

Lastly, the stellar kinematics are dominated by two components. Random motions, as shown by the high ($\sim$240 km·s^{-1}) velocity dispersion, dominate the nucleus, with the remaining regions dominated by stars rotating in a plane around the center with speeds up to 100 km·s^{-1}.

ACKNOWLEDGEMENTS

We thank the anonymous referee for reading the paper carefully and providing thoughtful comments that helped improving the quality of the paper. LGDH thanks CNPq. RR thanks CNPq and FAPERGS for financial support. NZD thanks to CNPq for partial funding. RAR thanks support from CNPq and FAPERGS. Based on observations obtained at the Gemini Observatory and processed using the Gemini IRAF package, which is operated by the Association of Universities for Research in Astronomy, Inc., under a cooperative agreement with the NSF on behalf of the Gemini partnership: the National Science Foundation (United States), the National Research Council (Canada), CONICYT (Chile), Ministerio de Ciencia, Tecnología e Innovación Productiva (Argentina), and Ministério da Ciência, Tecnologia e Inovação (Brazil). This study was financed in part by the Coordenação de Aperfeiçoamento de Pessoal de Nível Superior - Brasil (CAPES) - Finance Code 001.

REFERENCES

Adelman-McCarthy J. K., et al., 2006, The Astrophysical Journal Supplement Series, 162, 38
Allington-Smith J., et al., 2002, PASP, 114, 892
Baillard A., et al., 2011, A&A, 532, A74
Baldwin C., McDermid R. M., Kuntschner H., Maraston C., Conroy C., 2018, MNRAS, 473, 4698
Barth A. J., Filippenko A. V., Moran E. C., 1999, ApJ, 515, L61
Bertola F., Bettoni D., Danziger J., Sadler E., Sparke L., de Zeeuw T., 1991, ApJ, 373, 369
Bica E., 1988, A&A, 195, 76
Bruzual G., Charlot S., 2003, MNRAS, 344, 1000
Burtscher L., et al., 2015, A&A, 578, A47
Cappellari M., Emsellem E., 2004, PASP, 116, 138
Cardelli J. A., Clayton G. C., Mathis J. S., 1989, ApJ, 345, 245
Cesetti M., et al., 2009, A&A, 497, 41
Cid Fernandes R., Gu Q., Melnick J., Terlevich E., Terlevich R., Kunth D., Rodrigues Lacerda R., Joguet B., 2004, MNRAS, 355, 273
Cid Fernandes R., Mateus A., Sodré L., Stasińska G., Gomes J. M., 2005, MNRAS, 358, 363
Cid Fernandes R., et al., 2013, A&A, 557, A86
Conroy C., Gunn J. E., White M., 2009, ApJ, 699, 486
Conroy C., Villaume A., van Dokkum P. G., Lind K., 2018, ApJ, 854, 139
Dahmer-Hahn L. G., Riffel R., Rodríguez-Ardila A., Martins L. P., Kehrig C., Heckman T. M., Pastoriza M. G., Dametto N. Z., 2018, MNRAS, 476, 4459
Dametto N. Z., Riffel R., Pastoriza M. G., Rodríguez-Ardila A., Hernandez-Jimenez J. A., Carvalho E. A., 2014, MNRAS, 443, 1754
Diaz A. I., Terlevich E., Pagel B. E. J., 1985, MNRAS, 214, 41P
Diniz M. R., Riffel R. A., Riffel R., Crenshaw D. M., Storchi-Bergmann T., Fischer T. C., Schmitt H. R., Kraemer S. B., 2017, MNRAS, 469, 3286
Dopita M. A., et al., 2015, ApJ, 801, 42
Engelbracht C. W., Rieke M. J., Rieke G. H., Kelly D. M., Achtermann J. M., 1998, ApJ, 505, 639
Fernández-Ontiveros J. A., López-Sanjuan C., Montes M., Prieto M. A., Acosta-Pulido J. A., 2011, MNRAS, 411, L21
Fey A. L., Charlot P., 1997, ApJS, 111, 95
Forbes D. A., Georgakakis A. E., Brodie J. P., 2001, MNRAS, 325, 1431
Fosbury R. A. E., Mebold U., Goss W. M., Dopita M. A., 1978, MNRAS, 183, 549
Fosbury R. A. E., Snijders M. A. J., Boksenberg A., Penston M. V., 1981, MNRAS, 197, 235
Gabel J. R., Bruhweiler F. C., Crenshaw D. M., Kraemer S. B., Miskey C. L., 2000, ApJ, 532, 883
Girardi L., Bressan A., Bertelli G., Chiosi C., 2000, A&AS, 141, 371
Goddard D., et al., 2017a, MNRAS, 465, 688
Goddard D., et al., 2017b, MNRAS, 466, 4731
Heckman T. M., 1980, A&A, 87, 152
Hennig M. G., Riffel R. A., Dors O. L., Riffel R., Storchi-Bergmann T., Colina L., 2018, MNRAS,
Ho L. C., Filippenko A. V., Sargent W. L. W., Peng C. Y., 1997, ApJS, 112, 391
Hook I. M., Jørgensen I., Allington-Smith J. R., Davies R. L., Metcalfe N., Murowinski R. G., Crampton D., 2004, PASP, 116, 425
Kadler M., Kerp J., Ros E., Falcke H., Pogge R. W., Zensus J. A., 2004, A&A, 420, 467
Kotilainen J. K., Hyvönen T., Reunanen J., Ivanov V. D., 2012, MNRAS, 425, 1057
Kroupa P., 2001, MNRAS, 322, 231
Lançon A., Goldader J. D., Leitherer C., González Delgado R. M., 2001, ApJ, 552, 150
Mallmann N. D., et al., 2018, MNRAS, 478, 5491
Maraston C., 2005, MNRAS, 362, 799
Martins L. P., Rodríguez-Ardila A., Diniz S., Riffel R., de Souza R., 2013, MNRAS, 435, 2861
Mason R. E., et al., 2015, ApJS, 217, 13
McGregor P. J., et al., 2003, in Iye M., Moorwood A. F. M., eds, Proc. SPIEVol. 4841, Instrument Design and Performance for Optical/Infrared Ground-based Telescopes. pp 1581–1591, doi:10.1117/12.459448
Meneses-Goytia S., Peletier R. F., Trager S. C., Vazdekis A., 2015, A&A, 582, A97
Menezes R. B., Steiner J. E., Ricci T. V., 2014, MNRAS, 438, 2597
Menezes R. B., da Silva P., Ricci T. V., Steiner J. E., May D., Borges B. W., 2015, MNRAS, 450, 369
Milone A. D. C., Rickes M. G., Pastoriza M. G., 2007, A&A, 469, 89
Noël N. E. D., Greggio L., Renzini A., Carollo C. M., Maraston C., 2013, ApJ, 772, 58
Oliva E., Origlia L., Kotilainen J. K., Moorwood A. F. M., 1995, A&A, 301, 55
Origlia L., Moorwood A. F. M., Oliva E., 1993, A&A, 280, 536
Padilla N. D., Strauss M. A., 2008, MNRAS, 388, 1321
Pierce M., Brodie J. P., Forbes D. A., Beasley M. A., Proctor R., Strader J., 2005, MNRAS, 358, 419
Raimann D., Storchi-Bergmann T., Bica E., Alloin D., 2001, MNRAS, 324, 1087
Rembold S. B., et al., 2017, MNRAS, 472, 4382
Rieke G. H., Lebofsky M. J., Thompson R. I., Low F. J., Tokunaga A. T., 1980, ApJ, 238, 24
Riffel R., Borges Vale T., 2011, Ap&SS, 334, 351
Riffel R. A., Storchi-Bergmann T., 2011, MNRAS, 417, 2752
Riffel R., Pastoriza M. G., Rodríguez-Ardila A., Maraston C., 2007, ApJ, 659, L103

Riffel R., Pastoriza M. G., Rodríguez-Ardila A., Maraston C., 2008, MNRAS, 388, 803
Riffel R., Pastoriza M. G., Rodríguez-Ardila A., Bonatto C., 2009, MNRAS, 400, 273
Riffel R. A., Storchi-Bergmann T., Riffel R., Pastoriza M. G., 2010, ApJ, 713, 469
Riffel R., Riffel R. A., Ferrari F., Storchi-Bergmann T., 2011, MNRAS, 416, 493
Riffel R., et al., 2015, MNRAS, 450, 3069
Riffel R. A., Storchi-Bergmann T., Riffel R., Dahmer-Hahn L. G., Diniz M. R., Schönell A. J., Dametto N. Z., 2017, MNRAS, 470, 992
Röck B., Vazdekis A., Ricciardelli E., Peletier R. F., Knapen J. H., Falcón-Barroso J., 2016, A&A, 589, A73
Storchi-Bergmann T., Riffel R. A., Riffel R., Diniz M. R., Borges Vale T., McGregor P. J., 2012, ApJ, 755, 87
Sugai H., Malkan M. A., 2000, ApJ, 529, 219
Sugai H., et al., 2005, ApJ, 629, 131
Vazdekis A., Koleva M., Ricciardelli E., Röck B., Falcón-Barroso J., 2016, MNRAS, 463, 3409
Wilkinson D. M., Maraston C., Goddard D., Thomas D., Parikh T., 2017, MNRAS, 472, 4297
Winge C., Riffel R. A., Storchi-Bergmann T., 2009, ApJS, 185, 186
Worthey G., Faber S. M., Gonzalez J. J., Burstein D., 1994, ApJS, 94, 687
Wrobel J. M., 1984, ApJ, 284, 531
Xilouris E. M., Madden S. C., Galliano F., Vigroux L., Sauvage M., 2004, A&A, 416, 41
Zheng Z., et al., 2017, MNRAS, 465, 4572
Zhu G., Blanton M. R., Moustakas J., 2010, ApJ, 722, 491
Zibetti S., Gallazzi A., Charlot S., Pierini D., Pasquali A., 2013, MNRAS, 428, 1479
de Amorim A. L., et al., 2017, MNRAS, 471, 3727
van Dokkum P. G., 2001, PASP, 113, 1420
van Gorkom J. H., Knapp G. R., Raimond E., Faber S. M., Gallagher J. S., 1986, AJ, 91, 791

This paper has been typeset from a TEX/LATEX file prepared by the author.

Capítulo 5

Um estudo pancromático espacialmente resolvido dos 500 pc centrais de NGC 1052: excitação e cinemática do gás

Após a subtração da componente estelar, analisamos a excitação e cinemática da componente gasosa. Estes resultados, bem como uma discussão destes, se encontram na forma de um artigo que foi enviado à revista MNRAS em Maio de 2019, intitulado *A panchromatic spatially resolved study of the inner 500 pc of NGC 1052 - II. Gas excitation and kinematics.*

MNRAS 000, 1–16 (2019) Preprint 20 August 2019 Compiled using MNRAS LATEX style file v3.0

A panchromatic spatially resolved study of the inner 500 pc of NGC 1052 - II: Gas excitation and kinematics

L. G. Dahmer-Hahn [1]★, R. Riffel[1], T.V. Ricci[2], J. E. Steiner[3], T. Storchi-Bergmann[1], R. A. Riffel[4,5], R. B. Menezes[6], N.Z. Dametto[7], M. R. Diniz[4], J. C. Motter[1], D. Ruschel-Dutra[7]

[1]*Departamento de Astronomia, Universidade Federal do Rio Grande do Sul. Av. Bento Goncalves 9500, 91501-970, Porto Alegre, RS, Brazil.*
[2]*Universidade Federal da Fronteira Sul, Campus Cerro Largo, RS 97900-000, Brazil*
[3]*Instituto de Astronomia, Geofísica e Ciências Atmosféricas, Universidade de São Paulo, 05508-900, São Paulo, Brazil*
[4]*Universidade Federal de Santa Maria, Departamento de Física, Centro de Ciências Naturais e Exatas, 97105-900, Santa Maria, RS, Brazil*
[5]*Center for Astrophysical Sciences, Department of Physics and Astronomy, The Johns Hopkins University, Baltimore, MD 21218, USA*
[6]*Centro de Ciências Naturais e Humanas, Universidade Federal do ABC, 09210-580, SP, Brazil*
[7]*Departamento de Física - CFM - Universidade Federal de Santa Catarina, 476, 88040-900, Florianópolis, SC, Brazil*

Accepted XXX. Received YYY; in original form ZZZ

ABSTRACT

We map the optical and near-infrared (NIR) emission-line flux distributions and kinematics of the inner 320×535 pc^2 of the elliptical galaxy NGC 1052. The integral field spectra were obtained with the Gemini Telescope using the GMOS-IFU and NIFS instruments, with angular resolutions of 0.″88 and 0.″1 in the optical and NIR, respectively. We detect five kinematic components: (1 and 2) Two spatially unresolved components, being a broad line region visible in Hα, with a FWHM of ∼3200 km s^{-1} and an intermediate-broad component seen in the [OIII]$\lambda\lambda$4959,5007 doublet; (3) an extended intermediate-width component with 280<FWHM<450 km s^{-1} and centroid velocities up to 400 km s^{-1}, which dominates the flux in our data, attributed either to a bipolar outflow related to the jets, rotation in an eccentric disk or a combination of a disk and large-scale gas bubbles; (4 and 5) two narrow (FWHM<150 km s^{-1}) components, one visible in [OIII], and one visible in the other emission lines, extending beyond the field-of-view of our data, which is attributed to large-scale shocks. Our results suggest that the ionization within the observed field of view cannot be explained by a single mechanism, with photoionization being the dominant mechanism in the nucleus with a combination of shocks and photoionization responsible for the extended ionization.

Key words: galaxies: individual (NGC 1052) – galaxies: jets – galaxies: nuclei

1 INTRODUCTION

Depending on the main ionization source of a galaxy, different emission line intensities can be produced. While, for example, very young stellar populations tend to strongly ionize hydrogen if compared to other emission lines, active galactic nuclei (AGN) produce, among others, stronger optical [OIII] and [NII] lines (Kewley et al. 2001; Kauffmann et al. 2003, hereafter K01 and K03) if compared to hydrogen. Emission line ratios are, therefore, often used to discriminate between the possible ionization sources of galaxies (e.g. Baldwin et al. 1981, hereafter BPT).

A special class of galaxies is the Low Ionization Nuclear Emission Line Region (LINER, Heckman 1980), which is characterized by high values of [NII]λ6583Å/Hα, but lower values of [OIII]λ5007Å/Hβ if compared to Seyfert galaxies and quasars (K03). The nature of the LINERs is still matter of intense debate (e.g. Kehrig et al. 2012; Papaderos et al. 2013; Belfiore et al. 2015; Gomes et al. 2016; Belfiore et al. 2016), since many mechanisms are able to produce a LINER-like emission line spectrum besides low luminosity AGN (Ferland & Netzer 1983; Halpern & Steiner 1983), such as shocks (as initially proposed by Heckman 1980), post-asymptotic giant branch stars (pAGB) (Binette et al. 1994; Stasińska et al. 2008; Cid Fernandes et al. 2011; Yan & Blanton 2012) and starbursts with ages between 3 and 5 Myr, dominated by Wolf-Rayet stars (Barth & Shields 2000).

The hypothesis of a LINER powered by accretion onto a supermassive black hole has been confirmed in some sources. Ho et al. (1997) showed that, for a sample of 211 emission-line nuclei, about 20% have a broad component in their Hα line, with most of these objects belonging to the LINER class.

★ E-mail: dahmer.hahn@ufrgs.br

Recent studies using integral field unit (IFUs) data were able to isolate the components of the galaxies, searching for eventual central sources. From the SAURON sample, Sarzi et al. (2010) found a tight correlation between the stellar surface brightness and the flux of the Hβ recombination line. They also reported that hot evolved stars, probably pAGB stars, are the best candidates to ionize the gas. Loubser & Soechting (2013) found, for a sample of four central cluster galaxies (CCG) with LINER emission, that AGN photoionization models (with higher metallicity) are able to reproduce their spatially resolved line ratios, although they could not rule out models with shocks or photoionization by pAGB stars. Also, Ricci et al. (2014a,b, 2015) found in a sample composed of 10 LINERs, that most of them have emission compatible with a central AGN, although three of them have a circumnuclear structure with the shape of a disk, compatible with photoionization by pAGB stars and in one galaxy the ionization is compatible with shocks. By studying a sample of 14 Seyfert/LINER galaxies, Belfiore et al. (2015) reported that the observed extended emission is also consistent with ionization from hot evolved stars. A similar scenario was found in a series of papers (Kehrig et al. 2012; Papaderos et al. 2013; Gomes et al. 2016), where the authors used low spatial resolution data from Calar Alto Legacy Integral Field Area Survey, and found evidence of two different types of early-type galaxies (ETGs), which they classified as Type i and Type ii. A Type i ETG is a system with a nearly constant Hα equivalent width [EW(Hα)] in their extranuclear component, compatible with the hypothesis of photoionization by pAGB as the main driver of extended warm interstellar medium (wim) emission, whereas type ii ETGs are virtually wim-evacuated, with a very low outwardly increasing EW(Hα) ($\leq$ 0.5Å).

In order to further our understanding of galaxies with LINER emission, we conducted a study case for NGC 1052, an E4 galaxy at a distance of 19.1±1.4 Mpc, subject of a long and intense debate surrounding its LINER emission. For example, Koski & Osterbrock (1976) initially suggested that the gas ionization of the inner 2.″7×4.″0 is due to shocks, with Fosbury et al. (1978) presenting a detailed radiative shock model and Fosbury et al. (1981) finding no evidence of a compact source of non-stellar radiation capable of ionizing enough gas to produce the observed Balmer-line fluxes. On the other hand, Diaz et al. (1985) argued that the strengths of the [SIII]λ9069,λ9532 lines favor photoionization. Later, Sugai & Malkan (2000) studied NGC 1052 using mid infrared spectra and found evidence supporting shocks as the origin of ~80% of the excitation of this source. Gabel et al. (2000) also studied NGC 1052 and reported that emission-line fluxes obtained with the Faint Object Spectrograph attached to the Hubble Space Telescope can be simulated with simple photoionization models using a central source with a power law with spectral index α = -1.2. They also noted that simple model calculations using a gas with constant density do not match the intrinsic emission-line spectrum of NGC 1052 for any choice of density, requiring at least two different densities. Also, Dopita et al. (2015, hereafter D15) observed this galaxy with the IFS mode of the Wide Field Spectrograph, and reported the detection of two buoyant gas bubbles with ~1.5 kpc (15.″0) extending to both sides of the nucleus, which are expanding along the minor axis of the galaxy. They also found that, since two distinct densities can be found, a double-shock model explain better the data.

Broad Hydrogen emission line components were also reported for NGC 1052. Barth et al. (1999) used polarized light and confirmed a hidden Broad Line Region (BLR) on the Hα line. Later, Sugai et al. (2005, hereafter S05) observed this galaxy with the IFS mode of the Kyoto 3DII instrument mounted on the Subaru telescope, covering a ~3.″0×3.″0 FoV at ~0.″4 spatial resolution. They reported direct detection of a broad Hβ component, also finding evidence of three main kinematical components for the gas: a high-velocity bipolar outflow, low-velocity disk rotation, and a spatially unresolved nuclear component.

In radio wavelengths, this galaxy displays two jets with slightly different orientations. On kiloparsec scales, Wrobel (1984) found a radio jet oriented along the East-West direction, whereas on parsec scales, Fey & Charlot (1997) found a radio jet slightly bent toward the North-South direction. Recently, Baczko et al. (2016) calculated the parsec jet expansion velocity as β = v/c = 0.46 ± 0.08 and β = 0.69 ± 0.02 for the western and eastern jet, respectively.

In X-ray wavelengths, according to Kadler et al. (2004), NGC 1052 displays a compact core, best fitted by an absorbed power law with column density N_H = (0.6-0.8)×10^{22} cm^{-2}. Besides, they also reported various jet-related emissions and an extended region, also aligned with the radio synchrotron jet-emission.

In the first paper of this series (Dahmer-Hahn et al. 2019, hereafter paper I), aimed at shedding some light on the understanding of the physical mechanism behind the gas excitation in NGC 1052, we studied optical and near-infrared (NIR) stellar population properties of the inner 320×535 pc^2 of this galaxy. In Paper I, we fitted the stellar population simultaneously GMOS and NIFS datacubes for this galaxy. When using only the optical data, we found that its central region is dominated by old (t>10 Gyr) stellar populations, while when using NIR data we also found that the nucleus is dominated by an old stellar population but shows in addition a younger circumnuclear ring (~2.5 Gyr). In the combined optical and NIR datacube we found a dominance of older stellar populations. We also obtained stellar kinematics and we found that the stellar motions are dominated by a high (~240km s^{-1}) nuclear velocity dispersion, with stars also rotating around the center. Lastly, we measured equivalent widths of absorption features, both in the optical and in the NIR and found a drop in their values in the central regions of our FoV. We attributed this drop to the contribution of a featureless continuum emission from the low luminosity AGN (LLAGN).

Here in the second paper, we map the physical properties of the emitting gas using optical and near-infrared data free from the star light contamination. The data containing only the gas emission were obtained after subtracting the contribution of the stellar populations to the observed fluxes, as derived in the first paper. We looked for possible ionization mechanisms to explain the emission lines within the central 3.″5×5.″0 of NGC 1052. In order to achieve this, we use two main methods: direct emission-line fits, by identifying the kinematic components and obtaining spatially-resolved emission-line ratios, and the principal component analysis (PCA, Steiner et al. 2009) tomography technique. We also use literature radio data in order to search for correlations between the radio jet directions and our optical and NIR emission lines.

This paper is structured as follows: in Section 2, we present the data and its reduction, while in Section 3 we describe the emission line analysis. In Section 4, we present the results and in section 5 we discuss them. Lastly, in Section 6, we briefly summarize the main results found.

2 DATA AND REDUCTION

2.1 Optical Data

The data acquisition and reduction are detailed in Paper I. In short, optical data were obtained using the Gemini Multi-Object Spectrograph (GMOS) on IFU mode. The original Field of View is

3.″5×5.″0, with a natural seeing of 0.″88. The data were obtained using the B600 grating, resulting in a constant optical spectral resolution of ~1.8 Å. The reduction process and data treatment were performed following the steps described in Menezes et al. (2019): trimming, bias subtraction, bad pixel and cosmic ray removal, extraction of the spectra, GCAL/twilight flat correction, wavelength calibration, sky subtraction, flux calibration, correction of the differential atmospheric refraction, high spatial-frequency components removal with the Butterworth spatial filtering, "instrumental fingerprint" removal and Richardson-Lucy deconvolution. The final angular resolution is 0.″70. The integrated optical continuum image, as obtained from the integration of the datacube, is shown in the left part of panel c of Fig. 1.

2.2 NIR Data

The Near-Infrared (NIR) data were obtained using Gemini North Near-Infrared Integral Field Spectrograph (hereafter NIFS) with the ALTAIR adaptive optics system. The angular resolution of the raw data is 0.″1×0.″1. Since we applied a boxcar filter to improve the Signal-to-Noise ratio (S/N), the final spatial resolution is 0.″15×0.″15. The spectral resolution is $\lambda/\Delta\lambda = 6040$ for the J band and 5290 for the K band, corresponding to 50 and 57 km s^{-1} respectively. The data were reduced using the standard reduction scripts distributed by the Gemini team, which included trimming of the images, flat fielding, sky subtraction, wavelength and s-distortion calibrations and telluric absorption removal, flux calibration, differential atmospheric refraction correction, Butterworth spatial filtering and instrumental fingerprint removal. The final spectral coverage of the NIR data is 11472-13461 Å for the J band and 21060-24018 Å for the K band, and the final field of view is 2.″5×2.″5. More details of the data reduction procedure can be found in Paper I. The NIR K-band continuum image, as obtained from the integration of the datacube, is shown in the right map of panel c of Fig. 1.

2.3 Radio Data

In order to assess any correlation between the gas kinematics probed by our optical and NIR observations with the direction of the NGC 1052 radio jets, we show in Fig. 1 (panel b) the historical 20 cm total intensity map of its kiloparsec scale jet obtained by Wrobel (1984) using the Very Large Array (VLA). In Fig. 1 (panel d), we show the 2 cm total intensity map of the parsec scale jet of NGC 1052 obtained using the Very Long Baseline Array (VLBA) and made publicly available by the MOJAVE team (Monitoring of Jets in AGNs with VLBA Experiments, Lister et al. 2018).

3 EMISSION LINE FITTING

The emission line fluxes were measured in a pure emission line spectrum, free from the underlying stellar flux contributions. In order to obtain it, we used the optical and NIR stellar contents derived in Paper I, with E-MILES (Vazdekis et al. 2016) models and the STARLIGHT code (Cid Fernandes et al. 2004, 2005). In Paper I, optical and NIR stellar populations were modeled separately, but were also derived after combining both ranges. We chose to subtract the stellar populations which were derived separately for optical and NIR datacubes, since NIR data was degraded in order to match the optical resolution. Additionally, in order to remove lower-order noise, we fitted and subtracted a five degree polynomial function to each spectrum after subtracting the stellar content. The systemic velocity was derived from the modelling of the stellar kinematics from Paper I.

Close to the center of our FoV, a broad component is present in Hα. Since its distribution is unresolved by our data, we fitted this component separately, masking out the narrow components of [NII] and Hα, and forcing its spatial distribution to be the same of the PSF. The determined FWHM of this broad component is ~3200 km s^{-1}.

After subtracting this broad component, the emission line fitting was performed with IFSCUBE [1], which is a Python based package of spectral analysis routines. The code allows the simultaneous fitting of multiple Gaussian or Gauss-Hermite profiles in velocity space, with or without constraints or bounds. The algorithm includes integrated support for pixel-by-pixel uncertainties, weights and flags, subtraction of stellar population spectra, pseudo-continuum fitting, signal-to-noise ratio evaluation and equivalent width measurements. The actual fitting relies on SCIPY's implementation of Sequential Least Squares Programming.

Because of the complex kinematics of NGC 1052, two Gaussian functions were needed in order to fit each emission-line profile, one narrow (100 < FWHM < 150 km s^{-1}) and one with intermediate-width (hereafter IW, 280 < FWHM < 450 km s^{-1}). We tried more complex configurations, such as using two gauss-hermite polynomials or three gaussians for each emission line, but none of them contributed significantly to the quality of the fits.

Also, because of the complexity of the [NII] + Hα region, where six gaussian functions were needed in a short wavelength range, we chose to fit the whole optical spectrum at the same time, constraining the FWHM and centroid velocity of emission lines with similar ionization potential, critical density, and which are formed close to each other in the nebulae. We divided the emission lines in four groups, constrained to have the same kinematics as follows:

(i) Ionized hydrogen (Hα, Hβ and Hγ)
(ii) Doubly ionized oxygen ([OIII] λ4363, λ4959 and λ5007 Å)
(iii) Neutral oxygen ([OI] λ6300 and λ6360 Å)
(iv) Neutral and ionized nitrogen, and ionized sulfur ([NI]λ5200Å, [NII] λ5755,6548,6583Å and [SII] λ6716,6731Å)

We also performed the fitting using different configurations, such as forcing all emission lines to share the same double gaussian profile, or separating all emission lines. However, all these configurations point toward the same results, where only [OIII] behaves differently compared to the other emission lines.

4 RESULTS

4.1 Fluxes and Kinematics

The flux distribution maps of the narrow and IW components of Hβ and [OIII]λ5007Å emission lines are shown in the top panels of Fig 2. We decided not to show the [OI] , [NI], [NII] and [SII] maps because they follow both the kinematics and flux distribution of the HI lines. Also, we decided to plot Hβ maps instead of Hα since the later is blended with two [NII] emission lines. Over these panels, we show the orientation of the kiloparsec and parsec scale radio jets, represented by the white and black arrows, respectively. Over the narrow Hβ centroid velocity map, we also show in magenta the orientation of the gas bubbles identified by D15.

Although NGC 1052 has complex gas kinematics throughout

[1] publicly available in the internet https://bitbucket.org/danielrd6/ifscube

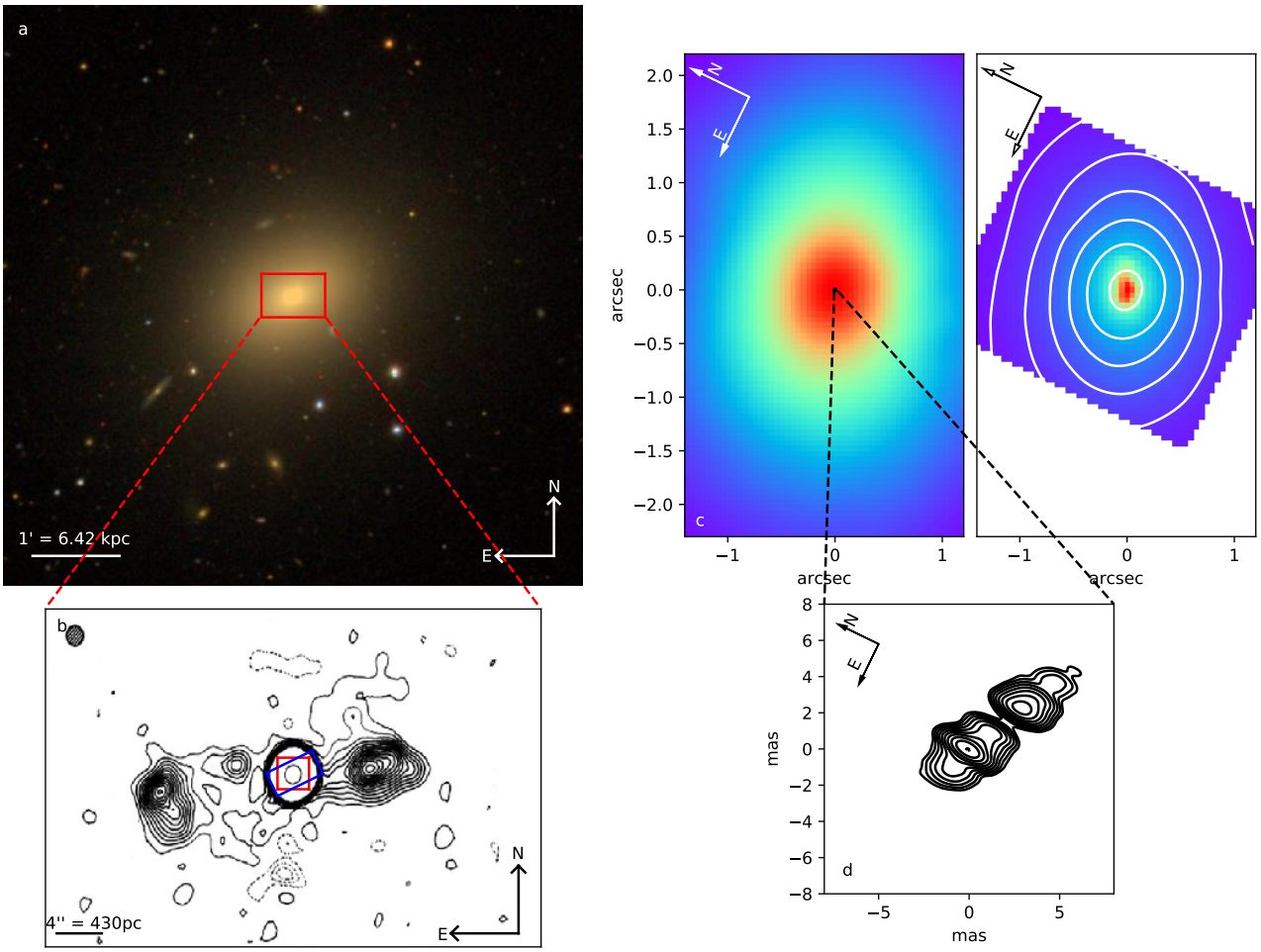

Figure 1. Panel a: SDSS image of NGC 1052 with the field of view of the panel b radio image in red. Panel b: NGC 1052 total intensity map obtained with the VLA at 20 cm (Wrobel 1984). The map peaks at 737 mJy/beam and contours are drawn at 500 μJy/beam x (-4,-3,-2,-1,1,2,3,4,5,6,7,8,9,10,11,12,13,14,15,800). Over this panel we indicate the GMOS FOV in blue and NIFS FOV in red. Panel c: left, optical continuum obtained with GMOS. In black, FOV of panel d radio image. Right, NIR k-band continuum obtained using NIFS. In white, optical contours of the GMOS-IFU continuum. Panel d: NGC 1052 total intensity map of the parsec scale jet obtained with the VLBA at 2 cm on 2012/March/27 (Lister et al. 2018). The bottom I contour is 1/512 of the peak of 0.551 Jy/beam, and the contours increase in steps of 2. The restoring beam dimensions are 1.40×0.50 mas at the position angle -6°.6.

the entire FoV, we selected three key regions where this complexity is more evident. We labeled them N, for the nuclear region, and A and B, which lie in the direction of the kiloparsec scale jet. In the second column, first row panel of Fig. 2, we indicate these three regions. The spectra and fits of the emission lines of these three regions are presented in Fig. 3.

In the middle and bottom panels of Fig 2, we present the centroid velocity and FWHM maps of the narrow and IW components of Hβ and [OIII]λ5007Å emission lines. We also overploted on the centroid velocity panels the orientations of kiloparsec and parsec scale radio jets in white and black arrows, and in magenta the orientation of D15 gas bubbles. The regions A, B and N are also marked over the Hβ IW centroid velocity panel.

In the nuclear region, a blue wing is visible in the nebular [OIII] emission lines. A third gaussian function was needed in order to fit this region. We show in Fig. 4 the spectra and fits of the [OIII] and Hβ of the central spaxel of region N. The FWHM derived for this component is 1380 km s^{-1}, and the centroid velocity is -490 km s^{-1}. This wing is not detected in the other emission lines.

4.2 Dust reddening

When calculating the dust reddening and flux ratios of NGC 1052, in order to avoid possible degeneracies introduced by the the emission-line fitting procedure, we decided to sum the fluxes of the narrow and IW components. The main reason behind this choice is the dominance of the IW component, with an integrated flux between 5 and 10 times larger if compared to the narrow component (see Fig 2), which resulted in a low S/N in the narrow component maps.

In order to estimate the dust reddening [E(B-V)], we followed Brum et al. (2019) and used the lines of Hα and Hβ applying the relation:

$$E(B-V) = \frac{0.81}{q(H\alpha) - q(H\beta)} log(\frac{H\alpha}{3.1 H\beta})$$

with $q(H\alpha) - q(H\beta) = 0.586$ obtained from the Cardelli et al. (1989) law and assuming 3.1 as the intrinsic ratio Hα/Hβ (which is typical for AGNs according to Osterbrock & Ferland 2006). The map is presented in Fig. 5.

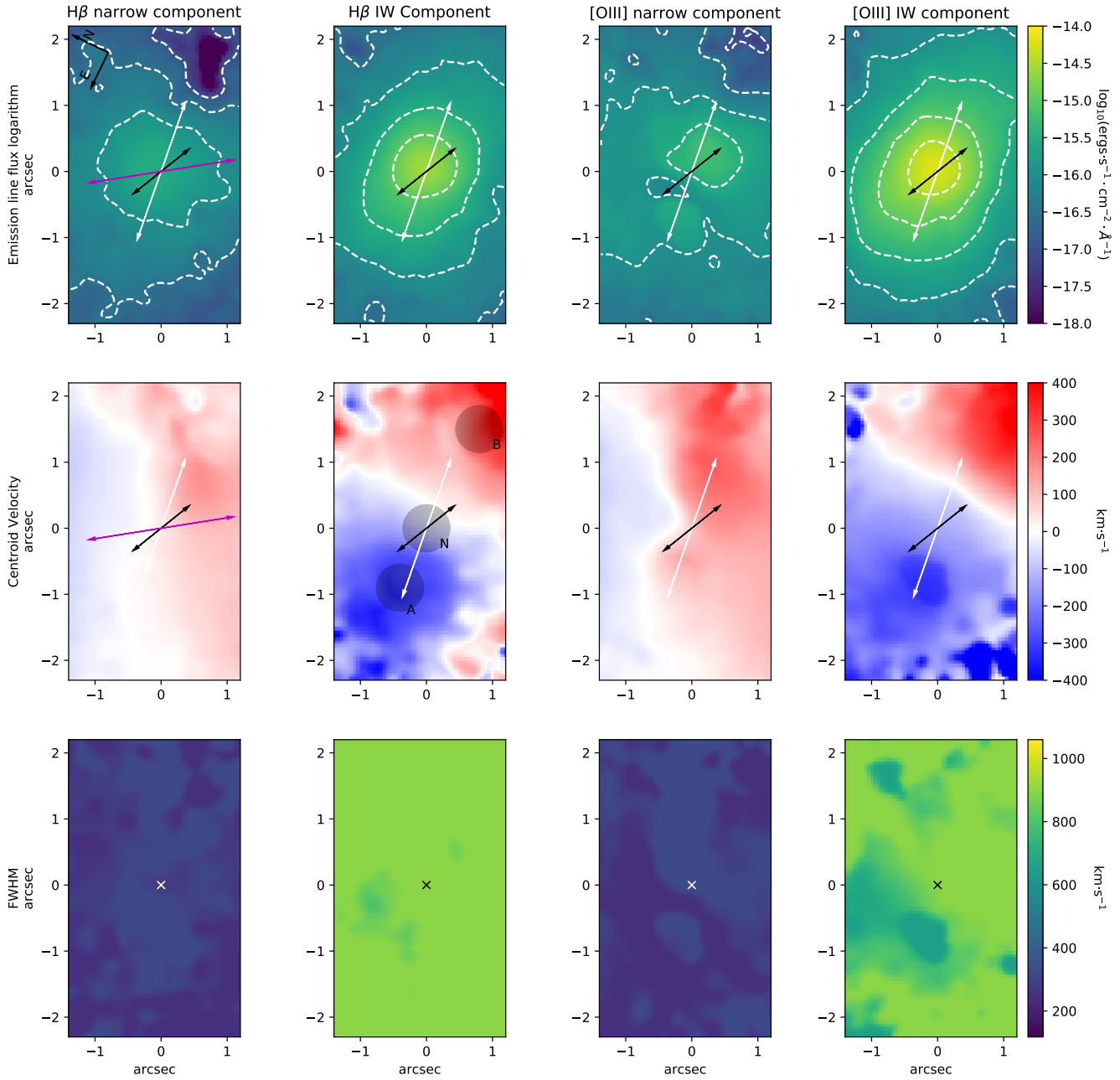

Figure 2. Emission line flux, centroid velocity and FWHM maps of Hβ and [OIII]λ5007Å narrow and IW emission lines. The size of the spaxels is 0.″05. First row shows emission line flux maps in log scale with contours drawn. We superimpose on the Hβ IW flux panel the three regions whose spectra are presented in Fig 3. Middle row panels show centroid velocity maps, where rest-frame emission is white. In the middle row panels, the white and black arrows represent the orientations of the kiloparsec and parsec scale jet, respectively. In the narrow Hβ centroid velocity map, the arrow in magenta represents the orientation of the gas bubbles identified by D15.

4.3 Electron temperature and density

In order to account for dust extinction, we corrected all optical emission lines by the E(B-V) values of Fig. 5. The electron temperature was then determined based on the [OIII](λ4959+λ5007)/λ4363 and [NII](λ6548+λ6583)/λ5755 ratios. To compute the electron density, we used the [SII]λ6716/λ6731 ratio (Osterbrock & Ferland 2006). The calculations were performed using the TEMDEN package present in the IRAF software (Shaw & Dufour 1995).

We show the density map in Fig 6, which was estimated assuming T_e=10.000 K. Since auroral emission lines are very feeble compared to their nebular counterparts, resulting in an overall low S/N, we decided to calculate temperature based in the integrated spectra of the regions N, A and B. We also extracted the integrated spectra of the circumnuclear (C) region, which we defined as the integrated datacube spectrum minus the spectrum of region N. In order to calculate these temperatures, we estimated the density based on the average map value within that region. The values of [OIII] and [NII] temperatures are listed in Table 1.

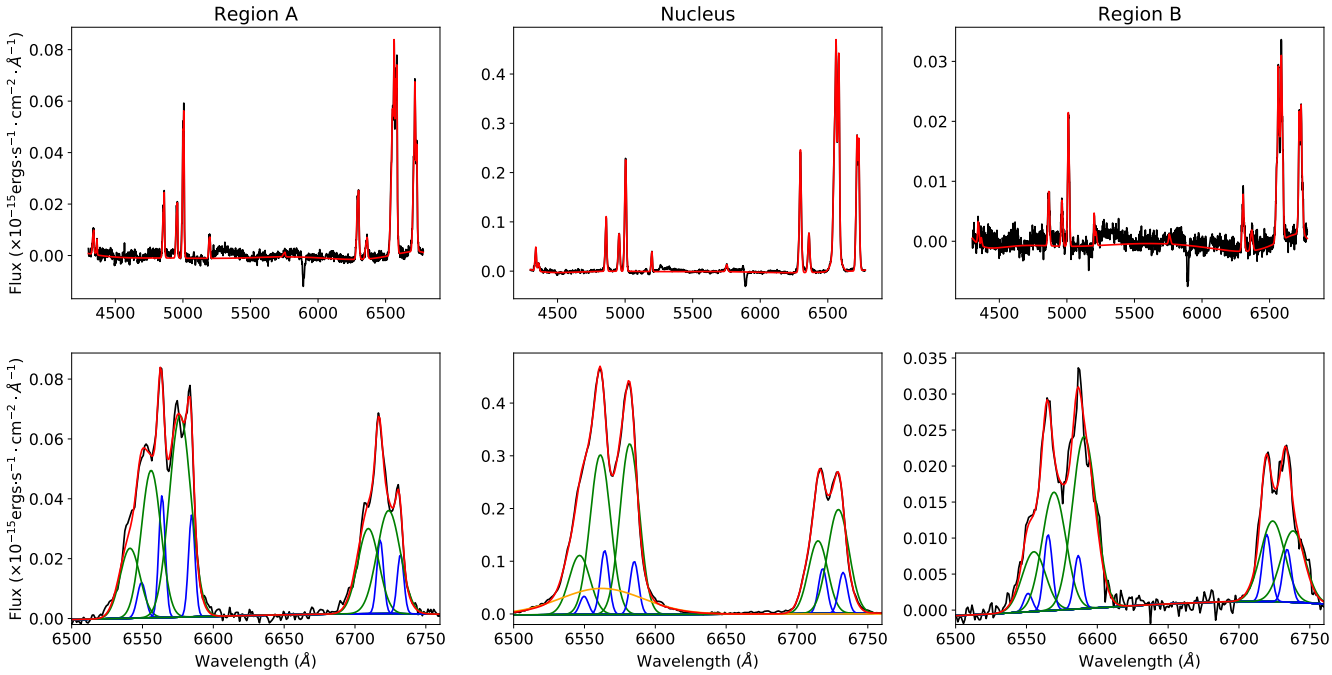

Figure 3. Fits of the optical emission lines of the central spaxel of the three regions marked in Fig. 2 after subtracting the contribution from the stellar population. The upper panels show the observed (black) and modeled spectrum (red). The bottom panels show in more detail the region between 6500 and 6760 Å. The different components of the modeled spectrum are shown in the bottom panels: narrow components are plotted in blue, IW components in green and the broad component is plotted in orange (central panel only).

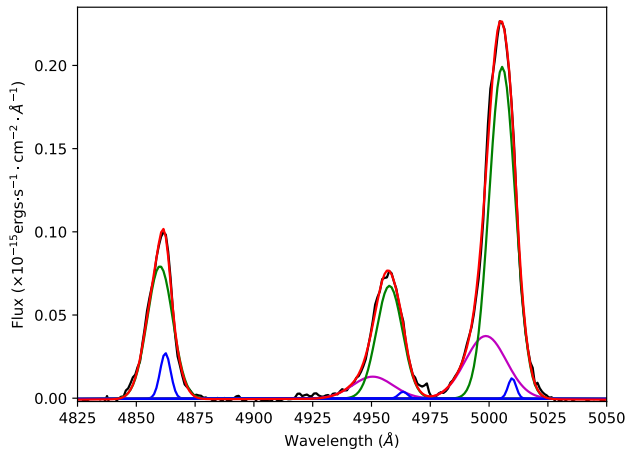

Figure 4. Fits of the Hβ and nebular [OIII] emissions of the central spaxel of region N, after subtracting the contribution from the stellar population. The observed and modeled spectra are shown in black and red, respectively. Narrow components are plotted in blue, IW components in green, and the [OIII] broad-intermediate components are plotted in magenta.

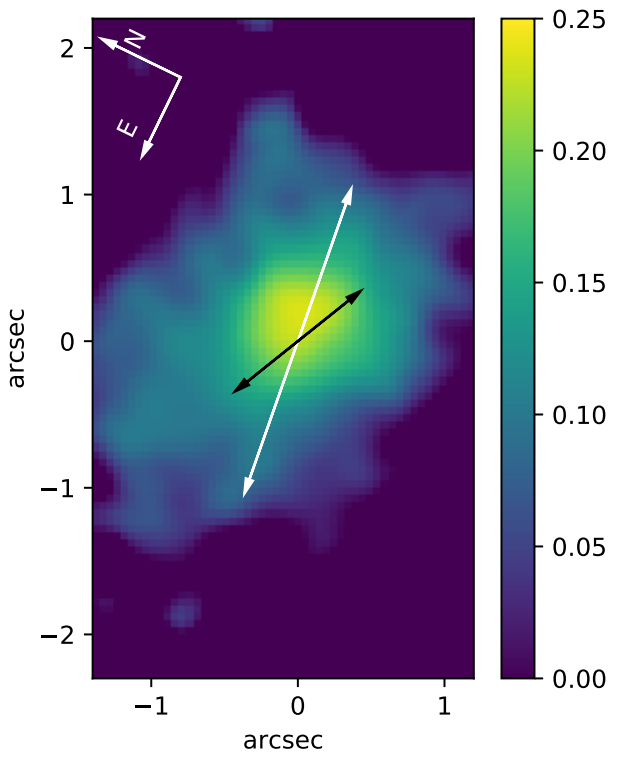

Figure 5. E(B-V) map for NGC 1052, derived from the Hβ/Hα line ratio.

As mentioned earlier, in the nuclear region, a blue wing is present in the nebular [OIII] emission lines. We found that adding another gaussian function in the fitting of auroral [OIII] emission produced degenerate results, between 14,000 and 30,000 K. For that reason, we do not present [OIII] temperature for the nuclear region.

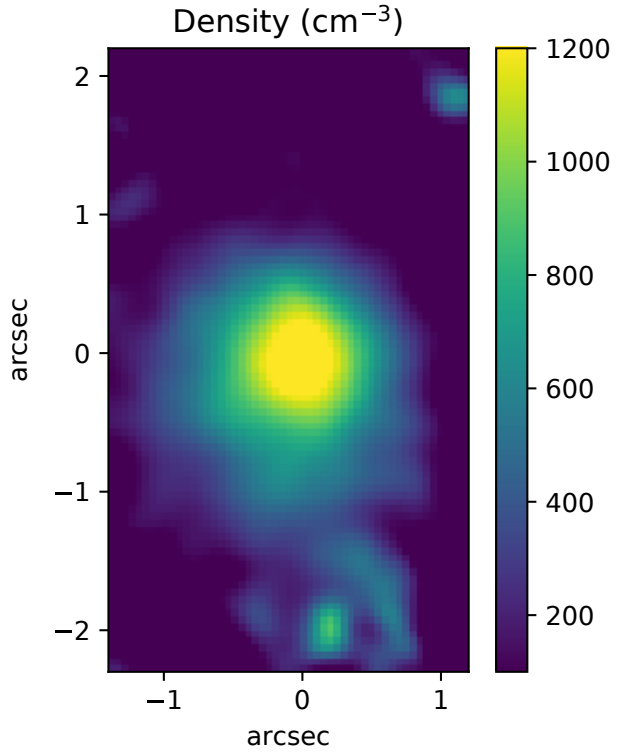

Figure 6. Density maps measured from the [SII]λ6716/λ6731 ratio.

Region	T$_{[OIII]}$ (10^3K)	T$_{[NII]}$ (10^3K)
N	—	12.75 ± 1.5
A	24.7 ± 4.3	10.9 ± 0.8
B	—	—
C	25.2 ± 2.8	11.4 ± 1.1

Table 1. Temperature and density of regions N, A, B and the integrated circumnuclear (C) regions.

4.4 Diagnostic Diagrams

Since we are testing the nature of the gas emission in NGC 1052, the fact that LINER-like line ratios can be produced by old stellar populations also needs to be tested. One way of doing this is by using the WHAN diagram (Cid Fernandes et al. 2011), defined as the equivalent width of the Hα emission versus the [NII]/Hα ratio. This diagram is divided in four regions: star forming, strong AGN, weak AGN and retired galaxies (i.e. galaxies that have stopped forming stars and are ionized by their hot low-mass evolved stars).

Since the Hα equivalent width is defined as the Hα flux divided by the average stellar flux below its emission, we used the stellar flux derived in Paper I. Also, since both the stellar and gas emission are affected by reddening, we used both fluxes before dereddening them. WHAN diagram is presented in Fig 7. We highlighted regions A, B and N. Also, we plotted in red the average values of the collapsed datacube.

We also employed BPT diagrams in order to understand the nature of the emission of NGC 1052. These diagrams uncover differences that do not appear in the flux maps. The maps of

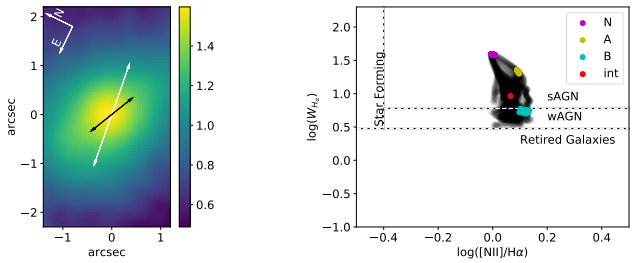

Figure 7. Left: EW$_{H\alpha}$ map. Right: WHAN diagram of NGC 1052. Over this panel, we highlighted regions A, B and N. Also, we plotted in red the average values for the collapsed datacube.

[OIII]λ5007Å/Hβ and [NII]λ6587Å/Hα are shown in Fig 8, and the respective diagnostic diagram is plotted in Fig 9. In order to disentangle the nature of NGC 1052 emission, in the first panel we superimposed the lines from the references K01 (blue), K03 (green), and K03 (red). These lines divide the diagram in four regions based on the main ionization mechanism: Star Forming, LINER, Seyfert and transition region. The three key regions of the galaxy (A, B and N, defined in Section 3) are colored and distinguished from the other regions. We also collapsed the datacube and plotted the average ratios in red. In all diagnostic diagrams, the emission-line ratios from all regions of NGC 1052 fall in the region occupied by LINERs.

To further help the characterization of NGC 1052, over the central panel of Fig 9 we superimposed sequences corresponding to Allen et al. (2008) shock models with solar metallicity and preshock density of 1 cm $^{-3}$. We created our grid with models of velocities between 200 and 500 km s^{-1}, and magnetic fields between 2.0 and 10.0 μG.

Lastly, we over plotted in the right panel of Fig 9, photoionization models generated with version 17.01 of CLOUDY, last described by Ferland et al. (2017). In order to generate these models, we followed Ricci et al. (2015) and assumed a plane-parallel geometry, a power law continuum with $f_\nu \propto \nu^{-1.5}$, which is typical for LINER-like AGNs according to Ho (2008) and a filing factor of 10^{-3}. We constructed two model grids, one for the nucleus and one for the extended regions. For the nucleus, we constructed our model grid with density values of 200 and 1500 cm^{-3} and a lower cut in the energy of the ionizing photons of 0.124 eV (the default value). For the extended region, the model grid was constructed with density values of 50 and 200 cm^{-3} and a lower cut in the energy of the ionizing photons of 27 eV (photons with less energy than 27 eV have already been absorbed by the most internal regions of the nucleus). Each grid was constructed with ionization parameter (U) of 3.4 and 3.6 (in agreement with the values derived previously for LINER-like AGNs Ferland & Netzer 1983; Halpern & Steiner 1983; Ho 2008) and metalicites of 0.8 Z$_\odot$, 1.0 Z$_\odot$, 1.5 Z$_\odot$ and 2.0 Z$_\odot$. For the other parameters, we used CLOUDY's default values.

In order to show how other line ratios vary over our FoV, we have also obtained emission line ratio maps of [NI]λ5200/Hβ, ([OI]λ6300+λ6360)/Hα, ([SII]λ6716+λ6731)/Hα and ([OI]λ6300+λ6360)/([OIII]λ4959+λ5007), which are presented in Fig 10.

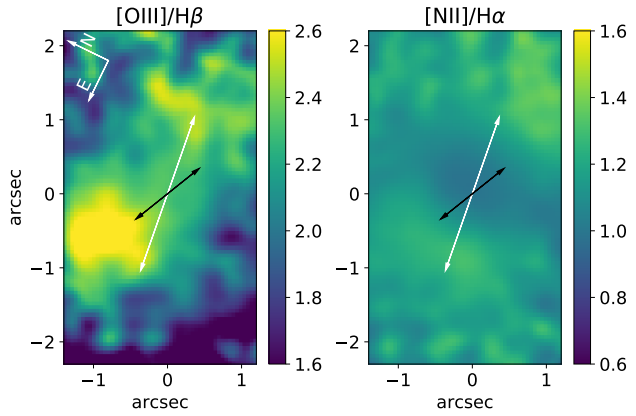

Figure 8. [OIII]λ5007Å/Hβ and [NII]λ6587Å/Hα maps for NGC 1052. In the left panel, the white arrow indicates the orientation of the kiloparsec scale radio jet and the black arrow indicates the orientation of the parsec scale jet.

4.5 Principal Component Analysis

One way to analyze data cubes is by means of the PCA Tomography technique (Steiner et al. 2009). In short, this procedure uses Principal Component Analysis to search for correlations between m spectral pixels across the n spatial pixels of data cubes. Meaningful information are stored in a few number of eigenvectors (or eigenspectra) whose associated variances are greater than the average noise of the data cube. Tomograms are related to the projection of the eigenvectors onto the data cube, i.e. it shows where the correlations between the wavelengths occur in the spatial dimension. This technique has shown useful in extracting information from data cubes (Ricci et al. 2014a; Menezes et al. 2013b).

We applied PCA Tomography to the GMOS data cube of NGC 1052. Eigenvectors 2, 3 and 6 and their associated tomograms are presented in Fig 11. They contain 2.4, 0.59 and 0.023 % of the total variance of the data cube respectively. Only these eigenvectors are shown as they are relevant to the discussion of this paper. The directions of kiloparsec and parsec scale radio jets are shown in tomograms 3 and 6, respectively.

On the other hand, we did not include the results from the PCA Tomography applied to the NIFS datacube, since all useful information is contained in the first eigenspectrum, which represents the bulge of the galaxy.

4.6 Near infrared emission lines

Five emission lines were detected in the NIR datacubes: [FeII]λ12570Å, Paβ, [FeII]λ13210Å, H_2 λ21218Å and H_2 λ22230Å. We present in Fig. 15, the J and K band spectra of the central spaxel of region N. Since the [FeII]λ13210Å and H_2 λ22230Å lines are weaker than the λ12570Å and λ21218Å lines, and both probe the same gas portion, we only show the maps of the later ones. Given the compactness of NIR emission lines, we decided to analyze this data through channel maps. This alternative method was required, since direct emission line fitting did not reveal any structure in either centroid velocity or FWHM maps. The emission line fluxes and channel maps of [FeII]λ12570Å, Paβ and H_2 λ21218Å are presented in Figs 12 to 14. We chose a constant bin size for the channels of 5Å, because it is a multiple of the binning after the synthesis, also providing a good S/N.

The NIR emission-line ratios can also be used as diagnostic diagrams to discriminate the dominant ionization mechanism of emission line galaxies (see for example Larkin et al. 1998; Rodríguez-Ardila et al. 2005; Riffel et al. 2013; Colina et al. 2015). In order to improve the determination of the dominant ionization mechanism behind NGC 1052, we present in Fig 16 two emission-line ratio diagrams from Maiolino et al. (2017). The purple square shows NGC 1052 position in these diagrams. Since a few of these lines are not in the wavelength range of our datacube, we measured the line fluxes from the NIR integrated spectrum of NGC 1052 presented by Mason et al. (2015). We performed these measurements after subtracting the stellar content of the spectrum, which was done by applying the same method described in Section 3 (i.e. E-MILES models and STARLIGHT code).

5 DISCUSSION

5.1 Fluxes and Kinematics

From Fig 2, it is possible to see that narrow components have a flux distribution which is oriented in the northeast/southwest direction. The kinematics of these emission lines are also aligned in the same direction, dividing the galaxy into northeast (blueshifted) and southwest (redshifted). A similar result was already reported by D15. Since this component extends beyond the edges of our FoV, with the same orientation, our narrow components are probably the same components observed by D15. According to their analysis, the best explanation for this data is the presence of two gas bubbles.

The [OIII] fluxes are also oriented in the northeast/southwest direction. However, the flux peak of [OIII] is off-centered ~0.″35 to the west of the continuum peak, in the direction of the parsec scale jet. Also, the kinematics of the [OIII] emissions are compatible with the other ones, with the exception of one region. To the west of our FoV, following the direction of the kiloparsec scale radio jet, the [OIII] narrow kinematics grows to higher values if compared to the other narrow emissions. These results seem to indicate that to the west of our FoV, narrow [OIII] is probably tracing the interaction of the kiloparsec radio jet with the environment.

The fluxes of IW components, in contrast, present approximately elliptical isocontours with a major axis oriented between kiloparsec and parsec scale radio jet directions. In addition, the kinematics of all IW components are similar to each other, with compatible FWHM and centroid velocity distributions. From Fig 2, it is possible to see that the blueshift velocities of this component reach their maximum in region A, beginning to fall afterwards. The redshifted portion, on the other hand, reaches its maximum in the borders of our FoV, suggesting that it might keep increasing. However, since it was not detected by the large (40.″0×25.″0) FoV of D15, it suggests that this component does not extend much further away from our FoV.

Also, in the [OIII] FWHM map, close to (0.″, -1.″), a drop in the FWHM is found, co-spatial with a rise in the velocity field of the [OIII] IW component. This happens because the fitting in this region is highly degenerate, as can be seen in Fig 3. However, there is no clear sign of a difference in the emission line behaviour in this same region.

One possible explanation for the kinematics of the IW is that it is caused by a bipolar outflow. In this scenario, the narrow components would trace the gas bubble identified by D15, whereas the IW component would trace an on-going outflow related to the radio jets. Supporting this hypothesis is the fact that this component is oriented

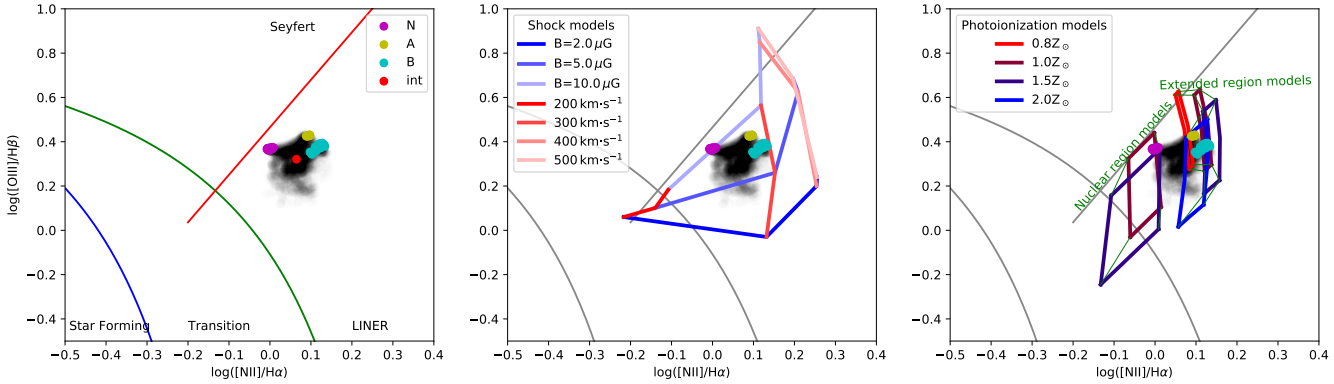

Figure 9. BPT diagram of NGC 1052. The three main regions from Fig. 2 are highlighted (magenta, yellow and cyan), as well as the integrated average of the galaxy (red). The other regions are plotted in black. In the first panel we plotted the lines of K01 (blue), K03 (green), and K03 (red). In the middle panel, we present shock models from Allen et al. (2008). In the right panel, we plot photoionization models generated with CLOUDY. Each metallicity was plotted with the same color, and green lines connect regions with the same density and ionization parameter.

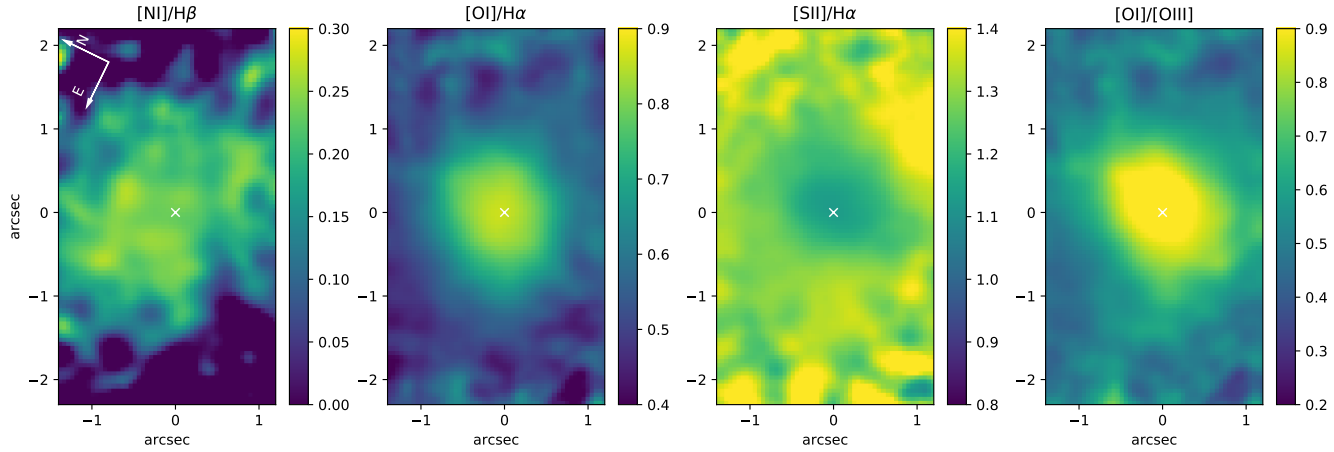

Figure 10. [NI]/Hβ, [OI]/Hα, [SII]/Hα and [OI]/[OIII] maps corrected by dust reddening.

along a direction between those of the parsec and kiloparsec radio jets.

In the above scenario, no component is tracing the gravitational potential of the galaxy. Thus, in order to test if this component can also be explained by a disk in circular motion, we followed Bertola et al. (1991) and assumed that the gas follows circular orbits in a plane with a rotation curve given by :

$$v_c = \frac{Ar}{(r^2 + c_0^2)^{p/2}}, \quad (1)$$

where r is the radius and A, c_0 and p are parameters to be determined. The observed radial velocity at a position (R,Ψ) on the plane of the sky is then given by:

$$v(R,\Psi) = v_{sys} + \frac{ARcos(\Psi - \Psi_0)sin\theta cos^p\theta}{\{R^2[sin^2(\Psi - \Psi_0) + cos^2\Theta cos^2(\Psi - \Psi_0)] + c_0^2 cos^2\Theta\}^{p/2}}, \quad (2)$$

where Θ is the disk inclination (Θ=0 being is a face-on disk), Ψ_0 is the position angle of the line of nodes and v_{sys} is the systemic velocity of the galaxy. We have fitted the above expression to the Hβ IW velocity field using our own script, which automatically searches for the center, inclination and velocity amplitude and has already been used in Paper I. The resulting model and the respective residuals are presented in the first two panels of Fig 17.

The fact that the model fits properly the entire FoV of the IW component, with all residuals smaller than 50 km s^{-1}, indicates that the kinematics of the IW component is well explained by a disk following circular motion. However, the value of two parameters indicate that, if this is indeed the case, the disk is not circular around the SMBH. First, as can be seen in Fig 17, the center of the rotation (magenta x) is located 0.″7 west of the continuum luminosity peak (black x), adopted as the location of the galaxy nucleus. Second, the systemic speed of this galaxy, as derived from the fitting of the IW kinematics, is 68 km s^{-1} higher than the systemic speed derived from the stellar model. Such eccentric disks have already been reported in the literature for other galaxies (e.g. M31 Menezes et al. 2013a). If that is the case, it is probably a consequence of the merger event experienced ∼1 Gyr ago with a gas-rich dwarf or spiral van Gorkom et al. (1986).

A third option to explain the IW gas kinematics is the combination of a rotation and an outflow component. In order to test this possibility we performed the fit of the data again, but setting the

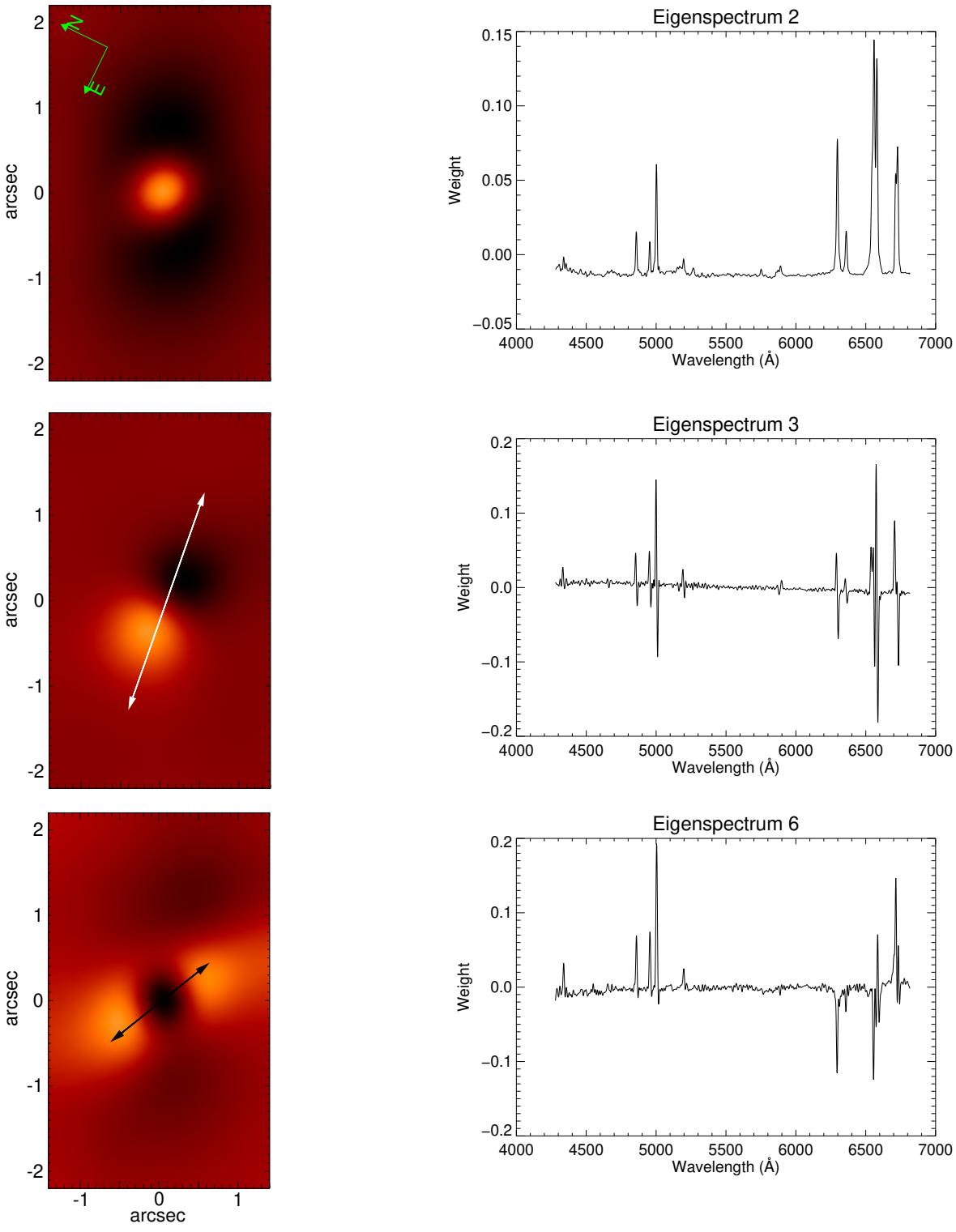

Figure 11. Eigenvectors 2, 3 and 6 for the PCA of NGC 1052. Over Eigenvector 3 map we plotted in white the orientation of the kiloparsec scale radio jet and over Eigenvector 6 map we plotted in black the orientation of the parsec scale jet.

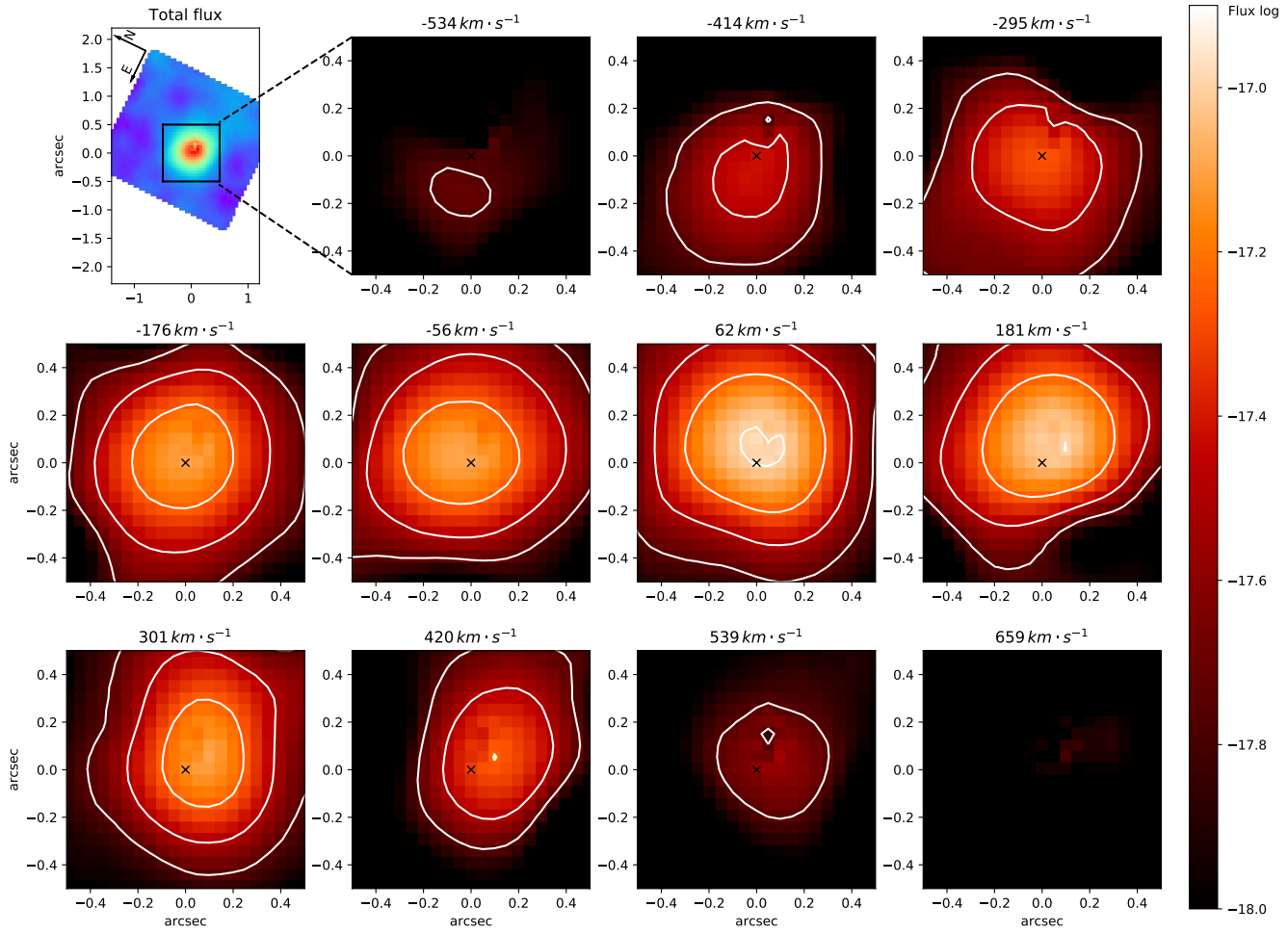

Figure 12. [Fe II]λ12570Å emission line flux and channel maps.

orientation of the line of nodes, the disk inclination and the kinematic center to those obtained from the fit of the stellar velocity field (Paper I). The resulting model and the respective residuals are presented in the last two panels of Fig 17. Looking at the residuals, it is possible to see that they are similar to the kinematics of the narrow components, but with higher values. One possible explanation for these results is that the blue residuals originate in the front part of the blue bubble, whereas the narrow kinematics would originate in the rear part of this bubble. Also, the red residuals would originated in the rear part of the red bubble, whereas the narrow kinematics would originate in the front part of this bubble. In this scenario, the radio jets would pass inside the bubbles with the SMBH and its torus located in between these bubbles.

Combined, these results allow us to conclude that NGC 1052 has at least five different kinematic components: i) the unresolved broad component visible in Hα, limited to the nucleus, originating in the BLR; ii) the unresolved intermediate-broad [O III], also limited to the nuclear region; iii) the IW component, detected in all emission lines and which is tracing either an outflow, an eccentric disk or a combination of a disk with large scale shocks; iv) the narrow components of the H I, [O I], [N I], [N II] and [S II], tracing the gas bubbles first detected by D15; v) the [O III] narrow component, which follows the fluxes and kinematics of the other narrow emission lines everywhere but to the west, where it is probably tracing the interaction of the kiloparsec radio jet with the environment

The presence of three distinct kinematic components in the emission line profiles of the nuclear spectrum of NGC 1052 has already been reported by S05, who analyzed the inner 3.″0x3.″0 region of the galaxy. Our results not only confirm their hypothesis, but also show that the kinematics are even more complex, with an unresolved [O III] component in the nucleus and a narrow [O III] component detached from the other narrow components to the west.

FWHM maps, on the other hand, do not highlight any major differences, mainly due to the narrow range we allowed them to vary. This narrow range was needed, since allowing higher FWHM variations caused IFSCUBE to not fit properly the noisy regions of the datacube.

5.2 Dust Reddening

The E(B-V) map peaks at ~0.25 mag inside the nuclear region N (see Fig 5). This value is lower than the values derived by both Gabel et al. (2000, E(B-V)=0.44) and D15 (E(B-V)=0.33). However, this difference is not significant, since the uncertainties in E(B-V) are high due to the difficulty in separating Hα from the adjacent [N II] lines.

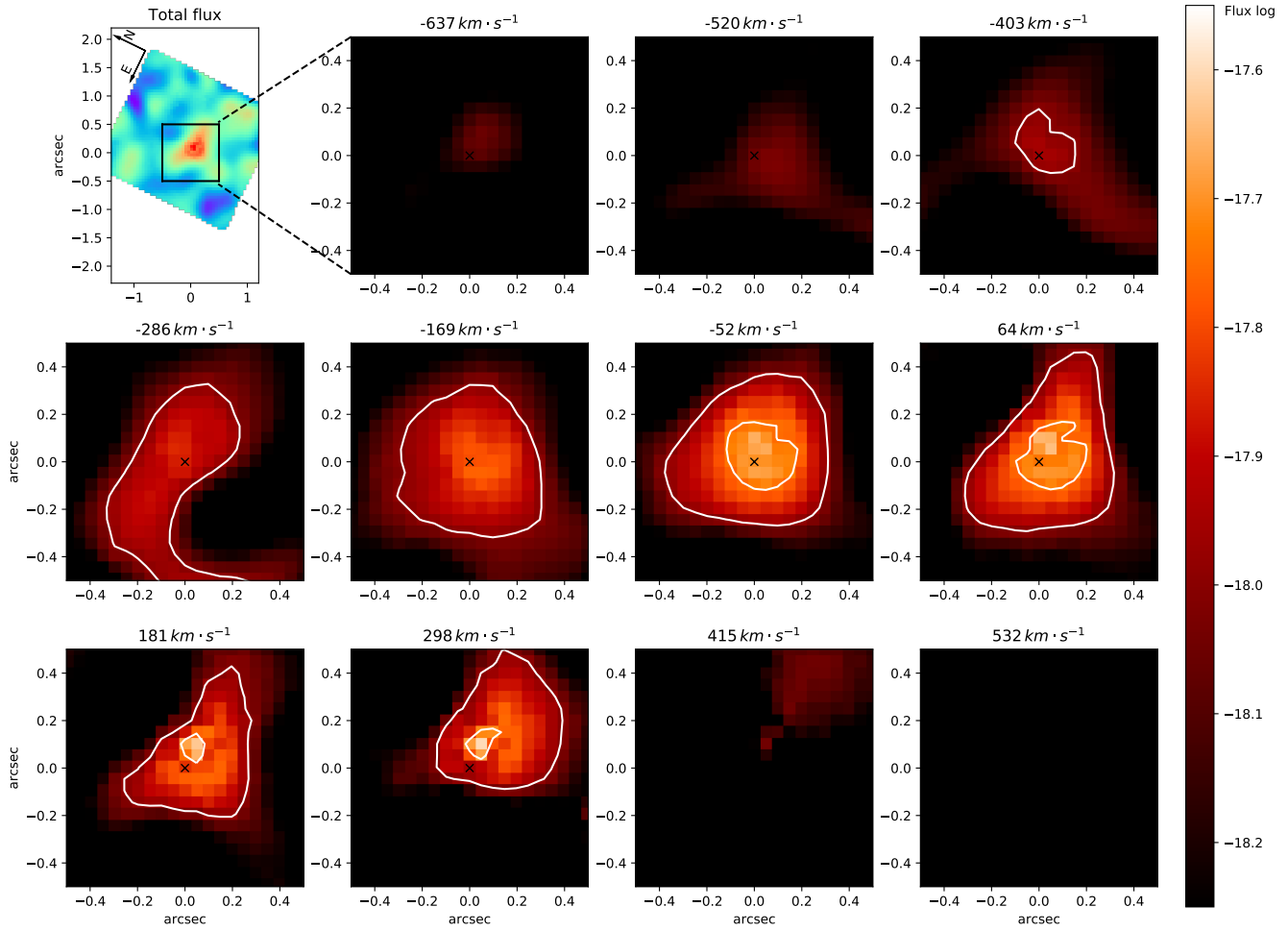

Figure 13. Paβ emission line flux and channel maps.

In the jets direction, the reddening is lower than in the vicinity of the nucleus, with an average value of 0.1 mag, but higher than the rest of the FoV, where the E(B-V) is negligible. These results show that this galaxy is not very affected by dust reddening, which is consistent with past results showing that this is the case for most elliptical galaxies (Padilla & Strauss 2008; Zhu et al. 2010).

5.3 Electron Temperature and Density

The density values derived by us (Fig 6) reveal that the highest values are seen inside the nuclear region N. While we found a density of $\sim$1200 cm^{-3} in the region N, the surrounding regions have densities close to or below the [SII]/[SII] sensitivity limit ($\lesssim$100 cm^{-3}).

The temperatures detected by us (Table 1), on the other hand, do not highlight a major difference between the nuclear region N and the surrounding regions. Temperature values measured from [NII] emission lines are between 10,000 and 13,000 K, with no significant difference in region N. Temperature measured from [OIII] have values closer to 25,000 K in regions A and C, and could not be measured in regions N and B.

The high temperatures measured from [OIII] are too high to be compatible with photoionization (Osterbrock & Ferland 2006). However, as indicated in Section 4.3, this value could not be measured in the nuclear region N. Temperatures measured from [NII], on the other hand, are compatible with photoionization in the three regions that we have been able to measure them.

The simple presence of a broad line profile in the HI lines indicates that direct photoionization by the AGN must be present in the nuclear region. This is compatible with the low temperatures measured from [NII]. However, a contribution coming from shocks cannot be fully discarded in this region, since the fitting of the profile of the [OIII]λ4363 emission line allows us to calculate values which are not compatible with photoionization.

Outside of region N, the high [OIII] temperatures and the low [NII] temperatures suggest that a single mechanism is not capable to fully explain the extended ionization observed. It is likely that both shocks and photoionization play a role in ionizing the gas in these extended regions.

5.4 Diagnostic Diagrams

The WHAN diagram of Fig 7 shows that the emission lines of NGC 1052 are typical of AGNs. This is important because it rules out ionization by hot low-mass evolved stars and also young stars, thus restraining the ionization mechanism of the galaxy to be either shocks or photoionization by the AGN.

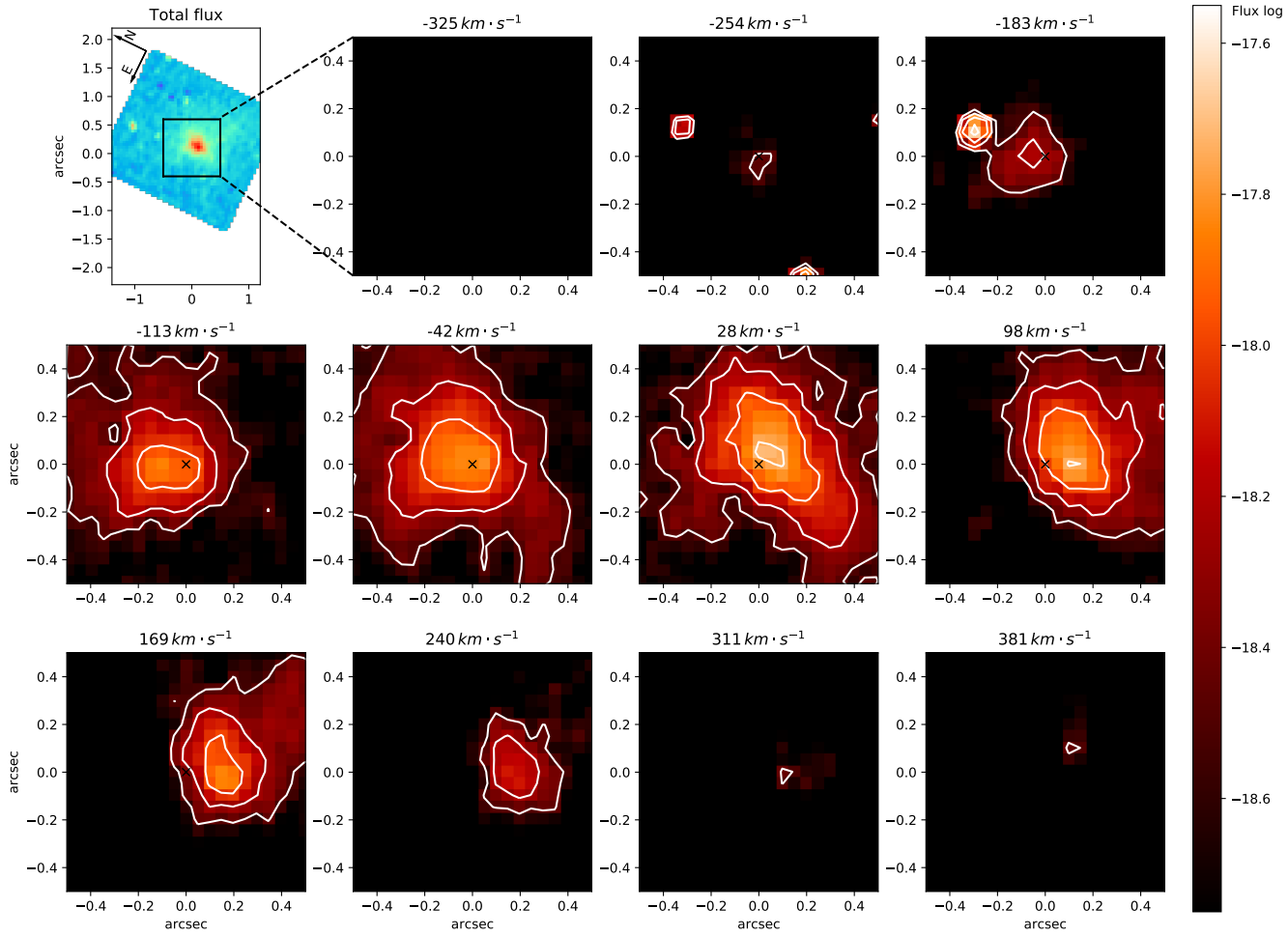

Figure 14. H_2 λ2121Å emission line flux and channel maps.

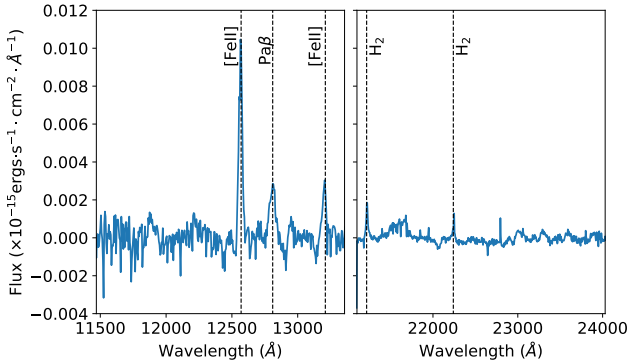

Figure 15. J and K band NIR spectra of the central spaxel of region N. The main emission lines are indicated.

Also, the [OIII]/Hβ and [NII]/Hα ratios (Fig 9) confirm that the LINER-like emission extends throughout the whole FoV, not being restricted to the nucleus of the galaxy. The regions A, B and N are compatible with ionization by shocks with velocities between 200 and 300 km s^{-1}, and a magnetic field between 5.0 and 10.0 μG (panel b of Fig 9). Besides that, region N is compatible with our photoionization models for the nucleus, whereas regions A and B are also compatible with our photoionization models for the extended region (panel c of Fig 9).

From Figs 8 and 10, it is possible to see that region N behaves differently when compared to the rest of the galaxy. Also from these figures, it is possible to see that all ratios are constant outside the nuclear region, with the exception of [OIII]/Hβ, which is slightly higher at regions A and B, if compared to the rest of our FoV. These results are compatible with our hypothesis of photoionization as the main ionizer inside region N, with the extended region of this galaxy being ionized by a combination of shocks and photoionization.

5.5 Principal Component Analysis

Eigenvectors that results from the PCA Tomography technique reveal the correlations between the wavelengths of the spectral dimension of a data cube. In the case of the optical data cube of NGC 1052, the second eigenvector shows strongly the characteristics of the AGN; but also that the emission lines are correlated with the Fe Iλ5270 and Na Dλ5893 stellar absorption features. This correlation is located in the nucleus of the galaxy. An interpretation for this result is that the featureless continuum from the AGN is decreasing the equivalent widths of the stellar absorption lines, which

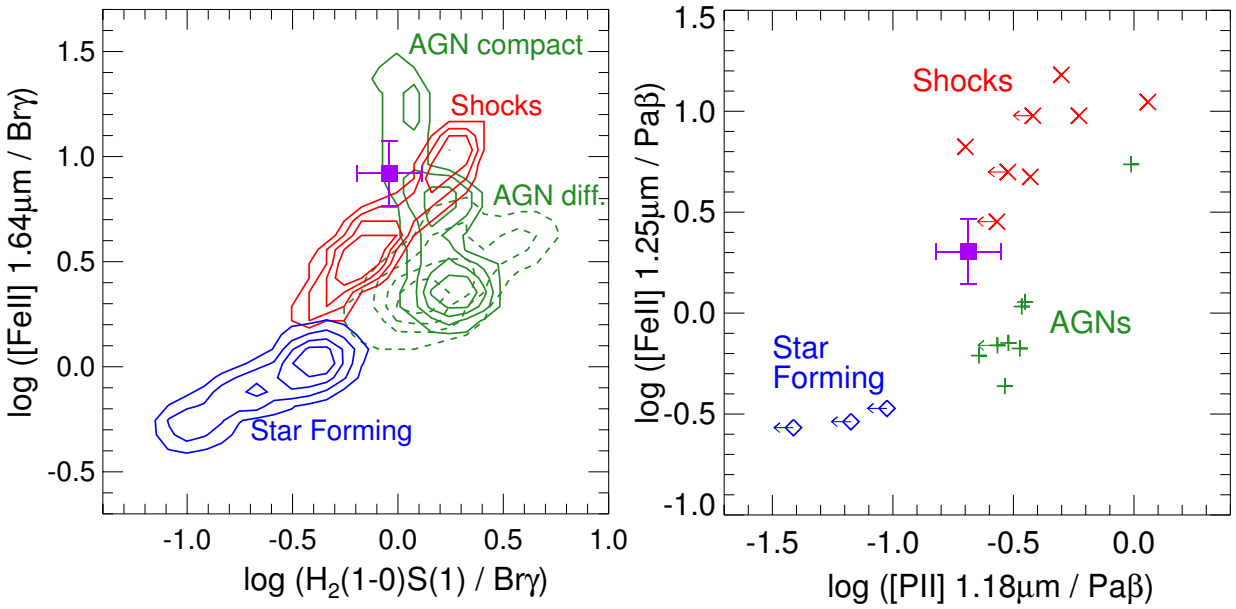

Figure 16. NIR emission line ratio diagrams from Maiolino et al. (2017). In both diagrams, the position of NGC 1052 is plotted in purple with error bars.

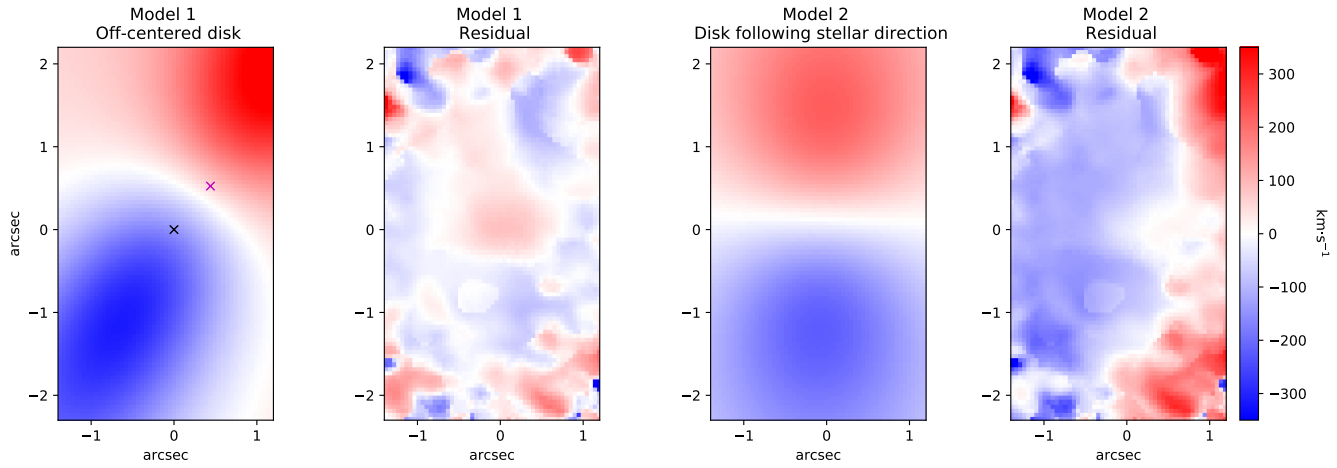

Figure 17. Two disk models of the Hβ IW kinematics with their respective residuals. The first model was obtained with all parameters free to vary, whereas the second model was obtained by setting the orientation of the nodes line, disk inclination and conematic center to the ones modeled for the stars. The black x in the second panel indicates the luminosity peak, whereas the magenta x indicates the center of the rotation.

was already discussed in Paper I. Similar cases were observed in the nuclei of the galaxies IC 1459 (Ricci et al. 2014a, 2015) and NGC 1566 (da Silva et al. 2017). In Eigenvector 3, one may see an anti-correlation between the red and the blue wings of the emission lines. This is associated with a bipolar structure seen in the spatial dimension with a position angle PA=81±1 degrees. This is usually a signature of a gas disc (Ricci et al. 2014a; da Silva et al. 2017). In Eigenvector 6, emission lines from elements with a low ionization potential ([OI] and [NII]) are anti-correlated with the emission lines from elements with higher ionization potential and with the HI lines. The tomogram shows that the nucleus is dominated by the low ionization emission while a bipolar structure, associated with the [OI] and the H I lines, is seen with a P.A. of 53±1 degree. This P.A. is similar to the direction of the parsec scale jet of NGC 1052. Given that Sawada-Satoh et al. (2016) detected a molecular torus perpendicular to this jet, we propose that Tomogram 6 is related to an ionization cone, i.e. ionizing photons are collimated by the torus in the direction of the bipolar structure that is seen in this image. Another result that supports this interpretation is the fact that the [OIII]/Hβ ratio is higher in the position of the structure that is located northeast from the nucleus (Fig 8).

It is clear that the position angle of the bipolar structure we associate with the ionization cone (PA=53±1) is different from that of the parsec scale radio jet (PA~66, as estimated by us based on

the mean PA of the jet components identified by Lister et al. 2019). Since the radio jet presumably originates in the inner accretion disc and the ionization cone is collimated by the molecular/dusty torus, we conclude that their projection on the sky is misaligned by ∼13 deg.

5.6 NIR emission lines

From Fig 12, it is possible to see that [FeII] channel maps are redshifted to the east and blueshifted to the west of the nucleus. Similar to the intermediate components of the optical emission lines, it shows that the orientation of [FeII] kinematics also lies between the orientation of kiloparsec and parsec scale radio jets. However, [FeII] emission is much more limited to the central region, undetected beyond 0.″5.

Paβ emission (Fig 13), on the other hand, does not show any kinematic features in the channel maps, with all velocity channels showing similar flux distributions, concentrated in the central regions. Lastly, H_2 channel maps (Fig 14) show that this emission line shows mostly blueshifts to the north of the nucleus and redshifts to the south, with an apparent line of nodes similar to that implied by the narrow-line kinematics. This orientation is also similar to that of the D15 gas bubbles.

Fig 16 reveals that the NIR emission lines of NGC 1052 are compatible with both photoionization by and AGN as well as shocks (produced by the radio jets), as seen in the two diagnostic diagrams. These results also help confirming that only one ionization mechanism is not capable of fully explaining the emission lines of NGC 1052.

6 CONCLUSIONS

In this work, we studied the gas excitation and kinematics of the inner 320×535 pc^2 of NGC 1052, both in the optical and in the NIR. Our results can be summarized as follows:

- At least five kinematic components are present in this galaxy:

(i) In the nucleus, an unresolved broad (FWHM∼3200 km s^{-1}) line is visible in Hα.
(ii) Also in the nucleus, an unresolved intermediate-broad component (FWHM∼1380 km s^{-1}) is seen in the [OIII]$\lambda\lambda$4959,5007 doublet.
(iii) An IW component (280<FWHM<450 km s^{-1}) with central peak velocities up to 400 km s^{-1}. Possible explanations for this feature are: an outflow, an eccentric disk or a combination of a disk with large scale shocks.
(iv) A narrow (FWHM<150 km s^{-1}) component, visible in the HI, [OI], [NI], [NII] and [SII] emission lines, which extends beyond the FoV of our data. This component is compatible with two previously detected gas bubbles, which were attributed to large-scale shocks.
(v) Another narrow (FWHM<150 km s^{-1}) emission, visible only in [OIII], which differs from the other narrow emission lines along the kiloparsec radio jet, probably tracing the interaction of the kiloparsec radio jet with the environment.

- When analyzing density, temperature and diagnostic diagrams, our results suggest that the ionization of the FoV of our data cannot be explained by one mechanism alone. Rather, our results suggest that photoionization is the dominant mechanism in the nucleus, with the extended regions being ionized by a combination of shocks and photoionization.
- We found that the dusty molecular torus is misaligned with the inner accretion disk by ∼13 deg in the plane of the sky.
- We confirmed the presence of an unresolved featureless continuum associated with the LLAGN
- From NIR data, we found that [FeII] is also oriented in a direction compatible with the radio jets, whereas H_2 is oriented in the direction of the narrow components.

ACKNOWLEDGEMENTS

We thank the anonymous referee for reading the paper carefully and providing thoughtful comments that helped improving the quality of the paper. LGDH, TVR and NZD thank CNPq. RR thanks CNPq, FAPERGS and CAPES for partial financial support to this project. This research has made use of data from the MOJAVE database that is maintained by the MOJAVE team (Lister et al. 2018). This study was financed in part by the Coordenação de Aperfeiçoamento de Pessoal de Nível Superior - Brasil (CAPES) - Finance Code 001.

REFERENCES

Allen M. G., Groves B. A., Dopita M. A., Sutherland R. S., Kewley L. J., 2008, ApJS, 178, 20
Baczko A.-K., Schulz R., Ros E., Kadler M., Perucho M., Wilms J., 2016, Galaxies, 4, 48
Baldwin J. A., Phillips M. M., Terlevich R., 1981, PASP, 93, 5
Barth A. J., Shields J. C., 2000, PASP, 112, 753
Barth A. J., Filippenko A. V., Moran E. C., 1999, ApJ, 515, L61
Belfiore F., et al., 2015, MNRAS, 449, 867
Belfiore F., et al., 2016, MNRAS, 461, 3111
Bertola F., Bettoni D., Danziger J., Sadler E., Sparke L., de Zeeuw T., 1991, ApJ, 373, 369
Binette L., Magris C. G., Stasińska G., Bruzual A. G., 1994, A&A, 292, 13
Brum C., et al., 2019, MNRAS, 486, 691
Cardelli J. A., Clayton G. C., Mathis J. S., 1989, ApJ, 345, 245
Cid Fernandes R., Gu Q., Melnick J., Terlevich E., Terlevich R., Kunth D., Rodrigues Lacerda R., Joguet B., 2004, MNRAS, 355, 273
Cid Fernandes R., Mateus A., Sodré L., Stasińska G., Gomes J. M., 2005, MNRAS, 358, 363
Cid Fernandes R., Stasińska G., Mateus A., Vale Asari N., 2011, MNRAS, 413, 1687
Colina L., et al., 2015, A&A, 578, A48
Dahmer-Hahn L. G., et al., 2019, MNRAS, 482, 5211
Diaz A. I., Terlevich E., Pagel B. E. J., 1985, MNRAS, 214, 41P
Dopita M. A., et al., 2015, ApJ, 801, 42
Ferland G. J., Netzer H., 1983, ApJ, 264, 105
Ferland G. J., et al., 2017, Rev. Mex. Astron. Astrofis., 53, 385
Fey A. L., Charlot P., 1997, ApJS, 111, 95
Fosbury R. A. E., Mebold U., Goss W. M., Dopita M. A., 1978, MNRAS, 183, 549
Fosbury R. A. E., Snijders M. A. J., Boksenberg A., Penston M. V., 1981, MNRAS, 197, 235
Gabel J. R., Bruhweiler F. C., Crenshaw D. M., Kraemer S. B., Miskey C. L., 2000, ApJ, 532, 883
Gomes J. M., et al., 2016, A&A, 588, A68
Halpern J. P., Steiner J. E., 1983, ApJ, 269, L37
Heckman T. M., 1980, A&A, 87, 152
Ho L. C., 2008, ARA&A, 46, 475
Ho L. C., Filippenko A. V., Sargent W. L. W., Peng C. Y., 1997, ApJS, 112, 391
Kadler M., Kerp J., Ros E., Falcke H., Pogge R. W., Zensus J. A., 2004, A&A, 420, 467
Kauffmann G., et al., 2003, MNRAS, 346, 1055
Kehrig C., et al., 2012, A&A, 540, A11

Kewley L. J., Dopita M. A., Sutherland R. S., Heisler C. A., Trevena J., 2001, ApJ, 556, 121
Koski A. T., Osterbrock D. E., 1976, ApJ, 203, L49
Larkin J. E., Armus L., Knop R. A., Soifer B. T., Matthews K., 1998, ApJS, 114, 59
Lister M. L., Aller M. F., Aller H. D., Hodge M. A., Homan D. C., Kovalev Y. Y., Pushkarev A. B., Savolainen T., 2018, ApJS, 234, 12
Lister M. L., et al., 2019, ApJ, 874, 43
Loubser S. I., Soechting I. K., 2013, MNRAS, 431, 2933
Maiolino R., et al., 2017, Nature, 544, 202
Mason R. E., et al., 2015, ApJS, 217, 13
Menezes R. B., Steiner J. E., Ricci T. V., 2013a, ApJ, 762, L29
Menezes R. B., Steiner J. E., Ricci T. V., 2013b, ApJ, 765, L40
Menezes R. B., Ricci T. V., Steiner J. E., da Silva P., Ferrari F., Borges B. W., 2019, MNRAS, 483, 3700
Osterbrock D. E., Ferland G. J., 2006, Astrophysics of gaseous nebulae and active galactic nuclei
Padilla N. D., Strauss M. A., 2008, MNRAS, 388, 1321
Papaderos P., et al., 2013, A&A, 555, L1
Ricci T. V., Steiner J. E., Menezes R. B., 2014a, MNRAS, 440, 2419
Ricci T. V., Steiner J. E., Menezes R. B., 2014b, MNRAS, 440, 2442
Ricci T. V., Steiner J. E., Menezes R. B., 2015, MNRAS, 451, 3728
Riffel R., Rodríguez-Ardila A., Aleman I., Brotherton M. S., Pastoriza M. G., Bonatto C., Dors O. L., 2013, MNRAS, 430, 2002
Rodríguez-Ardila A., Riffel R., Pastoriza M. G., 2005, MNRAS, 364, 1041
Sarzi M., et al., 2010, MNRAS, 402, 2187
Sawada-Satoh S., et al., 2016, ApJ, 830, L3
Shaw R. A., Dufour R. J., 1995, Publications of the Astronomical Society of the Pacific, 107, 896
Stasińska G., et al., 2008, MNRAS, 391, L29
Steiner J. E., Menezes R. B., Ricci T. V., Oliveira A. S., 2009, MNRAS, 395, 64
Sugai H., Malkan M. A., 2000, ApJ, 529, 219
Sugai H., et al., 2005, ApJ, 629, 131
Vazdekis A., Koleva M., Ricciardelli E., Röck B., Falcón-Barroso J., 2016, MNRAS, 463, 3409
Wrobel J. M., 1984, ApJ, 284, 531
Yan R., Blanton M. R., 2012, ApJ, 747, 61
Zhu G., Blanton M. R., Moustakas J., 2010, ApJ, 722, 491
da Silva P., Steiner J. E., Menezes R. B., 2017, MNRAS, 470, 3850
van Gorkom J. H., Knapp G. R., Raimond E., Faber S. M., Gallagher J. S., 1986, AJ, 91, 791

This paper has been typeset from a TEX/LATEX file prepared by the author.

Capítulo 6

Sumário e perspectivas

Neste trabalho, apresentamos os resultados obtidos na comparação entre diferentes bibliotecas de modelos no NIR, através de espectros longslit obtidos com o *Astrophysical Research Consortium Telescope*. Conhecendo as limitações do método, aplicamos a síntese combinando dados ópticos e NIR na galáxia NGC 1052, de modo a identificar tanto populações sensíveis ao óptico quanto populações sensíveis ao NIR. Por último, mapeamos a excitação e cinemática do gás desta galáxia afim de traçar a influência do SMBH nas propriedades em maior escala. Nossos principais resultados foram:

• Bibliotecas de modelos NIR com baixa resolução espectral produzem resultados que dependem mais na escolha da biblioteca do que na população estelar da galáxia estudada.

• De maneira geral, bibliotecas NIR com baixa resolução espectral tendem a superestimar a extinção por poeira e a quantidade de população estelar jovem.

• Para bibliotecas com alta resolução espectral, este cenário é consideravelmente melhor, com as duas bibliotecas testadas produzindo resultados compatíveis com os resultados encontrados no óptico.

• A partir de dados ópticos, a galáxia NGC 1052 apresenta população estelar velha em todos os pontos do cubo de dados GNIRS. No entanto, a partir de dados NIR, detectamos um anel de populações de idade intermediária, enquanto o núcleo mantém-se dominado por população velha.

• Ao combinar os dados ópticos com os dados NIR, a população estelar encontrada é novamente velha. A divergência entre os resultados ópticos e NIR pode ser explicada pela baixa razão sinal-ruído da banda J e a ausência de dados na banda H, a qual contém grande parte das absorções estelares no NIR.

• Pelo menos cinco componentes cinemáticas podem ser observadas no gás desta

galáxia:

1. No núcleo, uma componente larga ($\sim$3200km s^{-1}) pode ser observada em Hα
2. Também no núcleo, uma emissão não resolvida com $\sim$1380km s^{-1} aparece no dubleto [OIII]$\lambda\lambda$4959,5007
3. Uma componente de largura intermediária (280<FWHM<450km s^{-1}) com pico de velocidades atingindo 400km s^{-1}. Esta componente pode ser explicada por um outflow, um disco excêntrico ou uma combinação de um disco com choques
4. Uma componente estreita (FWHM<150km s^{-1}), visível nas emissões de HI, [OI], [NI], [NII] and [SII] e que se estende além de nosso campo de visão, compatível com choques em larga escala reportados na literatura
5. Outra componente estreita (FWHM<150km s^{-1}), visível apenas no [OIII] e que se comporta diferente das demais componentes estreitas na direção do jato em rádio

• A análise de densidade, temperatura e diagramas diagnóstico sugerem que a ionização em nosso campo de visão não pode ser explicada por apenas um mecanismo, de modo que choques e fotoionização são os melhores candidatos para se explicar o comportamento desta galáxia

• O toro de gás e poeira está desalinhado com o disco de acreção em 13 graus no plano do céu

• A partir de duas análises distintas, nós confirmamos uma queda nas larguras equivalentes na região nuclear. O cenário mais consistente para explicar esta queda é a presença de uma emissão sem traços causada pelo LLAGN.

• Utilizando dados NIR, nós encontramos que o [FeII] se orienta na mesma direção dos jatos em rádio, enquanto o H_2 é orientado na direção das componentes intermediárias

De maneira geral, é possível concluir que os modelos disponíveis na literatura são adequados para a realização de síntese de população estelar em galáxias dominadas por população estelar mais velha que 1 Gyr. No entanto, para estudos futuros, que serão aplicados à galáxias com formação estelar recente, são necessários novos modelos, os quais devem ser capazes de reproduzir adequadamente as absorções estelares em galáxias, além de possuírem uma resolução espectral adequada ($\sim$2000).

6.1 Perspectivas

.

Agora com a metodologia consolidada para galáxias com população estelar predominantemente velha, pretendemos dar prosseguimento de modo a incluir galáxias *late-type* em nossa análise. Desta maneira, propomos como próximos passos para o trabalho:

- O desenvolvimento de uma biblioteca de modelos a partir da biblioteca de estrelas do X-Shooter (Chen et al., 2014), que possui alta resolução espectral (R$\geqslant$60000), a qual incluirá estrelas quentes. Desta maneira, ela possibilitará a criação de modelos com idade t<1 Gyr. Estes modelos serão comparados com com os resultados obtidos no ítem anterior.

- Realizar a síntese utilizando a nova biblioteca em galáxias espirais e que hospedem um AGN. Dados NIR já estão observados para diversas galáxias (projeto *"NIFS survey of feeding and feedback processes in nearby Active Galaxies"* do Gemini Norte) e dados ópticos serão obtidos a partir do arquivo do Gemini e a partir dos projetos GN-2017B-Q-44-32 (1 galáxia observada) e GS-2018A-Q-225 (1 galáxia na fila).

Referências Bibliográficas

[1] ANTONUCCI, R. Unified models for active galactic nuclei and quasars. **Annual Review of Astronomy and Astrophysics**, v. 31, p. 473–521, 1993.

[2] BALDWIN, C., MCDERMID, R. M., KUNTSCHNER, H., MARASTON, C., CONROY, C. Comparison of stellar population model predictions using optical and infrared spectroscopy. **Monthly Notices of the Royal Astronomical Society**, v. 473, p. 4698–4721, February 2018.

[3] BARTH, A. J., FILIPPENKO, A. V., MORAN, E. C. Polarized Broad Hα Emission from the LINER Nucleus of NGC 1052. **Astrophysical Journal Letters**, v. 515, p. L61–L64, April 1999.

[4] BARTH, A. J., SHIELDS, J. C. LINER/HII "Transition" Nuclei and the Nature of NGC 4569. **Publications of the Astronomical Society of the Pacific**, v. 112, p. 753–767, June 2000.

[5] BECKMANN, V., SHRADER, C. R. **Active Galactic Nuclei**: August 2012.

[6] BELFIORE, F., MAIOLINO, R., BUNDY, K., THOMAS, D., MARASTON, C., WILKINSON, D., SÁNCHEZ, S. F., BERSHADY, M., BLANC, G. A., BOTHWELL, M., CALES, S. L., COCCATO, L., DRORY, N., EMSELLEM, E., FU, H., GELFAND, J., LAW, D., MASTERS, K., PAREJKO, J., TREMONTI, C., WAKE, D., WEIJMANS, A., YAN, R., XIAO, T., ZHANG, K., ZHENG, T., BIZYAEV, D., KINEMUCHI, K., ORAVETZ, D., SIMMONS, A. P-MaNGA Galaxies: emission-lines properties - gas ionization and chemical abundances from prototype observations. **Monthly Notices of the Royal Astronomical Society**, v. 449, p. 867–900, May 2015.

[7] BINETTE, L., MAGRIS, C. G., STASIŃSKA, G., BRUZUAL, A. G. Photoionization in elliptical galaxies by old stars. **Astronomy and Astrophysics**, v. 292, p. 13–19, December 1994.

[8] BRUZUAL, G., CHARLOT, S. Stellar population synthesis at the resolution of 2003. **Monthly Notices of the Royal Astronomical Society**, v. 344, p. 1000–1028, October 2003.

[9] CHEN, X. Y., LIANG, Y. C., HAMMER, F., PRUGNIEL, P., ZHONG, G. H., RODRIGUES, M., ZHAO, Y. H., FLORES, H. Comparing six evolutionary population synthesis models by performing spectral synthesis for galaxies. **Astronomy and Astrophysics**, v. 515, p. A101, June 2010.

[10] CHEN, Y.-P., TRAGER, S. C., PELETIER, R. F., LANÇON, A., VAZDEKIS, A., PRUGNIEL, P., SILVA, D. R., GONNEAU, A. The X-shooter Spectral Library (XSL). I. DR1: Near-ultraviolet through optical spectra from the first year of the survey. **Astronomy and Astrophysics**, v. 565, p. A117, May 2014.

[11] CID FERNANDES, R., GU, Q., MELNICK, J., TERLEVICH, E., TERLEVICH, R., KUNTH, D., RODRIGUES LACERDA, R., JOGUET, B. The star formation history of Seyfert 2 nuclei. **Monthly Notices of the Royal Astronomical Society**, v. 355, p. 273–296, November 2004.

[12] CID FERNANDES, R., MATEUS, A., SODRÉ, L., STASIŃSKA, G., GOMES, J. M. Semi-empirical analysis of Sloan Digital Sky Survey galaxies - I. Spectral synthesis method. **Monthly Notices of the Royal Astronomical Society**, v. 358, p. 363–378, April 2005.

[13] CID FERNANDES, R., STASIŃSKA, G., MATEUS, A., VALE ASARI, N. A comprehensive classification of galaxies in the Sloan Digital Sky Survey: how to tell true from fake AGN? **Monthly Notices of the Royal Astronomical Society**, v. 413, p. 1687–1699, May 2011.

[14] CID FERNANDES, ROBERTO. On tests of full spectral fitting algorithms. **Monthly Notices of the Royal Astronomical Society**, v. 480, n. 4, p. 4480–4488, Nov 2018.

[15] CONROY, C., GUNN, J. E., WHITE, M. The Propagation of Uncertainties in Stellar Population Synthesis Modeling. I. The Relevance of Uncertain Aspects of Stellar Evolution and the Initial Mass Function to the Derived Physical Properties of Galaxies. **Astrophysical Journal**, v. 699, p. 486–506, July 2009.

[16] CUSHING, M. C., RAYNER, J. T., VACCA, W. D. An Infrared Spectroscopic Sequence of M, L, and T Dwarfs. **Astrophysical Journal**, v. 623, p. 1115–1140, April 2005.

[17] DIAZ, A. I., TERLEVICH, E., PAGEL, B. E. J. Sulphur III lines and the excitation mechanism in NGC 1052. **Monthly Notices of the Royal Astronomical Society**, v. 214, p. 41P–45P, June 1985.

[18] DOPITA, M. A., HO, I.-T., DRESSEL, L. L., SUTHERLAND, R., KEWLEY, L., DAVIES, R., HAMPTON, E., SHASTRI, P., KHARB, P., JOSE, J., BHATT, H., RAMYA, S., SCHARWÄCHTER, J., JIN, C., BANFIELD, J., ZAW, I., JAMES, B., JUNEAU, S., SRIVASTAVA, S. Probing the Physics of Narrow-line Regions in Active Galaxies. III. Accretion and Cocoon Shocks in the LINER NGC 1052. **Astrophysical Journal**, v. 801, p. 42, March 2015.

[19] ELLISON, S. L., TEIMOORINIA, H., ROSARIO, D. J., MENDEL, J. T. The star formation rates of active galactic nuclei host galaxies. **Monthly Notices of the Royal Astronomical Society**, v. 458, p. L34–L38, May 2016.

[20] FERNÁNDEZ-ONTIVEROS, J. A., LÓPEZ-SANJUAN, C., MONTES, M., PRIETO, M. A., ACOSTA-PULIDO, J. A. The most recent burst of star formation in the massive elliptical galaxy NGC 1052. **Monthly Notices of the Royal Astronomical Society**, v. 411, p. L21–L25, February 2011.

[21] FERRARESE, L., MERRITT, D. A Fundamental Relation between Supermassive Black Holes and Their Host Galaxies. **Astrophysical Journal Letters**, v. 539, p. L9–L12, August 2000.

[22] FEY, A. L., CHARLOT, P. VLBA Observations of Radio Reference Frame Sources. II. Astrometric Suitability Based on Observed Structure. **Astrophysical Journal Supplement Series**, v. 111, p. 95–142, July 1997.

[23] FOSBURY, R. A. E., MEBOLD, U., GOSS, W. M., DOPITA, M. A. The active elliptical galaxy NGC 1052. **Monthly Notices of the Royal Astronomical Society**, v. 183, p. 549–568, June 1978.

[24] GABEL, J. R., BRUHWEILER, F. C., CRENSHAW, D. M., KRAEMER, S. B., MISKEY, C. L. Hubble Space Telescope Observations and Photoionization Modeling of the LINER Galaxy NGC 1052. **Astrophysical Journal**, v. 532, p. 883–894, April 2000.

[25] GEBHARDT, K., BENDER, R., BOWER, G., DRESSLER, A., FABER, S. M., FILIPPENKO, A. V., GREEN, R., GRILLMAIR, C., HO, L. C., KORMENDY, J., LAUER, T. R., MAGORRIAN, J., PINKNEY, J., RICHSTONE, D., TREMAINE, S. A Relationship between Nuclear Black Hole Mass and Galaxy Velocity Dispersion. **Astrophysical Journal Letters**, v. 539, p. L13–L16, August 2000.

[26] GOMES, J. M., PAPADEROS, P., KEHRIG, C., VíLCHEZ, J. M., LEHNERT, M. D., SÁNCHEZ, S. F., ZIEGLER, B., BREDA, I., DOS REIS, S. N., IGLESIAS-PÁRAMO, J., BLAND-HAWTHORN, J., GALBANY, L., BOMANS, D. J., ROSALES-ORTEGA, F. F., CID FERNANDES, R., WALCHER, C. J., FALCÓN-BARROSO, J., GARCíA-BENITO, R., MÁRQUEZ, I., DEL OLMO, A., MASEGOSA, J., MOLLÁ, M., MARINO, R. A., GONZÁLEZ DELGADO, R. M., LÓPEZ-SÁNCHEZ, Á. R., CALIFA COLLABORATION, . Warm ionized gas in CALIFA early-type galaxies. 2D emission-line patterns and kinematics for 32 galaxies. **Astronomy and Astrophysics**, v. 588, p. A68, April 2016.

[27] GREENE, J. E., HO, L. C. Active Galactic Nuclei with Candidate Intermediate-Mass Black Holes. **Astrophysical Journal**, v. 610, p. 722–736, August 2004.

[28] GREENE, J. E., HO, L. C., BARTH, A. J. Black Holes in Pseudobulges and Spheroidals: A Change in the Black Hole-Bulge Scaling Relations at Low Mass. **Astrophysical Journal**, v. 688, p. 159–179, November 2008.

[29] GREENE, J. E., PENG, C. Y., KIM, M., KUO, C.-Y., BRAATZ, J. A., IMPELLIZZERI, C. M. V., CONDON, J. J., LO, K. Y., HENKEL, C., REID, M. J. Precise Black Hole Masses from Megamaser Disks: Black Hole-Bulge Relations at Low Mass. **Astrophysical Journal**, v. 721, p. 26–45, September 2010.

[30] HARRISON, C. M. Impact of supermassive black hole growth on star formation. **Nature Astronomy**, v. 1, p. 0165, July 2017.

[31] HECKMAN, T. M. An optical and radio survey of the nuclei of bright galaxies - Activity in normal galactic nuclei. **Astronomy and Astrophysics**, v. 87, p. 152–164, July 1980.

[32] HO, L. C. Nuclear Activity in Nearby Galaxies. **Annual Review of Astronomy and Astrophysics**, v. 46, p. 475–539, September 2008.

[33] HU, J. The black hole mass-bulge mass correlation: bulges versus pseudo-bulges. **ArXiv e-prints**, August 2009.

[34] KADLER, M., KERP, J., ROS, E., FALCKE, H., POGGE, R. W., ZENSUS, J. A. Jet emission in ¡ASTROBJ¿NGC 1052¡/ASTROBJ¿ at radio, optical, and X-ray frequencies. **Astronomy and Astrophysics**, v. 420, p. 467–474, June 2004.

[35] KAUFFMANN, G., HECKMAN, T. M., TREMONTI, C., BRINCHMANN, J., CHARLOT, S., WHITE, S. D. M., RIDGWAY, S. E., BRINKMANN, J., FUKUGITA, M., HALL, P. B., IVEZIĆ, Ž., RICHARDS, G. T., SCHNEIDER, D. P. The host galaxies of active galactic nuclei. **Monthly Notices of the Royal Astronomical Society**, v. 346, p. 1055–1077, December 2003.

[36] KEHRIG, C., MONREAL-IBERO, A., PAPADEROS, P., VíLCHEZ, J. M., GOMES, J. M., MASEGOSA, J., SÁNCHEZ, S. F., LEHNERT, M. D., CID FERNANDES, R., BLAND-HAWTHORN, J., BOMANS, D. J., MARQUEZ, I., MAST, D., AGUERRI, J. A. L., LÓPEZ-SÁNCHEZ, Á. R., MARINO, R. A., PASQUALI, A., PEREZ, I., ROTH, M. M., SÁNCHEZ-BLÁZQUEZ, P., ZIEGLER, B. The ionized gas in the CALIFA early-type galaxies. I. Mapping two representative cases: NGC 6762 and NGC 5966. **Astronomy and Astrophysics**, v. 540, p. A11, April 2012.

[37] KORATKAR, A., BLAES, O. The Ultraviolet and Optical Continuum Emission in Active Galactic Nuclei: The Status of Accretion Disks. **Publications of the Astronomical Society of the Pacific**, v. 111, p. 1–30, January 1999.

[38] KORMENDY, J., BENDER, R., CORNELL, M. E. Supermassive black holes do not correlate with galaxy disks or pseudobulges. **Nature**, v. 469, p. 374–376, January 2011.

[39] KORMENDY, J., HO, L. C. Coevolution (Or Not) of Supermassive Black Holes and Host Galaxies. **Annual Review of Astronomy and Astrophysics**, v. 51, p. 511–653, August 2013.

[40] KORMENDY, J., RICHSTONE, D. Inward Bound—The Search For Supermassive Black Holes In Galactic Nuclei. **Annual Review of Astronomy and Astrophysics**, v. 33, p. 581, 1995.

[41] KOSKI, A. T., OSTERBROCK, D. E. Electron Temperature in the Elliptical Galaxy NGC 1052. **Astrophysical Journal Letters**, v. 203, p. L49, January 1976.

[42] LANÇON, A., MOUHCINE, M. The modelling of intermediate-age stellar populations. II. Average spectra for upper AGB stars, and their use. **Astronomy and Astrophysics**, v. 393, p. 167–181, October 2002.

[43] LE BERTRE, T. Optical and infrared observations of 23 carbon-rich stars. Modelling of the circumstellar dust shells. **Astronomy and Astrophysics**, v. 324, p. 1059–1070, August 1997.

[44] LE BORGNE, J.-F., BRUZUAL, G., PELLÓ, R., LANÇON, A., ROCCA-VOLMERANGE, B., SANAHUJA, B., SCHAERER, D., SOUBIRAN, C., VíLCHEZ-GÓMEZ, R. STELIB: A library of stellar spectra at R ˜ 2000. **Astronomy and Astrophysics**, v. 402, p. 433–442, May 2003.

[45] LE SIDANER, P., LE BERTRE, T. Optical and infrared observations of 27 oxygen-rich stars. Modelling of the circumstellar dust shells. **Astronomy and Astrophysics**, v. 314, p. 896–908, October 1996.

[46] LEJEUNE, T., CUISINIER, F., BUSER, R. Standard stellar library for evolutionary synthesis. I. Calibration of theoretical spectra. **Astronomy and Astrophysics Supplement Series**, v. 125, October 1997.

[47] LEJEUNE, T., CUISINIER, F., BUSER, R. A standard stellar library for evolutionary synthesis. II. The M dwarf extension. **Astronomy and Astrophysics Supplement Series**, v. 130, p. 65–75, May 1998.

[48] LESLIE, S. K., KEWLEY, L. J., SANDERS, D. B., LEE, N. Quenching star formation: insights from the local main sequence. **Monthly Notices of the Royal Astronomical Society**, v. 455, p. L82–L86, January 2016.

[49] LOUBSER, S. I., SOECHTING, I. K. The detailed nature of active central cluster galaxies. **Monthly Notices of the Royal Astronomical Society**, v. 431, p. 2933–2959, May 2013.

[50] LUTZ, D., MAINIERI, V., RAFFERTY, D., SHAO, L., HASINGER, G., WEIß, A., WALTER, F., SMAIL, I., ALEXANDER, D. M., BRANDT, W. N., CHAPMAN, S., COPPIN, K., FÖRSTER SCHREIBER, N. M., GAWISER,

E., GENZEL, R., GREVE, T. R., IVISON, R. J., KOEKEMOER, A. M., KURCZYNSKI, P., MENTEN, K. M., NORDON, R., POPESSO, P., SCHINNERER, E., SILVERMAN, J. D., WARDLOW, J., XUE, Y. Q. The LABOCA Survey of the Extended Chandra Deep Field South: Two Modes of Star Formation in Active Galactic Nucleus Hosts? **Astrophysical Journal**, v. 712, p. 1287–1301, April 2010.

[51] MAGORRIAN, J., TREMAINE, S., RICHSTONE, D., BENDER, R., BOWER, G., DRESSLER, A., FABER, S. M., GEBHARDT, K., GREEN, R., GRILLMAIR, C., KORMENDY, J., LAUER, T. The Demography of Massive Dark Objects in Galaxy Centers. **Astronomical Journal**, v. 115, p. 2285–2305, June 1998.

[52] MALLMANN, N. D., RIFFEL, R., STORCHI-BERGMANN, T., REMBOLD, S. B., RIFFEL, R. A., SCHIMOIA, J., DA COSTA, L. N., ÁVILA-REESE, V., SANCHEZ, S. F., MACHADO, A. D., CIROLINI, R., ILHA, G. S., NASCIMENTO, J. C. D. The first 62 AGN observed with SDSS-IV MaNGA - II. Resolvedstellar populations. **Monthly Notices of the Royal Astronomical Society**, v. 478, p. 5491–5504, August 2018.

[53] MAOZ, DAN, KORATKAR, ANURADHA, SHIELDS, JOSEPH C., HO, LUIS C., FILIPPENKO, ALEXEI V., STERNBERG, AMIEL. The Ultraviolet Spectra of LINERs: A Comparative Study. **Astronomical Journal**, v. 116, n. 1, p. 55–67, Jul 1998.

[54] MARASTON, C. Evolutionary population synthesis: models, analysis of the ingredients and application to high-z galaxies. **Monthly Notices of the Royal Astronomical Society**, v. 362, p. 799–825, September 2005.

[55] MARCONI, A., RISALITI, G., GILLI, R., HUNT, L. K., MAIOLINO, R., SALVATI, M. Local supermassive black holes, relics of active galactic nuclei and the X-ray background. **Monthly Notices of the Royal Astronomical Society**, v. 351, p. 169–185, June 2004.

[56] MARIGO, P., GIRARDI, L., BRESSAN, A., GROENEWEGEN, M. A. T., SILVA, L., GRANATO, G. L. Evolution of asymptotic giant branch stars. II. Optical to far-infrared isochrones with improved TP-AGB models. **Astronomy and Astrophysics**, v. 482, p. 883–905, May 2008.

[57] MENESES-GOYTIA, S., PELETIER, R. F., TRAGER, S. C., VAZDEKIS, A. Single stellar populations in the near-infrared. II. Synthesis models. **Astronomy and Astrophysics**, v. 582, p. A97, October 2015.

[58] MERLONI, A., HEINZ, S. A synthesis model for AGN evolution: supermassive black holes growth and feedback modes. **Monthly Notices of the Royal Astronomical Society**, v. 388, p. 1011–1030, August 2008.

[59] MILONE, A. D. C., RICKES, M. G., PASTORIZA, M. G. The elliptical galaxies NGC 1052 and NGC 7796. Stellar populations and abundance ratio α/Fe. **Astronomy and Astrophysics**, v. 469, p. 89–113, July 2007.

[60] OSTERBROCK, DONALD E., FERLAND, GARY J. **Astrophysics of gaseous nebulae and active galactic nuclei**: 2006.

[61] PAPADEROS, P., GOMES, J. M., VíLCHEZ, J. M., KEHRIG, C., LEHNERT, M. D., ZIEGLER, B., SÁNCHEZ, S. F., HUSEMANN, B., MONREAL-IBERO, A., GARCíA-BENITO, R., BLAND-HAWTHORN, J., CORTIJO-FERRERO, C., DE LORENZO-CÁCERES, A., DEL OLMO, A., FALCÓN-BARROSO, J., GALBANY, L., IGLESIAS-PÁRAMO, J., LÓPEZ-SÁNCHEZ, Á. R., MARQUEZ, I., MOLLÁ, M., MAST, D., VAN DE VEN, G., WISOTZKI, L. Nebular emission and the Lyman continuum photon escape fraction in CALIFA early-type galaxies. **Astronomy and Astrophysics**, v. 555, p. L1, July 2013.

[62] PENG, Y.-J., LILLY, S. J., KOVAČ, K., BOLZONELLA, M., POZZETTI, L., RENZINI, A., ZAMORANI, G., ILBERT, O., KNOBEL, C., IOVINO, A., MAIER, C., CUCCIATI, O., TASCA, L., CAROLLO, C. M., SILVERMAN, J., KAMPCZYK, P., DE RAVEL, L., SANDERS, D., SCOVILLE, N., CONTINI, T., MAINIERI, V., SCODEGGIO, M., KNEIB, J.-P., LE FÈVRE, O., BARDELLI, S., BONGIORNO, A., CAPUTI, K., COPPA, G., DE LA TORRE, S., FRANZETTI, P., GARILLI, B., LAMAREILLE, F., LE BORGNE, J.-F., LE BRUN, V., MIGNOLI, M., PEREZ MONTERO, E., PELLO, R., RICCIARDELLI, E., TANAKA, M., TRESSE, L., VERGANI, D., WELIKALA, N., ZUCCA, E., OESCH, P., ABBAS, U., BARNES, L., BORDOLOI, R., BOTTINI, D., CAPPI, A., CASSATA, P., CIMATTI, A., FUMANA, M., HASINGER, G., KOEKEMOER, A., LEAUTHAUD, A., MACCAGNI, D., MARINONI, C., MCCRACKEN, H., MEMEO, P., MENEUX, B., NAIR, P., PORCIANI, C., PRESOTTO, V., SCARAMELLA, R. Mass and Environment as

Drivers of Galaxy Evolution in SDSS and zCOSMOS and the Origin of the Schechter Function. **Astrophysical Journal**, v. 721, p. 193–221, September 2010.

[63] PETERSON, B. M. **An Introduction to Active Galactic Nuclei**: February 1997.

[64] PIERCE, M., BRODIE, J. P., FORBES, D. A., BEASLEY, M. A., PROCTOR, R., STRADER, J. Evolutionary history of the elliptical galaxy NGC 1052. **Monthly Notices of the Royal Astronomical Society**, v. 358, p. 419–431, April 2005.

[65] PIETRINFERNI, A., CASSISI, S., SALARIS, M., CASTELLI, F. A Large Stellar Evolution Database for Population Synthesis Studies. I. Scaled Solar Models and Isochrones. **Astrophysical Journal**, v. 612, p. 168–190, September 2004.

[66] RAIMANN, D., STORCHI-BERGMANN, T., BICA, E., ALLOIN, D. Stellar population gradients in normal and active galaxies. **Monthly Notices of the Royal Astronomical Society**, v. 324, p. 1087–1101, July 2001.

[67] RAMOS ALMEIDA, CRISTINA, RICCI, CLAUDIO. Nuclear obscuration in active galactic nuclei. **Nature Astronomy**, v. 1, p. 679–689, Oct 2017.

[68] RAYNER, J. T., CUSHING, M. C., VACCA, W. D. The Infrared Telescope Facility (IRTF) Spectral Library: Cool Stars. **Astrophysical Journal Supplement Series**, v. 185, p. 289–432, December 2009.

[69] REMBOLD, S. B., SHIMOIA, J. S., STORCHI-BERGMANN, T., RIFFEL, R., RIFFEL, R. A., MALLMANN, N. D., DO NASCIMENTO, J. C., MOREIRA, T. N., ILHA, G. S., MACHADO, A. D., CIROLINI, R., DA COSTA, L. N., MAIA, M. A. G., SANTIAGO, B. X., SCHNEIDER, D. P., WYLEZALEK, D., BIZYAEV, D., PAN, K., MÜLLER-SÁNCHEZ, F. The first 62 AGNs observed with SDSS-IV MaNGA - I. Their characterization and definition of a control sample. **Monthly Notices of the Royal Astronomical Society**, v. 472, p. 4382–4403, December 2017.

[70] RICCI, T. V., STEINER, J. E., MENEZES, R. B. IFU spectroscopy of 10 early-type galactic nuclei - II. Nuclear emission line properties. **Monthly Notices of the Royal Astronomical Society**, v. 440, p. 2442–2456, May 2014a.

[71] RICCI, T. V., STEINER, J. E., MENEZES, R. B. Integral field unit spectroscopy of 10 early-type galactic nuclei - I. Principal component analysis Tomography and nuclear activity. **Monthly Notices of the Royal Astronomical Society**, v. 440, p. 2419–2441, May 2014b.

[72] RICCI, T. V., STEINER, J. E., MENEZES, R. B. IFU spectroscopy of 10 early-type galactic nuclei - III. Properties of the circumnuclear gas emission. **Monthly Notices of the Royal Astronomical Society**, v. 451, p. 3728–3758, August 2015.

[73] RIFFEL, R., MASON, R. E., MARTINS, L. P., RODRíGUEZ-ARDILA, A., HO, L. C., RIFFEL, R. A., LIRA, P., GONZALEZ MARTIN, O., RUSCHEL-DUTRA, D., ALONSO-HERRERO, A., FLOHIC, H., MCDERMID, R. M., RAMOS ALMEIDA, C., THANJAVUR, K., WINGE, C. The stellar spectral features of nearby galaxies in the near infrared: tracers of thermally pulsing asymptotic giant branch stars? **Monthly Notices of the Royal Astronomical Society**, v. 450, p. 3069–3079, July 2015.

[74] RIFFEL, R., PASTORIZA, M. G., RODRíGUEZ-ARDILA, A., BONATTO, C. Probing the near-infrared stellar population of Seyfert galaxies. **Monthly Notices of the Royal Astronomical Society**, v. 400, p. 273–290, November 2009.

[75] RIFFEL, R. A., STORCHI-BERGMANN, T., RIFFEL, R., DAHMER-HAHN, L. G., DINIZ, M. R., SCHÖNELL, A. J., DAMETTO, N. Z. Gemini NIFS survey of feeding and feedback processes in nearby active galaxies - I. Stellar kinematics. **Monthly Notices of the Royal Astronomical Society**, v. 470, p. 992–1016, September 2017.

[76] RIFFEL, R. A., STORCHI-BERGMANN, T., RIFFEL, R., DAVIES, R., BIANCHIN, M., DINIZ, M. R., SCHÖNELL, A. J., BURTSCHER, L., CRENSHAW, M., FISCHER, T. C. Gemini NIFS survey of feeding and feedback processes in nearby active galaxies - II. The sample and surface mass density profiles. **Monthly Notices of the Royal Astronomical Society**, v. 474, n. 1, p. 1373–1389, Feb 2018.

[77] RIFFEL, ROGÉRIO. **Estudo da região HII galáctica NGC 2579**. UFSM, 03 2004. Dissertação de Mestrado – Universidade Federal de Santa Maria.

[78] RIFFEL, ROGÉRIO, RODRíGUEZ-ARDILA, ALBERTO, BROTHERTON, MICHAEL S., PELETIER, REYNIER, VAZDEKIS, ALEXAND RE, RIFFEL, ROGEMAR A., MARTINS, LUCIMARA PIRES, BONATTO, CHARLES, ZANON DAMETTO, NATACHA, DAHMER-HAHN, LUIS GABRIEL. Optical/NIR stellar absorption and emission-line indices from luminous infrared galaxies. **Monthly Notices of the Royal Astronomical Society**, v. 486, n. 3, p. 3228–3247, Jul 2019.

[79] RÖCK, B., VAZDEKIS, A., RICCIARDELLI, E., PELETIER, R. F., KNAPEN, J. H., FALCÓN-BARROSO, J. MILES extended: Stellar population synthesis models from the optical to the infrared. **Astronomy and Astrophysics**, v. 589, p. A73, May 2016.

[80] SARZI, M., SHIELDS, J. C., SCHAWINSKI, K., JEONG, H., SHAPIRO, K., BACON, R., BUREAU, M., CAPPELLARI, M., DAVIES, R. L., DE ZEEUW, P. T., EMSELLEM, E., FALCÓN-BARROSO, J., KRAJNOVIĆ, D., KUNTSCHNER, H., MCDERMID, R. M., PELETIER, R. F., VAN DEN BOSCH, R. C. E., VAN DE VEN, G., YI, S. K. The SAURON project - XVI. On the sources of ionization for the gas in elliptical and lenticular galaxies. **Monthly Notices of the Royal Astronomical Society**, v. 402, p. 2187–2210, March 2010.

[81] SCHMIDT, A. A., COPETTI, M. V. F., ALLOIN, D., JABLONKA, P. Population synthesis methods - Discussion and tests on the solution uniqueness. **Monthly Notices of the Royal Astronomical Society**, v. 249, p. 766–778, April 1991.

[82] SCHNEIDER, P. **Extragalactic Astronomy and Cosmology: An Introduction**: 2015.

[83] SCHÖNELL, ASTOR J., STORCHI-BERGMANN, THAISA, RIFFEL, ROGEMAR A., RIFFEL, ROGÉRIO, BIANCHIN, MARINA, DAHMER-HAHN, LUIS G., DINIZ, MARLON R., DAMETTO, NATACHA Z. Gemini NIFS survey of feeding and feedback in nearby active galaxies - III. Ionized versus warm molecular gas masses and distributions. **Monthly Notices of the Royal Astronomical Society**, v. 485, n. 2, p. 2054–2070, May 2019.

[84] SHANKAR, F., SALUCCI, P., GRANATO, G. L., DE ZOTTI, G., DANESE, L. Supermassive black hole demography: the match between the local and accreted

mass functions. **Monthly Notices of the Royal Astronomical Society**, v. 354, p. 1020–1030, November 2004.

[85] SILVERMAN, J. D., GREEN, P. J., BARKHOUSE, W. A., KIM, D.-W., KIM, M., WILKES, B. J., CAMERON, R. A., HASINGER, G., JANNUZI, B. T., SMITH, M. G., SMITH, P. S., TANANBAUM, H. The Luminosity Function of X-Ray-selected Active Galactic Nuclei: Evolution of Supermassive Black Holes at High Redshift. **Astrophysical Journal**, v. 679, p. 118–139, May 2008.

[86] SOLTAN, A. Masses of quasars. **Monthly Notices of the Royal Astronomical Society**, v. 200, p. 115–122, July 1982.

[87] STANLEY, F., ALEXANDER, D. M., HARRISON, C. M., ROSARIO, D. J., WANG, L., AIRD, J. A., BOURNE, N., DUNNE, L., DYE, S., EALES, S., KNUDSEN, K. K., MICHAŁOWSKI, M. J., VALIANTE, E., DE ZOTTI, G., FURLANETTO, C., IVISON, R., MADDOX, S., SMITH, M. W. L. The mean star formation rates of unobscured QSOs: searching for evidence of suppressed or enhanced star formation. **Monthly Notices of the Royal Astronomical Society**, v. 472, p. 2221–2240, December 2017.

[88] STASIŃSKA, G., VALE ASARI, N., CID FERNANDES, R., GOMES, J. M., SCHLICKMANN, M., MATEUS, A., SCHOENELL, W., SODRÉ, L., JR., SEAGAL COLLABORATION, . Can retired galaxies mimic active galaxies? Clues from the Sloan Digital Sky Survey. **Monthly Notices of the Royal Astronomical Society**, v. 391, p. L29–L33, November 2008.

[89] STORCHI-BERGMANN, T., RAIMANN, D., BICA, E. L. D., FRAQUELLI, H. A. The Frequency of Nuclear Star Formation in Seyfert 2 Galaxies. **Astrophysical Journal**, v. 544, p. 747–762, December 2000.

[90] SUGAI, H., HATTORI, T., KAWAI, A., OZAKI, S., KOSUGI, G., OHTANI, H., HAYASHI, T., ISHIGAKI, T., ISHII, M., SASAKI, M., TAKEYAMA, N., YUTANI, M., USUDA, T., HAYASHI, S. S., NAMIKAWA, K. Subarcsecond Structure and Velocity Field of Optical Line-emitting Gas in NGC 1052. **Astrophysical Journal**, v. 629, p. 131–138, August 2005.

[91] SUGAI, H., MALKAN, M. A. Mid-Infrared Infrared Space Observatory Spectroscopy of the Prototypical LINER NGC 1052: Shocks Reconsidered. **Astrophysical Journal**, v. 529, p. 219–223, January 2000.

[92] URRY, C. M., PADOVANI, P. Unified Schemes for Radio-Loud Active Galactic Nuclei. **Publications of the Astronomical Society of the Pacific**, v. 107, p. 803, September 1995.

[93] VAN GORKOM, J. H., KNAPP, G. R., RAIMOND, E., FABER, S. M., GALLAGHER, J. S. The distribution and kinematics of H I in the active elliptical galaxy NGC 1052. **Astronomical Journal**, v. 91, p. 791–807, April 1986.

[94] VAZDEKIS, A., KOLEVA, M., RICCIARDELLI, E., RÖCK, B., FALCÓN-BARROSO, J. UV-extended E-MILES stellar population models: young components in massive early-type galaxies. **Monthly Notices of the Royal Astronomical Society**, v. 463, p. 3409–3436, December 2016.

[95] VAZDEKIS, A., SÁNCHEZ-BLÁZQUEZ, P., FALCÓN-BARROSO, J., CENARRO, A. J., BEASLEY, M. A., CARDIEL, N., GORGAS, J., PELETIER, R. F. Evolutionary stellar population synthesis with MILES - I. The base models and a new line index system. **Monthly Notices of the Royal Astronomical Society**, v. 404, p. 1639–1671, June 2010.

[96] WROBEL, J. M. Radio continuum activity in the elliptical galaxy NGC 1052. **Astrophysical Journal**, v. 284, p. 531–543, September 1984.

[97] YAN, R., BLANTON, M. R. The Nature of LINER-like Emission in Red Galaxies. **Astrophysical Journal**, v. 747, p. 61, March 2012.

[98] ZIER, C., BIERMANN, P. L. Binary black holes and tori in AGN. II. Can stellar winds constitute a dusty torus? **Astronomy and Astrophysics**, v. 396, p. 91–108, December 2002.

[99] ZUBOVAS, K., BOURNE, M. A. Do AGN outflows quench or enhance star formation? **Monthly Notices of the Royal Astronomical Society**, v. 468, p. 4956–4967, July 2017.

Apêndices

A.1 Levantamento Gemini NIFS de processos de alimentação e retroalimentação em galáxias ativas próximas: I - Cinemática estelar

Aqui apresentamos os resultados obtidos pelo grupo AGNIFS na cinemática estelar de AGNs. Estes resultados foram publicados na revista MNRAS em Setembro de 2017, intitulado *Gemini NIFS survey of feeding and feedback processes in nearby Active Galaxies: I - Stellar kinematics.*

Mon. Not. R. Astron. Soc. **000**, 1–19 (2014) Printed 22 May 2017 (MN LATEX style file v2.2)

Gemini NIFS survey of feeding and feedback processes in nearby Active Galaxies: I - Stellar kinematics

Rogemar A. Riffel[1]⋆, Thaisa Storchi-Bergmann[2], Rogerio Riffel[2], Luis G. Dahmer-Hahn[2], Marlon R. Diniz[1], Astor J. Schönell[2], Natacha Z. Dametto[2]
[1] *Departamento de Física, Centro de Ciências Naturais e Exatas, Universidade Federal de Santa Maria, 97105-900, Santa Maria, RS, Brazil*
[2] *Departamento de Astronomia, Instituto de Física, Universidade Federal do Rio Grande do Sul, CP 15051, 91501-970, Porto Alegre, RS, Brazil*

Accepted 1988 December 15. Received 1988 December 14; in original form 1988 October 11

ABSTRACT

We use the Gemini Near-Infrared Integral Field Spectrograph (NIFS) to map the stellar kinematics of the inner few hundred parsecs of a sample of 16 nearby Seyfert galaxies, at a spatial resolution of tens of parsecs and spectral resolution of 40 km s^{-1}. We find that the line-of-sight (LOS) velocity fields for most galaxies are well reproduced by rotating disk models. The kinematic position angle (PA) derived for the LOS velocity field is consistent with the large scale photometric PA. The residual velocities are correlated with the hard X-ray luminosity, suggesting that more luminous AGN have a larger impact in the surrounding stellar dynamics. The central velocity dispersion values are usually higher than the rotation velocity amplitude, what we attribute to the strong contribution of bulge kinematics in these inner regions. For 50% of the galaxies, we find an inverse correlation between the velocities and the h_3 Gauss-Hermitte moment, implying red wings in the blueshifted side and blue wings in the redshifted side of the velocity field, attributed to the movement of the bulge stars lagging the rotation. Two of the 16 galaxies (NGC 5899 and Mrk 1066) show an S-shape zero velocity line, attributed to the gravitational potential of a nuclear bar. Velocity dispersion (σ) maps show rings of low-σ values ($\sim 50 - 80$ km s^{-1}) for 4 objects and "patches" of low-σ for 6 galaxies at 150–250 pc from the nucleus, attributed to young/ intermediate age stellar populations.

Key words: galaxies: kinematics and dynamics – galaxies: active – galaxies: ISM – infrared: galaxies

1 INTRODUCTION

Active Galactic Nuclei (AGN) characterize a critical phase in galaxy evolution in which its nuclear super-massive black hole (SMBH) is being fed due to gas accretion to the nuclear region. Once the accretion disk surrounding the SMBH is formed, feedback processes begin to occur, comprising jets of relativistic particles emitted from the inner rim of the accretion disk, winds emanating from outer regions of the disk and radiation emitted by the hot gas in the disk or by its corona (Frank, King & Raine. 2002; Elvis 2000; Ciotti et al. 2010). The AGN feeding and feedback processes couple the growth of the SMBHs and their host galaxies, and are claimed to explain the correlation between the mass of the SMBH and the mass of the galaxy bulge (Ferrarese & Ford 2005; Somerville et al. 2008; Kormendy & Ho 2013). The feeding processes are a necessary condition to trigger the nuclear activity, while the feedback processes are now a fundamental ingredient in galaxy evolution models: without AGN feedback, the models cannot reproduce the properties of the massive galaxies – these galaxies end up forming too many stars (Springel et al. 2005; Fabian 2012; Terrazas et al. 2016).

The study of feeding and feedback processes in AGNs requires a detailed mapping of the gas and stellar kinematics in the vicinity of the central engine. Usually these studies are based on high spatial resolution Integral Field Spectroscopy (IFS, e.g. Fathi et al. 2006; Barbosa et al. 2009, 2014; Sánchez et al. 2009; Hicks et al. 2009, 2013; Storchi-Bergmann et al. 2007, 2009, 2010; Mazzalay et al. 2014; Riffel et al. 2013; Riffel & Storchi-Bergmann 2011a; Riffel, Storchi-Bergmann & Riffel 2014; Diniz et al. 2015). To isolate and quantify gas streaming motions towards the center of galaxies or gas outflows from the nucleus through the gas kinematics, it is necessary to properly map the motions of the gas due to the gravitational potential of the galaxy. A way to map the gravitational potential of the galaxies is by two-dimensional

⋆ E-mail: rogemar@ufsm.br

Table 1. Sample: (1) Galaxy's name; (2) redshift; (3) nuclear activity; (4) Hubble type as quoted in NED; (5) Spectral Resolution in Å; (6) Angular Resolution; (7) Spectral Band; (8) Gemini project code; (9) total exposure time; (10) hard X-ray luminosity (14-195 keV) from the Swift-BAT 60-month catalogue (Ajello et al. 2012) ;(11) reference for the stellar kinematics.

1 Galaxy	2 z	3 Act.	4 Hub. Type	5 Sp. R.	6 An. R.	7 B	8 Project ID	9 Exp. T.	10 log L_X [erg s^{-1}]	11 Ref.
NGC788	0.014	Sy2	SA0/a?(s)	3.5	0.″13	K	GN-2015B-Q-29	4400	43.2	a
NGC1052†	0.005	Sy2	E4	3.4	0.″14	KI	GN-2010B-Q-25	2400	41.9	a
NGC2110	0.008	Sy2	SAB0$^-$	3.4	0.″15	KI	GN-2010B-Q-25	3600	43.3	b
NGC3227	0.004	Sy1.5	SAB(s)a pec	3.4	0.″13	KI	GN-2016A-Q-6	2400	42.3	a
NGC3516	0.009	Sy1.5	(R)SB0^0?(s)	3.6	0.″15	K	GN-2015A-Q-3	4500	42.7	a
NGC4051†	0.002	Sy1	SAB(rs)bc	3.2	0.″17	K	GN-2006A-SV-123	4500	41.5	c
NGC4235	0.008	Sy1	SA(s)a edge-on	3.4	0.″13	KI	GN-2016A-Q-6	4000	42.3	a
NGC4388	0.008	Sy2	SA(s)b? edge-on	3.5	0.″14	K	GN-2015A-Q-3	800	43.3	a
NGC5506	0.006	Sy1.9	Sa pec edge-on	3.5	0.″15	K	GN-2015A-Q-3	4000	43.1	a
NGC5548†	0.017	Sy1	(R')SA0/a(s)	3.5	0.″20	KI	GN-2012A-Q-57	2700	43.4	a
NGC5899†	0.009	Sy2	SAB(rs)c	3.5	0.″12	KI	GN-2013A-Q-48	4600	42.1	a
NGC5929†	0.008	Sy2	Sab? pec	3.2	0.″12	KI	GN-2011A-Q-43	6000	–	d
Mrk607†	0.009	Sy2	Sa? edge-on	3.5	0.″12	KI	GN-2012B-Q-45	6000	–	a
Mrk766	0.013	Sy1.5	(R')SB(s)a?	3.5	0.″19	KI	GN-2010A-Q-42	3300	42.8	a
Mrk1066†	0.012	Sy2	(R)SB0$^+$(s)	3.3	0.″15	KI	GN-2008B-Q-30	4800	–	e
Mrk1157†	0.015	Sy2	(R')SB0/a	3.5	0.″12	KI	GN-2009B-Q-27	3300	–	f

†These galaxies do not follow all selection criteria and are part of the complementary sample.
a – This work; b – Diniz et al. (2015); c – Riffel et al. (2008); d – Riffel et al. (2015a); e – Riffel & Storchi-Bergmann (2011a); f – Riffel & Storchi-Bergmann (2011b)

mapping of the stellar kinematics. So far, studies available for nearby galaxies show that the stellar kinematics usually present regular rotation within the inner kiloparsec (e.g. Barbosa et al. 2006; Ganda et al. 2006) and thus can be used to isolate possible non-circular motions from the gas kinematics (e.g. Riffel et al. 2008; Riffel & Storchi-Bergmann 2011a; Diniz et al. 2015).

Adaptive optics IFS at 10-m class telescopes provides an unprecedented possibility to map the stellar kinematics of nearby galaxies at spatial resolutions of a few tens of parsecs. So far, adaptive optics systems are available mainly in near-infrared (near-IR) wavelengths, where the dust extinction at the central regions of galaxies is less important than at optical bands. In addition, strong absorption CO bands are present in the spectra of galaxies, originated in giant and super-giant stars that dominate the continuum emission in the central regions (e.g. Maraston 2005; Riffel et al. 2015c). Thus, near-IR IFS at 10-m telescopes provides a unique tool to map the stellar kinematics at central region of active galaxies, at unprecedented spatial resolution, by fitting the CO absorption band-heads (e.g. Riffel et al. 2015b).

In this paper, we map the stellar kinematics of the inner 3″×3″ of a sample of 16 nearby Seyfert galaxies. This work is part of a larger project in which our group AGNIFS (*AGN Integral Field Spectroscopy*) aims to study the feeding and feedback processes of a sample of 30 nearby Seyfert galaxies, selected by their X-ray luminosity. The kinematic maps presented here will be used to isolate gas non-circular motions in future works by our group and to quantify gas inflows and outflows.

This paper is organized as follows: section 2 presents the sample and a description of the observations and data reduction procedure, while the spectral fitting procedure is presented in sec. 3. The resulting stellar kinematics maps are presented and discussed in section 4 and the kinematic derived parameters are compared with those characterizing the large scale disks of the host galaxies in section 5.1. Finally, section 6 presents the main conclusions of this work.

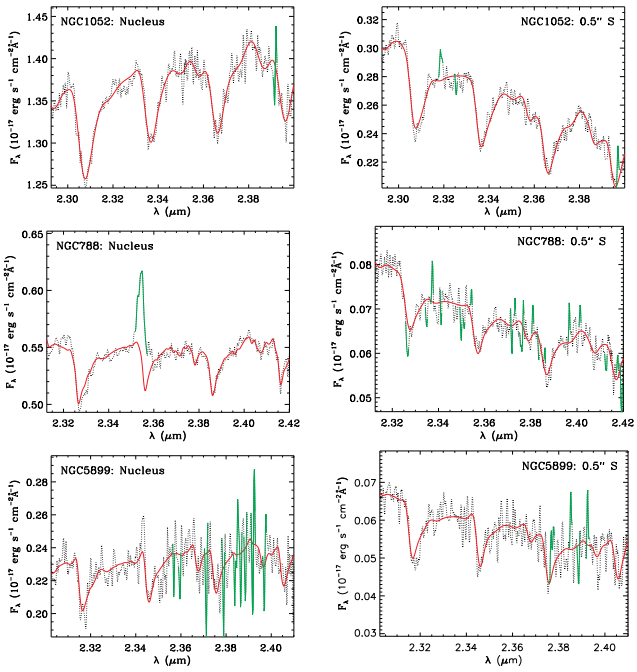

Figure 1. Examples of fits for the nuclear spectrum (left) and typical extra nuclear spectrum (right) for NGC 1052 (top panels), NGC 788 (center panels) and NGC 5899 (bottom panels). The observed spectra are shown as black dotted lines, the best fitted models as red continuous lines and the masked regions (following the criteria explained in the text) during the fits are shown in green.

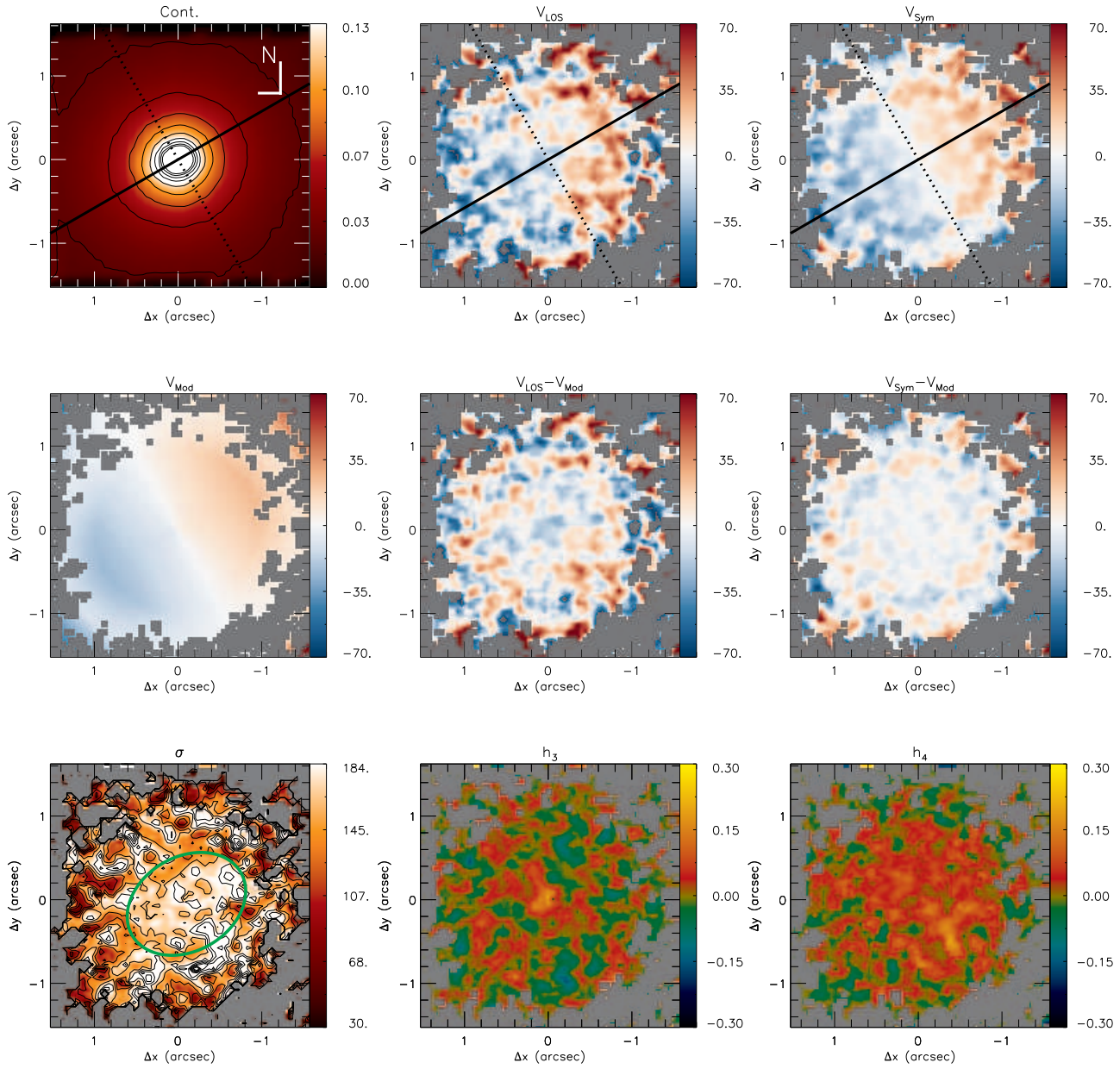

Figure 2. NGC 788: Top-left: K-band continuum image obtained by averaging the spectra, with the color bar shown in units of 10^{-17} erg s^{-1} cm^{-2} Å^{-1}; top-middle: stellar velocity field; top-right: symmetrized velocity field; middle-left: rotating disk model; middle-middle: residual map for the symmetrized velocity field; middle-right: residual map for the observed velocity field; bottom-left: stellar velocity dispersion; bottom-middle: h_3 Gauss-Hermite moment and bottom-right: h_4 Gauss-Hermite moment. Gray regions are masked locations and correspond to regions where the signal-to-noise of the spectra was not high enough to get reliable fits. The continuous line identifies the orientation of the line of nodes and the dotted line marks the orientation of the minor axis of the galaxy. North is up and East left in all maps. The color bar for velocity, model, residual maps and σ show the velocities in units of km s^{-1} and the systemic velocity of the galaxy was subtracted from the observed velocities.

2 SAMPLE AND OBSERVATIONS

2.1 The sample

Our sample comprises 16 AGN host galaxies: 8 from a large Gemini proposal (PI Storchi-Bergmann) to obtain NIFS (Near-Infrared Integral Field Spectrograph) observations of 20 AGN selected from the Swift-BAT 60-month catalogue (Ajello et al. 2012) to have 14–195 keV luminosities $L_X \geqslant 10^{41.5}$ erg s^{-1}, and 8 from previous similar NIFS observations by our group of nearby AGN hosts. Four of these 8 galaxies have similar L_X luminosities and 4 are not in the Swift-BAT catalog. One additional source (Mrk 79) was observed in previous run with similar NIFS configuration, but the signal-to-noise ratio of the CO absorption banheads was not high enough to allow stellar kinematics measurements. By the end of 2018, we

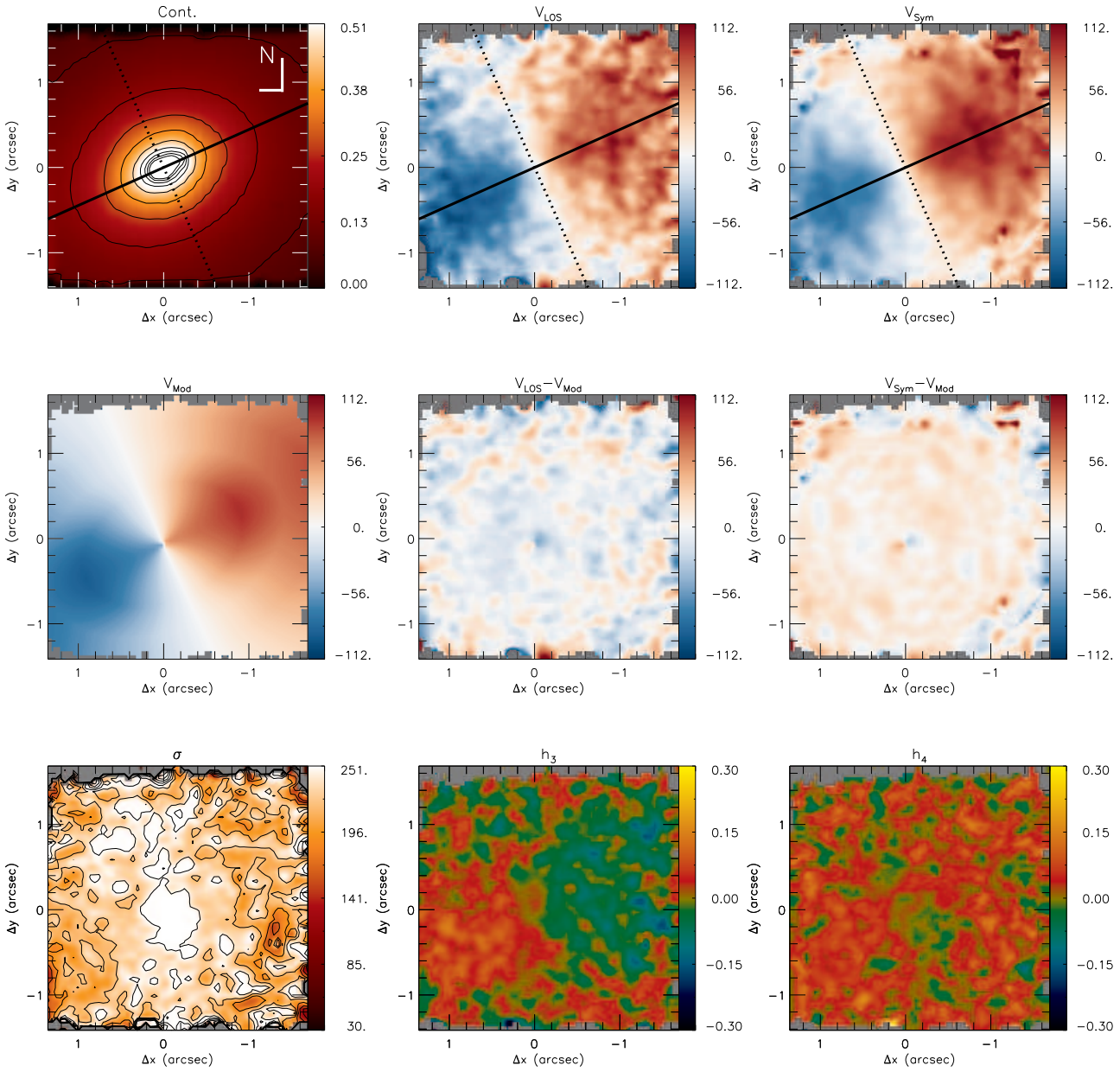

Figure 3. Same as Fig. 2 for NGC 1052.

should have additional observations of another 13 galaxies of the large proposal and thus will have in the end a total of 29 galaxies comprising 20 Swift-BAT selected galaxies plus the 8 galaxies included in the present study (plus Mrk 79) that comprise what we call a "complementary sample", and identified by the symbol † in Table 1.

Additional criteria for the sample is that the redshift is z≲0.015, and to be accessible for NIFS ($-30° < \delta < 73°$). The L_X criterium above defining the sample of the large proposal was adopted because the the Swift-BAT 14–195 keV band measures direct emission from the AGN rather than scattered or re-processed emission, and is much less sensitive to obscuration in the line-of-sight than soft X-ray or optical wavelengths, allowing a selection based only on the AGN properties. In order to assure that we would be able to probe the feeding and feedback processes via the gas kinematics we further selected the galaxies having previously observed extended gas emission (e.g. Schmitt & Kinney 2000) and [O III]λ5007 luminosities. We have excluded from the sample a few galaxies that had guiding problems in the observations. A complete characterization of the sample will be presented in a forthcoming paper (Riffel et al., in preparation).

So far, we have already observed 20 galaxies with NIFS, but only for 16 of them we were able to measure the stellar kinematics by fitting the K-band CO absorption bands at 2.3 μm. We were not able to obtain reliable fits of the remaining four objects (Mrk 3, Mrk 79, NGC 4151 and NGC 1068) due to the dilution of the K-

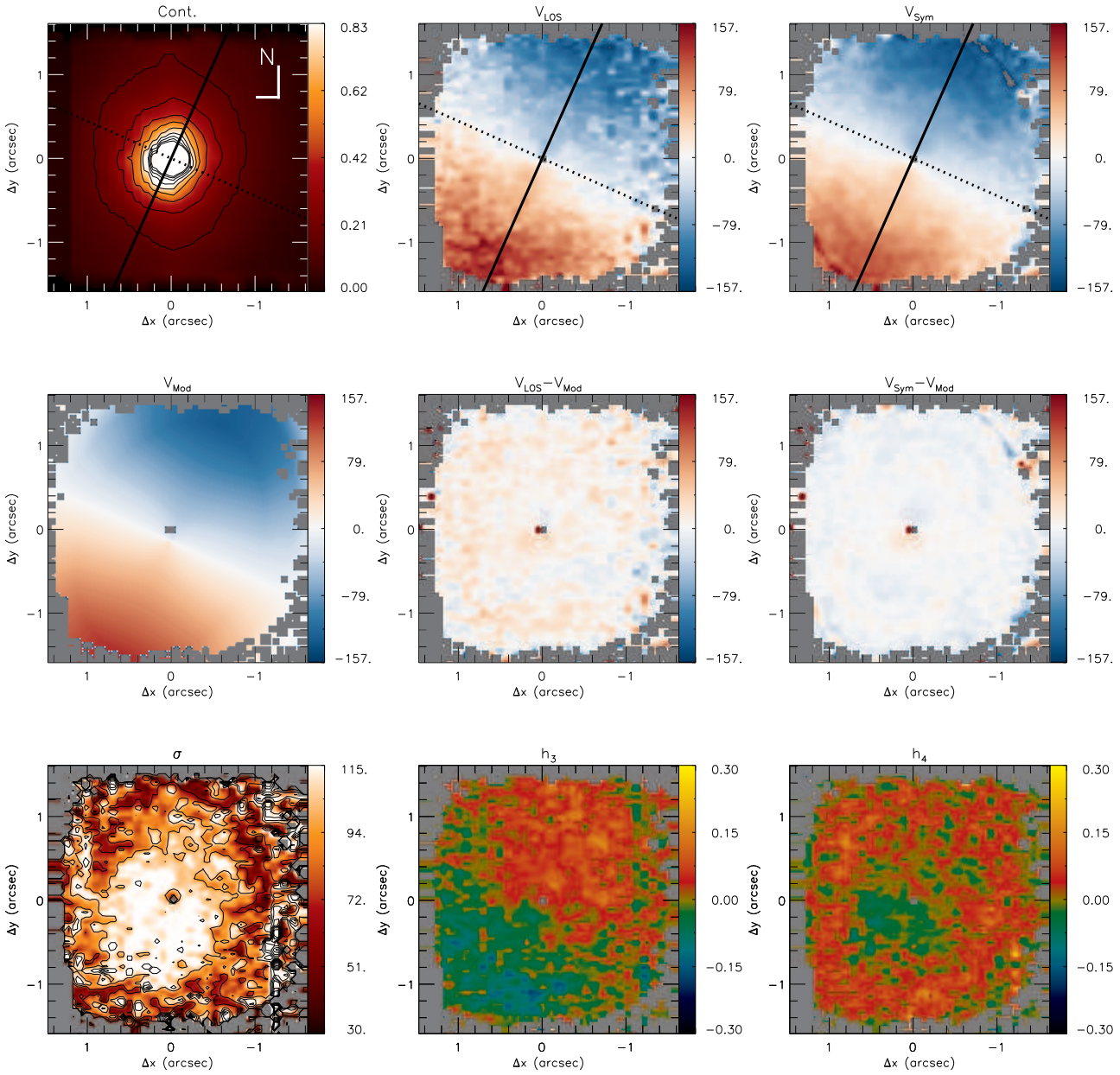

Figure 4. Same as Fig. 2 for NGC 3227.

band CO band-heads due to strong continuum emission. For the latter two, the stellar kinematics has already been studied using the H-band spectra (Onken et al. 2014; Storchi-Bergmann et al. 2012). The 16 galaxies selected for the present study are listed in Table 1, together with relevant information.

2.2 Observations

We used the Gemini Near-Infrared Integral Field Spectrograph (NIFS, McGregor et al. 2003) to observe the galaxies listed in Table 1. All observations were obtained using the Gemini North Adaptive Optics system ALTAIR from 2008 to 2016. The observations followed the standard Object-Sky-Sky-Object dither sequence, with off-source sky positions since all targets are extended, and individual exposure times that varied according to the target. The "HK_G0603" filter and the "Kl_G5607" and "K_G5605" gratings were used during the observations. Most of the observations were performed in the K_l band, with the spectra centred at 2.3 μm, while for five galaxies the spectra were obtained at the K band and centred at 2.2 μm. The spectral range for the K_l data is $\sim$ 2.080 – 2.500 μm and for the K band is $\sim$ 1.980 – 2.400 μm. Both ranges include the ^{12}CO and ^{13}CO absorption band-heads at $\sim$2.3 μm for all galaxies, used to measure the stellar kinematics.

The spectral resolution ranges between 3.2 and 3.6 Å, as obtained from the measurement of the full width at half maximum (FWHM) of ArXe lamp lines, used to wavelength calibrate the

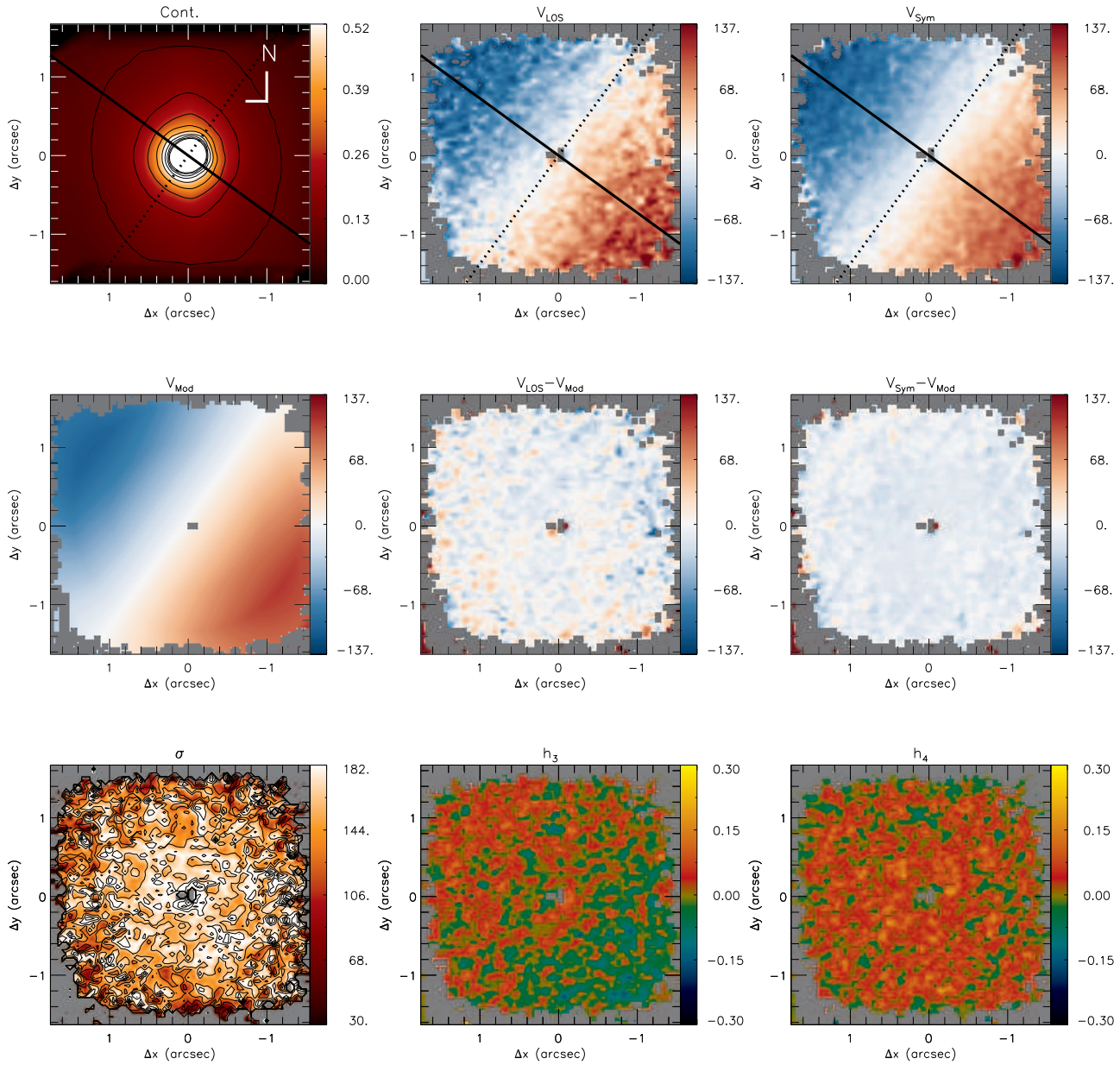

Figure 5. Same as Fig. 2 for NGC 3516.

spectra, close to the central wavelength. This translates to resolutions in the range 42-47 km s^{-1} in the velocity space. The angular resolution is in the range 0.″12–0.″20, derived from the FWHM of flux distribution of the standard stars, corresponding to few tens of parsecs at the distance of most galaxies. More details about the observations are shown in Table 1.

2.3 Data reduction

The data reduction followed the standard procedure and was accomplished by using tasks specifically developed for NIFS data reduction, contained in the NIFS package, which is part of GEMINI IRAF package, as well as generic IRAF tasks and IDL scripts. The data reduction procedure included the trimming of the images, flat-fielding, sky subtraction, wavelength and s-distortion calibrations. The telluric absorptions have been removed using observations of telluric standard stars with A spectral type. These stars were used to flux calibrate the spectra of the galaxies by interpolating a black body function to their spectra. Finally, datacubes were created for each individual exposure at an angular sampling of 0.″05×0.″05 and combined in a final datacube for each galaxy. All datacubes cover the inner $\sim 3'' \times 3''$, with exception of the datacube for NGC 4051 that covers the inner $\sim 3'' \times 4''$, via spatial dithering during the observations (Riffel et al. 2008).

The median value of the signal-to-noise ratio (S/N) in the continuum of our sample ranges from 10 to 30, with the maxi-

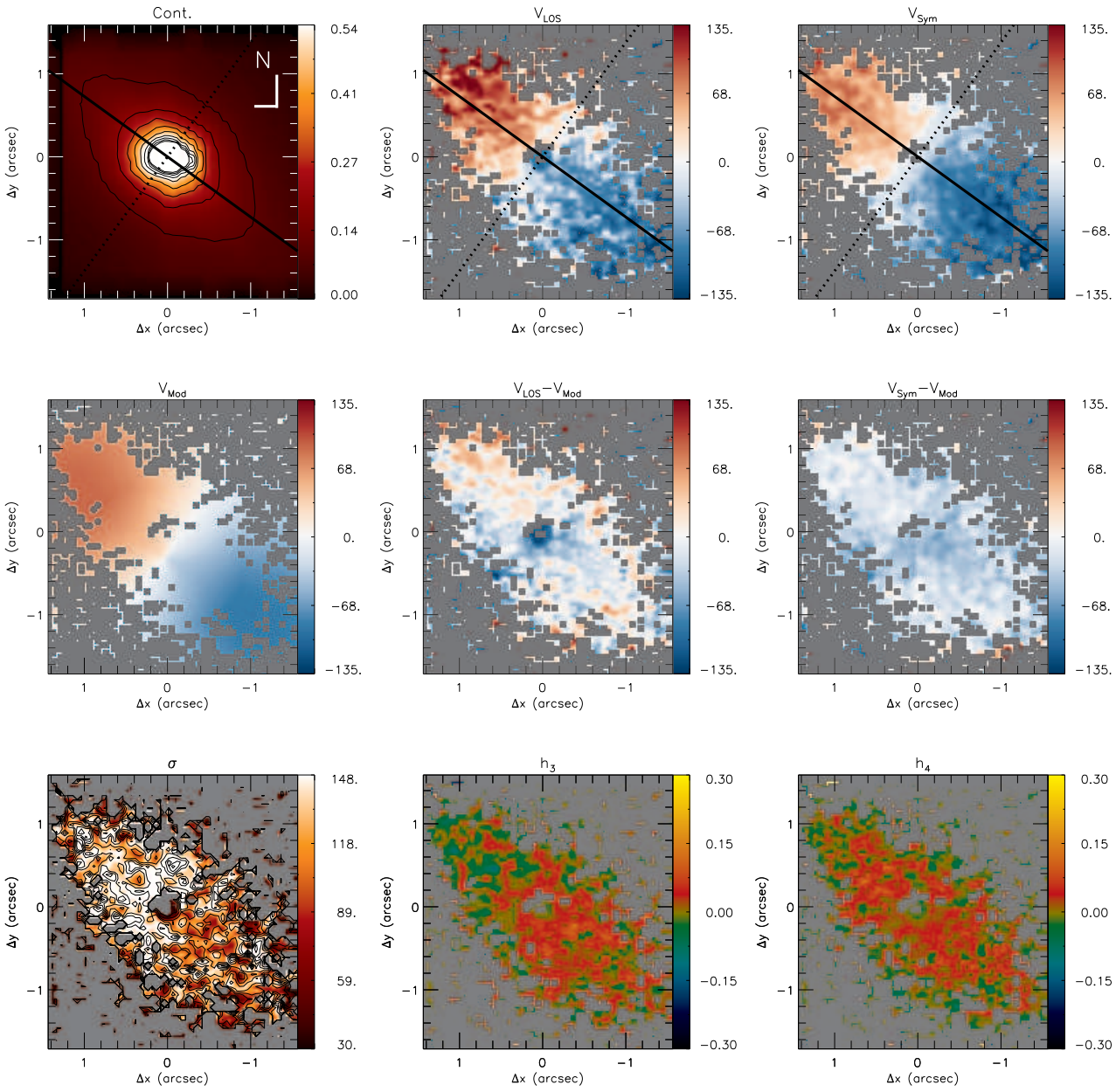

Figure 6. Same as Fig. 2 for NGC 4235.

mum value of up to S/N∼100 observed for the nuclear spectrum of NGC 4051. The median value of the S/N for the ^{12}CO (2-0) band-head at 2.29 μm is larger than 3 for all galaxies of the sample.

Detailed descriptions of the observations and data reduction procedures for the galaxies already analyzed are presented in Riffel, Storchi-Bergmann & Nagar (2010) for Mrk 1066, Riffel & Storchi-Bergmann (2011b) for Mrk 1157, Diniz et al. (2015) for NGC 2110 and Riffel et al. (2008) for NGC 4051. For the remaining objects a more detailed discussion will be presented in a forthcoming paper (Riffel et al., in preparation).

3 SPECTRAL FITTING

The stellar line-of-sight velocity distribution (LOSVD) of each galaxy was obtained by fitting the spectra within the spectral range ∼2.26–2.40 μm (rest wavelengths), which includes the CO absorption band-heads from ∼2.29 to ∼2.40 μm (Winge, Riffel & Storchi-Bergmann 2009), usually among of the strongest absorption lines in the central region of galaxies (e.g. Riffel, Rodríguez-Ardila & Pastoriza 2006; Riffel et al. 2015c). The used spectral range also includes weaker absorption lines from Mg I and Ca I at 2.26–2.28 μm. The spectra were fitted by using the penalized Pixel-Fitting PPXF method (Cappellari & Emsellem 2004), that finds the best fit to a galaxy spectrum by convolving

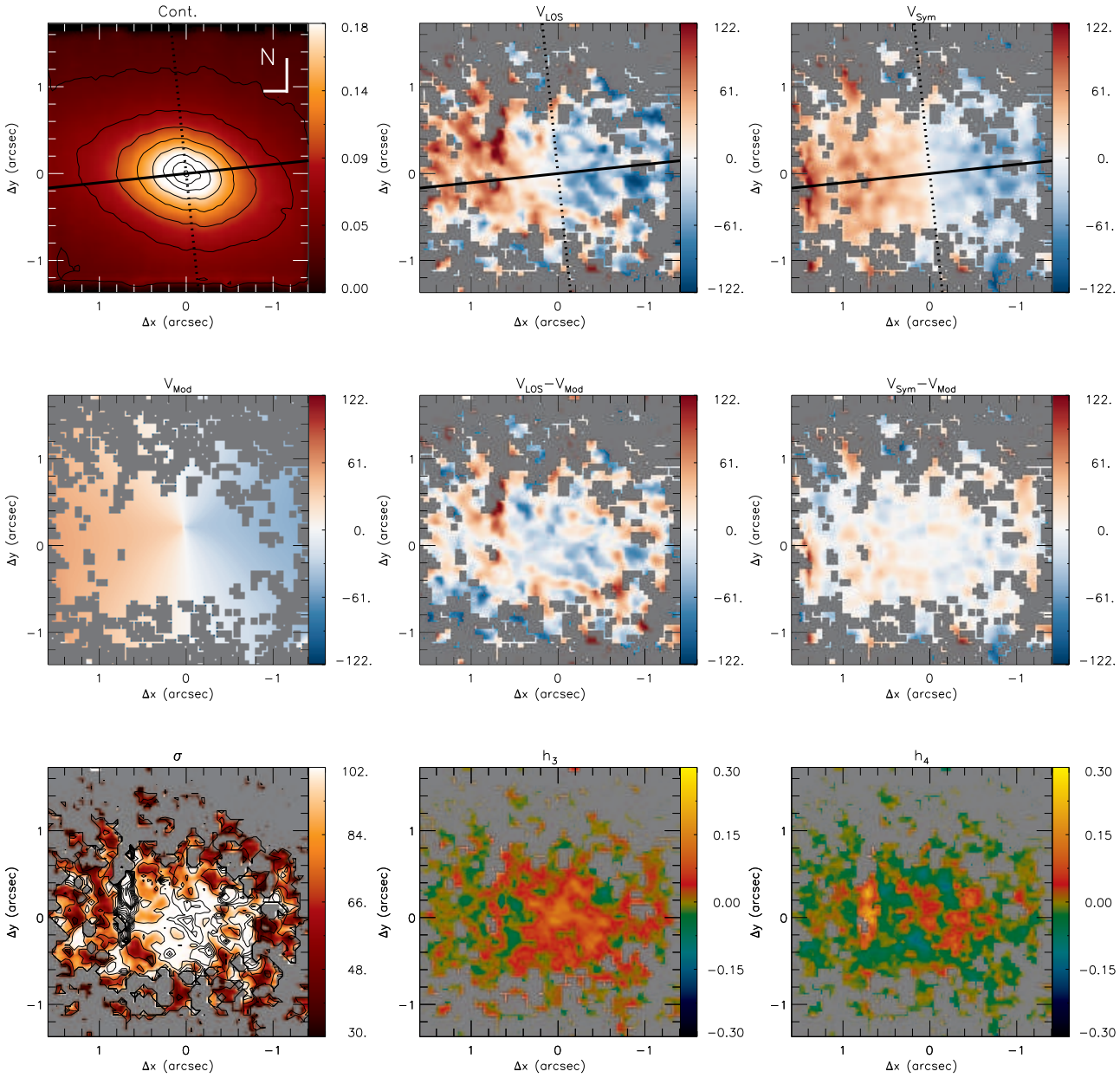

Figure 7. Same as Fig. 2 for NGC 4388.

stellar spectra templates with a given LOSVD, under the assumption that it is reproduced by Gauss-Hermite series.

The PPXF code requires the use of spectral templates that are used to reproduce the galaxy's spectrum. We used the spectra of the Gemini library of late spectral type stars observed with the Gemini Near-Infrared Spectrograph (GNIRS) IFU and NIFS (Winge, Riffel & Storchi-Bergmann 2009) as stellar templates. The spectral resolution of the stellar library is very similar to that of the spectra of the galaxies of our sample and the library includes stars with spectral types from F7 to M5, minimizing the template mismatch problem.

The spectral range used in the fit includes the [Ca VIII]λ2.321 μm emission line, which "contaminates" the (3-1)^{12}CO bandhead and affects the stellar kinematics measurements (Davies et al. 2006; Riffel et al. 2008). The [Ca VIII] is seen at the nucleus and close vicinity, being unresolved for most galaxies of our sample and we have excluded its spectral region from the fit when the line is present. In addition, we used the *clean* parameter of PPXF to reject all spectral pixels deviating more than 3σ from the best fit, in order to exclude possible remaining sky lines and spurious features.

In Figure 1 we present examples of typical fits for the galaxies NGC 1052, NGC 788 and NGC 5899. The left panels show the fits for the nuclear spectrum, while extra-nuclear spectra are shown at the right panels, extracted at 0.″5 south of the nucleus – chosen to represent typical extra-nuclear spectra. The observed

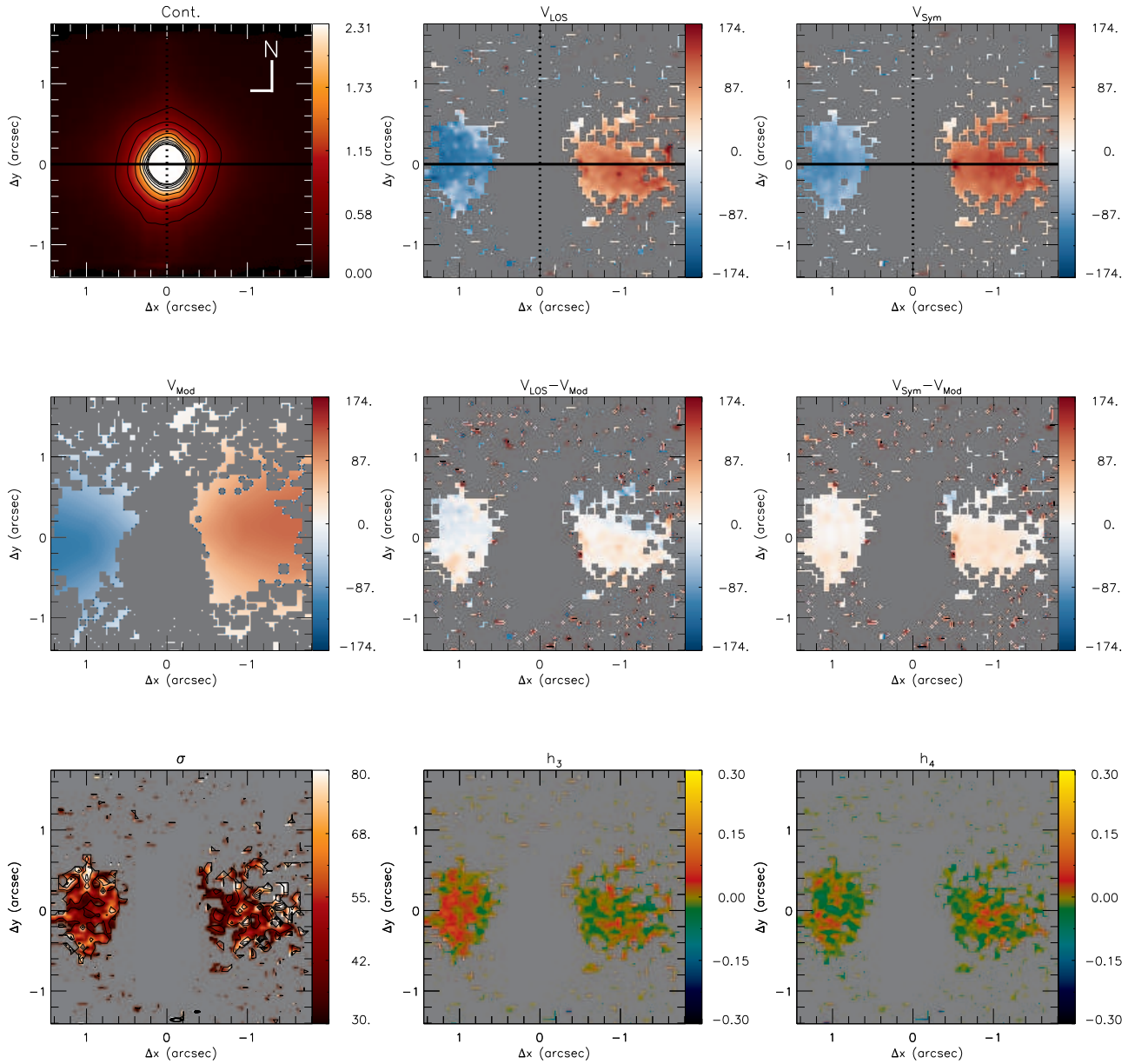

Figure 8. Same as Fig. 2 for NGC 5506.

spectra are shown as black dotted lines, the fits are shown in red and the regions masked during the fits, following the criteria explained above, are shown in green. As can be seen for NGC 788, the cleaning procedure properly excluded the region affected by the [Ca VIII]λ2.321 μm emission line, as well as spurious features. For all galaxies, the standard deviations of the residuals (observed – model) are similar to that of the galaxy spectra derived within a 200 Å spectral window, blue-ward to the first CO absorption bandhead, meaning that the spectra are well reproduced by the models.

The PPXF code returns as output, measurements for the radial velocity (V_{LOS}), stellar velocity dispersion (σ), and higher order Gauss-Hermite moments (h_3 and h_4) for each spatial position, as well as their associated uncertainties. Using the results of the fit, we have constructed two-dimensional maps for each fitted parameter (V_{LOS}, σ, h_3 and h_4), which are presented in the next section.

4 STELLAR KINEMATICS

Figures 2–12 show the resulting maps for the stellar kinematics of our sample. The stellar kinematics for NGC 4051, NGC 2110, NGC 5929, Mrk 1066 and Mrk 1157 was already discussed in previous works by our group (see references in Table 1). Thus, we present the corresponding maps for these galaxies in Figures A1–A5 of the Appendix A, to be published on-line only.

In order to characterize the LOS velocity fields, we have sym-

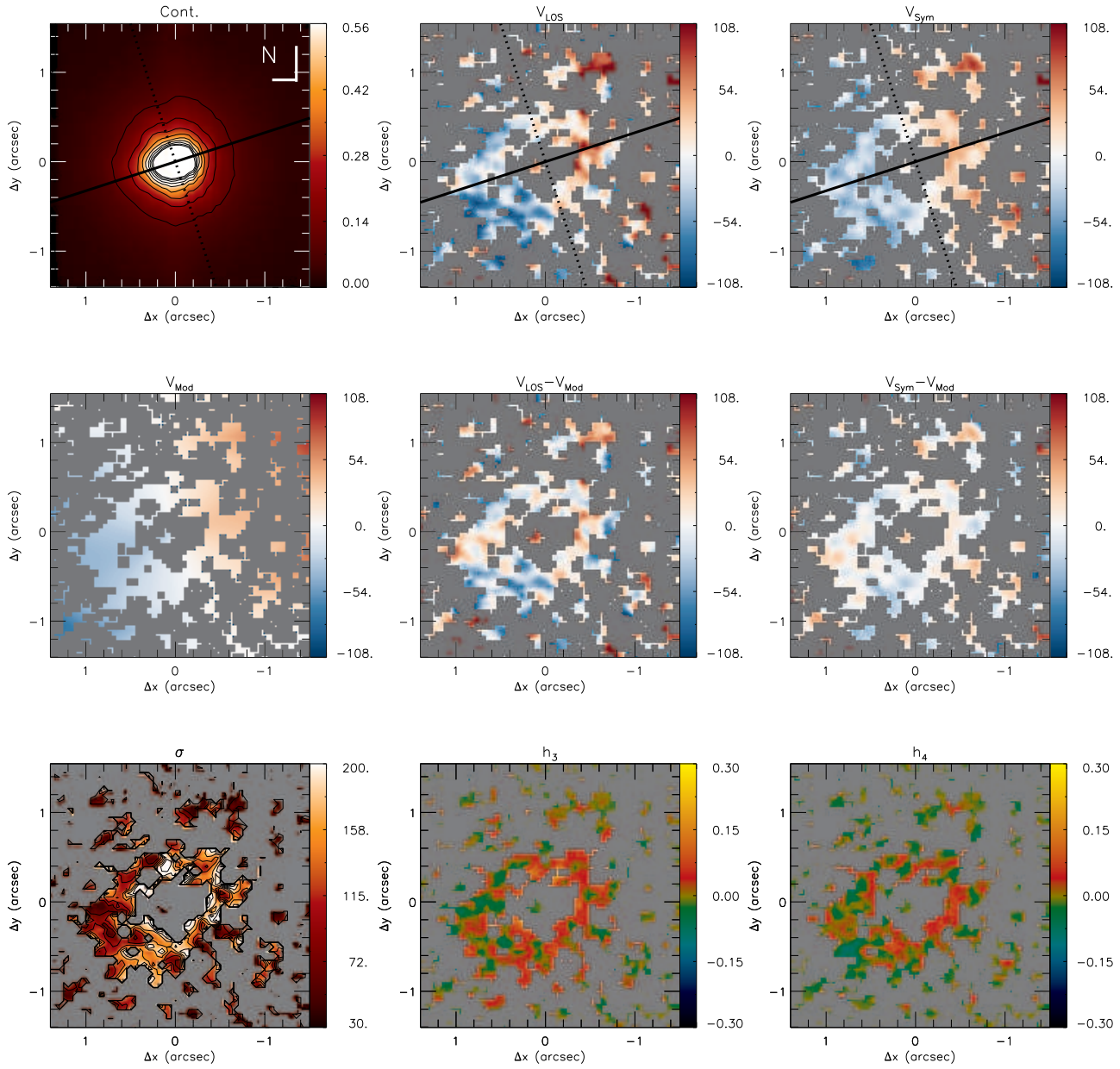

Figure 9. Same as Fig. 2 for NGC 5548.

metrized the stellar velocity field, using the *fit_kinematic_pa*[1] routine. This routine measures the global kinematic position-angle and systemic velocity of the galaxy from integral field observations of the galaxy's kinematics. The method is described in Krajnović et al. (2006). Cappellari et al. (2007) and Krajnović et al. (2011) show examples of application of the method to study the large-scale stellar kinematics of large sample of galaxies of the SAURON and ATLAS^{3D} surveys.

In addition, we fitted the LOS velocity fields by a rotating disk model. The model was obtained using the DiskFit routine (Sellwood & Spekkens 2015; Sellwood & Sánchez 2010; Spekkens & Sellwood 2007; Reese et al. 2007; Barnes & Sellwood 2003; Kuzio de Naray et al. 2012) to fit the symmetrized velocity fields. This code fits non-parametric kinematic models to a given velocity field allowing the inclusion of circular and non-circular motions in a thin disk. Examples of application of this code for the gas and stellar kinematics of the inner region of active galaxies are shown in Fischer et al. (2015) and Riffel et al. (2015a), respectively. We fitted the symmetrized velocity field, instead of the observed one, as the rotating disk model is expected to be symmetric and small fluctuations in velocity due to higher uncertainties at some locations would result in a worse model for the stellar kine-

[1] This routine was developed by M. Cappellari and is available at http://www-astro.physics.ox.ac.uk/ mxc/software

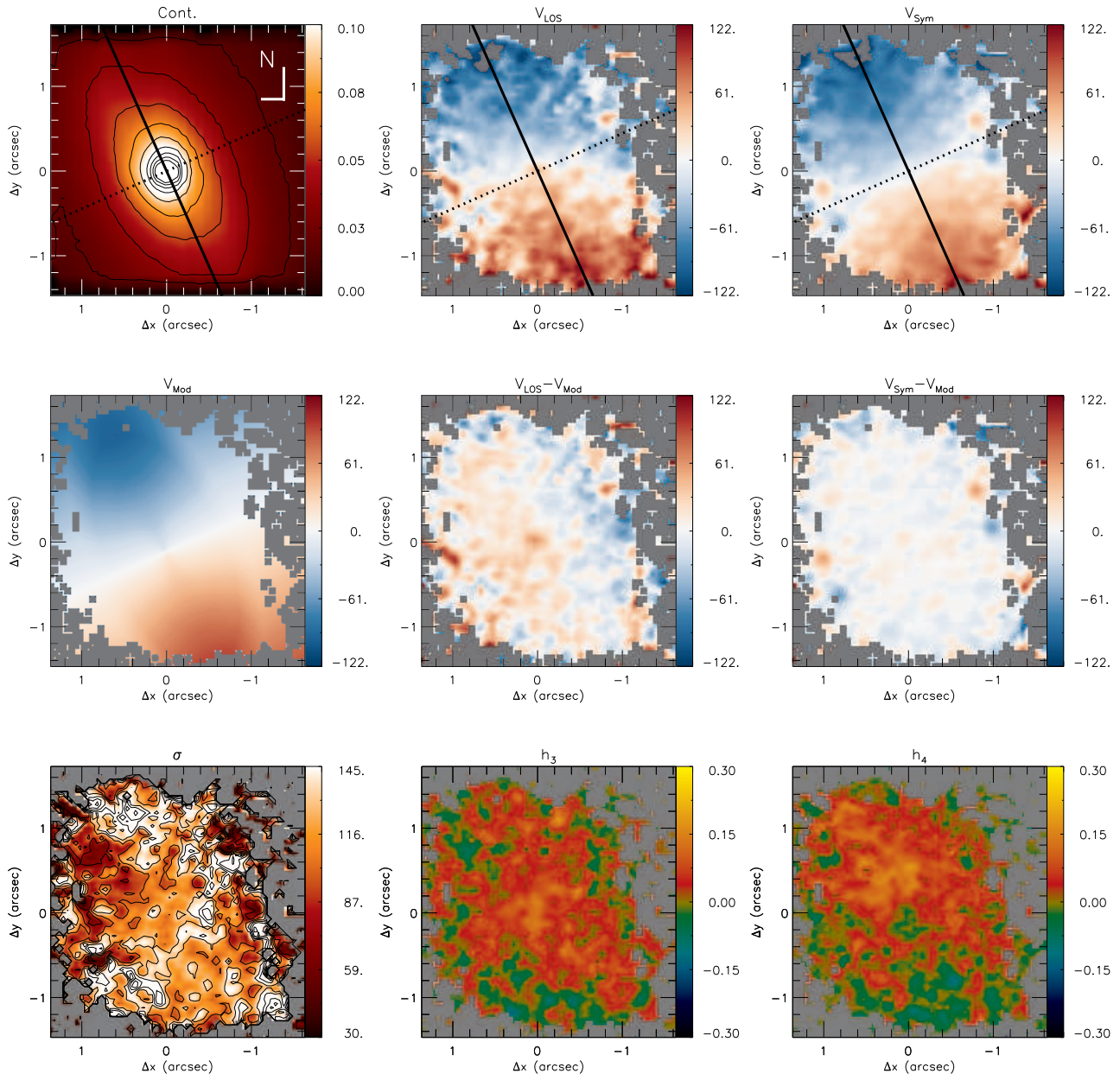

Figure 10. Same as Fig. 2 for NGC 5899.

matics. During the fit, we have fixed the kinematical center to the position of the peak of the continuum emission and the systemic velocity and orientation of the line of nodes of the galaxy were fixed as the values obtained from the symmetrization of the velocity field, in order to reduce the number of parameters to be fitted. The ellipticity and disk inclination were allowed to vary during the fit and the resulting fitted values for each galaxy are shown in Table 2.

Figures 2–12 are organized as follows:

- Top-left panel: K-band image, obtained as the average flux between 2.20 and 2.30 μm. The continuous line shows the orientation of the kinematic major axis and the dotted line shows the orientation of the minor axis of the galaxy, obtained from the symmetrization of the stellar velocity field. The color bar shows the flux scale in units of 10^{-17} erg s^{-1} cm^{-2} Å^{-1}.
- Top-center panel: Measured LOS stellar velocity field obtained from the fit of the spectra using the PPXF routine (Cappellari & Emsellem 2004), following the procedure described in Section 3.
- Top-right panel: Symmetrized velocity field. The color bar is shown in units of km s^{-1} and the systemic velocity of the galaxy was subtracted.
- Middle-left panel: Rotating disk model, obtained by fitting the symmetrized velocity field.
- Middle-center panel: Residual map obtained by subtracting the rotating disk model from the observed velocity field.

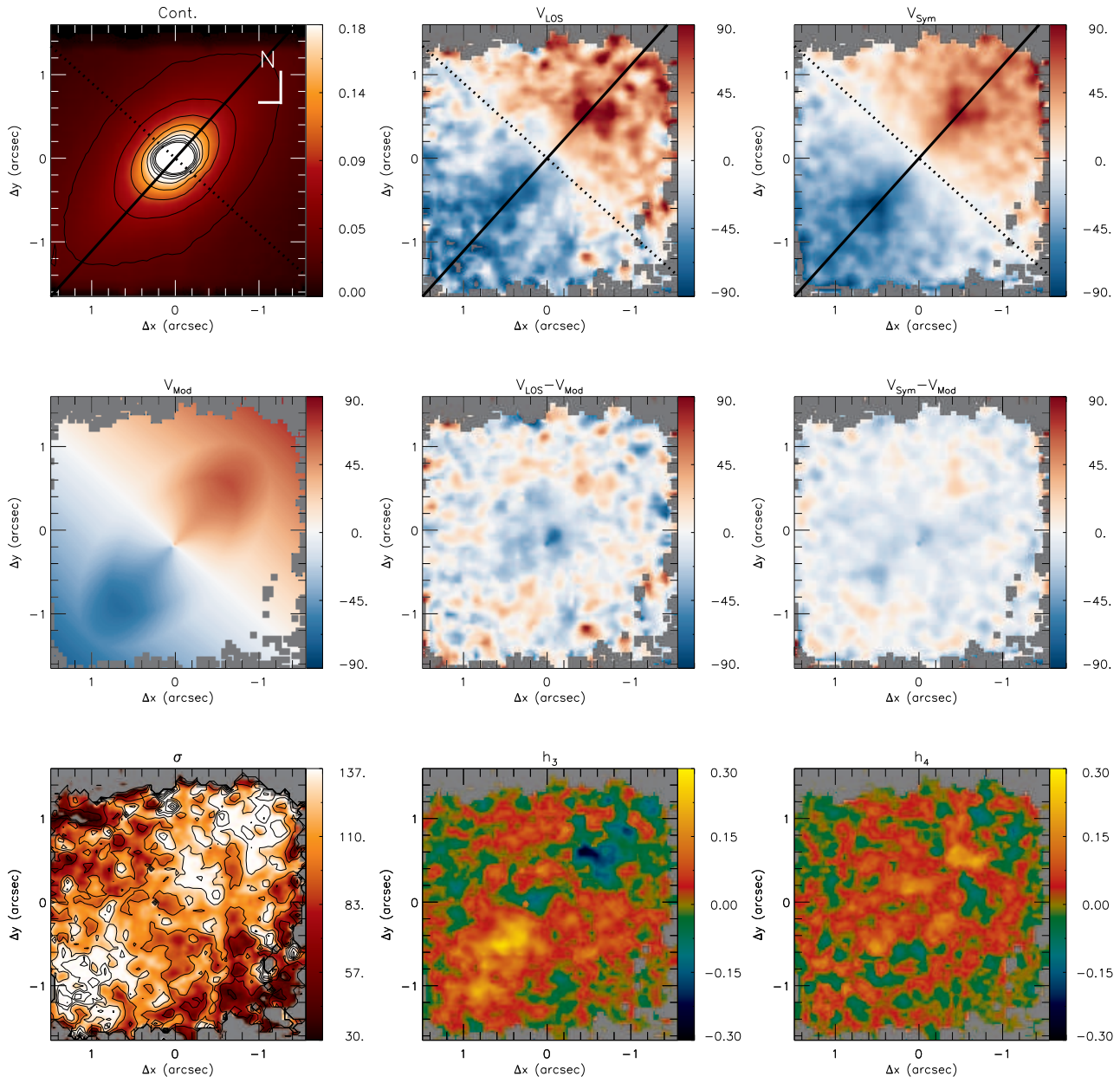

Figure 11. Same as Fig. 2 for Mrk 607.

• Middle-right panel: Residual map obtained by subtracting the rotating disk model from the symmetrized velocity field, constructed in order to verify if the velocity field is well reproduced by the model.

• Bottom-left panel: Stellar velocity dispersion (σ) map. The color bar shows the σ in km s^{-1} units.

• Bottom-center panel: map for the h_3 Gauss-Hermite moment. The h_3 moment measures asymmetric deviations of the LOSVD from a Gaussian velocity distribution (van der Marel & Franx 1993; Gerhard 1993; Riffel 2010). High (positive) h_3 values correspond to the presence of red wings in the LOSVD while low (negative) h_3 values correspond to the presence of blue wings.

• Bottom-right panel: map for the h_4 Gauss-Hermite moment, that measures symmetric deviations of the LOSVD relative to a Gaussian velocity distribution. High (positive) h_4 values indicate LOSVD is more "pointy" than a Gaussian, while low (negative) h_4 values indicate profiles more "boxy" than a Gaussian.

In all figures, North is up and East to the left and the gray regions represent masked locations. In these regions it was not possible to obtain good fits due to low signal-to-noise ratio of the spectra or due to the non detection of absorption lines (e.g. due to the dilution of the absorption lines by strong AGN continuum emission). The masked regions correspond to locations where the uncertainty in velocity or velocity dispersion is higher than 30 km s^{-1}, while for most other locations the uncertainties are smaller than 15 km s^{-1}.

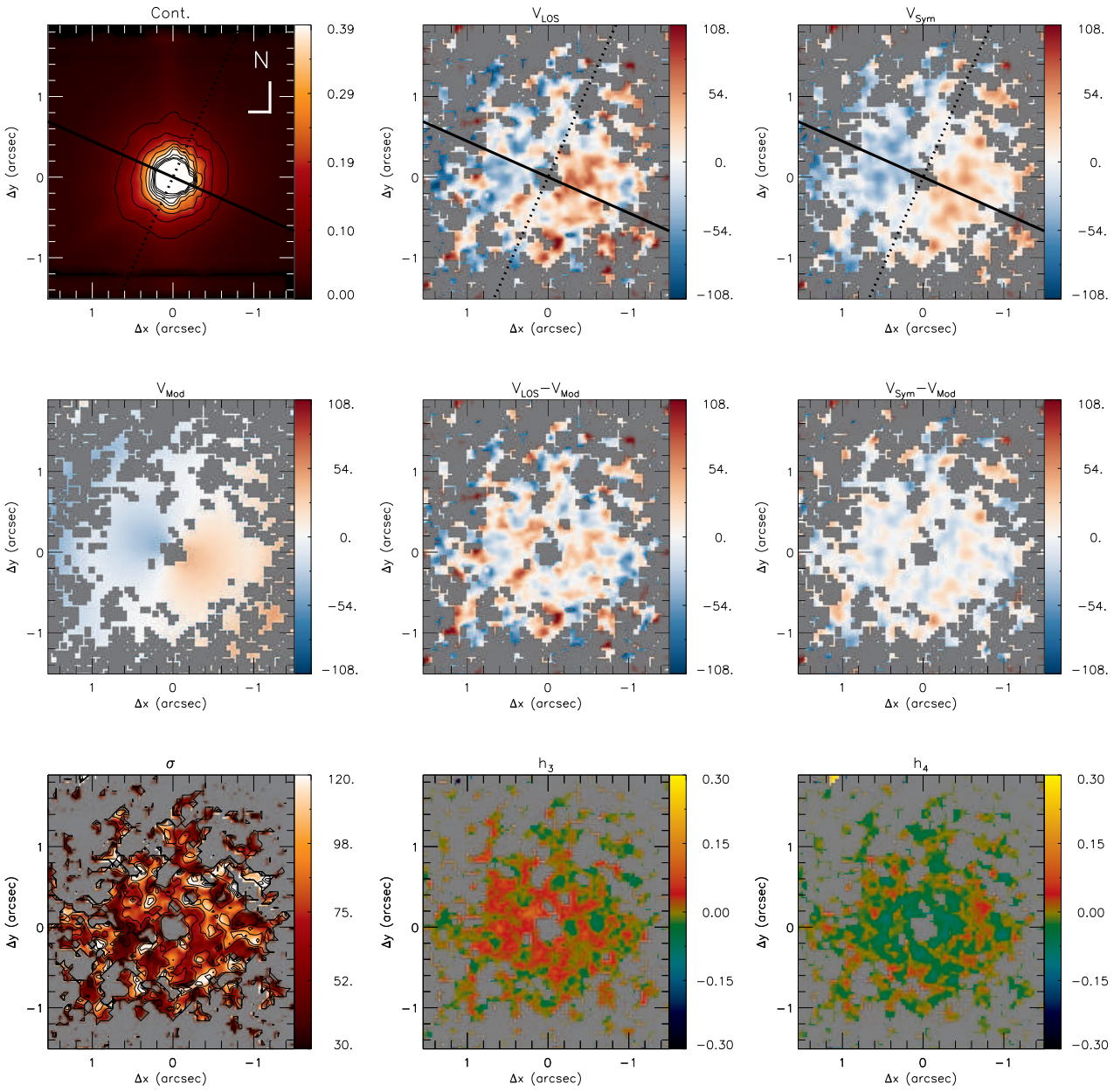

Figure 12. Same as Fig. 2 for Mrk 766.

A rotating disk pattern is recognized in the LOS velocity field for all galaxies, with a straight zero velocity line for most of them. For two galaxies – Mrk 1066 (Riffel & Storchi-Bergmann 2011a) and NGC 5899 (Fig. 10) – an *S* shape zero velocity line is observed, which is a signature of the presence of a nuclear bar or spiral arms in these galaxies (e.g. Combes et al. 1995; Emsellem et al. 2006). For most galaxies, the maximum amplitude of the rotation curve is expected to be observed outside of the NIFS FoV. The rotation disk signature is clearly seen in the one one-dimensional plots shown in Fig. B1, obtained by averaging the velocity and σ values within a pseudo-slit with width of 0.″25 oriented along the major axis of the galaxy. The deprojected velocity amplitude within the NIFS FoV ranges from $\sim$ 50 to $\sim$300 km s^{-1}.

For 5 galaxies, the maximum σ value is smaller than 100 km s^{-1}, 7 have maximum σ in the range 100–150 km s^{-1} and 4 show the maximum $\sigma > 150$ km s^{-1}. In addition, distinct structures of low-σ values ($\sim$50-80 km s^{-1}) are seen in the the maps: low$-\sigma$ rings or partial rings are seen for Mrk 1066, Mrk 1157, NGC 5929 and NGC 788. These rings have been identified by visual inspection and are marked in the corresponding σ maps as green ellipses. In all cases the size of the structures is larger than the spatial resolution and the σ decrease is larger than the velocity resolution of the data. These structures have been attributed to intermediate-age stellar populations (ages in the range 100-700 Myr; e.g. Riffel et al. 2010, 2011), with origin in kinematically colder regions that still preserve the kinematics of the

gas from which they have been formed. Patches of low-σ are seen for Mrk 607, NGC 2110, NGC 3516, NGC 4051, NGC 4235 and NGC 5899, while three objects (NGC 1052, NGC 3227 and NGC 4388) show a centrally peaked σ distribution. These rings and partial rings are located at distances from the nucleus ranging between 150 and 250 pc. Nuclear σ values for each galaxy are presented in the last column of Table 2, obtained by fitting the nuclear spectrum integrated within a circular aperture with radius of 75 pc.

Most galaxies show low h_3 values ($-0.10< h_3 <0.10$), suggesting that their LOSVDs are well represented by a Gaussian velocity distribution. Exceptions are Mrk 607, Mrk1066 and NGC 4051 that show h_3 values larger than 0.15. For 8 galaxies (NGC 1052, NGC 2110, NGC 3227, NGC 3516, NGC 4051, NGC 5506, Mrk 607 and Mrk 1066), the h_3 map is anti-correlated with the velocity field, with positive h_3 values seen at locations where rotation velocities are observed in blueshifts and negative h_3 values associated to regions where the rotation velocities are observed in redshifts. A similar trend (but not so clear) is observed for other four galaxies (NGC 4235, NGC 4388, NGC 5929 and Mrk 1157). In Fig. B2 of the Appendix B we present plots of the LOS velocity vs. h_3 for all galaxies, which show this anti-correlation clearly. The anti-correlation seen between h_3 and the LOS velocity can be interpreted as due do the contribution of stars rotating slower than those in the galaxy disk, probably due to motion in the galaxy bulge (e.g. Emsellem et al. 2006; Ricci, Steiner & Menezes 2016).

The h_4 moment maps show small values at most locations for all galaxies, with $-0.05 < h_4 < 0.05$. For some galaxies, that present strong low-σ structures (e.g., Mrk 1066, Mrk 607 and NGC 4051), higher positive h_4 values are observed co-spatial with the low-σ regions. This is also seen in the plots presented in Fig. B2, that show a trend of higher values of σ being observed in regions with negative h_4 values, while small σ values being associated to positive h_4 values. We interpret this correlation between low-σ and high h_4 values as an additional support to the presence of young/intermediate age stars at these locations, as more peaked velocity distributions are expected for young stars (as they are located in a thin disk structure).

The rotating disk models reproduce well the observed velocity fields for all galaxies, as seen in the residual velocity maps that show values smaller than 20 km s^{-1} at most locations. Table 2 shows the model parameters for each galaxy. The systemic velocities from the table are relative to the heliocentric frame. The deprojected velocity amplitude of the galaxies of our sample ranges from ~60 km s^{-1} (for NGC 4051 - a Sc galaxy) to ~340 km s^{-1}(for NGC 3516 - a S0 galaxy).

5 DISCUSSIONS

5.1 Comparison between kinematic and large scale disk parameters

Table 2 shows the parameters derived from the symmetrization (using the FitKinematicPA routine) and from the fit of the rotation disk model (using the DiskFit code) of the velocity fields. These parameters can be compared to those obtained for the large scale disks. The position angle (PA) of the major axis from NED[2] (Ψ_{0NED}), shown in Table 2 is derived from the K_S band photometry obtained from the Two Micron All Sky Survey (2MASS, Jarrett et al. 2003). The ellipticity (e_{NED}) and inclination (i_{NED}) of the disk are also obtained from the apparent major (a) and minor (b) axis available on NED database from K_S images, as $e_{NED} = 1 - \frac{b}{a}$ and i_{NED} = acos(b/a), respectively.

In the left panel of Figure 13 we present a plot of the large scale photometric PA of the major axis *versus* the kinematic PA derived from our NIFS velocity fields, constructed using the values of Ψ_0 shown in Table 2. This plot shows that the small scale kinematic PA is in approximate agreement with the large scale photometric one. The mean PA offset is $< \Psi_0 - \Psi_{0NED} >= 3.9° \pm 5.7°$. Only for three galaxies (NGC 5548, Mrk 766 and NGC 3516) there are significant discrepancies between small scale kinematic and large scale photometric major axes. NGC 5548 and Mrk 766 are almost face on galaxies and thus it is hard to obtain a precise determination of Ψ_0, both from photometry and kinematics, justifying the discrepancy. For NGC 3516 the Ψ_{0NED} is distinct from that observed in optical images ($\Psi_0 = 56°$, Schmitt & Kinney 2000) and from the stellar kinematics based on optical IFS ($\Psi_0 = 53°$, Arribas et al. 1993). On the other hand, the Ψ_{0NED} for NGC 3516 is very similar to the orientation of the bar of the galaxy ($\Psi_0 = -10°$, Veilleux et al. 1993) and thus the value of Ψ_{0NED} may be biased due to the bar, that is stronger in near-IR bands.

Previous studies have found similar results. For example, the morphological study by Malkan, Gorjian& Tam (1998) of the inner kiloparsecs of nearby active galaxies showed that the resulting classification of the small scale structure was very similar to the one given in the Third Reference Catalog (RC3, Corwin, Buta & de Vaucouleurs 1994), showing that not only the kinematic PA at small scale but also the photometric PA at small scale is similar to that at large scale.

Barbosa et al. (2006) used the Gemini Multi-Object Spectrograph (GMOS) IFU to map the stellar kinematics of the inner 200–900 pc of six nearby active galaxies by fitting the stellar absorption lines of the Calcium triplet around 8500Å and also found that the kinematic position angle at small scale is in good agreement with the large scale photometric measurements. Dumas et al. (2007) used optical IFS to map the stellar and gas kinematics of the central kiloparsec of a matched sample of nearby Seyfert and inactive galaxies at angular resolutions ranging from 0.″9 to 2.″5, using the SAURON IFU on the William Herschel Telescope. They found that the orientations of the kinematic line of nodes are very similar with those derived from large scale photometry for both active and inactive galaxies. Falcón-Barroso et al. (2006) present the stellar kinematics of a sample of 24 spiral galaxies using the SAURON IFU. Their sample includes only 5 active nuclei and they found misaligned photometric and kinematic axes for 9 objects in their sample (only one being an active galaxy), interpreted as being due to non-axisymmetric structures (as bars) and more easily detected at low galaxy inclinations.

The middle and right panels of Figure 13 show the comparison between the large photometric (y-axis) and small kinematic (x-axis) scale disk inclination and ellipticity, respectively. In contrast to the orientation of the major axis of the galaxy, these parameters do not follow the same distribution at small and large scale. For most cases, both the inclination and the ellipticity of the disk at large scale are larger than that derived for the inner 3″×3″. This result can be interpreted as being due to the fact that the large scale measurements are dominated by the disk component as they are estimated from the apparent major and minor axis measurements obtained from large scale K_S images, while at small scale, the near-IR emission is dominated by emission from evolved red stars at the

[2] NASA/IPAC Extragalactic Database available at *http : //ned.ipac.caltech.edu/*

Table 2. Kinematic parameters obtained by symmetrize the stellar velocity. Col. 1: Galaxy name; cols 2-3: systemic velocity (V_s) corrected for the heliocentric frame and orientation of the line of nodes (Ψ_0) derived from the symmetrization of the velocity fields; cols 4-5: disk ellipticity (e) and inclination (i) derived by modeling the velocity field using the DiskFit routine; cols: 6-8: orientation of the major axis, ellipticity and inclination of the large scale disk, as available at NED; col 9: the nuclear stellar velocity dispersion measured within a circular aperture with 150 pc diameter.

	FitKinematicPA		DiskFit		Large Scale Disk			
Galaxy	V_s (km s^{-1})	$\Psi_0(^\circ)$	e	$i(^\circ)$	$\Psi_{0NED}(^\circ)$	e_{NED}	$i_{NED}(^\circ)$	σ(km s^{-1})
NGC788	4034	120±3	0.07±0.01	20.8±0.2	100	0.67	42.3	187±4
NGC1052	1442	114±3	0.32±0.01	47.5±0.2	120	0.71	45.6	245±4
NGC2110	2335	156±3	0.26±0.01	42.5±0.3	160	0.63	38.7	238±5
NGC3227	1174	156±3	0.30±0.01	45.4±0.2	152	0.88	62.0	130±7
NGC3516	2631	54±3	0.05±0.01	18.2±0.8	7	0.69	43.9	186±3
NGC4051	717	130±9	0.20±0.01	37.3±0.9	142	0.84	56.6	72±3
NGC4235	2276	54±3	0.25±0.01	41.2±0.5	50	0.94	70.1	183±12
NGC4388	2537	96±3	0.11±0.01	27.7±0.3	89	0.95	71.3	106±6
NGC5506	1878	96±3	0.48±0.01	58.7±0.3	90	0.97	76.1	-
NGC5548	5128	108±3	0.51±0.04	60.9±6.8	60	0.34	19.9	276±22
NGC5899	2616	24±3	0.54±0.01	62.7±0.3	25	0.92	67.7	147±9
NGC5929	2491	30±9	0.51±0.01	60.7±0.5	38	0.69	43.9	134±5
MRK607	2781	138±3	0.47±0.01	58.2±0.1	135	0.94	70.1	132±4
MRK766	3855	66±3	0.05±0.02	18.2±3.7	110	0.77	50.2	78±6
MRK1066	3583	120±3	0.36±0.01	50.2±0.3	140	0.92	66.4	103±4
MRK1157	4483	114±3	0.29±0.01	45.1±0.9	95	0.88	61.3	92±4

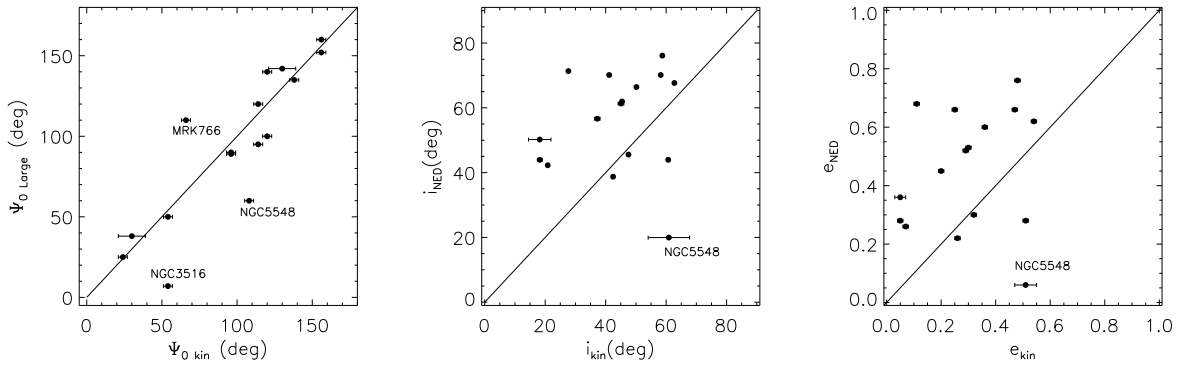

Figure 13. Comparison of large scale photometric (y-axis) and small scale kinematic (x-axis) PAs (left), inclination (middle) and ellipticity (right). Continuous lines show one-to-one relations.

bulge of the galaxy (e.g. Maraston 2005; Riffel et al. 2015c), which play an important role in the observed morphology and kinematics observed with NIFS.

5.2 Gravitational potentials and comparison with previous studies

The velocity residual maps for all galaxies of our sample show small values, indicating that the stellar velocity fields are well reproduced by the rotating disk model, with kinematic axes that follows the same orientation of large scale measurements. In addition, the deprojected rotation velocity amplitude is always larger than the mean velocity dispersion, indicating the the stellar kinematics of the galaxies of our sample are dominated by regular rotation. We can compare our results with previous studies of the stellar kinematics of active and inactive galaxies.

Dumas et al. (2007) present the stellar kinematics of a sample of 39 active galaxies and a matched control sample, selected to have similar blue magnitudes, Hubble type and inclinations. They found that the stellar kinematics of both active and inactive galaxies show regular rotation patterns typical of disc-like systems. A similar result was found by Barbosa et al. (2006) using higher angular resolution (<1.″0) IFS with Gemini Telescopes of a sample of six nearby Seyfert galaxies. In addition, they found partial rings of low-σ values at 200–400 pc from the nucleus for three galaxies, interpreted as tracers of recently formed stars that partially keep the cold kinematics of the original gas from which they have formed. Falcón-Barroso et al. (2006) present kinematic maps for a sample of nearby spiral galaxies obtained with the SAURON IFU, which show regular stellar rotation for most galaxies. However, kinematic decoupled components are frequently seen in the inner region, as sudden changes in the velocity field, which are often associated with a drop in the σ and anti-correlated h_3 values with respect to the V_{LOS}. In addition, they found kinematic signatures of non-axisymmetric structures for 37% of the galaxies of their sample (only one harboring an AGN). For 20 % of their sample (5 galaxies,

none of them harboring an AGN) they found kinematic signatures of bars as predicted in N-body simulations of barred potentials (e.g. Kuijken & Merrifield 1995; Bureau & Athanassoula 2005).

Hubble Space Telescope (HST) H-band images up to 10″ radius and ground-based near-infrared and optical images of a matched Seyfert versus non-Seyfert galaxy sample of 112 nearby galaxies show a statistically significant excess of bars among the Seyfert galaxies at practically all length-scales (Laine et al. 2002). In addition, they also found that Seyfert galaxies always show a preponderance of "thick" bars compared to the bars in non-Seyfert galaxies. On the other hand, recent results show that AGN hosts at $0.2 < z < 1.0$ show no statistically significant enhancement in bar fraction compared to inactive galaxies (e.g Cheung et al. 2015). Large scale bars are seen for 28.5% of face-on spiral hosts of AGN, as obtained from the study of more the 6.000 AGN hosts of from the Sloan Digital Sky Survey (SDSS; Alonso, Coldwell & Lambas 2013).

Our kinematic maps suggest the presence of nuclear bars in only 2 galaxies: Mrk 1066 and NGC 5899, as revealed by the presence of an S shape zero velocity line observed in the V_{LOS} maps (e.g. Combes et al. 1995; Emsellem et al. 2006). This corresponds to only 12.5% of our sample, although the statistics is low so far and this result is preliminary. The rest of the galaxies are dominated by rotation. The difference in the proportion of barred galaxies or non-axisymmetric structures in our study relative to that of Falcón-Barroso et al. (2006) may be due to the small number of objects in both studies, and to the difference in the field-of-view (FoV) of the two studies. Our FoV ($3'' \times 3''$) is smaller than those of previous studies, making it more difficult to identify kinematic signatures of bars as predicted in N-body simulations (e.g. Bureau & Athanassoula 2005), as double-hump rotation curves, broad σ profiles with a plateau at moderate radii and $h_3 - V_{LOS}$ correlation over the projected bar length. On the other hand, the photometric detection of bars mentioned above are mainly obtained using large scale images. Thus, our results suggest that the motion of the stars is dominated by the gravitational potential of the bulge, as the FoV of our observations is smaller than the bulge length for all galaxies.

In order to further investigate how the galactic potentials and deviations from ordered rotation are related to the host galaxy and AGN, we plotted the mean value of the modulus of the residual velocities ($< |V_{res}| >$), where $V_{res} = V_{LOS} - V_{mod}$, against the Hubble index and hard X-ray (14-195 keV) luminosity (L_X) from the Swift-BAT 60-month catalogue (Ajello et al. 2012), which measures direct emission from the AGN. These plots are shown in Figure 14. For four galaxies of our sample (MRK1066, MRK1157, MRK607 and NGC5929), there are no X-ray luminosities available in the BAT catalogue and thus the $< |V_{res}| >$ vs. plot contains only 12 points. The $< |V_{res}| >$ was estimated as the mean value of 10.000 bootstrap realizations in which for each interaction the $|V_{res}|$ is calculated for a sample selected randomly among the values observed in the residual map. The standard deviation in the simulated $|V_{res}|$ represents the intrinsic scatter of each residual map and is used as the uncertainty for $< |V_{res}| >$.

The top panel of Fig. 14 shows that there is no correlation between $< |V_{res}| >$ and Hubble index, with a Pearson correlation coefficient of only $R = 0.12$. This result shows that large scale structures do not affect significantly the stellar kinematics of the inner kiloparsec of the galaxies of our sample.

On the other hand, the bottom panel of Fig. 14 suggests that $< |V_{res}| >$ is correlated with L_X. We computed a Pearson correlation coefficient of $R = 0.74$, with less than 1 % of probability that

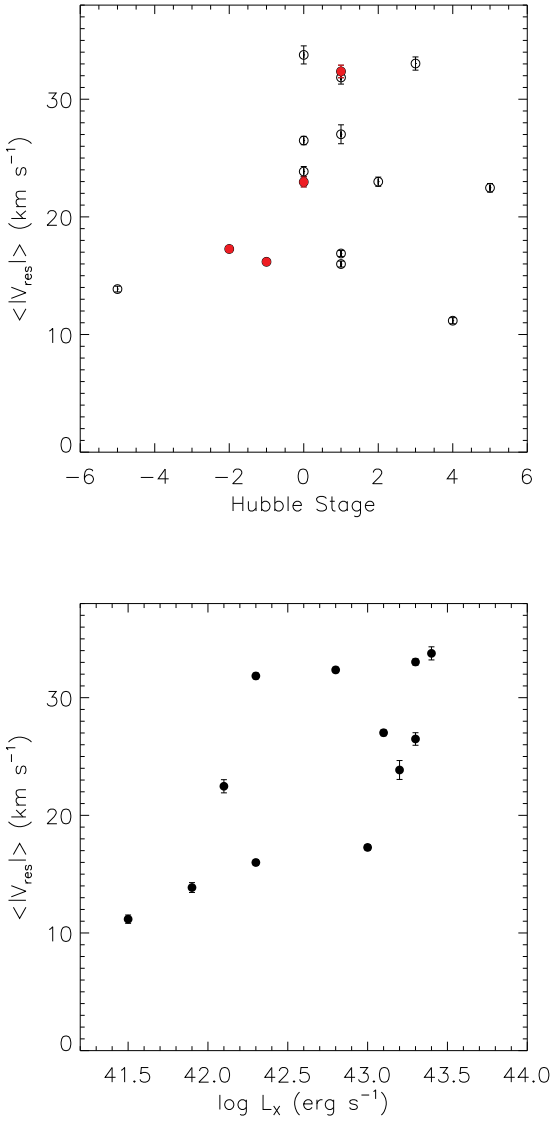

Figure 14. Plots of the standard deviation of the residual maps ($< |V_{res}| >$) vs. Hubble index (top) and X-ray luminosity (L_X, bottom). In the top panel, filled circles correspond to barred galaxies.

this distribution of points can be generated by a random distribution. Although the number of points is small, this trend may mean that more luminous AGN have a larger impact in the surrounding stellar dynamics. As a speculation, we propose that strong AGN may quench circum-nuclear star formation in the galaxy disk and thus the stellar motions have a more important component of bulge star kinematics. On the other hand, for lower luminosity AGNs, the active nuclei may not be powerful enough the quench the star formation and thus the stellar dynamics has a stronger contribution from stars more recently formed in the plane of the galaxy.

5.3 Implications to AGN feeding and star formation

The velocity dispersion maps show structures of lower σ than the surroundings (~50–80 km s^{-1}) for 10 galaxies (62 %)

of our sample. Such velocity dispersion drops are commonly reported in the literature (e.g. Bottema 1989, 1993; Fisher 1997; García-Lorenzo, Mediavilla & Arribas 1999; Emsellem et al. 2001; Márquez et al. 2003; Falcón-Barroso et al. 2006; Barbosa et al. 2006) and have been interpreted as being tracers of relatively recent star formation as compared to the bulge stellar population (e.g. Emsellem et al. 2001, 2006; Márquez et al. 2003; Barbosa et al. 2006; Riffel et al. 2008). Indeed, stellar population synthesis using near-IR IFS with NIFS reveal that the low-σ rings seen in Mrk1066 and Mrk1157 are associated to an intermediate-age stellar population (<700 Myr; Riffel et al. 2010, 2011).

The low-σ structures may be related to accretion of gas to the inner kiloparsec of galaxies as a result of streaming motions towards the nucleus along nuclear bars or dust spirals, observed for several active galaxies by our group (e.g. Fathi et al. 2006; Riffel et al. 2008; Storchi-Bergmann et al. 2009; Riffel et al. 2013; Diniz et al. 2015; Schnorr-Müller et al. 2014, 2016, 2017; Lena et al. 2015) and other groups (e.g. van de Ven & Fathi 2009; Sánchez et al. 2009; Smajić et al. 2015). Several works have been aimed to investigate the presence of nuclear bars and dust spirals in active and inactive galaxies using high resolution HST images (Laine et al. 2002; Pogge & Martini 2002; Simões Lopes et al. 2007; Martini, Dicken & Storchi-Bergmann 2013). These studies reveal an excess of bars in Seyfert galaxies, when compared to a matched sample of inactive galaxies (Laine et al. 2002) and dust structures seem to be present in all early type AGN hosts, while only 26 % of inactive early type show significant dust in the nuclear region (Simões Lopes et al. 2007). For late type galaxies, large amount of dust is observed for both active and inactive galaxies (Simões Lopes et al. 2007).

The observed gas inflows mentioned above can lead to the accumulation of large reservoirs of gas that can feed both star formation and the AGN. In such scenario, it would be expected that low-σ structures should be more frequent in active than in inactive galaxies. However, several studies report the presence of low-σ structures in inactive galaxies. For example, Falcón-Barroso et al. (2006) found that at least 46 % of their sample of spiral galaxies show σ-drops, most of them being inactive. A similar result is reported by Ganda et al. (2006), who found central σ drops for many objects of their sample of 18 spiral galaxies. On the other hand, these drops are not commonly observed in elliptical galaxies (Emsellem et al. 2004). Thus, the presence of low-σ may be related to recent star formation in the inner kiloparsec of the galaxies of our sample, but possibly unrelated to the nuclear activity.

5.4 The stellar kinematics and AGN Feeding and Feedback processes

This paper is the first of a series in which we will investigate the AGN feeding and feedback processes using J and K band NIFS observations of a sample of nearby active galaxies selected using as main criteria the hard X-ray luminosity. The results presented here will be used to compare gas and stellar kinematics in order to isolate non-circular motions, by constructing residual maps between the observed velocity fields for the ionized (traced by [Fe II] and H recombination lines) and molecular (traced by H_2 emission lines) gas and the rotating disk models presented here. The analysis of the residual maps, together with velocity channel maps along the emission-line profiles, will allow us to identify possible gas inflows and outflows. Similar methodology has already been successfully used by our AGNIFS group (e.g. Riffel et al. 2008; Riffel & Storchi-Bergmann 2011a; Riffel et al. 2013; Riffel & Storchi-Bergmann 2011b; Diniz et al. 2015). The gas inflow and outflow rates can be compared with AGN properties (e.g. bolometric luminosity and accretion rate) to draw a picture of the feeding and feedback processes in AGNs.

6 CONCLUSIONS

We used near-IR integral field spectroscopy to map the stellar kinematics of the inner 3″×3″ of a sample of 16 nearby Seyfert galaxies. We present maps for the radial velocity, velocity dispersion and higher order Gauss Hermite moments, obtained by fitting the CO stellar absorptions in the K-band. The observed velocity fields were symmetrized and modeled by a thin rotating disk in order to derive kinematical parameters. The main results of this work are:

- The observed velocity fields for all galaxies show regular rotation. In addition, for two galaxies (Mrk 1066 and NGC 5899) the velocity field shows an *S* shape zero velocity line which is interpreted as a signature of nuclear bars.
- The residuals of the modeling of the stellar velocity field are correlated with the hard X-ray luminosity, suggesting that the nuclear source plays a role on the observed stellar dynamics of the inner kiloparsec of the galaxies, with stronger AGNs showing less ordered stellar orbits than weak AGNs.
- The velocity dispersion maps show low-σ ($\sim$ 50 – 80 km s^{-1}) rings for 4 galaxies (Mrk 1066, Mrk 1157, NGC 5929 and NGC 788) or "patches" of low-σ structures (for Mrk 607, NGC 2110, NGC 3516, NGC 4051, NGC 4235 and NGC 5899) at typical distances of 200 pc, interpreted as being originated in young/intermediate age stellar populations. Centrally peaked σ maps are observed for three galaxies (NGC 1052, NGC 3227 and NGC 4388).
- The h_3 moment is anti-correlated with the velocity field for 8 galaxies (NGC 1052, NGC 2110, NGC 3227, NGC 3516, NGC 4051, NGC 5506, Mrk 607 and Mrk 1066) – positive h_3 values seen at locations where the velocity field shows blueshifts and $h_3 < 0$ for locations where the velocity field shows redshifts. The presence of these wings are attributed to the contribution of stars from the galaxy bulge that present lower rotation velocities.
- The h_4 maps show small values at most locations for all galaxies. For the galaxies with low-σ rings, higher h_4 values are observed co-spatially with the ring, being interpreted as an additional signature of young/intermediate age stars at these locations.
- The observed velocity fields are well reproduced by a rotating disk model, with deprojected velocity amplitudes in the range ~60–340 km s^{-1}.
- The orientations of the line of nodes derived from the small scale velocity fields are similar to the photometric major axis orientations of the large scale disks, while the disk ellipticity and inclination are smaller at small scale, as compared to those at large scale.

The stellar kinematics and rotating disk models derived in this work will be compared to the gas kinematics and flux distributions in future studies with the aim of isolating and quantifying non-circular motions in the gas of the galaxies of our sample in order to map and quantify feeding and feedback processes in our AGN sample.

ACKNOWLEDGMENTS

We thank an anonymous referee for useful suggestions which helped to improve the paper. Based on observations obtained at the Gemini Observatory, which is operated by the Association of Universities for Research in Astronomy, Inc., under a cooperative agreement with the NSF on behalf of the Gemini partnership: the National Science Foundation (United States), the Science and Technology Facilities Council (United Kingdom), the National Research Council (Canada), CONICYT (Chile), the Australian Research Council (Australia), Ministério da Ciência e Tecnologia (Brazil) and south-eastCYT (Argentina).

This research has made use of the NASA/IPAC Extragalactic Database (NED) which is operated by the Jet Propulsion Laboratory, California Institute of Technology, under contract with the National Aeronautics and Space Administration. We acknowledge the usage of the HyperLeda database (http://leda.univ-lyon1.fr). *R.A.R.* and *R. R.* thank to CNPq and FAPERGS for financial support.

REFERENCES

Ajello, M., Alexander, D. M., Greiner, J., Madejski, G. M., Gehrels, N., Burlon, D., 2012, ApJ, 749, 21.
Alonso, M. S., Coldwell, G., Lambas, D. G., 2013, A&A, 549, A141.
Arribas, S., Mediavilla, E., García-Lorenzo, B., Del Burgo, C., 1997, ApJ, 490, 227.
Barbosa, F. K. B., Storchi-Bergmann, T., Cid Fernandes, R., Winge, C., & Schmitt, H. 2006, MNRAS, 371, 170.
Barbosa, F. K. B., Storchi-Bergmann, T., Cid Fernandes, R., Winge, C., Schmitt, H., 2009, MNRAS, 396, 2.
Barbosa, F. K., Storchi-Bergmann, McGregor, P., Vale, T. B., Riffel, R. A.., 2014, MNRAS, 455, 2353.
Barnes, E. I., Sellwood, J. A., 2003, AJ, 125, 1164.
Bottema R., 1989, A&A, 221, 236
Bottema R., 1993, A&A, 275, 16.
Bureau M., Athanassoula E., 2005, ApJ, 626, 159
Cappellari & Emsellem, 2004, PASP, 116, 138.
Cappellari, M. et al., 2007, MNRAS, 379, 418.
Cheung, E. et al., 2015, MNRAS, 447, 506.
Ciotti, L., et al. 2010, ApJ 717, 707
Combes, F., Boissé, P., Mazure, A. & Blanchard, A., 1995, Galaxies and Cosmology, Springer-Verlag, Berlin, Germany.
Corwin, H.G., Buta, R.J., de Vaucouleurs, G. 1994, AJ, 108, 2128
Davies, R. I., Thomas, J., Genzel, R., Mueller Sánchez, F., Tacconi, L. J., Sternberg, A., Eisenhauer, F., Abuter, R., Saglia, R., & Bender, R., 2006, AJ, 646, 754.
Diniz, M. R., Riffel, R. A., Storchi-Bergmann, T., Winge, C., 2015, MNRAS, 453, 1727.
Dumas, G., Mundell, C. G., Emsellem, E., & Nagar, N. M. 2007, MNRAS, 379, 1249.
Emsellem E., Greusard D., Combes F., Friedli D., Leon S., Pécontal E., Wozniak H., 2001, A&A, 368, 52
Emsellem E. et al., 2004, MNRAS, 352, 721
Emsellem, E., Fathi, K., Wozniak, H., Ferruit, P., Mundell, C. G., Schinnerer, E. 2006, MNRAS, 365, 367.
Elvis, M. 2000, ApJ, 545, 63
Fabian, A. 2012, ARA&A, 50, 455
Falcón-Barroso, J. et al., 2006, MNRAS, 369, 529.
Fathi, K., Storchi-Bergmann, T., Riffel, R. A., Winge, C., Axon, D. J., Robinson, A., Capetti, A., & Marconi, A., 2006, ApJl, 641, L25.
Ferrarese, L. & Ford, H. 2005, SSRv, 116, 523
Fisher D., 1997, AJ, 113, 950
Fischer, T. C., Crenshaw, D. M., Kraemer, S. B., Schmitt, H. R., Storchi-Bergmann, T., Riffel, R. A., 2015, ApJ, 799, 234.
Frank, J, King, A. & Raine, D. J., 2002, Accretion Power in Astrophysics, Cambridge Univ. Press
Ganda, K., Falcón-Barroso, J., Peletier, R. F., Cappellari, M., Emsellem, E., McDermid, R. M., de Zeeuw, P. T., Carollo, C. M., 2006, MNRAS, 367, 46.
García-Lorenzo B., Mediavilla E., Arribas S., 1999, ApJ, 518, 190
Gerhard , O. E., 1993, MNRAS, 265, 213.
Hicks, E. K. S., Davies, R. I., Malkan, M. A., Genzel, R., Tacconi, L. J.; Sánchez, F. M., Sternberg, A., 2009, ApJ, 696, 448.
Hicks, E. et al. 2013, ApJ, 768, 107
Jarrett, T. H.; Chester, T.; Cutri, R.; Schneider, S. E.; Huchra, J. P., 2003, AJ, 125, 525.
Kormendy, J. & Ho, L. C, 2013, ARA&A, 51, 511
Krajnović, D., Cappellari, M., de Zeeuw, P. T., Copin, Y., 2006, MNRAS, 366, 787.
Krajnović, D. et al., 2011, MNRAS, 414, 2993.
Kuijken K., Merrifield M. R., 1995, ApJ, 443, L13
Kuzio de Naray, R., Arsenault, C. A., Spekkens, K., Sellwood, J. A., McDonald, M., Simon, J. D., Teuben, P., 2012, MNRAS, 427, 2523.
Laine, S., Shlosman, I.,Knapen, J. H., Peletier, R. F., 2002, ApJ, 567, 97.
Lena, D., Robinson, A., Storchi-Bergman, T., Schnorr-Müller, A., Seelig, T., Riffel, R. A., Nagar, N. M., Couto, G. S., Shadler, L., 2015, ApJ, 806, 84.
Malkan, M. A.; Gorjian, V.; Tam, R., 1998, ApJS, 117, 25.
Maraston, C., 2005, MNRAS, 362, 799.
Márquez I., Masegosa J., Durret F., González Delgado R. M., Moles M., Maza J., Prez E., Roth M., 2003, A&A, 409, 459
Martini, P., Dicken, D., Storchi-Bergmann, T., 2013, MNRAS, 420, 2249
Mazzalay, X. et al. 2014, MNRAS, 438, 2036
McGregor, P. J. et al., 2003, Proceedings of the SPIE, 4841, 1581.
Moriondo, G.; Baffa, C.; Casertano, S.; Chincarini, G.; Gavazzi, G.; Giovanardi, C.; Hunt, L. K.; Pierini, D.; Sperandio, M.; Trinchieri, G., 1999, A&AS, 137, 101.
Onken, C. et al., 2014, ApJ, 791, 37.
Pogge R. W., Martini P., 2002, ApJ, 569, 624
Reese, A. S., Williams, T. B., Sellwood, J. A., Barnes, E. I., Powell, B. A., 2007, AJ, 133, 2846.
Ricci, T. V., Steiner, J. E., Menezes, R. B., 2016, MNRAS, 463, 3860.
Riffel, R. A., Storchi-Bergmann, T., Winge, C., McGregor, P. J., Beck, T., Schmitt, H., 2008, MNRAS, 385, 1129.
Riffel, R. A., Storchi-Bergmann, T., Nagar, N. M., 2010, MNRAS, 404, 166.
Riffel, Rogemar A., 2010, Ap&SS, 327, 239.
Riffel, Rogemar A. & Storchi-Bergmann, T., Riffel, R., & Pastoriza, M. G., 2010, ApJ, 713, 469.
Riffel, R. A., Storchi-Bergmann, T., 2011, MNRAS, 411, 469.
Riffel, R. A., Storchi-Bergmann, T., 2011, MNRAS, 417, 2752.
Riffel et al. 2013, MNRAS, 430, 2249
Riffel, R. A., Storchi-Bergmann, T., & Riffel, R., ApJL, 2014, 780, 24.
Riffel, R. A., Storchi-Bergmann, T., Riffel, R., 2015, MNRAS, 451, 358.
Riffel, R. A. et al. 2015, MNRAS, 446, 2823.
Riffel, R. et al. 2015, MNRAS, 450, 3069.

Riffel, R., Rodríguez-Ardila, A., Pastoriza, M. G., 2006, A&A, 457, 61.
Riffel, R., Riffel, Rogemar A., Ferrari, F., & Storchi-Bergmann, T., 2011, MNRAS, 416, 493.
Schnorr-Müller, A., Storchi-Bergmann, T., Ferrari, F., Nagar, N. M., 2017, MNRAS, 466, 4370
Schnorr-Müller, A., Storchi-Bergmann, T., Robinson, A., Lena, D., Nagar, N. M., 2016, MNRAS, 457, 972
Schnorr-Mller, A., Storchi-Bergmann, T., Nagar, N. M., Robinson, A., Lena, D., Riffel, R. A., Couto, G. S., 2014, MNRAS, 437, 1708.
Schönell, A. J., Riffel, R. A., Storchi-Bergmann, T., Winge, C., 2014, MNRAS, 445, 414.
Schmitt, H. R., & Kinney, A. L., 2000, ApJS, 128, 479.
Sellwood, J. A., Spekkens, K., 2015, arXiv:1509.07120
Sellwood, J. A., Sánchez, R. Z., 2010, MNRAS, 404, 1733.
Simoes Lopes, R. et al. 2007, ApJ, 655, 718
Spekkens, K., Sellwood, J. A., 2007, ApJ, 664, 204.
Sánchez, F. M., Davies, R. I., Genzel, R., Tacconi, L. J., Eisenhauer, F., Hicks, E. K. S., Friedrich, S., & Sternberg, A., 2009, ApJ, 691, 749.
Somerville et al. 2008, MNRAS, 391, 481
Smajić, S. Moser, L., Eckart, A., Busch, G., Combes, F., García-Burillo, S., Valencia-S., M., Horrobin, M., 2015, A&A, 583, A104.
Springel et al. 2005, MNRAS, 361, 776
Storchi-Bergmann, T., Dors Jr., O., Riffel, R. A., Fathi, K., Axon, D. J., & Robinson, A., 2007, ApJ, 670, 959.
Storchi-Bergmann, T., McGregor, P. Riffel, Rogemar A., Simões Lopes, R., Beck, T., Dopita, M., 2009, MNRAS, 394, 1148.
Storchi-Bergmann, T., Simões Lopes, R., McGregor, P. Riffel, Rogemar A., Beck, T., Martini, P., 2010, MNRAS, 402, 819.
Storchi-Bergmann, T., Riffel, R. A., Riffel, R., Diniz, M., Borges Vale, T., McGregor, P., 2012, ApJ, 755, 87.
Terrazas, B. A., Bell, E. F., Henriques, B. M. B., White, S. D. M., Cattaneo, A., Woo, J., 2016, ApJL, 830, L12.
van der Marel, R.P. & Franx, M. 1993, ApJ, 407, 525
van de Ven, G., & Fathi, K., 2009, arXiv:0905.3556v1
Veilleux, S., Tully, R. B., Bland-Hawthorn, J. 1993, AJ, 105, 1318
Winge, C., Riffel, Rogemar A., Storchi-Bergmann, T., 2009, ApJS, 185, 186.

APPENDIX A: STELLAR KINEMATICS BASED ON ALREADY PUBLISHED DATA

Figures A1 – A5 show maps for the stellar kinematics of galaxies with previous measurements already published by our group.

APPENDIX B: ONE-DIMENSIONAL CUTS FOR THE STELLAR KINEMATICS

Figure B1 shows one-dimensional cuts along the major axis of the galaxies for the LOS velocity (left) and σ (rigth). Plots of the LOS velocity (V_{LOS}) vs. h_3 and σ vs. h_4 using all spaxels are shown in Figure B2.

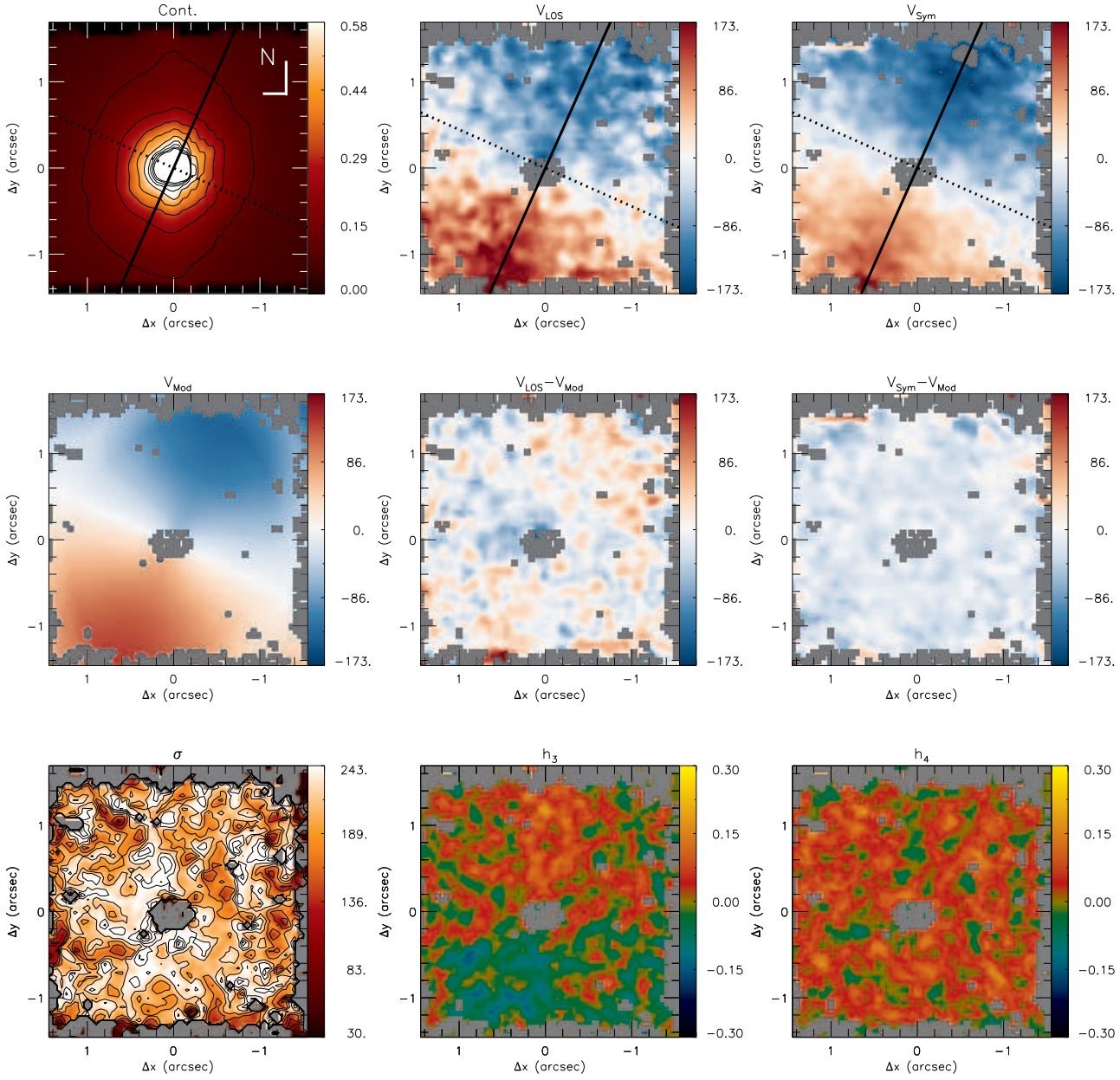

Figure A1. Same as Fig. 2 for NGC 2110. The original stellar kinematics measurements are presented in Diniz et al. (2015)

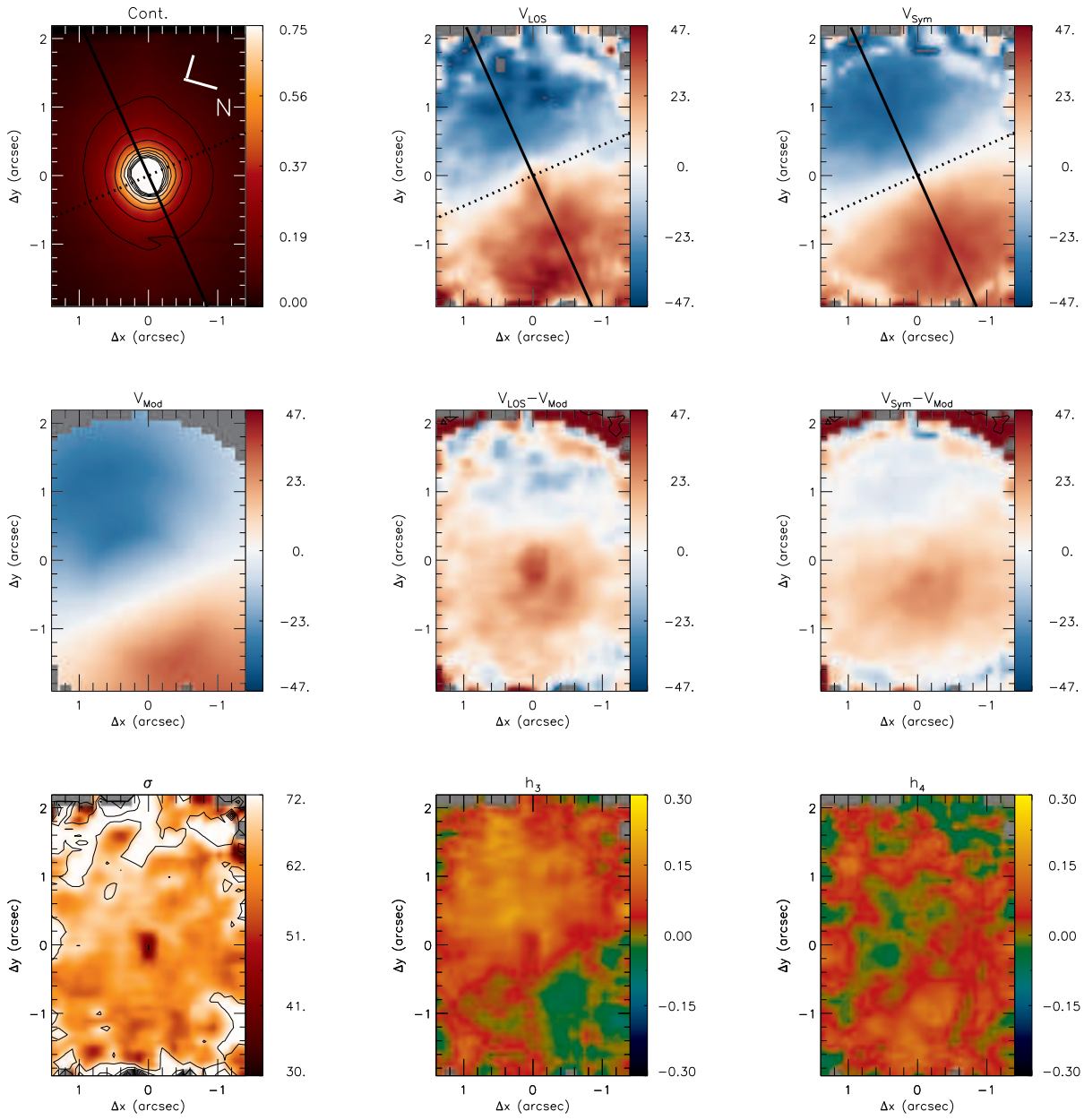

Figure A2. Same as Fig. 2 for NGC 4051. The original stellar kinematics measurements are presented in Riffel et al. (2008)

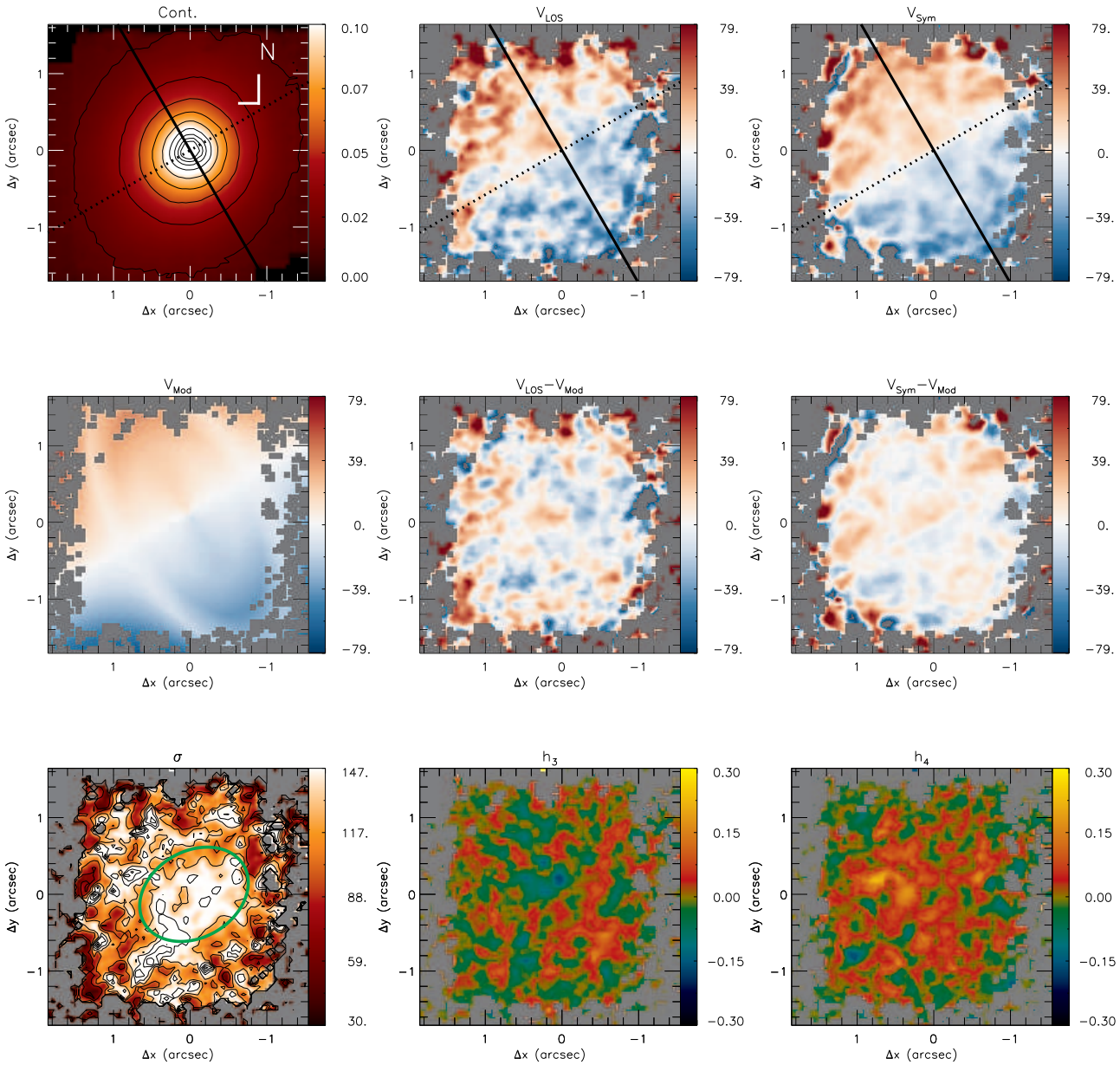

Figure A3. Same as Fig. 2 for NGC 5929. The original stellar kinematics measurements are presented in Riffel et al. (2015a)

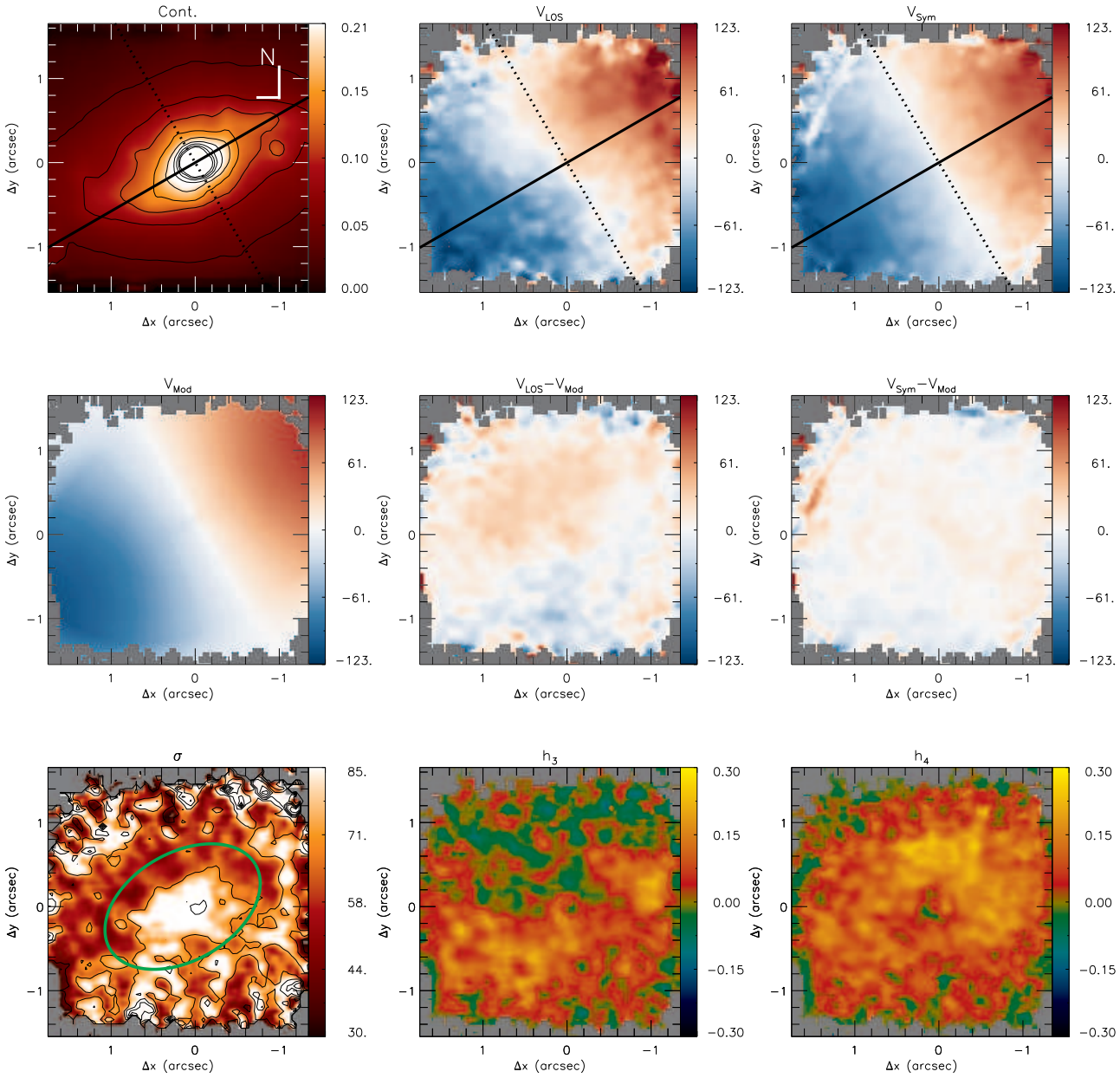

Figure A4. Same as Fig. 2 for Mrk 1066. The original stellar kinematics measurements are presented in Riffel & Storchi-Bergmann (2011a)

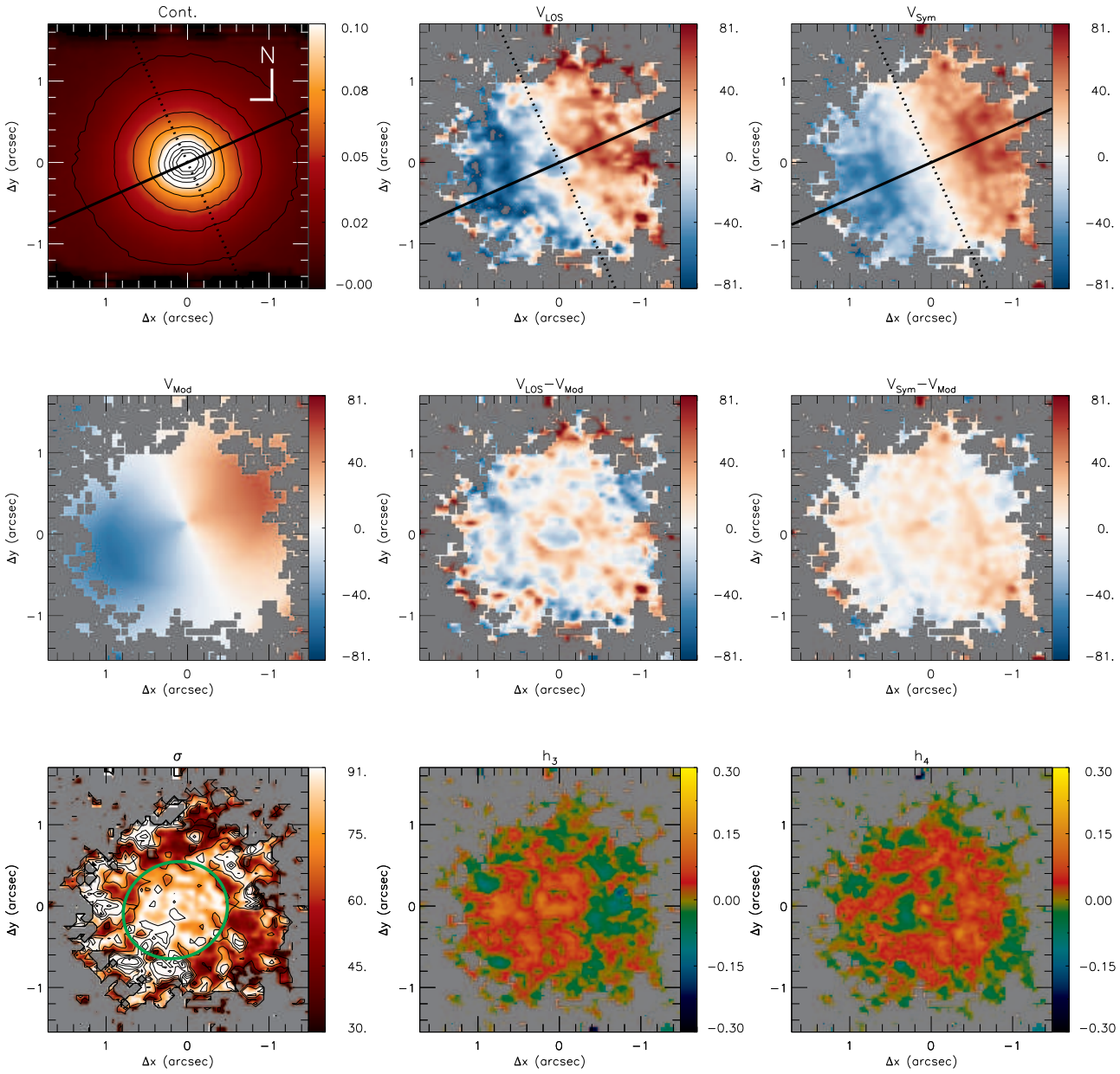

Figure A5. Same as Fig. 2 for Mrk 1157. The original stellar kinematics measurements are presented in Riffel & Storchi-Bergmann (2011b)

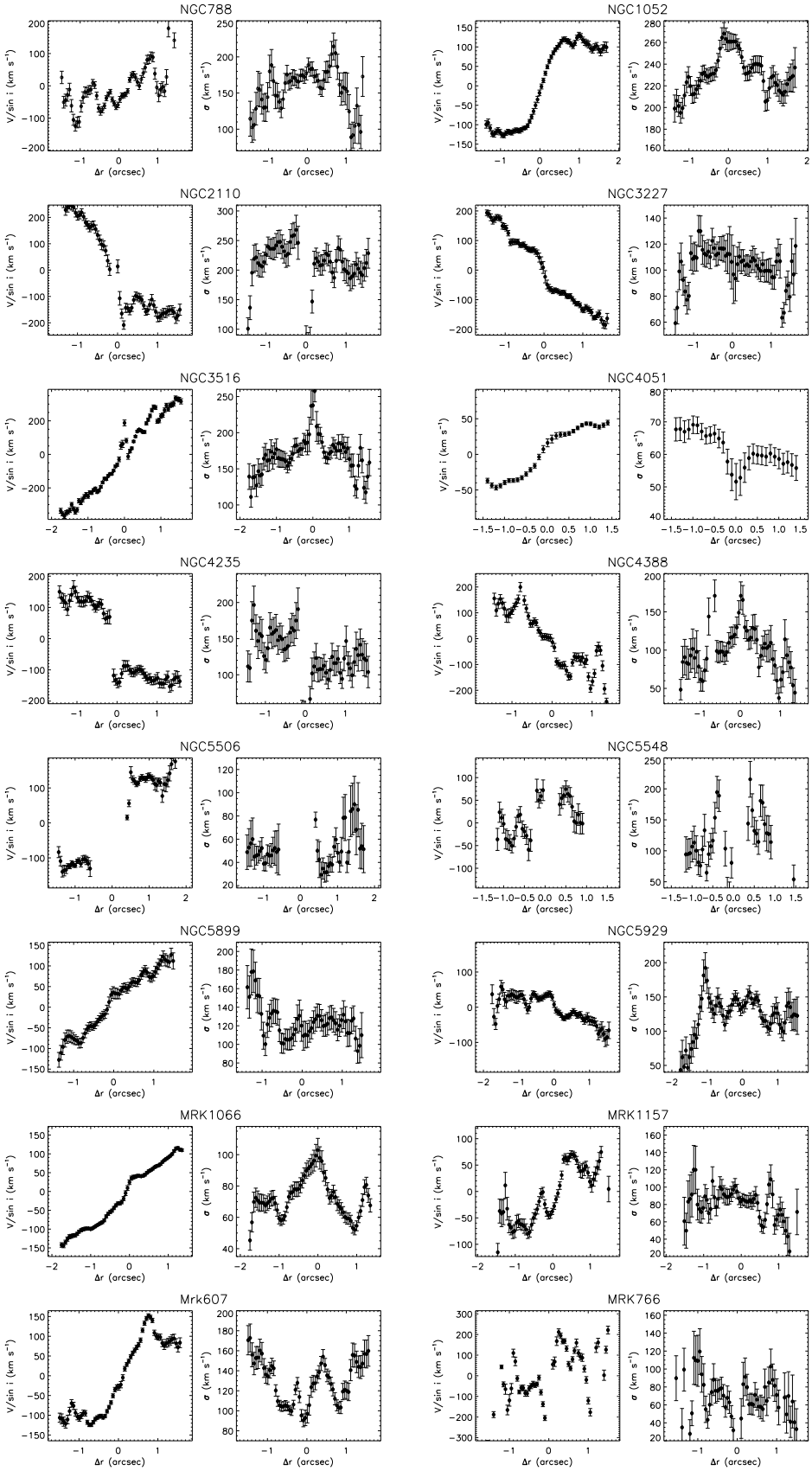

Figure B1. One-dimensional cuts along the major axis of the galaxies obtained by averaging the observed velocities within a pseudo-slit with 0.″25 width. The orientation of the major axis and the inclination of the disk used in these plots are from Table.2.

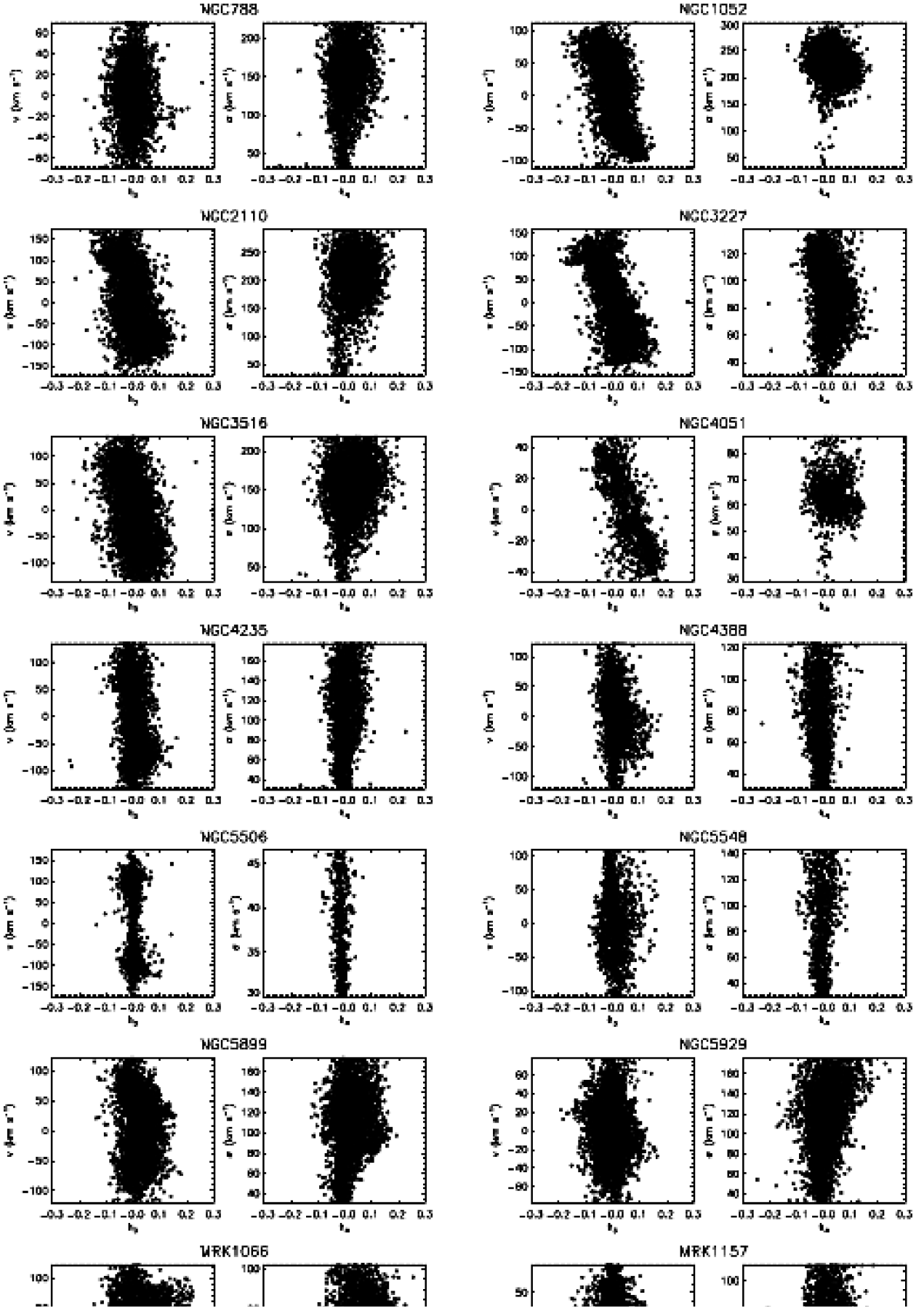
NGC788
NGC1052
NGC2110
NGC3227
NGC3516
NGC4051
NGC4235
NGC4388
NGC5506
NGC5548
NGC5899
NGC5929
MRK1066
MRK1157

A.2 Levantamento Gemini NIFS de processos de alimentação e retroalimentação em galáxias ativas próximas: II - Amostra e perfis de densidade de massa superficial

Aqui apresentamos a amostra e os resultados obtidos pelo grupo AGNIFS sobre a amostra e perfis de densidade de massa. Estes resultados foram publicados na revista MNRAS em Fevereiro de 2018, intitulado *Gemini NIFS survey of feeding and feedback processes in nearby Active Galaxies: II - The sample and surface mass density profiles.*

MNRAS 000, 1–18 (2017) Preprint 2 November 2017 Compiled using MNRAS LATEX style file v3.0

Gemini NIFS survey of feeding and feedback processes in nearby Active Galaxies: II -The sample and surface mass density profiles

R. A. Riffel[1⋆], T. Storchi-Bergamann[2], R. Riffel[2], R. Davies[3], M. Bianchin[1], M. R. Diniz[1], A. J. Schönell[2,4], L. Burtscher[5], M. Crenshaw[6], T. C. Fischer[7], L. G. Dahmer-Hahn[2], N. Z. Dametto[2], D. Rosario[8]

[1] *Departamento de Física, CCNE, Universidade Federal de Santa Maria, 97105-900, Santa Maria, RS, Brazil*
[2] *Departamento de Astronomia, IF, Universidade Federal do Rio Grande do Sul, CP 15051, 91501-970, Porto Alegre, RS, Brazil*
[3] *Max-Planck-Institut für extraterrestrische Physik, Postfach 1312, D-85741, Garching, Germany*
[4] *Instituto Federal de Educação, Ciência e Tecnologia Farroupilha, BR287, km 360, Estrada do Chapadão, 97760-000, Jaguari - RS, Brazil*
[5] *Leiden Observatory, Leiden University, PO Box 9513, 2300 RA Leiden, The Netherlands*
[6] *Department of Physics and Astronomy, Georgia State University, Astronomy Offices, 25 Park Place, Suite 605, Atlanta, GA 30303, USA*
[7] *Astrophysics Science Division, Goddard Space Flight Center, Code 665, Greenbelt, MD 20771, USA.*
[8] *Department of Physics, Durham University, South Road, Durham DH1 3LE, UK*

Accepted XXX. Received YYY; in original form ZZZ

ABSTRACT

We present and characterize a sample of 20 nearby Seyfert galaxies selected for having BAT 14–195 keV luminosities $L_X \geq 10^{41.5}$ ergs s^{-1}, redshift $z \leq 0.015$, being accessible for observations with the Gemini Near-Infrared Field Spectrograph (NIFS) and showing extended [OIII]λ5007 emission. Our goal is to study Active Galactic Nuclei (AGN) feeding and feedback processes from near-infrared integral-field spectra, that include both ionized (H II) and hot molecular (H_2) emission. This sample is complemented by other 9 Seyfert galaxies previously observed with NIFS. We show that the host galaxy properties (absolute magnitudes M_B, M_H, central stellar velocity dispersion and axial ratio) show a similar distribution to those of the 69 BAT AGN. For the 20 galaxies already observed, we present surface mass density (Σ) profiles for H II and H_2 in their inner ∼500 pc, showing that H II emission presents a steeper radial gradient than H_2. This can be attributed to the different excitation mechanisms: ionization by AGN radiation for H II and heating by X-rays for H_2. The mean surface mass densities are in the range $(0.2 \leq \Sigma_{HII} \leq 35.9)\,M_\odot\,pc^{-2}$, and $(0.2 \leq \Sigma_{H2} \leq 13.9)\times10^{-3}\,M_\odot\,pc^{-2}$, while the ratios between the H II and H_2 masses range between ∼200 to 8000. The sample presented here will be used in future papers to map AGN gas excitation and kinematics, providing a census of the mass inflow and outflow rates and power as well as their relation with the AGN luminosity.

Key words: galaxies: active – galaxies: nuclei – infrared: galaxies

1 INTRODUCTION

The co-evolution of Active Galactic Nuclei (AGN) and galaxies is now an accepted paradigm that permeates recent reviews (Kormendy & Ho 2013; Heckman & Best 2014). But the conclusions put forth in these reviews are mostly based on surveys of integrated galaxy properties, and the feeding and feedback processes that lead to the co-evolution have been implemented in models in a simplistic way Somerville et al. (2008); Springel et al. (2005); Croton et al. (2006). This is due to the lack of observational constraints from spatially resolved studies. Physical motivated models Hopkins & Quataert (2010) show that the relevant feeding processes occur within the inner kiloparsec, that can only be resolved in nearby galaxies. The large quantities of dust in the inner kiloparsec of AGN, estimated to range from 10^5 to 10^7 $M_\odot$ (Simões Lopes et al. 2007; Martini, Dicken & Storchi-Bergmann 2013; Audibert et al.

⋆ E-mail: rogemar@ufsm.br

2017) and the associated large content of molecular gas (10^7 to 10^9 $M_\odot$) points to the importance of looking for signatures of the feeding in the molecular gas within the nuclear region. Recently it has also been argued that the feedback in the form of massive outflows is also dominated by molecular gas (Sakamoto et al. 2010; Aalto et al. 2012; Veilleux et al. 2013), at least in LIRGS or ULIRGS (Ultra Luminous Infrared Galaxies).

The co-evolution scenario, and the feeding of gas to the inner kiloparsec of galaxies when they are in the active phase, implies that the galaxy bulge grows in consonance with the SMBH. Since the early studies of Terlevich and collaborators (e.g. Terlevich et al. 1990), it has been argued that the excess blue light and dilution of the absorption features of the nuclear spectra of active galaxies was due to young stars. Subsequent long-slit studies (Storchi-Bergmann et al. 2000; Cid Fernandes et al. 2004; Davies et al. 2007; Kauffmann & Heckman 2009) have found an excess contribution of young to intermediate age stars to the stellar population in the inner kiloparsec of active galaxies when compared to non-active ones. This result has led to the proposition of an evolutionary scenario (Storchi-Bergmann et al. 2001; Davies et al. 2007; Hopkins 2012), in which the gas inflow to the nuclear region first triggers star formation in the circumnuclear region, and is then followed by the ignition of the nuclear activity.

Observational constraints for the feeding and feedback processes can be obtained via spatially resolved studies of nearby active galaxies using integral field spectroscopy (IFS). The radiation from the AGN heats and ionizes the surrounding gas in the galaxy up to hundreds of pc (and even kpc) scales. The heating excites rotational and vibrational states of the H_2 molecule that then emits in the near-IR, and the AGN radiation ionizes the gas that, in turn, emits permitted and forbidden lines that can be used to probe the ionized gas kinematics and excitation. Emission from both the molecular and ionized gas phases can be observed in the near-IR domain, where the effects of dust extinction is minimized. In the near-infrared, IFS at 10 meter class telescopes has been used to probe the feeding and feedback processes in nearby active galaxies, by mapping and modeling the molecular and ionized gas kinematics in the inner kiloparsec of active galaxies – on 10–100 pc scales – leading to insights on both the feeding and feedback mechanisms. For high signal-to-noise ratio in the continuum, the stellar kinematics as well as the age distribution of the stellar population have also been mapped. So far, these studies show that (i) Emission from molecular (H_2) and ionized gases present distinct flux distributions and kinematics. The H_2 emission is distributed all around the nucleus, seems to be located in the plane of the galaxy, shows low velocity dispersion ($<100\,km\,s^{-1}$) and is dominated by rotational motion. In few cases, a very steep rotation curve is observed, suggesting the presence of compact molecular disks Riffel & Storchi-Bergmann (2011a); Schönell et al. (2014); Hicks et al. (2013); Mazzalay et al. (2014). In a number of cases, streaming motions towards the central regions were mapped along nuclear spiral arms with estimated inflow rates in total molecular gas ranging from a few tenths to a few solar masses per year (Riffel et al. 2008; Riffel, Storchi-Bergmann & Winge 2013; Davies et al. 2009; Müller-Sánchez et al. 2009; Diniz et al. 2015). (ii) The ionized gas emission is more collimated and shows higher velocity dispersion ($>100\,km\,s^{-1}$) than the molecular gas, seems to extend to high latitudes and its kinematics comprises both rotation and outflow (e.g. Riffel et al. 2006; Riffel, Storchi-Bergmann & Nagar 2010; Müller Sánchez et al. 2011; Riffel, Storchi-Bergmann & Winge 2013; Barbosa et al. 2014; Storchi-Bergmann et al. 2010). (iii) Only for a few cases, the study of stellar population was done using near-IR IFS. These works show the presence of young to intermediate age ($\sim10^8$ yr) stars, usually in ~100 pc rings (e.g. Riffel et al. 2010, 2011c; Storchi-Bergmann et al. 2012), that correlate with rings of low velocity dispersion. This correlation has been interpreted as being a signature of the co-evolution of the bulge and SMBH: as the estimated mass inflow rates are ~3 orders of magnitude larger than the accretion rate to the AGN, most of the molecular gas that is accumulated in the nuclear regions of AGNs is forming new stars in the inner few hundred parsecs of the galaxy, leading to the growth of the bulge.

Most of the results summarized above were obtained by studying individual galaxies, selected using distinct criteria, and a study of a well-defined, comprehensive sample is of fundamental importance to understand the relation among AGN feeding, feedback and galaxy evolution (e.g. Davies et al. 2017). In the present work, we describe a sample of nearby active galaxies that are being observed with the Gemini Near-Infrared Integral Field Spectrograph (NIFS). Our aim with these observations is to study the details of the inner few hundreds of parsecs of AGNs and better constrain the feeding and feedback processes. This is the second paper of a series in which we will be mapping the gas excitation and kinematics, as well as the stellar population characteristics and kinematics. In the first paper (Riffel et al. 2017), we have presented and discussed stellar kinematics measurements for 16 galaxies of the sample and in forthcoming papers we will analyse the emission-line flux distributions, gas kinematics and map the stellar populations. This paper is organized as follows: Section 2 describes the selection criteria of the sample, the instrument configuration, observations, data reduction and compare nuclear and large scale properties of the galaxies. In section 3 we present and discuss measurements of the molecular and ionized gas masses and surface densities for the galaxies already observed and Section 4 discusses the implications of the derived amount of gas to the AGN feeding process and star formation. Finally, section 5 presents the conclusions of this work.

2 DEFINITION OF A SAMPLE AND OBSERVATIONS

2.1 The sample

In order to select out an AGN sample, we used the Swift-BAT 60-month catalogue (Ajello et al. 2012), and selected nearby galaxies with 14–195 keV luminosities $L_X \geq 10^{41.5}$ ergs s^{-1} and redshift $z \leq 0.015$. The hard (14–195 keV) band of the Swift-BAT survey measures direct emission from the AGN rather than scattered or re-processed emission, and is much less sensitive to obscuration in the line-of-sight than

soft X-ray or optical wavelengths, allowing a selection based only on the AGN properties. Davies et al. (2015) describe a southern hemisphere sample selected in a similar way and discuss its rationale for studying AGN feeding and feedback processes (see also, Davies et al. 2017). Although their sample includes brighter and closer galaxies then ours, being composed by galaxies with $\log L_X = 42.4 - 43.7$ and $z < 0.01$.

As additional criteria, the object must be accessible for Gemini NIFS ($-30° < \delta < 73°$) and its nucleus being bright/pointy enough to guide the observations or with natural guide stars available in the field. Finally, we only have included in the sample galaxies already previously observed in the optical and with extended [O III]λ5007 emission available in the literature. We have used this constraint in order to ensure that we will have extended gas emission to allow spatially resolve its kinematics and look for possible inflows and outflows. From our previous experience, a galaxy that shows extended [O III] emission will also have a similarly extended [Fe II] or Paβ emission. Table 1 presents the resulting sample, which is composed of 20 galaxies. In addition, we included 9 galaxies observed with NIFS by our group in previous works (shown below the horizontal line in Table 1). These aditional galaxies may be used as a complementary sample in forthcoming works.

Figure 1 shows a plot of L_X vs. z for all Swift BAT AGN with $z \leq 0.05$ and accessible to Gemini North ($-30^0 < \delta < 73^0$).Green diamonds show the galaxies accessible to Gemini North that satisfy the following criteria: $L_X \geq 10^{41.5}$ ergs s^{-1} and $z \leq$0.015, while the red squares show our main sample (objects that satisfy all the requirements above). The cyan $\times$ symbols show the objects of the complementary sample detected in the Swift-BAT 60-month catalogue. The red dotted line shows the detection limit of the Swift 60-month catalogue and the vertical and horizontal lines show the L_X and z cuts used to define our sample, respectively.

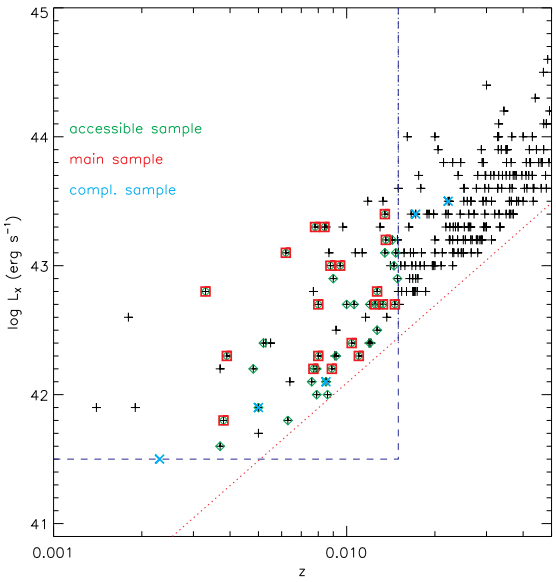

Figure 1. Plot of L_X vs. z for the galaxies of our sample. Black crosses show all objects (257) with $\log L_X > 41.5$ at the Swift BAT 60-month catalogue, green diamonds represent objects (43) accessible by NIFS ($-30° < \delta < 73°$), red squares represent our main sample (20) and cyan crosses are objects from our complementary sample detected in Swift BAT. All points at $z < 0.015$ make up what we call "the restricted BAT sample", composed by 69 galaxies. The red dotted line shows the detection limit of Swift and the dashed lines show the limits in L_X and z used the NIFS sample ($L_X \geq 10^{41.5}$ ergs s^{-1} and $z \leq$0.015).

2.2 Characterization of the sample

It is well known that hard X-ray emission is a good tracer of nuclear activity in galaxies, and thus a X-ray selected sample is representative of the population of AGN within the limited volume. However, besides the limits in X-ray luminosity and redshift, we included a constraint based on the detection of [O III]λ5007 emission line in order to increase the rate of detection of extended emission in near-IR lines, necessary to map the gas kinematics and flux distributions. In order to test if this additional criteria produces any bias on our sample, as compared to objects selected only on the basis of their X-ray emission, we compare the distribution of physical properties of the nucleus and host galaxies of the BAT sample (composed of galaxies with $L_X \geq 10^{41.5}$ ergs s^{-1} and redshift $z \leq$0.015) with the distributions of our main and complementary samples.

The total number of galaxies in the 60 month BAT catalogue that follows the constraints above is 69 galaxies (hereafter we will call this sample as the "restricted BAT sample"), while our main sample is composed of 20 objects, as shown in Table 1. In the left panel of Figure 2 we present a histogram for the distribution of L_X of our main sample in bins of $\log L_X = 0.3$ crosshatched histogram, overlaid on the histogram for the restricted BAT sample, which is shown in gray. As can be observed in this plot, both samples show a very similar distribution with mean luminosities of $< \log L_X >= 42.6 \pm 0.1$ erg s^{-1} and $< \log L_X >= 42.7 \pm 0.1$ erg s^{-1} for the BAT and our main sample, respectively. We performed a Kolmogorov-Smirnov (K-S) statistic test to estimate the K-S confidence index (KS) and the probability of the two distributions being drawn from the same distribution (P). The resulting parameters are $KS = 0.143$ and $P = 0.886$, indicating that both restricted BAT and main samples have a probability of ∼89 % of being originated from the same distribution. Thus, the inclusion of the additional selection criteria of having extended [O III] emission already published and being observable with NIFS does not change significantly the distribution of the sample in terms of X-ray luminosities and our main sample can be considered a representative sample of nearby AGNs within adopted constrains in X-ray luminosity and redshift. It is already well known that a close correlation between the [O III] and hard X-ray luminosities is observed for AGNs (e.g. Lamperti et al. 2017) and that a better correlation is found if the sample is selected based on the X-ray luminosity than if it is drawn from [O III] luminosity (Heckman & Best 2014). As our sample is based on the X-ray luminosity, the similarity in the X-ray distribution is both samples is expected.

Five galaxies of the complementary sample have X-ray luminosities available in the 60 month BAT catalogue. Including these sources, the distribution of galaxies shows an extension to lower X-ray luminosities as seen in the central panel of Fig. 2, filling the low-luminosity "gap" seen in the main sample, as only one galaxy of the complementary sam-

Table 1. The sample. (1) Galaxy name; (2) Redshift; (3) Morphological classification; (4) Nuclear Activity (from quoted in NED), (5) Swift 14-195 keV luminosity, (6) [O III]λ5007 luminosity in units of ergs s^{-1}, (7) reference for the [O III] luminosity. Table 2 list the galaxies already observed.

(1) Galaxy	(2) z	(3) Hubble Type	(4) Nuc. Act.	(5) $\log(L_X)$	(6) $\log(L_{OIII})$	(7) Ref.
		Main sample				
NGC788	0.014	SA0/a?(s)	Sy2	43.20	41.06	a
NGC1068	0.004	(R)SA(rs)b	Sy2	41.80	41.53	b
NGC1125	0.011	(R')SB0/a?(r)	Sy2	42.30	39.69	c
NGC1194	0.013	SA0$^+$?	Sy1	42.70	39.60	b
NGC2110	0.008	SAB0$^-$	Sy2	43.30	40.64	a
Mrk3	0.014	S0?	Sy2	43.40	41.83	b
NGC2992	0.008	Sa pec	Sy2	42.20	41.42	a
NGC3035	0.015	SB(rs)bc	Sy1	42.70	39.83	c
NGC3081	0.008	(R)SAB0/a(r)	Sy2	42.70	41.58	a
NGC3227	0.004	SAB(s)a pec	Sy1.5	42.30	40.84	a
NGC3393	0.013	(R')SB(rs)a?	Sy2	42.70	41.58	b
NGC3516	0.009	(R)SB0^0?(s)	Sy1.5	43.00	41.02	b
NGC3786	0.009	SAB(rs)a pec	Sy1.8	42.20	40.59	a
NGC4151	0.003	(R')SAB(rs)ab?	Sy1.5	42.80	42.19	a
NGC4235	0.008	SA(s)a edge-on	Sy1	42.30	39.31	a
Mrk766	0.013	(R')SB(s)a?	Sy1.5	42.80	41.10	b
NGC4388	0.008	SA(s)b? edge-on	Sy2	43.30	41.26	b
NGC4939	0.010	SA(s)bc	Sy1	42.40	40.64	c
NGC5506	0.006	Sa pec edge-on	Sy1.9	43.10	40.97	a
NGC5728	0.009	SAB(r)a?	Sy2	43.00	41.47	a
		Complementary Sample				
NGC1052	0.005	E4	Sy2	41.90	–	–
NGC4051	0.002	SAB(rs)bc	Sy1	41.50	–	–
NGC5548	0.017	(R')SA0/a(s)	Sy1	43.40	41.37	b
NGC5899	0.009	SAB(rs)c	Sy2	42.10	–	–
NGC5929	0.008	Sab? pec	Sy2	–	–	–
Mrk79	0.022	SBb	Sy1	43.50	41.58	b
Mrk607	0.009	Sa? edge-on	Sy2	–	–	–
Mrk1066	0.012	(R)SB0$^+$(s)	Sy2	–	–	–
Mrk1157	0.015	(R')SB0/a	Sy2	–	–	–

References: a: Wittle (1992), b: Schmitt et al. (2003), c: Gu et al. (2006); d: Noguchi et al. (2010); e: Zhu et al. (2011).

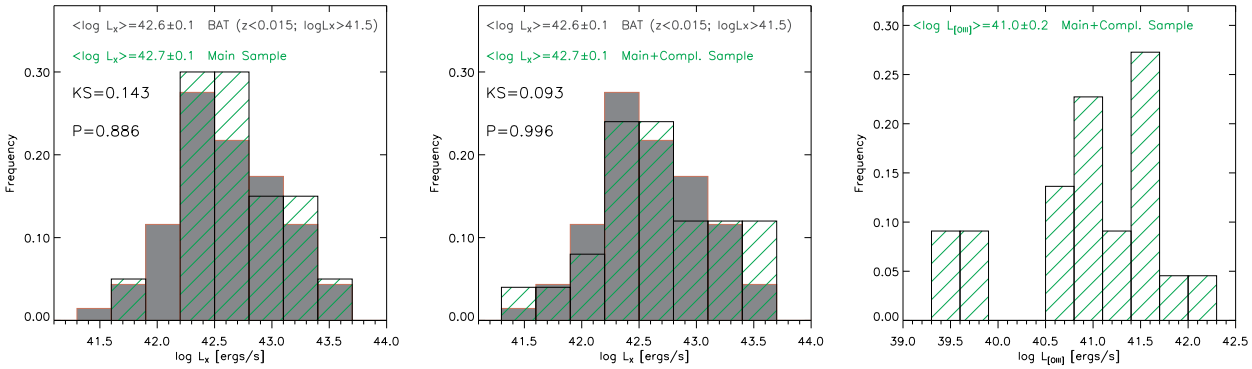

Figure 2. Histograms for the distribution of X-ray and [O III]λ 5007 luminosities of the galaxies of our sample. The left panel shows the distribution of $\log L_X$ of all galaxies with $L_X \geq 10^{41.5}$ ergs s^{-1} and $z \leq 0.015$ from the 60 month BAT catalogue (the "restricted BAT" sample) in gray, with the distribution of our main sample overploted and crosshatched green histogram. In the central panel, the complementary sample is included and the right panel shows the distribution of the [O III]λ 5007 luminosities for our sample, including the two objects from the complementary sample with [O III] luminosities available. All histograms were constructed using a bin of $\log L_X = 0.3$ erg s^{-1} and the mean values for each distribution are shown at the top of each panel. The results for the K-S statistical test (*KS* and *P*) are shown are shown for the first two panels.

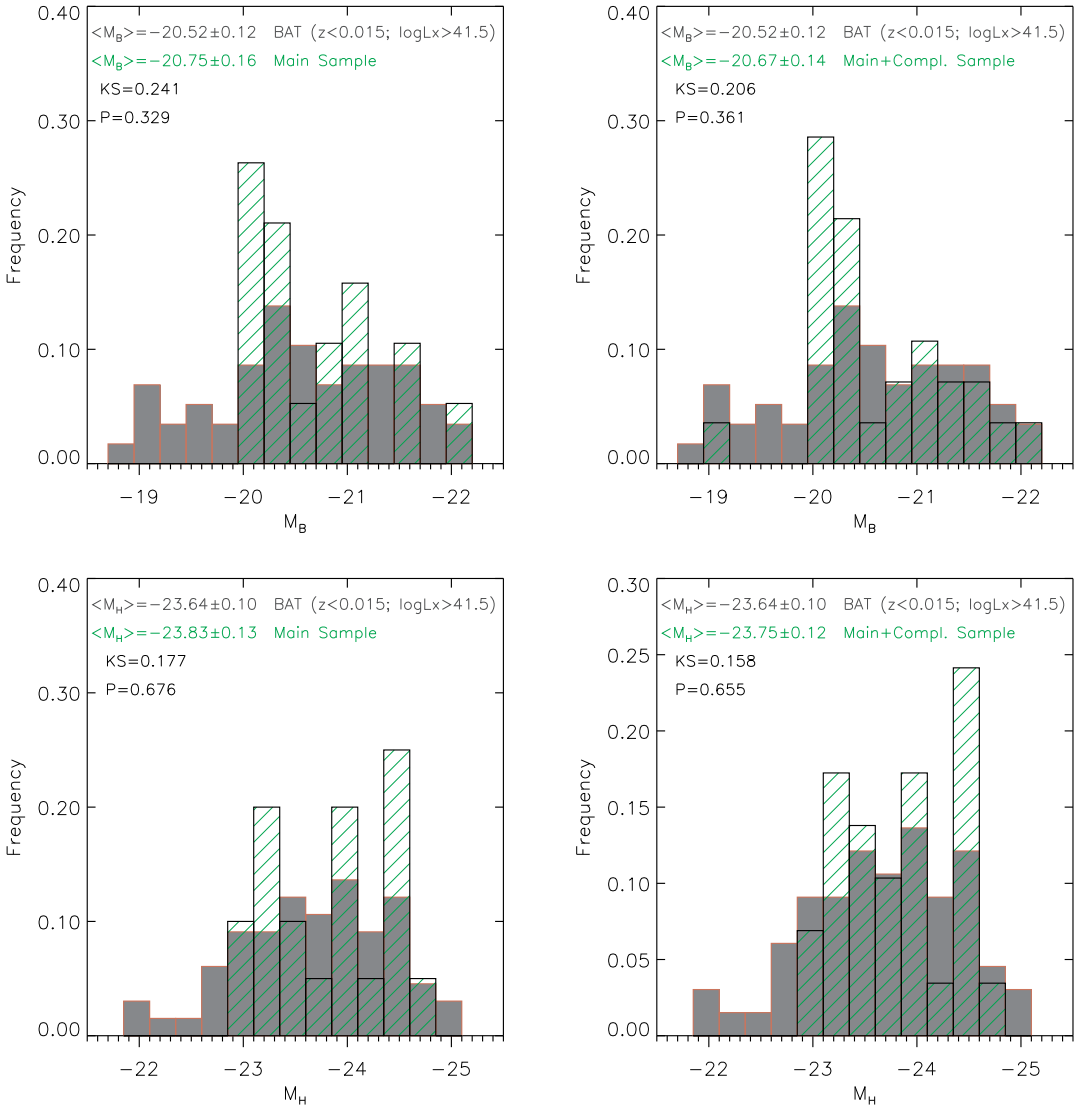

Figure 3. Distribution of B (top) and H (bottom) band absolute magnitudes for the galaxies of the main sample (left) and main+complementary sample (right) in bins of 0.25 mag. The distribution of the BAT sample is shown as the gray histogram. The results for the K-S statistical test (*KS* and *P*) are shown in each panel.

ple shows $\log L_X > 42.3$. However, the averaged luminosity does not change, as the complementary sample includes also two high luminosity objects (NGC 5548 and Mrk 79). The K-S test indicates that the inclusion of these sources makes the sample even more similar to the restricted BAT sample, with almost 100 % of probability of both samples follow the same distribution in L_X. Besides the 20 galaxies of our main sample, [O III]λ5007 luminosities are available for two galaxies of the complementary sample. Our combined (main + complementary) sample shows [O III]λ5007 luminosities in the range $L_{[OIII]} = (0.2 - 155) \times 10^{40}$ erg s^{-1}, with a mean value of $< \log L_{[OIII]} >= 41.0 \pm 0.2$ erg s^{-1}.

We compiled physical properties of the host galaxies from the Hyperleda database [1] (Makarov et al. 2014) and NED[2]. In figures 3 and 4 we present histograms for the absolute B (top panels of Fig. 3) and H magnitudes (bottom panels of Fig. 3), the nuclear stellar velocity dispersion (top panels of Fig. 4) and axial ratio (bottom panels of Fig. 4). Both magnitudes correspond to apertures that include the the total emission of the host galaxy. The left panels of these figures show the distribution of these properties for the main sample, while the right panels show the same properties for the combined sample. As in Fig. 2 the restricted BAT sample is shown as the gray histogram.

The B absolute magnitude M_B was obtained from the Hyperleda database, and is available for 58 objects from the restricted BAT sample and for 28 galaxies of our sample, the only exception being NGC 3035. The mean value of M_B for

[1] The Hyperleda database is available at *http://leda.univ-lyon1.fr/*

[2] NASA/IPAC Extragalactic Database available at *http://ned.ipac.caltech.edu/*

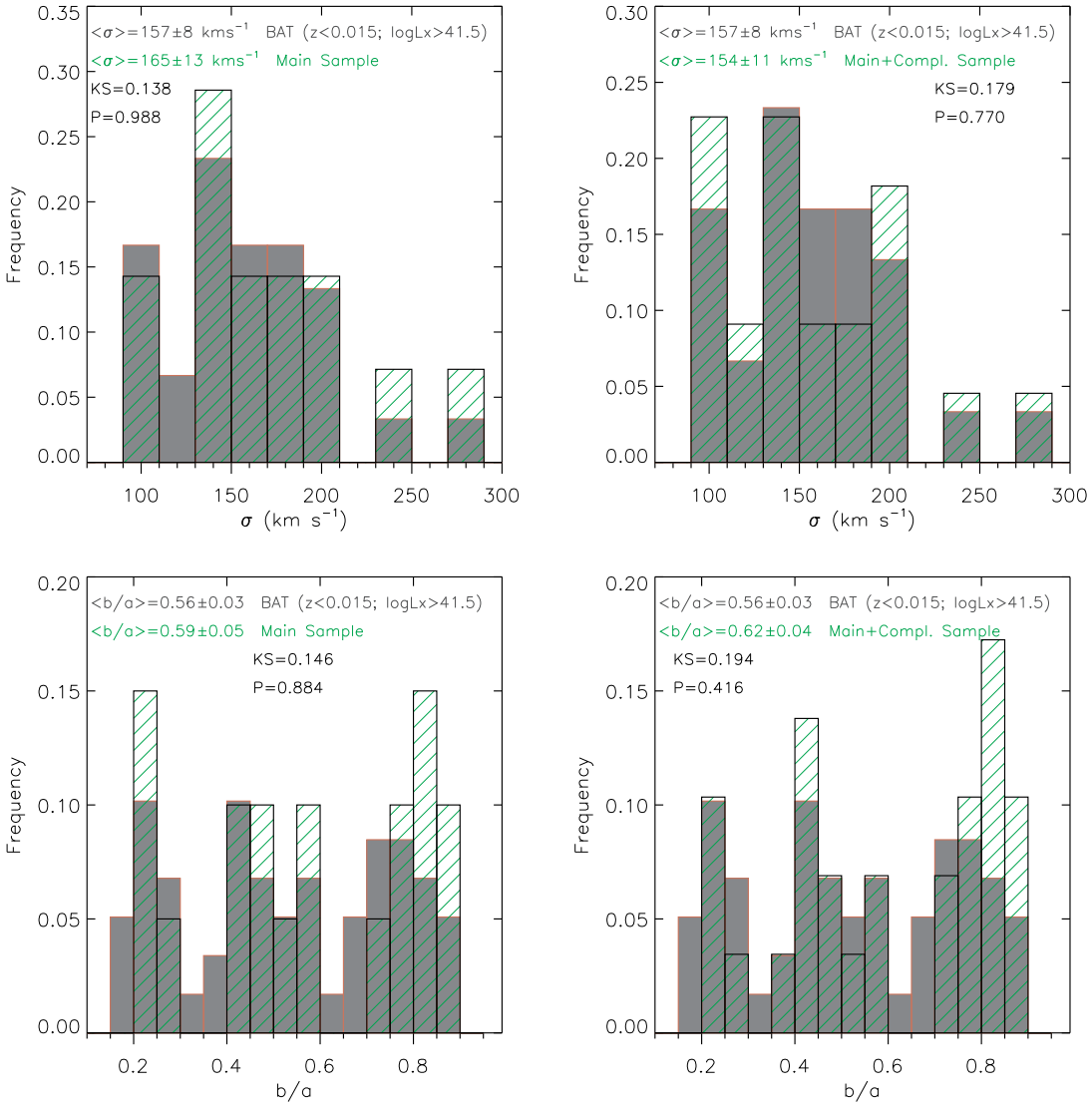

Figure 4. Distribution of central stellar velocity dispersion (top) and axial ratio (bottom) for the galaxies of the main sample (left) and main+complementary sample (right). The distribution of the restricted BAT sample is shown in gray scale on the background. Bins of 20 km s^{-1} are used in the histograms for the velocity dispersion and of 0.05 for the axial ratio. The results for the K-S statistical test (*KS* and *P*) are shown in each panel.

our main sample ($M_B = -20.75 \pm 0.16$ mag) is similar to that of the BAT sample ($M_B = -20.52 \pm 0.12$ mag), but the distributions are somewhat distinct as the BAT sample includes more low luminosity galaxies with $M_B > -20$ mag. The K-S test results gives a probability of ∼33 % that the main and restricted BAT samples follow the same distribution in M_B, while including the complementary sample, this probability increases to ∼36 %, being still small.

The total H absolute magnitude was obtained from the apparent H magnitudes from the The Two Micron All Sky Survey catalogue[3] (2MASS, Skrutskie et al. 2006). The H band is dominated by emission from the galaxy bulges and its luminosity can be used as a proxy for stellar mass of the galaxy (Davies et al. 2015, 2017). As for M_B, the distribution of the galaxies of our main sample is similar to that of the composite sample and the mean value of M_H for both samples are very similar to that observed for the BAT sample. However, for M_H the K-S test indicates that there about 68 % of probability of both samples follow the same distribution. A similar P value is found if we include the complementary sample.

In Figure 4 we show histograms for the distribution of the nuclear stellar velocity dispersion (σ – top panels) and axial ratio (b/a – bottom panels). The σ values were obtained from the Hyperleda database and are standardized to an aperture of 0.595 h^{-1} kpc. Measurements of σ are available at Hyperleda database for 30 galaxies of the restricted BAT sample, 14 galaxies of the main sample and 8 objects of the complementary sample. The histograms for σ were constructed using bins of 20 km s^{-1}. As seen in

[3] Available at *http://vizier.u-strasbg.fr/viz-bin/VizieR*

Fig. 4 the distribution of σ values for the main and restricted BAT samples are similar, with mean σ values of $<\sigma>=165\pm13\,\mathrm{km\,s^{-1}}$ and $<\sigma>=157\pm8\,\mathrm{km\,s^{-1}}$, respectively. By including the complementary sample, the fraction of objects with $\sigma\leq120\,\mathrm{km\,s^{-1}}$ increases, while the mean σ values are still consistent with that of the restricted BAT sample, as observed at the top-right panel of Fig. 4. The K-S test returns $P=0.988$, meaning that the restricted BAT and main samples follow the same distribution in σ (with almost 99 % of probability), while including the complementary sample, this probability decreases to 77 %, being still high.

Considering that the central σ values are representative of the bulge of the galaxies, we can use the $M_\bullet-\sigma$ relation (e.g. Ferrarese & Merritt 2000; Gebhardt et al. 2000; Tremaine et al. 2002; Ferrarese & Ford 2005; Graham et al. 2011) to determine the mass of the central supermassive black hole ($M_\bullet$). Using equation 3 from Kormendy & Ho (2013) and the σ values from Fig. 4, we obtain $(0.15\lesssim M_\bullet\lesssim 13.5)\times10^8\,\mathrm{M_\odot}$ and mean values of $<M_\bullet>\approx1.3\times10^8\,\mathrm{M_\odot}$ for the main sample and $<M_\bullet>\approx9.8\times10^7\,\mathrm{M_\odot}$ including the complementary sample.

The main goals of our project are to map and quantify AGN feeding and feedback process via gas inflows and outflows. While inflows are usually restricted to the plane of the galaxy disk (e.g. Riffel et al. 2008; Riffel, Storchi-Bergmann & Winge 2013), outflows do not show any preferential orientation (Schmitt et al. 2001; Barbosa et al. 2014; Schönell et al. 2017). Thus, in order to optimize the search for inflows and outflows, it is desirable that the sample of galaxies show a wide range of disk orientations. The bottom panels of Figure 4 show histograms for the axial ratio b/a for our sample and restricted BAT sample (where a and b are the semi-major and semi-minor axes of the galaxy obtained from the Hyperleda database, measured at the isophote 25 mag/arcsec^2 in the B-band surface brightness distribution). Measurements of the axial ratio are available for all galaxies of our sample and for 59 objects of the restricted BAT sample. The bottom panels of Fig. 4 show histograms for the axial ratio in bins of 0.05. The mean values of b/a of our main samples are similar to that of the restricted BAT sample and including the complementary sample. Our sample shows a wide range of axial ratios, from nearly edge-on galaxies ($b/a\sim0.2$, corresponding to a disk inclination $i\sim80^\circ$) to nearly face-on galaxies ($b/a\sim0.9$, $i\sim25^\circ$). The K-S test shows a probability of 88 % of the main and restricted BAT samples follow the same distribution in axial ratio, while including the complementary sample, the K-S test results in $P=0.416$, suggesting that the complementary sample includes a bias in the axial ratio distribution.

2.3 Observations

The Integral Field Spectroscopic observations of the galaxies of our sample have been obtained with the Gemini Near-Infrared Integral Field Spectrograph (NIFS, McGregor et al. 2003) operating with the Gemini North adaptive optics module ALTAIR. NIFS has a square field of view of $\approx3\farcs0\times3\farcs0$, divided into 29 slices with an angular sampling of $0\farcs1\times0\farcs04$. The observations of our sample are part of a Large and Long Program (LLP) approved by Brazilian National Time Allocation Committee (NTAC) and have started in semester 2015A and are planned to be concluded in 2019B. Some galaxies shown in Table 1 were observed as part of previous proposals by our group. The data comprise J and K(K$_l$)-band observations at angular resolutions in the range 0.″12–0.″20, depending on the performance of the adaptive optics module and velocity resolution of about $40\,\mathrm{km\,s^{-1}}$ at both bands.

Emission lines from high, low-ionization and molecular gas, as well as strong CO absorptions, are usually observed at these spectral bands in spectra of active galaxies (e.g. Riffel, Rodríguez-Ardila & Pastoriza 2006), allowing the mapping of the gas kinematics, distribution, excitation, extinction and the stellar kinematics. The relatively high spatial and spectral resolutions, together with the spatial coverage, make this an unprecedented data set to map the AGN feeding and feedback processes in nearby galaxies. The on-source exposure time for each galaxy is in the range 0.7–1.7 hours at each band, expected to result in a signal-to-noise ratio $snr>10$, which allows the fitting of the emission and absorption lines. The observations have been following the standard object-sky-object dithering sequence and the data reduction have been done following the standard procedures of spectroscopic data treatment.

2.4 Data reduction

The data reduction for the J and K band are being performed following the same procedure used in previous works (e.g. Riffel et al. 2008; Diniz et al. 2015; Riffel et al. 2017), including the trimming of the images, flat-fielding, sky subtraction, wavelength and s-distortion calibrations and correction of the telluric absorptions. The spectra are then flux calibrated by interpolating a black body function to the spectrum of the telluric standard star. Finally, datacubes for each individual exposure are created with an angular sampling of $0\farcs05\times0\farcs05$. These cubes are then mosaicked using the continuum peak as reference and median combined to produce a single final datacube for each band.

Table 2 presents a summary of the observation logs for the galaxies already observed. The angular resolution at J (PSF$_J$) and K (PSF$_K$) was estimated by measuring the full width at half maximum (FWHM) of the telluric standard star flux distributions. The uncertainties in the measurements are about 0.″03 for all galaxies at both bands. The spectral resolution at the J and K band was estimated from the FWHM of emission lines of the Ar and ArXe lamps used to wavelength calibration, respectively. For the J band we fitted the profiles of typical lines observed near 1.25 μm, while for the K band the spectral resolution was estimated from lines seen around 2.2 μm. The spectral resolution ranges from 1.7 to 2.0 Å at the J band, corresponding to an instrumental broadening ($\sigma_{inst}=\frac{FWHM}{2.355}\frac{c}{\lambda_c}$) of 17–20 $\mathrm{km\,s^{-1}}$. At the K band the spectral resolutions ranges from 3 to 3.7 Å, translating into $\sigma_{inst}\approx17-21\,\mathrm{km\,s^{-1}}$.

3 MOLECULAR AND IONIZED GAS SURFACE MASS DENSITY

We use the available data to discuss the radial distribution of ionized and molecular gas for galaxies already ob-

Table 2. Observations. (1) Galaxy name; (2) Gemini project identification; (3) J and (4) K-band on-source exposure time; (5) J and (6) K-band angular resolution estimated from the FWHM of the flux distribution of the telluric standard star; (7) J and (8) K-band spectral resolution estimated from the FWHM of the Arc Lamp lines used for wavelength calibrate the datacubes; (9) References to published studies using this dataset.

(1) Galaxy	(2) Programme	(3) J Exp. T. (seconds)	(4) K Exp. T. (seconds)	(5) PSF_J (arcsec)	(6) PSF_K (arcsec)	(7) $FWHM_J$ (Å)	(8) $FWHM_K$ (Å)	(9) Refs.
			Main sample					
NGC788	GN-2015B-Q-29	7×400	11×400	0.13	0.13	1.9	3.5	a
NGC1068	GN-2006B-C-9*	27×90	27×90	0.14	0.11	1.7	3.0	b, c, d
NGC2110	GN-2015B-Q-29	6×400	–	0.13	–	1.9	–	a, e
–	GN-2010B-Q-25	-	6×600	0.15	–	–	3.4	–
Mrk3	GN-2010A-Q-5*	6×600	6×600	0.13	0.13	2.0	3.2	–
NGC3227	GN-2016A-Q-6	6×400	6×400	0.13	0.12	1.8	3.5	a
NGC3516	GN-2015A-Q-3	10×450	10×450	0.17	0.15	1.8	3.5	a
NGC4151	GN-2006B-C-9*	8×90	8×90	0.16	0.12	1.6	3.3	f, g, h
NGC4235	GN-2016A-Q-6	9×400	10×400	0.12	0.13	1.8	3.5	a
Mrk766	GN-2010A-Q-42	6×550	6×550	0.21	0.19	1.7	3.5	a, j
NGC4388	GN-2015A-Q-3	–	2×400	–	0.19	–	3.7	a
NGC5506	GN-2015A-Q-3	10×400	10×400	0.15	0.18	1.9	3.6	a
			Complementary Sample					
NGC1052	GN-2010B-Q-25	6×610	4×600		0.15	1.7		a
NGC4051	GN-2006A-SV-123	–	6×750	–	0.18	–	3.2	a, k
NGC5548	GN-2012A-Q-57	12×450	12×450	0.28	0.20	1.7	3.5	a, l
NGC5899	GN-2013A-Q-48	10×460	10×460	0.13	0.13	1.8	3.4	a
NGC5929	GN-2011A-Q-43	10×600	10×600	0.12	0.12	1.7	3.2	a, m, n
Mrk79	GN-2010A-Q-42	6×520	6×550	0.25	0.25	1.8	3.5	o
Mrk607	GN-2012B-Q-45	10×500	12×500	0.14	0.14	2.0	2.2	a
Mrk1066	GN-2008B-Q-30	8×600	8×600	0.13	0.15	1.7	3.3	a, p, q, r, s
Mrk1157	GN-2009B-Q-27	8×550	8×550	0.11	0.12	1.8	3.5	a, t, u

* From Gemini Science Archive

References: a: Riffel et al. (2017); b: Storchi-Bergmann et al. (2012); c: Riffel et al. (2014); d: Barbosa et al. (2014); e: Diniz et al. (2015); f: Storchi-Bergmann et al. (2009), g: Storchi-Bergmann et al. (2010); h: Riffel, Storchi-Bergmann & McGregor (2009); i: Schönell et al. (2014); k: Riffel et al. (2008); l: Schönell et al. (2017); m: Riffel, Storchi-Bergmann & Riffel (2014); n: Riffel, Storchi-Bergmann & Riffel (2015); o: Riffel, Storchi-Bergmann & Winge (2013); p: Riffel et al. (2010); q: Riffel, Storchi-Bergmann & Nagar (2010); r: Riffel & Storchi-Bergmann (2011a); s: Ramos Almeida et al. (2014); t: Riffel et al. (2011c); u: Riffel & Storchi-Bergmann (2011b).

served. The fluxes of the $H_2\lambda 2.12\,\mu$m and Brγ emission lines can be used to estimate the mass of hot molecular and ionized gas, respectively. Following Osterbrock & Ferland (2006) and Storchi-Bergmann et al. (2009), the mass of ionized ($M_{\rm HII}$) gas can be obtained from

$$\left(\frac{M_{\rm HII}}{M_\odot}\right) = 3\times10^{19}\left(\frac{F_{\rm Br\gamma}}{\rm erg\,cm^{-2}\,s^{-1}}\right)\left(\frac{D}{\rm Mpc}\right)^2\left(\frac{N_e}{\rm cm^{-3}}\right)^{-1}, \quad (1)$$

where D is the distance to the galaxy, $F_{\rm Br\gamma}$ is the Brγ flux and N_e is the electron density, assuming an electron temperature of 10^4K. We have adopted an electron density of $N_e = 500\,{\rm cm^{-3}}$, which is a typical value for the inner few hundred pcs of AGNs as determined from the [S II]$\lambda\lambda$6717,6730 lines (e.g. Dors et al. 2014; Brum et al. 2017).

Under the assumptions of local thermal equilibrium and excitation temperature of 2000 K, the mass of hot molecular gas ($M_{\rm H2}$) can be obtained from (e.g. Scoville et al. 1982; Riffel et al. 2014):

$$\left(\frac{M_{H_2}}{M_\odot}\right) = 5.0776\times10^{13}\left(\frac{F_{H_2\lambda2.1218}}{\rm erg\,s^{-1}\,cm^{-2}}\right)\left(\frac{D}{\rm Mpc}\right)^2, \quad (2)$$

where $F_{H_2\lambda2.1218}$ is the H_2 (2.1218μm) emission-line flux.

We used the equations 1 and 2 to calculate the molecular and ionized gas mass density spaxel-by-spaxel by defining the gas surface mass densities of the molecular and ionized gas as $\Sigma_{\rm H2} = \frac{M_{H_2}}{A_s}$ and $\Sigma_{\rm HII} = \frac{M_{\rm HII}}{A_s}$, respectively, where A_s is the area of each spaxel. Using the calculated values of $\Sigma_{\rm H2}$ and $\Sigma_{\rm HII}$ we constructed the surface mass density profiles shown in Figures 5–9. Following Barbosa et al. (2006), we calculated the position (r) of each spaxel in the plane of the disk as $r = \alpha R$, where

$$R = \sqrt{(x-x_0)^2 + (y-y_0)^2}$$

is the position projected in the plane of the sky (observed

position) and

$$\alpha = \sqrt{\cos^2(\Psi - \Psi_0) + \sin^2(\Psi - \Psi_0)/\cos^2(\mathrm{i})},$$

where Ψ_0 is the orientation of the line of nodes, i is the disk inclination and $\Psi = \tan^{-1}\left(\frac{y-y_0}{x-x_0}\right)$ with (x,y) being the spaxel coordinates and (x_0, y_0) the location of the kinematical center. Then, the surface mass density profiles were constructed by averaging the surface mass densities within concentric rings in the galaxy plane with width of dr =25 pc. For all galaxies we fixed the (x_0, y_0) as the position of the continuum peak and included only spaxels with flux measurements for the corresponding emission lines. For most galaxies, the $H_2\lambda 2.12\,\mu$m and Brγ flux maps have already been published by our group in the references listed in the last column of Table 2. Although the Brγ line is weaker than Paβ, its use is justified due to the fact that using Brγ and $H_2\,\lambda 2.12$ lines, both ionized and molecular masses are derived from the same spectral band and thus the ratio between them is less sensitive to uncertainties in the flux calibrations and extinction, as both lines are are close in wavelength. For two galaxies (NGC 1052 and NGC 5548), the Brγ line was not detected in our spectra and thus we used the Paβ emission line to estimate $M_{\rm HII}$ by assuming the theoretical ratio between the fluxes of Paβ and Brγ of 5.85 for the Case B recombination (Osterbrock & Ferland 2006). The references for the corresponding measurements as well as the discussion about the fitting procedures are listed in the last column of Table 3. This table presents also the adopted Φ_0 and i values, most of them from Riffel et al. (2017), who obtained these values by fitting the observed stellar velocity fields by rotation disk models and from the application of the technique of kinemetry to the measured kinematics. For Mrk 3 and Mrk 79 we used the disk geometric parameters from the Hyperleda database (Makarov et al. 2014), for NGC 1068 from Davies et al. (2007) and for NGC 4151 those presented in Onken et al. (2014).

The top panels of figures 5–9 present for each galaxy the profiles for $\Sigma_{\rm H2}$ in black, in units of 10^{-3} M$_\odot$ pc^{-2}, and $\Sigma_{\rm HII}$ in red in units of M$_\odot$ pc^{-2}. The dotted blue line represents the K-band surface brightness profile obtained from a continuum image derived by averaging the fluxes between 2.23 and 2.30 μm. This profile is shown in units of $C\times$erg s^{-1} cm^{-2} Å^{-1} arcsec^{-2} – where C is an arbitrary constant to put the profile in similar units to those of the mass density profiles – to be used as a tracer of the stellar mass distribution. The bottom panel shows the ratio between $\Sigma_{\rm HII}$ and $\Sigma_{\rm H2}$ or equivalently $\frac{M_{\rm HII}}{M_{H_2}}$, calculated considering only spaxels in which both Brγ and $H_2\lambda 2.12$ flux measurements are available. The dotted horizontal line shows the mean value of $\frac{M_{\rm HII}}{M_{H_2}}$, indicated at the top-right corner of this panel and calculated from the $\Sigma_{\rm HII}/\Sigma_{\rm H2}$ profile. The dashed lines represent the standard error, calculated as the ratio between the standard deviation of the Σ at each ring and the number of spaxels used to compute Σ.

For all galaxies, the ionized and molecular gas mass density profiles decrease with the distance to the nucleus, with the ionized gas showing a steeper gradient for most galaxies. This behavior can be attributed to the different nature of the excitation mechanisms for the ionized and molecular gas: while the former is excited by the AGN radiation, the latter is dominated by thermal excitation through heating of the surrounding gas by X-rays emitted by the AGN (e.g. Dors et al. 2012; Riffel et al. 2013; Colina et al. 2012). As X-rays are less blocked by the surrounding gas, they penetrate in the disk more uniformly in all directions, so that the H_2 flux distributions are also more uniform than those of the ionized gas. The ionized gas usually shows more collimated flux distributions, as the AGN UV radiation is at least partially blocked by the dusty torus. The only exception is NGC 1068, that shows an increase in $\Sigma_{\rm H2}$ between 25 and 75 pc due to the presence of an expanding molecular gas ring (e.g. Müller-Sánchez et al. 2009; Riffel et al. 2014; Barbosa et al. 2014). Both the ionized and molecular surface density profiles usually decrease more slowly with distance from the nucleus than the K-band brightness profile. The fact that the gas mass density profiles are less steep than the stellar brightness profile is probably due to the fact that the gas has (more recently than the stars) settled in a disc, while the stellar density profile is dominated by stars from the galaxy bulge. The bottom panels for each galaxy shows the radial profile for $\frac{M_{\rm HII}}{M_{H_2}}$, that confirm the trend that ionized gas shows an steeper decrease in surface mass density than the molecular gas, as the $\frac{M_{\rm HII}}{M_{H_2}}$ for most galaxies have the highest values at the nucleus or at small distances from it. The mean values of $< \frac{M_{\rm HII}}{M_{H_2}} >$, indicated at the top-left corner of each panel, range from ∼200 for Mrk 607 to ∼8000 for NGC 5506.

Table 3 shows the total mass of ionized and hot molecular gas for each galaxy by summing up the masses from all spaxels with detected Brγ and $H_2\lambda 2.12\,\mu$m emission. The uncertainties in the masses are not included in this table, they are dominated by the uncertainty in flux calibration and can be up to 20 %. The mass of ionized gas is in the range $(3-440)\times10^4$ M$_\odot$, while that for the hot molecular gas ranges from 50 to 3 000 M$_\odot$. The mean surface mass density for the ionized and molecular gas, shown in Table 3 are in the ranges (0.2–35.9) M$_\odot$ pc^{-2} and (0.2–13.9)$\times10^{-3}$ M$_\odot$ pc^{-2}. These values are in good agreement with those previously obtained, summarized by Schönell et al. (2017) in their Table 1. The distribution of ionized and molecular masses and surface mass densities for the galaxies of our sample are presented in Figure 10.

In order to further investigate the distribution of ionized and molecular gas in the inner few hundreds of parsercs of the galaxies of our sample, we constructed normalized radial profiles by dividing the $M_{\rm HII}/M_{\rm H2}$ value at each radial bin by the nuclear value ($r < 25$ pc). These profiles are shown in Figure 11. Seyfert 1 galaxies (Mrk 766, Mrk 79, NGC 3227, NGC 3516, NGC 4051, NGC 4151 and NGC 5548) are shown as red continuous lines and Seyfert 2 galaxies (Mrk 1066, Mrk 1157, Mrk 3, Mrk 607, NGC 1052, NGC 1068, NGC 2110, NGC 4388, NGC 5506, NGC 5899, NGC 5929, NGC 788) as blue dashed lines. These profiles confirm the result already mentioned above that the ionized gas has an steeper surface mass profile, as for most galaxies the $M_{\rm HII}/M_{\rm H2}$ decreases with the distance to the nucleus. In addition, Figure 11 shows that there is no significant difference for the distribution of ionized and molecular gas for Seyfert 1 and Seyfert 2 nuclei.

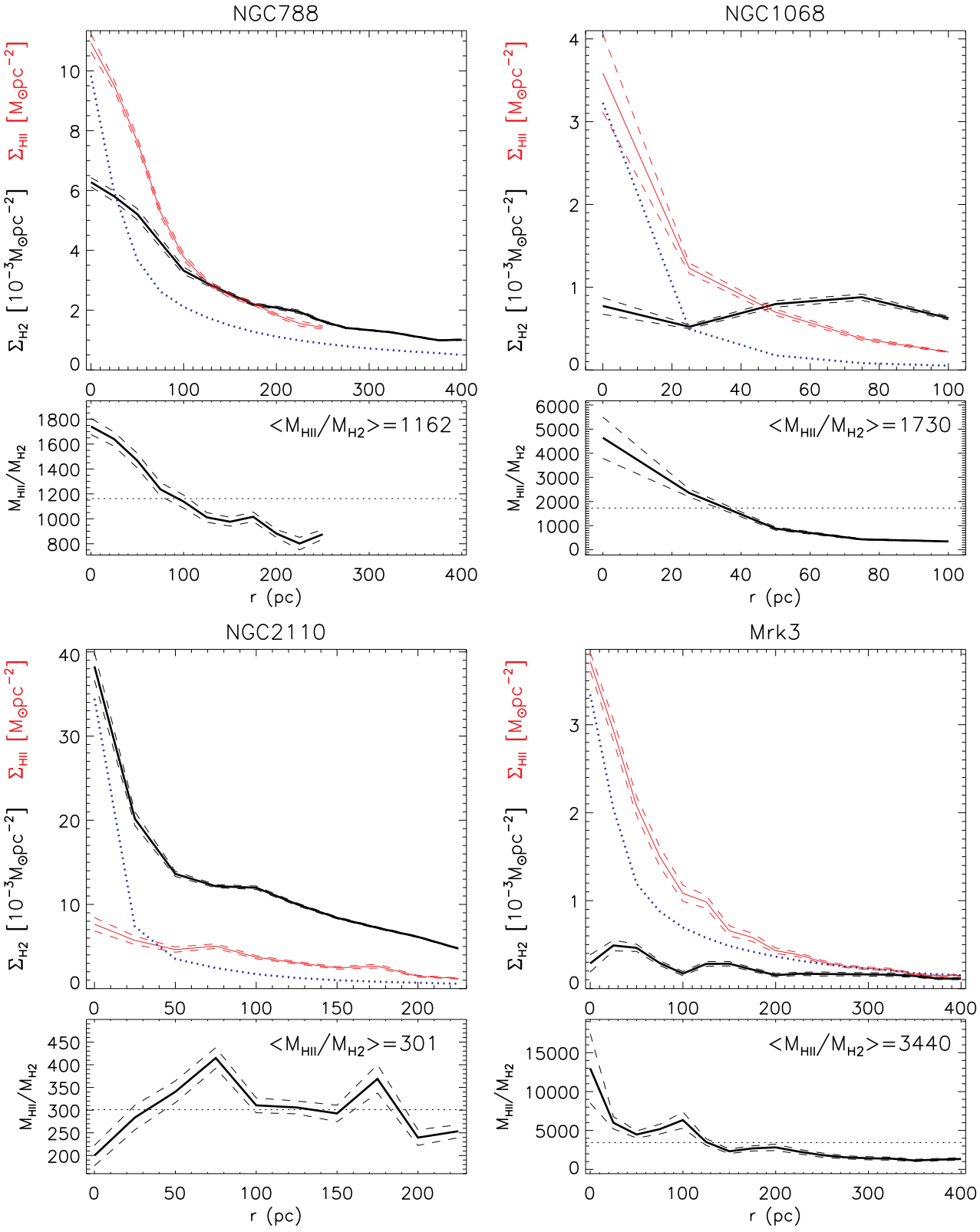

Figure 5. The top panels show the surface mass density profiles for the hot molecular (black) and ionized (red) for a radial bin of 25 pc at the plane of the galaxy. The profiles are shown as continuous lines and the dashed lines shows the standard error variation. The K-band surface brightness is shown as a dotted blue line in units of $C\times$erg s^{-1} cm^{-2} Å^{-1} arcsec^{-2}, where C is an arbitrary constant. The bottom panels show the ratio ratio between the mass of ionized and molecular gas variation for the same radial bin, considering only spaxels with measurements of both masses. The mean value of the ratio $< M_{\rm HII}/M_{\rm H2} >$ is shown at the top-right corner of the corresponding panel. The geometric parameters of the disk, used in the deprojection are shown in Table 3. In this figure, we show the profiles for NGC 788, NGC 1068, NGC 2110 and Mrk 3.

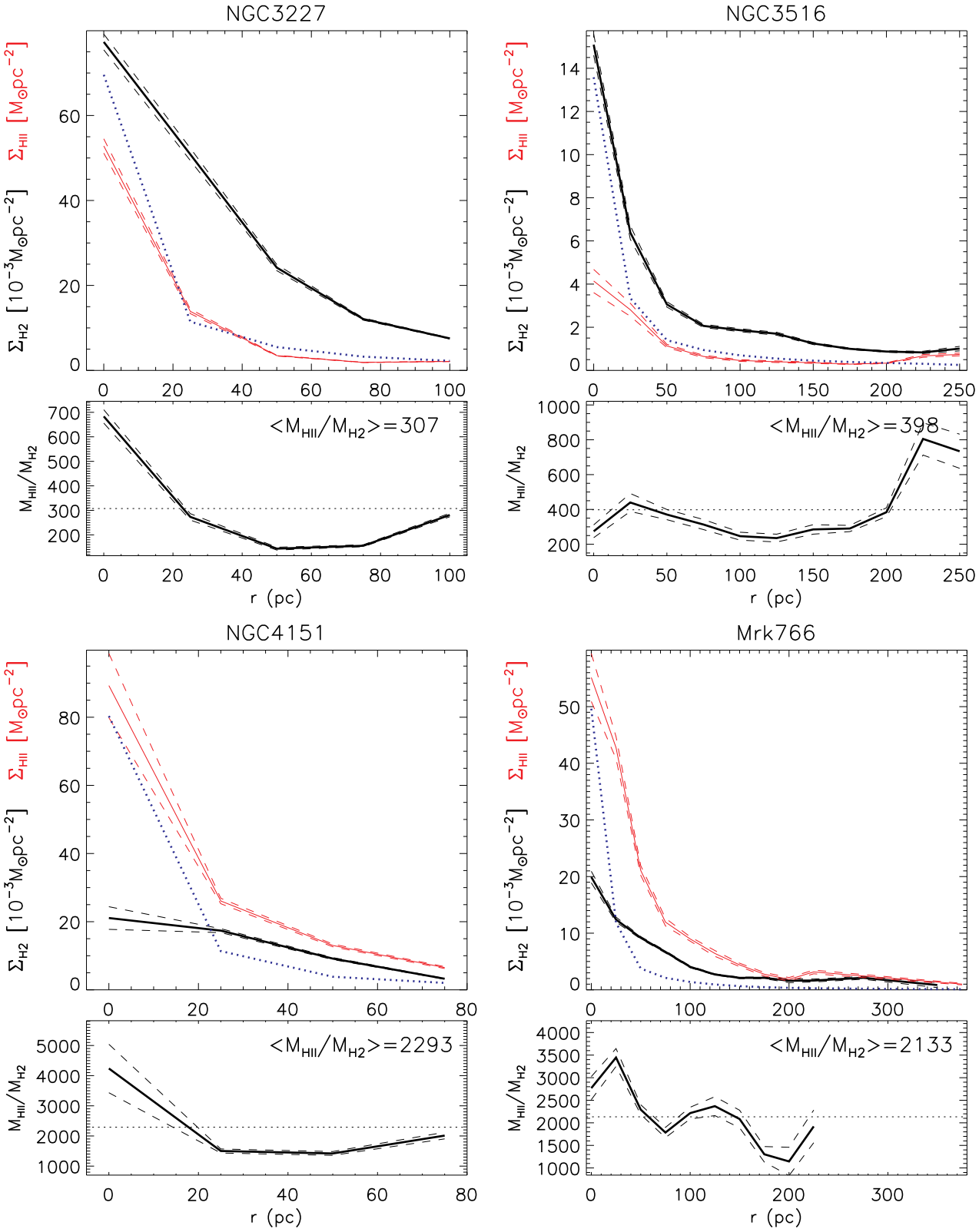

Figure 6. Same as Fig. 5 for NGC 3227, NGC 3516, NGC 4151 and Mrk 766.

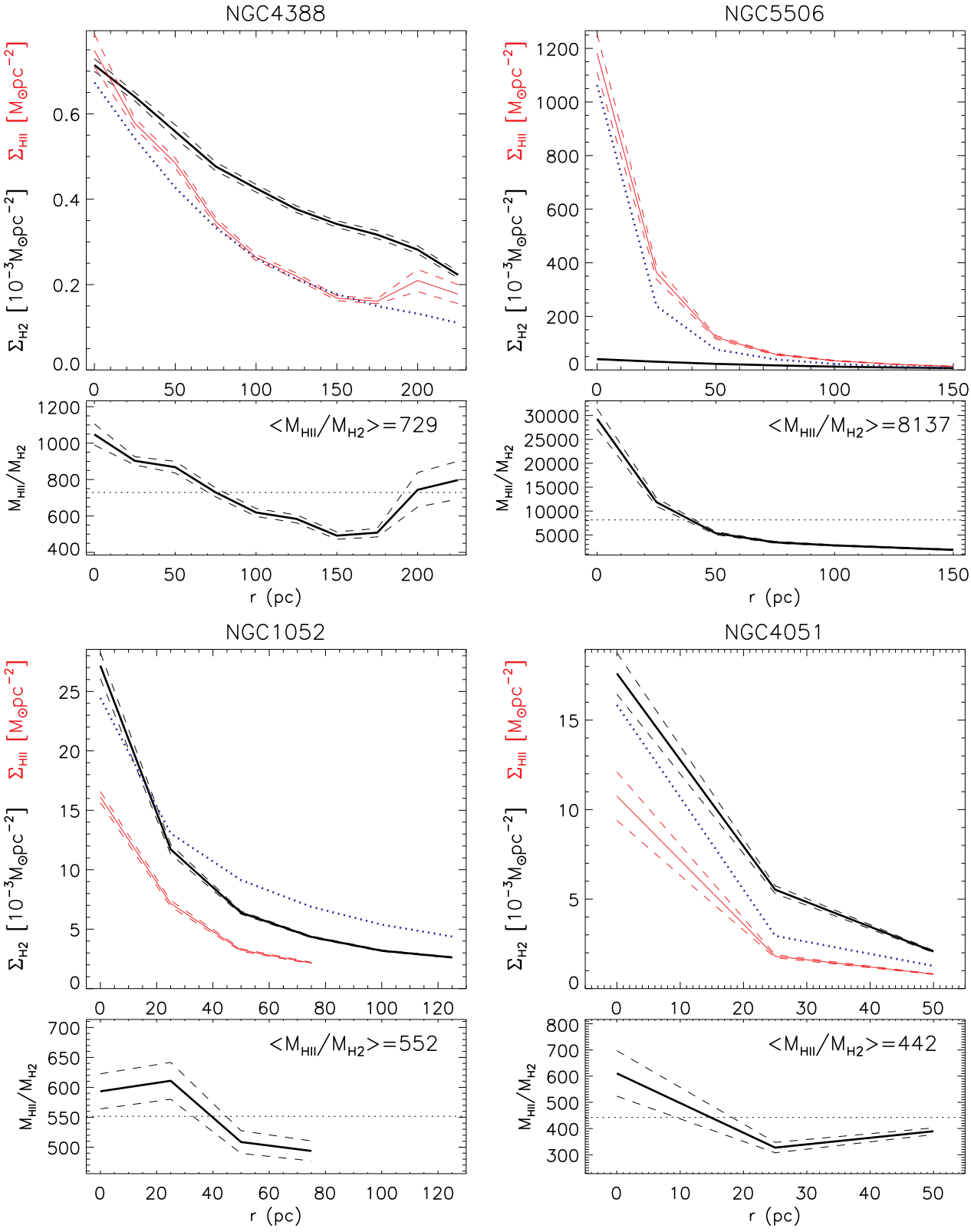

Figure 7. Same as Fig. 5 for NGC 4388, NGC 5506, NGC 1052 and NGC 4051.

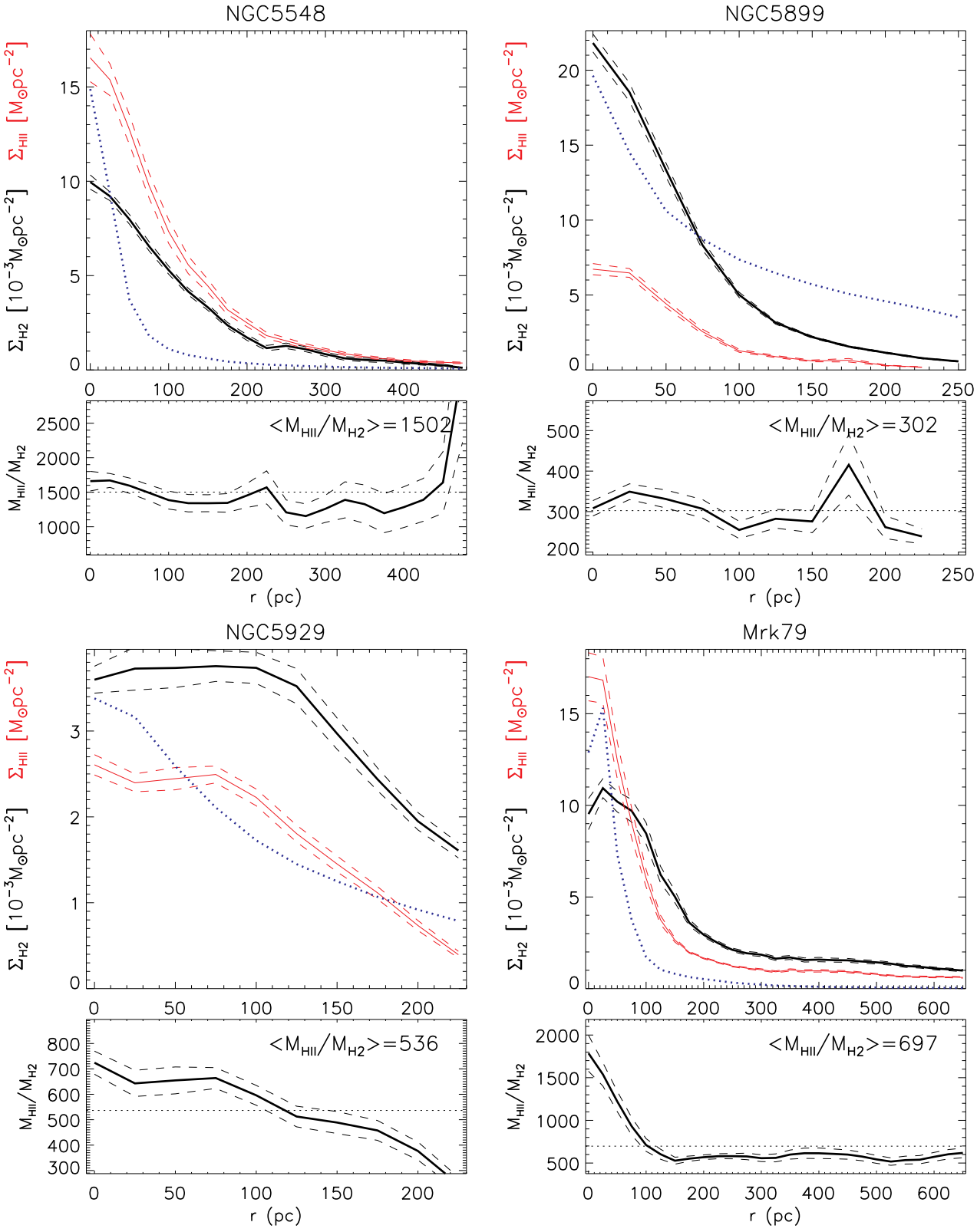

Figure 8. Same as Fig. 5 for NGC 5548, NGC 5899, NGC 5929 and Mrk 79.

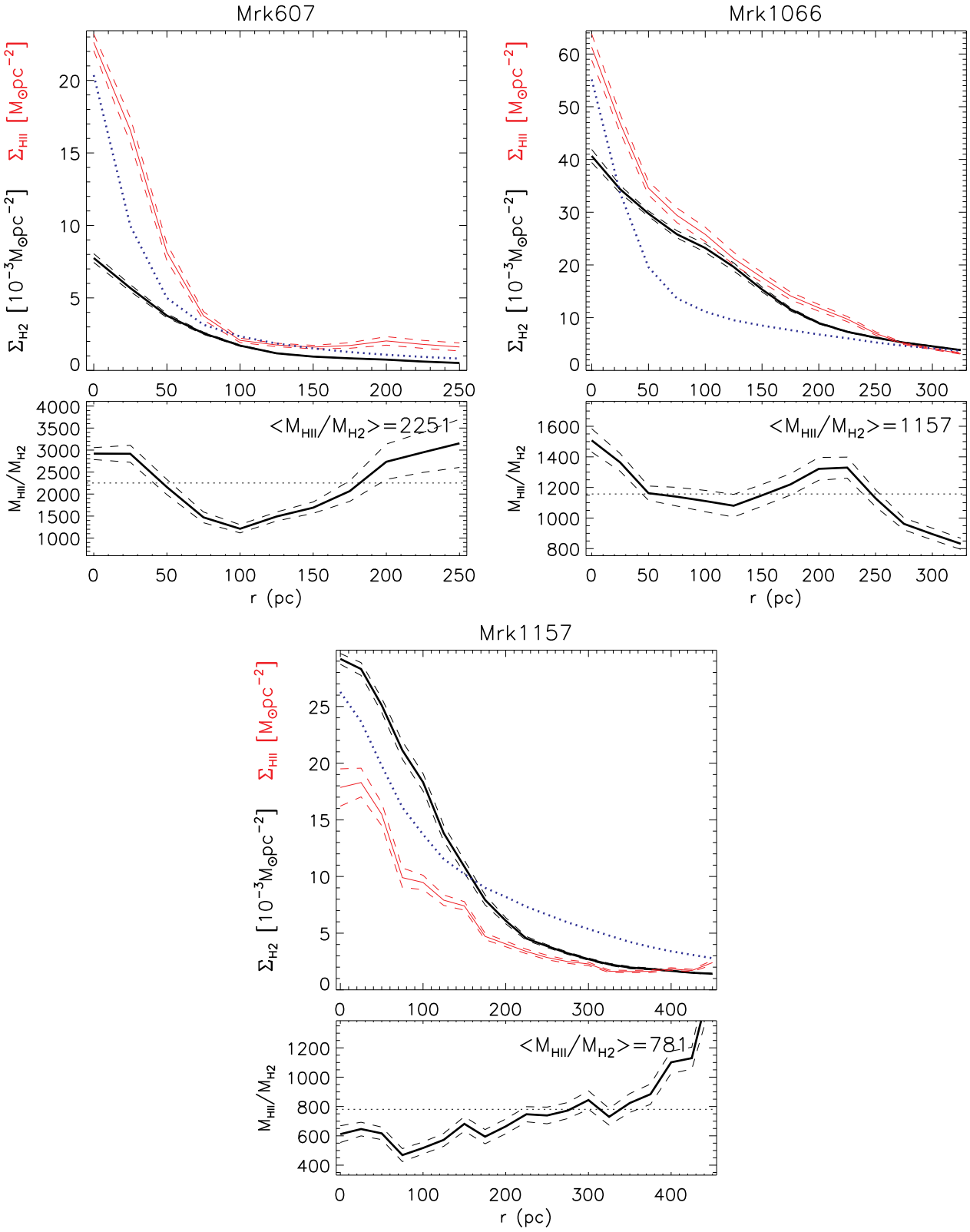

Figure 9. Same as Fig. 5 for Mrk 607, Mrk 1066 and Mrk 1157.

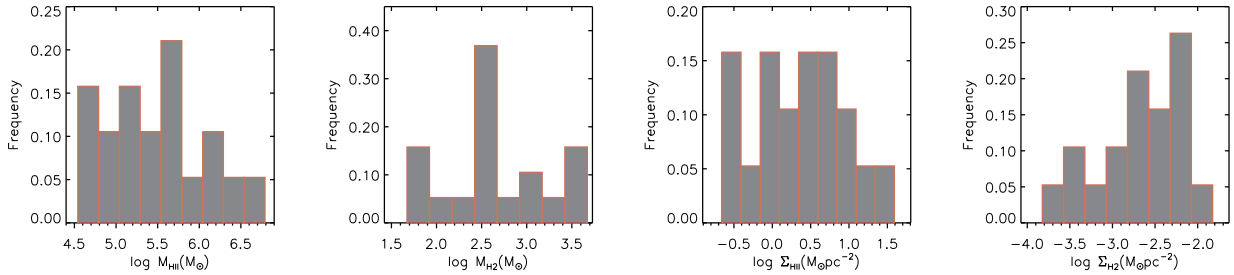

Figure 10. Histograms for M_{HII}, Σ_{HII}, M_{H2} and Σ_{H2} for our sample, constructed using the values from Table 3 using a bin of 0.25 dex.

Table 3. Molecular and ionized gas masses and surface densities. (1) Name of the galaxy; (2) Total mass of ionized gas; (3) Area for the Brγ emission; (4) Average surface mass density for the ionized gas; (5) Total mass of hot molecular gas; (6) Area for the $H_2\,\lambda2.12$ emission; (7) Average surface mass density for the hot molecular gas; (8) Average star formation density; (9) total star formation rate; (10) and (11) orientation of the major axis and inclination of the disk, used in the deprojection from Riffel et al. (2017), except for Mrk 3 and Mrk 79 (from Hyperleda database Makarov et al. 2014), NGC 1068 (from Davies et al. 2007) and NGC 4151 (from Onken et al. 2014); (12) AGN bolometric luminosity estimated from the 14-195 keV luminosity; (13) mass accretion rate onto the SMBH; (14) Reference for the $H_2\,\lambda2.12$ and Brγ flux maps.

(1) Galaxy	(2) M_{HII} $10^4 M_\odot$	(3) A_{HII} 10^4pc^2	(4) $<\Sigma_{HII}>$ $M_\odot$/pc^2	(5) M_{H2} $10^2 M_\odot$	(6) A_{H2} 10^4pc^2	(7) $<\Sigma_{H2}>$ $10^{-3} M_\odot$/pc^2	(8) $<\Sigma_{SFR}>$ $10^{-3} M_\odot$/yr kpc^2	(9) SFR $10^{-4} M_\odot$/yr	(10) Ψ_0 deg	(11) i deg	(12) log L_{bol} erg/s	(13) $\dot{m}$ 10^{-3} $M_\odot$/yr	(14) Ref.
Main Sample													
NGC788	36.11	8.30	4.35	10.90	70.25	1.55	1.96	1.63	120	20.8	44.4	49.2	a
NGC1068	3.47	15.59	0.22	0.54	15.86	0.34	0.03	0.05	145	40.0	42.8	1.1	b
NGC2110	28.17	11.00	2.56	15.66	23.79	6.59	0.93	1.03	156	42.5	44.6	65.4	c
Mrk3	22.39	59.90	0.37	0.47	31.03	0.15	0.06	0.38	15	31.7	44.7	87.2	d
NGC3227	17.87	2.69	6.64	7.81	5.95	13.12	3.54	0.95	156	45.4	43.4	4.1	a
NGC3516	11.62	15.94	0.73	3.87	30.63	1.26	0.16	0.26	54	12.8	44.2	27.9	a
NGC4151	59.22	5.93	9.99	2.87	5.72	5.02	6.27	3.72	85	23.0	44.0	16.0	e
Mrk766	51.60	2.93	17.60	3.75	6.53	5.74	13.85	4.06	66	18.2	44.0	16.0	f
NGC4388	4.36	18.37	0.24	0.67	22.31	0.30	0.03	0.06	96	27.7	44.6	65.4	a
NGC5506	439.64	12.26	35.86	8.89	12.00	7.41	37.53	46.01	96	58.7	44.3	37.0	a
Complementary Sample													
NGC1052	6.18	0.92	6.70	3.00	7.56	3.96	3.58	0.33	114	47.5	42.9	1.4	g
NGC4051	3.64	2.13	1.71	0.86	2.91	2.94	0.53	0.11	24	37.3	42.5	0.5	h
NGC5548	74.49	85.30	0.87	3.80	15.70	2.42	0.21	1.76	108	60.9	44.7	87.2	i
NGC5899	8.10	3.81	2.12	3.60	23.45	1.53	0.72	0.27	24	62.7	43.1	2.4	a
NGC5929	14.70	23.77	0.62	3.94	28.86	1.37	0.13	0.30	30	60.7	–	–	j
Mrk79	169.24	163.24	1.04	26.90	179.32	1.50	0.26	4.29	73	35.6	44.8	116.4	k
Mrk607	51.85	20.30	2.55	2.06	28.49	0.72	0.93	1.89	138	58.2	–	–	a
Mrk1066	305.89	31.45	9.73	30.11	45.02	6.69	6.04	19.0	120	50.2	–	–	l
Mrk1157	188.70	65.13	2.90	28.24	89.60	3.15	1.11	7.22	114	45.1	–	–	m

a: Schonell et al., in prep.; b: Riffel et al. (2014); c: Diniz et al. (2015) ; d: Fischer et al., in prep.; e: Storchi-Bergmann et al. (2009)
f: Schönell et al. (2014); g: Dahmer-Hahn et al, in prep.; h: Riffel et al. (2008); i: Schönell et al. (2017); j: Riffel, Storchi-Bergmann & Riffel (2015);
k: Riffel, Storchi-Bergmann & Winge (2013); l: Riffel, Storchi-Bergmann & Nagar (2010); m: Riffel & Storchi-Bergmann (2011b)

4 FEEDING THE AGN AND STAR FORMATION

We can estimate the accretion rate ($\dot{m}$) to the AGN in each galaxy by

$$\dot{m} = \frac{L_{bol}}{c^2 \eta}, \quad (3)$$

where L_{bol} is the AGN bolometric luminosity, c is the light speed and η is the efficiency of conversion of the rest mass energy of the accreted material into radiation. The AGN bolometric luminosity can be estimated from the hard X-ray luminosity by (Ichikawa et al. 2017)

$$\log L_{bol} = 0.0378(\log L_X)^2 - 2.03 \log L_X + 61.6, \quad (4)$$

where L_X is the hard X-ray (14-195 keV) luminosity. The resulting $\dot{m}$ values using the X-ray luminosities from Table 1 and assuming $\eta \approx 0.1$ (e.g. Frank, King & Raine 2002), are shown in Table 3. The $\dot{m}$ for our sample ranges from 10^{-4} (for NGC 4051) to 10^{-1} $M_\odot$ yr^{-1} (for Mrk 79), with a mean value of $<\dot{m}>\sim 0.03$ $M_\odot$ yr^{-1}.

The surface mass density profiles of Figs. 5–9 show that most of the ionized and molecular gas masses listed in Table 3 are concentrated within the inner ~300 pc of the galaxies. The ionized gas mass alone would be enough to feed the central AGN for an activity cycle of $10^7 - 10^8$ yr. The hot molecular gas mass is typically 3 orders of magnitudes lower than that of the ionized gas, but this gas is just the heated surface of a probably much larger molecular gas reservoir of colder molecular gas, that may be $10^5 - 10^7$ times

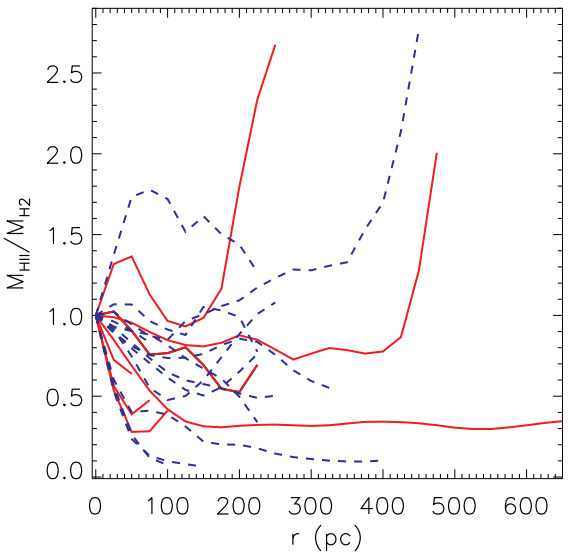

Figure 11. Normalized (by the nuclear value) radial profiles of $M_{\rm HII}/M_{\rm H2}$. Seyfert 1 galaxies are shown as continuous red lines and Seyfert 2 galaxies as dashed blue lines.

more massive (Dale et al. 2005; Müller-Sánchez et al. 2006; Mazzalay et al. 2013), implying that the masses of the cold molecular gas probably range from $10^7 - 10^9$ M$_\odot$.

We conclude that, within the inner 300 pc of our sample, there is at least $\sim 10^2$ times more gaseous mass than the necessary to feed the AGN. Most of this mass will not feed the AGN and might be consumed by star formation. The pioneer work by Schmidt (1959) showed that the star formation rate (*SFR*) is directly related to the gas density, while Kennicutt (1998) derived a relation between the SFR surface density (Σ_{SFR}) and the ionized gas mass surface density ($\Sigma_{\rm HII}$) so that the former can be obtained from the latter as

$$\frac{\Sigma_{SFR}}{M_\odot yr^{-1} kpc^{-2}} = (2.5 \pm 0.7) \times 10^{-4} \left(\frac{\Sigma_{\rm HII}}{M_\odot pc^{-2}} \right)^{1.4}, \quad (5)$$

where $\Sigma_{\rm HII}$ is the surface mass density.

Using the equation above, we obtained the mean values of the star formation density $<\Sigma_{SFR}>$ for each galaxy, shown in Table 3, which varies from 3×10^{-5} to 3.8×10^{-2} $M_\odot yr^{-1} kpc^{-2}$. We point out that these should be minimum values, as we are considering only the ionized gas, and there should much more molecular gas than traced by the hot molecular gas phase that we have observed. Considering the area of the Brγ emission quoted in Table 3, we obtain a wide range of minimum total star formation rate of 10^{-6}–10^{-3} M$_\odot$ yr^{-1} (shown in Table 3). These values of *SFR* are smaller smaller than those usually obtained for the nucleus of star-forming galaxies and circumnuclear rings of star formation ($SFR \sim 10^{-3}$ M$_\odot$ yr^{-1}) (e.g. Wold & Galliano 2006; Shi, Gu & Peng 2006; Dors et al. 2008; Galliano & Alloin 2008; Falcón-Barroso et al. 2014; Riffel et al. 2016). Considering a scenario in which the total mass would be used to form stars, the estimated masses for our sample would allow the star formation for about 10^9 yr at the current star formation rate.

Thus, considering the derived mass accretion rate, the star formation rate and the mass of molecular and ionized gas, we conclude that the mass reservoirs of the galaxies of our sample are much larger than that needed to power the central AGN and star formation, thus allowing the coexistence of recent star formation (as evidenced by low-stellar velocity dispersion structures seen in some galaxies, Riffel et al. 2017) and the nuclear activity.

5 CONCLUSIONS

We characterized a sample of 20 nearby X-ray selected Seyfert galaxies being observed with the NIFS instrument of the Gemini North Telescope plus a complementary sample of 9 additional galaxies already observed with NIFS. We also present and discuss mean radial profiles within the inner kiloparsec for the ionized and molecular gas surface mass densities for the galaxies already observed: 11 from the main X-ray sample and 9 galaxies from the complementary sample. Our main conclusions are:

- The average values of X-ray luminosities are $<\log L_X>= 42.6 \pm 0.1$ erg s^{-1} for the main sample and $<\log L_X>= 42.4 \pm 0.1$ erg s^{-1} for the main plus complementary sample. The [O III]λ5007 luminosities are in the range $L_{[OIII]} = (0.2-155) \times 10^{40}$ erg s^{-1}, with a mean value of $<\log L_{[OIII]}>= 41.0 \pm 0.2$ erg s^{-1}.
- The M_B and M_H distributions for the restricted BAT sample (all galaxies with $L_X \geq 10^{41.5}$ ergs s^{-1} and $z \leq 0.015$ from the 60 month BAT catalogue) and our sample are very similar, indicating that the additional criteria used in the definition of our sample does not include any bias in terms of these properties. The mean values for our sample are $< M_B >= -20.75 \pm 0.16$ and $< M_H >= -23.83 \pm 0.13$.
- The mean value of the central stellar velocity dispersion of the total sample is 154 ± 11 km s^{-1}, being essentially the same as that of the X-ray sample only.
- The axial ratio b/a of the total sample ranges from 0.2 (corresponding to a disk inclination of $i \sim 80°$, almost edge-on) to 0.9 ($i \sim 25°$, almost face-on).
- We constructed mean radial profiles for the surface mass density of the ionized ($\Sigma_{\rm HII}$) and hot molecular ($\Sigma_{\rm H2}$) gas for the 20 galaxies already observed, derived from the Brγ and H$_2\lambda$2.12μm fluxes. Both profiles decrease with the distance from the nucleus for most galaxies, with the ionized gas showing a steeper gradient. The only exception is NGC 1068, which shows an increase in $\Sigma_{\rm H2}$ at 25–75 pc from the nucleus due to the presence of a molecular gas ring. We attribute this difference in behavior to the distinct origin of the gas emission: while for the H$^+$ the emission is due to recombination of ionized gas by the AGN, for the H$_2$ the excitation is mostly thermal due to the heating of the gas by X-rays that penetrate deeper into the surrounding gas in the galaxy plane.
- The mean surface mass density for the ionized and molecular gas are in the ranges (0.2–35.9) M$_\odot$ pc^{-2} and (0.2–13.9)$\times 10^{-3}$ M$_\odot$ pc^{-2}, respectively, while the ratio between them ranges from ∼200 for Mrk 607 to ∼8000 for NGC 5506. The mean star formation surface density is <

$\Sigma_{SFR} >= (4.09 \pm 0.44) \times 10^{-3} M_\odot\,yr^{-1}\,kpc^{-2}$, while the star formation rates range from 10^{-6} to 10^{-3} $M_\odot\,yr^{-1}$, with the accretion rate onto the SMBH ranging from 10^{-4} to 10^{-1} $M_\odot$ yr^{-1}.

- The total mass of ionized gas within the inner $\sim 100-500$ pc is in the range $(3-440) \times 10^4\,M_\odot$, while that of hot molecular gas ranges between 50 and 3000 $M_\odot$. Considering also that the mass of cold molecular gas is usually $\sim 10^5$ times larger than that of hot molecular gas for AGN in general, we estimate a total mass of gas in the region ranging from 10^6 to 10^8 $M_\odot$. Comparing these masses with the typical accretion rates above, it can be concluded that they are much larger than that necessary to feed a typical AGN cycle of of $10^7 - 10^8$ yr. The fate of this gas is probably the formation of new stars in the region (the AGN-Starburst connection).

ACKNOWLEDGMENTS

We thank an anonymous referee for useful suggestions which helped to improve the paper. Based on observations obtained at the Gemini Observatory, which is operated by the Association of Universities for Research in Astronomy, Inc., under a cooperative agreement with the NSF on behalf of the Gemini partnership: the National Science Foundation (United States), the Science and Technology Facilities Council (United Kingdom), the National Research Council (Canada), CONICYT (Chile), the Australian Research Council (Australia), Ministério da Ciência e Tecnologia (Brazil) and south-eastCYT (Argentina). This research has made use of the NASA/IPAC Extragalactic Database (NED) which is operated by the Jet Propulsion Laboratory, California Institute of Technology, under contract with the National Aeronautics and Space Administration. We acknowledge the usage of the HyperLeda database (http://leda.univ-lyon1.fr). This publication makes use of data products from the Two Micron All Sky Survey, which is a joint project of the University of Massachusetts and the Infrared Processing and Analysis Center/California Institute of Technology, funded by the National Aeronautics and Space Administration and the National Science Foundation. The Brazilian authors acknowledge support from FAPERGS, CNPq and CAPES. L.B. was partly supported by a DFG grant within the SPP 1573 "Physics of the interstellar medium".

REFERENCES

Aalto, S. et al. 2012, A&A, 573, 44
Ajello, M., Alexander, D. M., Greiner, J., Madejski, G. M., Gehrels, N., Burlon, D., 2012, ApJ, 749, 21.
Audibert, A., Riffel, R., Sales, D. A., Pastoriza, M. G., Ruschel-Dutra, D., 2017, MNRAS, 464, 2139.
Barbosa, F. K. B., Storchi-Bergmann, T., Cid Fernandes, R., Winge, C., & Schmitt, H. 2006, MNRAS, 371, 170.
Barbosa, F. K., Storchi-Bergmann, McGregor, P., Vale, T. B., Riffel, R. A.., 2014, MNRAS, 455, 2353.
Bigiel, F., Leroy, A., Walter, F., Brinks, E., de Blok, W. J. G., Madore, B., Thornley, M. D., 2008, AJ, 136, 2846.
Bradt, H. V., Burke, B. F., Canizares, C. R., Greenfield, P. E., Kelley, R. L., McClintock, J. E., van Paradijs, J. & Koski, A. T., 1978, ApJ, 226, 111.
Brum, C., Riffel, R. A., Storchi-Bergmann, T., Robinson, A., Schnorr Müller, A., Lena, D., 2017, MNRAS, 469, 3405.
Cid Fernandes, R. et al. 2004, MNRAS, 355, 273
Colina, L. et al., 2015, A&A, 578, 48.
Dale, D. A., Sheth, K., Helou, G., Regan, M. W., & Hüttemeister, S., 2005, ApJ, 129, 2197.
Davies, R. I. et al. 2007, ApJ, 671, 1388
Davies, R. I., Maciejewski, W., Hicks, E. K. S., Tacconi, L. J., Genzel, R., Engel, H., 2009, ApJ, 702, 114.
Davies, R. I, et al., 2015, ApJ, 806, 127.
Davies, R. I, et al., 2017, MNRAS, 466, 4917.
de Vaucouleurs, G., de Vaucouleurs, A., Corwin, H. G., Jr., et al. 1991, Third Reference Catalogue of Bright Galaxies, Volume I: Explanations and references, Volume II: Data for galaxies between 0h and 12h, Volume III: Data for galaxies between 12h and 24h (New York: Springer)
Diniz, M. R., Riffel, R. A., Stochi-Bergmann, T., Winge, C., 2015, MNRAS, 453, 1727.
Dors, O. L., Storchi-Bergmann, T., Riffel, R. A., Schmidt, A. A, 2008, A&A, 482, 59.
Dors, O. L., Riffel, R. A., Cardaci, M. V., Hägele, G. F., Krabbe, A. C., Pérez-Montero, E., Rodrigues, I., 2012, MNRAS, 422, 252.
Dors, O. L., Cardaci, M., Hägele, G., Krabbe, A., 2014, MNRAS, 442, 1291.
Durré M. & Mould J., 2014, ApJ, 784, 79.
Croton D., et al., 2006, MNRAS, 365, 11
Falcoón-Barroso, J., Ramos Almeida, C., Böker, T., Schinnerer, E., Knapen, J. H., Lanǫn, A., Ryder, S., 2014, MNRAS, 438, 329.
Ferrarese, L., & Merritt, D., 2000, ApJ, 539, L9.
Ferrarese, L. & Ford, H. 2005, SSRv, 116, 523
Ferruit, P., Mundell, C. G., Nagar, N. M., Emsellem, E., Pécontal, E., Wilson, A. S., Schinnerer, E. 2004, MNRAS, 352, 1180.
Frank, J, King, A. & Raine, D. J., 2002, Accretion Power in Astrophysics, Cambridge Univ. Press
Ciotti, L., et al. 2010, ApJ 717, 707
Elvis, M. 2000, ApJ, 545, 63
Fabian, A. 2012, ARA&A, 50, 455
Frank, J., King, A. R., & Raine, D. J. 2002, Accretion Power in Astrophysics (3rd ed.; Cambridge: Cambridge Univ. Press)
Galliano, E., & Alloin, D. 2008, A&A, 487, 519.
Gebhardt, K., Bender, R., Bower, G., Dressler, A., Faber, S. M., Filippenko, A. V., Green, R., Grillmair, C., Ho, L. C., Kormendy, J., Lauer, T. R., Magorrian, J., Pinkney, J., Richstone, D., & Tremaine, S., 2000, ApJ, 539, L13.
González Delgado, R.M., Heckman, T. & Leitherer, C. 2001, ApJ, 546, 845.
González Delgado, R. M., Arribas, S., Pérez, E., Heckman, T., 2002, ApJ, 579, 188.
Graham, A. W., Onken, C. A., Athanassoula, E., Combes, F., 2011, MNRAS, 412, 2211.
Gu, Q., Melnick, J., Cid Fernandes, R., Kunth, D., Terlevich, E., Terlevich, R., 2006, MNRAS, 366, 480.
Heckman, T. M. & Best, P. N. 2014, ARA&A, 52, 589.
Hicks, E. K. S., Davies, R. I., Maciejewski, W., Emsellem, E., Malkan, M. A., Dumas, G., Müller-Sánchez, F., Rivers, A., 2013, ApJ, 768, 107.
Hopkins & Quataert 2010, MNRAS, 407, 1529
Hopkins, P. F. 2012, MNRAS, 420, 8.
Ichikawa, K., Ricci, C., Ueda, Y., Matsuoka, K., Toba, Y., Kawamuro, T., Trakhtenbrot, B., Koss, M. J., 2017, ApJ, 835, 74.
Kauffmann & Heckman 2009, MNRAS, 397, 135
Kennicutt, R. C., 1998, ARAA, 36, 189.
Kennicutt, R. C. et al., 2007, ApJ, 671, 333.
Kormendy, J. & Ho, L. C, 2013, ARA&A, 51, 511
Lamperti, I. et al., 2017, MNRAS, 467, 540.

Makarov, D., Prugniel, P., Terekhova, N., Courtois, H., Vauglin, I., 2014, A&A, 570, 13
Malkan, M. A., Gorjian, V. & Tam, R., 1998, ApJS, 117,25.
Martini, P., et al. 2013, MNRAS, 420, 2249
Mazzalay, X. et al., 2013, MNRAS, 428, 2389.
Mazzalay, X. et al., 2014, MNRAS, 438, 2036.
McGregor, P. J., Hart, J., Conroy, P. G., Pfitzner, M. L., Bloxham, G. J., Jones, D. J., Downing, M. D., Dawson, M., Young, P., Jarnyk, M., &Van Harmelen, J. 2003, Proceedings of the SPIE, 4841, 1581.
Mulchaey, J. S., Wilson, A. S., Bower, G. A., Heckman, T. M., Krolik, J. H., Miley, G. K., 1994, ApJ, 433, 625.
Müller-Sánchez F., Davies R. I., Eisenhauer F., Tacconi L. J., Genzel R., Sternberg A., 2006, A&A, 454, 492.
Müller-Sánchez, F., Davies, R. I., Genzel, R., Tacconi, L. J., Eisenhauer, F., Hicks, E. K. S., Friedrich, S., & Sternberg, A., 2009, ApJ, 691, 749.
Müller Sánchez, F. et al. 2011, ApJ, 739, 69
Nagar, N. M., Wilson, A. S., Mulchaey, J. S. & Gallimore, J. F., 1999, ApJS, 120, 209.
Noguchi, K., Terashima, Y., Ishino, Y., Hashimoto, Y., Koss, M., Ueda, Y., Awaki, H., 2010, ApJ, 711, 144.
Onken, C. et al., 2014, ApJ, 791, 37.
Osterbrock, D. E. & Ferland, G. J., 2006, Astrophysics of Gaseous Nebulae and Active Galactic Nuclei, Second Edition, University Science Books, Mill Valley, California.
Ramos Almeida, C. et al., 2014, MNRAS, 445, 1130.
Riffel, R. A.., Sorchi-Bergmann, T., Winge, C., Barbosa, F. K. B., 2006, MNRAS, 373, 2.
Riffel, R. A., Storchi-Bergmann, T., Winge, C., McGregor, P., Beck, T. & Schmitt, H., 2008, MNRAS, 385, 1129
Riffel, R. A., Storchi-Bergmann, T., McGregor, P., 2009, ApJ, 698, 1767
Riffel, R. A.., Storchi-Bergmann, T. & Nagar, N. M., 2010, MNRAS, 404, 166.
Riffel, R. A.. & Storchi-Bergmann, T., Riffel, R., & Pastoriza, M. G., 2010, ApJ, 713, 469.
Riffel, R. A.. & Storchi-Bergmann, T., 2011, MNRAS, 411, 469.
Riffel, R. A.. & Storchi-Bergmann, T., 2011, MNRAS, 417, 2752.
Riffel, R. A., Storchi-Bergmann, T., Winge, C., 2013, 430, 2249.
Riffel, R. A., Vale, T. B., Storchi-Bergmann, T., McGregor, P. J., 2014, MNRAS, 442, 656.
Riffel, R. A., Storchi-Bergmann, T., Riffel, R., ApJ, 2014, 780, 24.
Riffel, R. A., Storchi-Bergmann, T., Riffel, R., 2015, MNRAS, 451, 3587.
Riffel, R. A. et al. 2016, MNRAS, 461, 4192.
Riffel, R. A. et al. 2017, MNRAS, 470, 992.
Riffel, R., Rodríguez-Ardila, A. & Pastoriza, M. G., 2006, A&A, 457, 61.
Riffel, R., Pastoriza, M. G., Rodríguez-Ardila, A., Bonatto, C., 2009, MNRAS, 400, 273.
Riffel, R., Riffel, R. A.., Ferrari, F., Storchi-Bergmann, T., 2011. MNRAS, 416, 493.
Riffel, R., Rodríguez-Ardila, A., Aleman, I., Brotherton, M. S., Pastoriza, M. G., Bonatto, C., Dors, O. L., 2013, MNRAS, 430, 2002.
Rosario D. J., Whittle M., Nelson C. H. & Wilson A. S., 2010, MNRAS, 408, 565.
Schmidt, M., 1959, ApJ, 129, 243.
Schmitt, H. R., Ulvestad, J. S., Antonucci, R. R. J., Kinney, A. L., 2001, ApJS, 132, 199.
Schmitt, H. R., Donley, J. L., Antonucci, R. R. J., Hutchings, J. B., Kinney, A. L., 2003, ApJS, 148, 327.
Scoville, N. Z., Hall, D. N. B., Kleinmann, S. G., & Ridgway, S. T. 1982, 253, 136.
Shankar, F. et al. 2009, ApJ, 690, 20
Sakamoto, K.et al. 2010, ApJ, 725, L228
Schnorr-Müller A., Storchi-Bergmann T., Nagar N. M., Robinson A., Lena D., Riffel R. A. & Couto G. S., 2014, MNRAS, 437, 1708,
Schonel, A. J., Riffel, R. A., Stochi-Bergmann, T., Winge, C., 2014, MNRAS, 445, 414.
Schonel, A. J., Riffel, R. A., Stochi-Bergmann, T., Riffel, R., 2017, MNRAS, 464, 1771.
Simoes Lopes et al. 2007, ApJ, 655, 718
Shi, L., Gu, Q. S., & Peng, Z. X. 2006, A&A, 450, 15.
Skrutskie, M., F. et al., 2006, AJ, 131, 1163.
Somerville et al. 2008, MNRAS, 391, 481
Springel et al. 2005, MNRAS, 361, 776
Storchi-Bergmann, T., Winge, C., Ward, M. & Wilson, A. S., 1999, MNRAS, 304, 35.
Storchi-Bergmann et al. 2000, ApJ, 544, 747.
Storchi-Bergmann et al. 2001, ApJ, 559, 147
Storchi-Bergmann, T., McGregor, P. J., Riffel, R. A., Simões Lopes, R., Beck, T., Dopita, M., 2009, MNRAS, 394, 1148.
Storchi-Bergmann, T., Simões Lopes, R., McGregor, P. Riffel, R. A.., Beck, T., Martini, P., 2010, MNRAS, 402, 819.
Storchi-Bergmann, T., Riffel, R. A.., Riffel, R., Diniz, M. R., Borges Vale, T., McGregor, P. J., 2012, ApJ, 755, 87.
Terlevich E. et al. 1990, MNRAS, 242, 271.
Tremaine, S., Gebhardt, K., Bender, R., Bower, G., Dressler, A., Faber, S. M., Filippenko, A. V., Green, R., Grillmair, C., Ho, L. C., Kormendy, J., Lauer, T. R., Magorrian, J., Pinkney, J., & Richstone, D., 2002, ApJ, 574, 740.
Ulvestad J. S. & Wilson A. S., 1983, ApJl, 264, L7.
Veilleux, S. et al. 2013, ApJ, 776, 27
Zhu, G., Zaw, I., Blanton, M. R., Greenhill, L. J., 2011, ApJ, 742, 73.
Weaver, K. A., Mushotzky, R. F., Serlemitsos, P. J., Wilson, A. S., Elvis, M. & Briel, U., 1995, ApJ, 442, 597.
Whittle, M. 1992, ApJS, 79,49
Wold, M., Galliano, E., 2006, MNRAS, 369, 47.

This paper has been typeset from a TEX/LATEX file prepared by the author.

A.3 Absorções estelares e índices de linhas de emissão no óptico e NIR a partir de galáxias luminosas no infravermelho

Aqui apresentamos uma discussão sobre as absorções estelares em uma comparação direta com os modelos de populações estelares simples. Estes resultados foram publicados na revista MNRAS em Fevereiro de 2018, sob o título *Optical/NIR stellar absorption and emission-line indices from luminous infrared galaxies.*

MNRAS **000**, 1–20 (2018) Preprint 16 April 2019 Compiled using MNRAS LATEX style file v3.0

Optical/NIR stellar absorption and emission-line indices from luminous infrared galaxies

Rogério Riffel[1⋆], Alberto Rodríguez-Ardila[2,9], Michael S. Brotherton[3], Reynier Peletier[4], Alexandre Vazdekis[5], Rogemar A. Riffel[6], Lucimara Pires Martins[7], Charles Bonatto[1], Natacha Zanon Dametto[1], Luis Gabriel Dahmen-Hahn[1], Jessie Runnoe [3,8], Miriani G. Pastoriza[1], Ana L. Chies-Santos [1], Marina Trevisan[1]

[1] *Departamento de Astronomia, Universidade Federal do Rio Grande do Sul, Av. Bento Gonçalves 9500, 91501-970, Porto Alegre, RS, Brasil.*
[2] *Laboratório Nacional de Astrofísica/MCT - Rua dos Estados Unidos 154, Bairro das Nacões. CEP 37504-364, Itajubá, MG, Brasil*
[3] *Department of Physics and Astronomy, University of Wyoming, Laramie, WY 82071, USA*
[4] *Kapteyn Astronomical Institute, University of Groningen, Postbus 800, 9700 AV, Groningen, The Netherlands*
[5] *Instituto de Astroísica de Canarias, Vía Láctea, S/N, E-38205, La Laguna, Tenerife, Spain*
[6] *Departamento de Física, CCNE, Universidade Federal de Santa Maria (UFSM), 97105-900 Santa Maria, RS, Brazil*
[7] *NAT - Universidade Cruzeiro do Sul, Rua Galvão Bueno, 868, 01506-000, São Paulo, SP, Brazil.*
[8] *Department of Astronomy, University of Michigan, 1085 S. University Ave., Ann Arbor, MI 48109, USA*
[9] *Divisão de Astrofísica, Instituto Nacional de Pesquisas Espaciais, 12227-010, São José dos Campos, SP, Brazil*

Accepted XXX. Received YYY; in original form ZZZ

ABSTRACT

We analyze a set of optical-to-near-infrared long-slit nuclear spectra of 16 infrared-luminous spiral galaxies. All of the studied sources present H_2 emission, which reflects the star-forming nature of our sample, and they clearly display H I emission lines in the optical. Their continua contain many strong stellar absorption lines, with the most common features due to Ca I, Ca II, Fe I, Na I, Mg I, in addition to prominent absorption bands of TiO, VO, ZrO, CN and CO. We report a homogeneous set of equivalent width (EW) measurements for 45 indices, from optical to NIR species for the 16 star-forming galaxies as well as for 19 early type galaxies where we collected the data from the literature. This selected set of emission and absorption-feature measurements can be used to test predictions of the forthcoming generations of stellar population models. We find correlations among the different absorption features and propose here correlations between optical and NIR indices, as well as among different NIR indices, and compare them with model predictions. While for the optical absorption features the models consistently agree with the observations,the NIR indices are much harder to interpret. For early-type spirals the measurements agree roughly with the models, while for star-forming objects they fail to predict the strengths of these indices.

Key words: stars: AGB and post-AGB – galaxies: bulges – galaxies: stellar content – galaxies: evolution

1 INTRODUCTION

One challenge in modern astrophysics is to understand galaxy formation and evolution. Both processes are strongly related to the star-formation history (SFH) of galaxies. Thus, the detailed study of the different stellar populations found in galaxies is one of the most promising ways to shed some light on their evolutionary histories. So far, stellar population studies have been concentrated mainly in the optical spectral range (e.g. Bica 1988; Worthey et al. 1994; Trager et al. 2000; Sánchez-Blázquez et al. 2006; González Delgado et al. 2015; Goddard et al. 2017; Martín-Navarro et al. 2018). In the near infrared, (0.8-2.4μm, NIR) even with some work dating back to the 1980s (e.g. Rieke et al. 1980), stellar pop-

⋆ E-mail: riffel@ufrgs.br. Visiting Astronomer at the Infrared Telescope Facility, which is operated by the University of Hawaii under Cooperative Agreement no. NCC 5-538 with the National Aeronautics and Space Administration, Office of Space Science, Planetary Astronomy Program.

ulation studies have just started to become more common in the last two decades (Origlia et al. 1993, 1997; Riffel et al. 2007, 2008, 2009; Cesetti et al. 2009; Lyubenova et al. 2010; Chies-Santos et al. 2011a,b; Riffel et al. 2011c; Kotilainen et al. 2012; Martins et al. 2013b; La Barbera et al. 2013; Zibetti et al. 2013; Noël et al. 2013; Dametto et al. 2014; Riffel et al. 2015; Baldwin et al. 2017; Dametto et al. 2019; Alton et al. 2018; Dahmer-Hahn et al. 2018, 2019; Francois et al. 2018, for example). Models have shown that the NIR spectral features provide very important insights, particularly into the stellar populations dominated by cold stars (e.g. Maraston 2005; Riffel et al. 2007; van Dokkum & Conroy 2012; Conroy & van Dokkum 2012; Zibetti et al. 2013; Riffel et al. 2015; Röck 2015; Röck et al. 2016). For example, the stars in the thermally pulsing asymptotic giant branch (TP-AGB) phase may be responsible for nearly half of the luminosity in the K band for stellar populations with an ago of ∼ 1 Gyr (Maraston 1998, 2005; Salaris et al. 2014).

One common technique to study the unresolved stellar content of galaxies is the fitting of a combination of simple stellar populations (SSPs) to obtain the SFH. However, due to difficulties in theoretical treatment (Maraston 2005; Marigo et al. 2008; Noël et al. 2013) and the lack of complete empirical stellar libraries in the NIR, (Lançon et al. 2001; Chen et al. 2014; Riffel et al. 2015; Villaume et al. 2017) the available SSP models produce discrepant results (e.g. Baldwin et al. 2017), thus making it very difficult to reliably analyse the SFH in the NIR.

On the other hand, the stellar content and chemical composition of the unresolved stellar populations of galaxies can also be obtained by the study of the observed absorption features present in their integrated spectra. So far, we still lack a comprehensive NIR dataset to compare with model predictions, required to make improvements to the models and to lead to a better understanding of the role played by the cooler stellar populations in the integrated spectra of galaxies.

Among the best natural laboratories to study these kinds of stellar content are *infrared galaxies*, sources that emit more energy in the infrared (∼5-500μm) than at all the other wavelengths combined (Sanders & Mirabel 1996; Sanders et al. 2003). The relevance of studying these galaxies lies particularly in the fact that they are implicated in a variety of interesting astrophysical phenomena, including the formation of quasars and elliptical galaxies (e.g. Genzel et al. 2001; Veilleux 2006; Wang et al. 2006). When studying luminous infrared galaxies in the Local Universe, it is possible to obtain high-angular-resolution observations of these objects, thus allowing the investigation of their very central regions. Comparison of such objects with those at higher redshifts may help to understand the SFH over cosmic times.

With the above in mind, we obtained optical and NIR spectra of a sub-sample of galaxies selected from the *IRAS* Revised Bright Galaxy Sample present in the Local Universe. These galaxies are believed to be experiencing massive star formation, making them suitable for studying their most important spectral features that can be used as proxies to test and constrain stellar-population models. As part of a series of papers aimed at studying the stellar population and gas emission features, here we provide measurements for the most conspicuous emission and absorption features, and present new correlations between absorption features. The outline of the paper is as follows. In §2 we describe the observations and data reduction. The results are presented and discussed in §3. Final remarks are made in §5.

2 OBSERVATIONS AND DATA REDUCTION

Our sample is composed of 16 Local Universe ($v_r \lesssim 6400$ km s^{-1}) galaxies that are very bright in the infrared (see Tab. 1). They were selected from the *IRAS* Revised Bright Galaxy Sample, which is regarded as a statistically complete sample of 629 galaxies, with 60 μm flux density $\gtrsim 5.24$ Jy. Galaxies chosen for this study were those with $\log(L_{fir}/L_\odot) \gtrsim 10.10$, accessible from the Infrared Telescope Facility (IRTF) and the Wyoming Infrared Observatory (WIRO, see below), and bright enough to reach a S/N ∼ 100 in the K-band within a reasonable on-source integration time.

2.1 Near Infrared Data

Cross-dispersed near-infrared (NIR) spectra in the range 0.8-2.4 μm were obtained on October 4, 6, and 7 in 2010 with the SpeX spectrograph (Rayner et al. 2003) attached to the NASA 3 m IRTF telescope at the Mauna Kea observing site. The detector is a 1024×1024 ALADDIN 3 InSb array with a spatial scale of 0.15″/pixel. A 0.8″×15″ slit was used during the observations, giving a spectral resolution of R∼ 1000 (or $\sigma = 127$ km s^{-1}). Both the arc lamp spectra and the night-sky spectra are consistent with this value (Riffel et al. 2013a). The observations were done by nodding in an Object-Sky-Object pattern with typical individual integration times of 120 s and total on-source integration times between 18 and 58 minutes. During the observations, A0 V stars were observed near each target to provide telluric standards at similar air masses. These stars were also used to flux calibrate the galaxy spectra by using black body functions to calibrate the observed spectra of the standard stars. The seeing varied between 0.4″–0.7″ over the different nights and there were no obvious clouds.

We reduced the NIR observations following the standard data reduction procedures given by Riffel et al. (2006, 2013b). In short, spectral extraction and wavelength calibration were performed using SPEXTOOL, software developed and provided by the SpeX team for the IRTF community (Cushing et al. 2004). The area of the integrated region is listed in Tab. 1. Each extraction was centred at the peak of the continuum-light distribution for every object of the sample. No effort was made to extract spectra at positions different from the nuclear region, even though some objects show evidence of extended emission, as this goes beyond the scope of this analysis. Telluric absorption correction and flux calibration were applied to the individual 1-D spectra by means of the IDL routine *xtellcor* (Vacca et al. 2003).

2.2 Optical Data

For completeness, the same sample was also observed in the optical range on nearly the same dates as the NIR data were collected with the WIRO Long Slit Spectrograph. The instrument is attached to the University of Wyoming's 2.3-meter telescope, located on Jelm Mountain at WIRO. The Cassegrain-mounted instrument uses a Marconi 2k×2k CCD

detector. During our observations we used a 900 l/mm grating in first order to obtain spectra from approximately 4000-7000 Å calibrated with a CuAr comparison lamp. Given our 4-arc-second slit oriented North-South, the resolution was R~1200. Due to the relatively large spatial extent of these low-redshift objects, we offset the telescope pointing by two arc-minutes to obtain sky spectra uncontaminated by galaxy light. The seeing varied between 1-2 arc-seconds during the nights of observation. We reduced the spectra using standard techniques in IRAF[1]. Table 1 shows the observation log along with extraction apertures. The 1-D wavelength and flux-calibrated spectra were then corrected for redshift, determined from the average z measured from the position of [S III] 0.953μm, Paδ, He I 1.083μm, Paβ and Brγ.

Examples of the final reduced spectra, from optical to NIR (~0.4μm —2.4μm) are presented in Figure 1, for the remaining galaxies see Appendix A . For each galaxy we show the optical, z+J, H and K bands, from top to bottom, respectively. It is worth mentioning that the optical and NIR data do not share the same apertures, and the slit was not generally oriented at the same position angles. However, since we are interested in the nuclear region, the different slit orientations should not introduce large discrepancies in the measurements. The ordinate axis represents the monochromatic flux in units of $10^{-15}\,\mathrm{erg\,cm^{-2}\,s^{-1}}$ Å^{-1}. The position of the most common and expected emission and absorption lines are indicated as dotted (red) and dashed (blue) lines, respectively.

3 RESULTS

3.1 Emission-line spectra

A visual inspection of the data reveals a wide diversity of emission-line strengths and species. The most common emission features detected are: Hβ, [O III] 4959, 5007 Å, [N II] 6548, 6583 Å, Hα, [S II] 6716,6730 Å, [S III] 9531 Å, Paδ, [C I] 9824, 9850 Å, Paβ, He I 10830 Å, [P II] 11886 Å, [Fe II] 12570, 16436 Å, Pa α H_2 19570 Å, H_2 21218 Å, and Brγ.

Emission-line fluxes for each object of the sample were measured by fitting a Gaussian function to the observed profile and then integrating the flux under the curve. The LINER software (Pogge & Owen 1993) was used for this purpose. No attempt to correct for stellar absorption was made before measuring the emission lines. This was done because NIR models with adequate spectral resolution (to allow the measurements of the weaker emission lines) are not available for the younger ages. Martins et al. (2013a) have shown that the underlying stellar population has only a strong effect on the hydrogen recombination emission lines, with the largest differences in fluxes being about 25 per cent. This value is within the largest uncertainties on the fluxes values too. For completeness, we have not subtracted the stellar features from the optical range too.

The results, including 3σ uncertainties, are listed in Tables 3 and 4. For most of our targets, these measurements are made public for the first time. In addition, we computed the extinction coefficient, C_{ext}, for the NIR using the intrinsic value of 5.88 for the flux ratio of Paβ/Brγ (Hummer & Storey 1987, using case B). The Cardelli et al. (1989) extinction law was used, and the values obtained for the coefficients are listed in Tables 3 and 4.

3.2 The continuum spectra

The main goal of this section is to characterize the continuum emission observed in our sample and compare it to other data in the literature. To help in the visual inspection[2] of the individual spectra, we normalized the continuum emission to unity in two regions free from emission/absorption features taken from Riffel et al. (2011b). The NIR spectra were normalized at 20925 Å and then sorted according to their continuum shapes. For a proper comparison with the optical portion of the spectrum, we normalized the optical spectra at 5300 Å and plotted them in the same order as the NIR spectra (Figs. 4 and 5).

A first-order inspection of Figure 4 allows us to infer that, contrary to what happens in Seyfert galaxies (Riffel et al. 2006), there seems to be no correlation between activity type (LINERs or SFGs) and continuum shape. In fact, these very bright infrared galaxies present a continuum shape very similar to what is found in fainter HII sources and normal galaxies, as reported by Martins et al. (2013a), which may indicate that the LINER spectrum of these galaxies is powered by starburst instead of a low-luminosity AGN. In addition, the continua of all the optical spectra look very similar.

A large diversity of atomic absorption lines and molecular bands is also apparent in the spectra. These features are seen from the very blue optical end to the red end of the observed NIR spectral region. The most common atomic absorption features are due to Ca I, Ca II, Fe I, Si I, Na I and Mg I, besides the prominent absorption bands of CH, MgH, TiO, VO, ZrO and CO. These features are identified in Fig. 1. It is clear in these figures that some of the most important features predicted for intermediate-age stellar populations, which are expected to be enhanced in the RGB and TP-AGB stellar phases (Maraston 2005; Riffel et al. 2007, 2015), are detected in the spectra. Among these features are the ZrO/CN/VO at 9350 Å, the 10560 Å VO, 1.1 μm CN and 1.6 μm and 2.3 μm CO bands.

3.2.1 Towards a homogeneous NIR index definition

The Equivalent Widths (EWs) of these features offer coarse but robust information about the stellar content of a galaxy spectrum, and therefore they can be used as powerful diagnostics of the stellar content of galaxies. Contrary to the optical range, where there exist indices defined in a homogeneous way by the Lick group (see Worthey et al. 1994, and references), in the NIR there is no such homogeneous set of definitions covering the full NIR wavelength range, and authors tend to use their own definitions (e.g. Riffel et al. 2007, 2008; Silva et al. 2008; Mármol-Queraltó et al. 2009;

[1] IRAF is distributed by the National Optical Astronomy Observatories, which are operated by the Association of Universities for Research in Astronomy, Inc., under cooperative agreement with the National Science Foundation.

[2] Emission lines and equivalent widths of the absorption features were measured on the spectra previous to normalization.

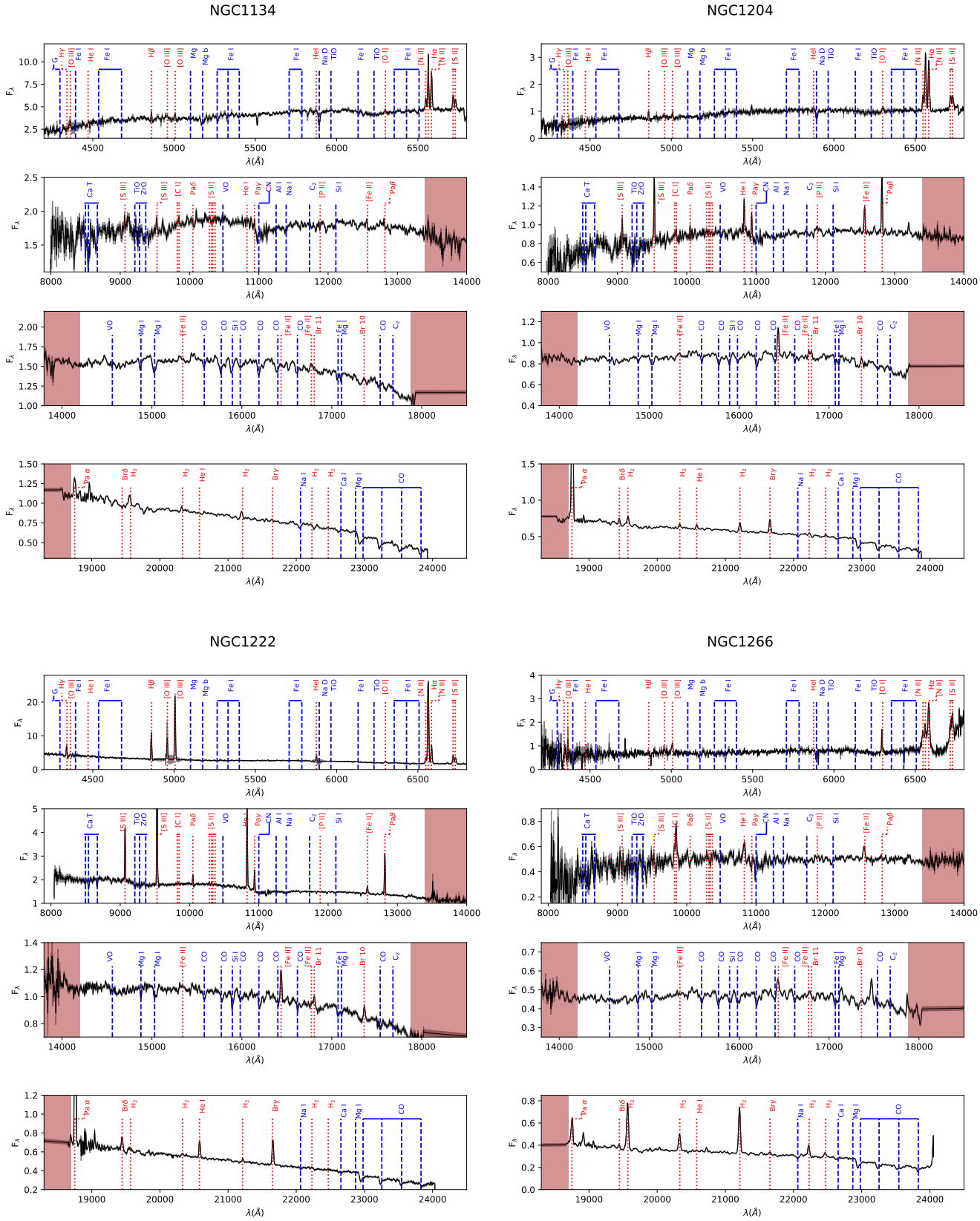

Figure 1. Final reduced and redshift-corrected spectra for NGC 1134, NGC 1204, NGC 1222 and NGC 1266. For each galaxy we show from top to bottom the optical, $z + J$, H , and K bands, respectively. The flux is in units of 10^{-15} erg cm^{-2} s^{-1}. The shaded grey area represents the uncertainties and the brown area indicates the poor transmission regions between different bands. The remaining spectra are shown in online material.

Table 1. Near-Infrared observation log and basic sample properties.

Source	α	δ	z	Obs. Date	Exp. Time (s)	Airmass	PA (deg)	Size (pc×pc)	Activity	$\log(\frac{L_{IR}}{L_\odot})^\star$ (13)	Morphology
NGC 23	00h09m53.4s	+25d55m26s	0.0157202	2010 10 07	29 × 120	1.04	330	1348 × 270	SFG[1]	11.05	SBa
NGC 520	01h24m35.1s	+03d47m33s	0.0080367	2010 10 04	16 × 120	1.04	300	689 × 138	SFG[2]	10.91	S0
NGC 660	01h43m02.4s	+13d38m42s	0.0029152	2010 10 06	24 × 120	1.01	33	237 × 50	Sy2/HII[2,3,4]	10.49	SBa pec
NGC 1055	02h41m45.2s	+00d26m35s	0.0036267	2010 10 04	16 × 120	1.07	285	466 × 62	LINER/HII[2,3,4]	10.09	Sbc
NGC 1134	02h53m41.3s	+13d00m51s	0.0129803	2010 10 04	16 × 120	1.11	0	1113 × 223	SFG[5]	10.83	S?
NGC 1204	03h04m39.9s	-12d20m29s	0.0154058	2010 10 07	16 × 120	1.23	66	1321 × 264	LINER[6]	10.88	S0/a
NGC 1222	03h08m56.7s	-02d57m19s	0.0082097	2010 10 06	24 × 120	1.13	315	598 × 141	SFG[7]	10.60	S0 pec
NGC 1266	03h16m00.7s	-02d25m38s	0.0077032	2010 10 07	18 × 120	1.09	0	661 × 132	LINER[7]	10.46	SB0 pec
UGC 2982	04h12m22.4s	+05d32m51s	0.0177955	2010 10 04	9 × 120	1.11	295	1526 × 305	SFG[8]	11.30	SB
NGC 1797	05h07m44.9s	-08d01m09s	0.0154111	2010 10 07	16 × 120	1.23	66	1321 × 264	SFG[1]	11.00	SBa
NGC 6814	19h42m40.6s	-10d19m25s	0.0056730	2010 10 07	16 × 120	1.17	0	486 × 97	Sy 1[7]	10.25	SBbc
NGC 6835	19h54m32.9s	-12d34m03s	0.0057248	2010 10 06	22 × 120	1.21	70	368 × 98	SFG[9]	10.32	SBa
UGC 12150	22h41m12.2s	+34d14m57s	0.0214590	2010 10 04	15 × 120	1.08	37	1656 × 368	LINER/HII[10]	11.29	SB0/a
NGC 7465	23h02m01.0s	+15d57m53s	0.0066328	2010 10 06	12 × 120	1.03	340	569 × 114	LINER/Sy 2[11]	10.10	SB0
NGC 7591	23h18m16.3s	+06d35m09s	0.0165841	2010 10 07	16 × 120	1.03	0	1422 × 284	LINER[7]	11.05	SBbc
NGC 7678	23h28m27.9s	+22d25m16s	0.0120136	2010 10 04	16 × 120	1.01	90	927 × 206	SFG[12]	10.77	SBc

Table Notes: SFG: Star-Forming Galaxies (Starburst or HII galaxies). LINER/HII were assumed to be pure LINERs in the text. The galaxies are listed in order of right ascension, and the number of exposures refers to on-source integrations. The slit width is 0.8″. References - 1: Balzano (1983); 2: Ho et al. (1997a); 3: Ho et al. (1997b); 4: Filho et al. (2004); 5: Condon et al. (2002); 6: Sturm et al. (2006); 7: Pereira-Santaella et al. (2010); 8: Schmitt et al. (2006); 9: Coziol+98; 10: Veilleux et al. (1995); 11: Ferruit et al. (2000); 12: Gonçalves et al. (1998); 13: Sanders et al. (2003);

Table 2. Optical observation log. The slit was oriented North-South.

Source	Obs. Date	Exp. Time (s)	Airmass	Size (pc×pc)
NGC 23	2010 10 04	600	1.20	2359 × 1348
NGC 520	2010 10 03	600	1.28	4307 × 689
NGC 660	2010 10 04	600	1.18	437 × 250
NGC 1055	2010 10 04	600	1.36	544 × 311
NGC 1134	2010 10 04	600	1.14	12243 × 1113
NGC 1204	2010 10 04	600	1.68	2312 × 1321
NGC 1222	2010 10 03	600	1.42	3344 × 704
NGC 1266	2010 10 03	600	1.39	6440 × 661
UGC 2982	2010 10 04	600	1.27	2670 × 1526
NGC 1797	2010 10 02	600	1.56	11893 × 1321
UGC 12150	2010 10 03	600	1.03	18401 × 1840
NGC 7465	2010 10 03	600	1.12	3270 × 569
NGC 7591	2010 10 03	600	1.21	13154 × 1422
NGC 7678	2010 10 04	600	1.18	1803 × 1030

Table Notes: The slit width is 4″.

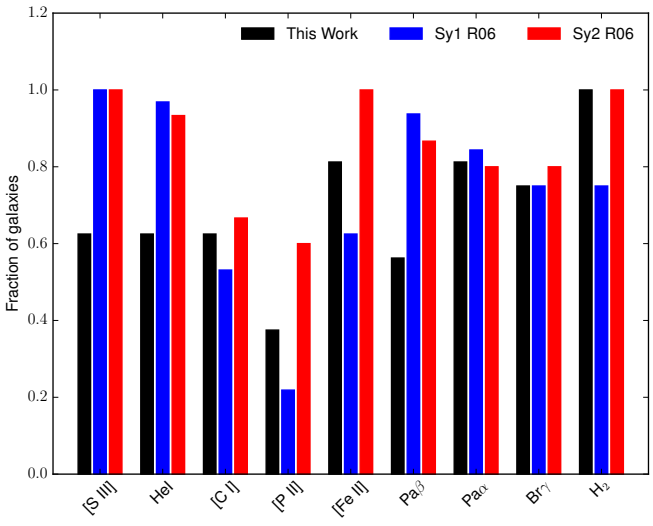

Figure 2. Histogram showing statistics of the most common NIR emission lines.

Cesetti et al. 2009; Kotilainen et al. 2012; Riffel et al. 2011a, 2015; Röck et al. 2017), and therefore it is very difficult to compare results from different investigations.

With this in mind, here we create a set of definitions for absorption features found in the NIR. We used two SSPs from the IRTF-based EMILES models (Vazdekis et al. 2016; Röck 2015; Röck et al. 2016), with 1.0 Gyr and 10 Gyr, solar metallicity, calculated with the PADOVA evolutionary tracks and with $\sigma = 228\mathrm{km\,s^{-1}}$. We added up their light fractions (normalized to unity at λ=12230Å) as follows:

$$F_{\rm comb} = 0.5\frac{F_\lambda^{1Gyr}}{F_{\lambda=12230}^{1Gyr}} + 0.5\frac{F_\lambda^{10Gyr}}{F_{\lambda=12230}^{10Gyr}}.$$

To this resulting spectrum we added Gaussians to model emission-lines profiles. These lines are located at the wavelengths of the most common emission lines detected in galaxies in this spectral region (see Sec. 3.1) with Full Width at Half Maximums (FWHMs) characteristic of galaxies observed with SpeX with the configuration used here ($25\text{Å} \lesssim \mathrm{FWHM} \lesssim 40\text{Å}$) with arbitrary flux values. We employed the ELPROFILE routine of the IFSCUBE package[3]

[3] available at: https://bitbucket.org/danielrd6/ifscube.git

Table 3. Emission line fluxes in units of $1x10^{-15}$ erg cm^{-2} s^{-1}.

Line	Ion	NGC23	NGC520	NGC660	NGC1055	NGC1134	NGC1204	NGC1222	NGC1266
	C_{ext}	–	–	3.42±0.13	–	–	2.95±0.14	1.06±0.05	6.74±0.73
4861	Hβ	20.40±1.16	–	0.86±0.26	–	6.06±0.37	0.30±0.06	49.30±0.65	–
4959	[O III]	30.70±3.13	–	3.37±0.41	–	8.25±0.72	1.69±0.48	47.30±0.75	–
5007	[O III]	10.50±3.13	2.16±0.30	1.15±0.41	–	2.81±0.72	0.58±0.48	140.00±0.75	4.27±0.64
6548	[N II]	108.00±3.26	1.60±0.31	6.25±0.53	1.41±0.32	12.90±1.41	5.75±0.43	14.20±0.40	14.30±1.07
6563	Hα	83.80±3.89	8.68±0.44	17.20±0.46	4.97±0.34	40.50±0.95	20.50±0.42	222.00±0.43	11.40±0.76
6583	[N II]	27.90±3.89	6.96±0.49	18.60±0.48	4.56±0.39	38.30±1.21	18.60±0.42	49.70±0.45	30.60±0.87
6716	[S II]	46.50±1.92	3.29±0.46	5.15±0.48	1.25±0.29	14.60±1.23	5.76±1.23	20.70±0.48	18.70±1.16
6730	[S II]	34.70±1.92	3.07±0.55	4.88±0.61	1.31±0.44	12.90±1.50	5.69±1.23	19.90±0.57	21.10±1.16
9069	[S III]	14.80±3.96	–	–	–	–	10.30±1.40	32.80±1.59	–
9531	[S III]	15.70±3.96	–	23.90±0.94	–	–	11.90±0.54	72.60±1.49	–
9824	[C I]	1.57±0.60	–	2.10±0.27	–	–	1.15±0.30	1.55±0.49	–
9850	[C I]	5.15±0.60	–	2.53±0.27	–	–	1.88±0.30	0.97±0.49	9.21±1.06
10049	Paδ	–	–	2.55±0.22	–	–	1.03±0.08	4.05±0.31	–
10122	He II	–	–	2.78±0.22	–	–	1.34±0.08	–	–
10830	He I	22.30±2.60	–	13.30±0.41	–	–	9.24±0.56	53.80±0.77	6.26±0.83
10938	Paγ	5.65±1.58	–	8.57±0.31	–	–	2.78±0.27	12.90±0.76	–
11470	[P II]	–	–	1.82±1.09	–	–	1.17±0.27	–	–
11886	[P II]	–	–	3.68±1.09	–	–	1.70±0.19	–	–
12567	[Fe II]	10.50±0.87	–	13.90±0.65	–	–	5.16±0.20	6.32±0.43	3.19±0.51
12820	Paβ	–	–	29.00±0.60	–	–	12.10±0.20	28.20±0.37	0.75±0.08
12950	[Fe II]	–	–	1.21±0.15	–	–	1.35±0.25	–	–
13209	[Fe II]	–	–	6.60±0.24	–	–	4.49±0.39	–	–
15342	[Fe II]	–	–	–	–	–	1.52±0.36	–	–
16436	[Fe II]	14.20±3.46	3.87±0.14	15.70±0.90	–	–	6.51±0.36	4.65±0.18	2.90±0.38
16773	[Fe II]+Br11	31.50±1.34	–	–	–	–	2.65±0.50	–	–
17360	Br10	–	–	–	–	–	1.60±0.13	–	–
18750	Paα	–	35.40±0.30	60.20±1.64	–	–	61.10±0.33	69.30±0.57	8.03±0.34
19446	Brδ	–	2.07±0.28	5.67±0.53	–	–	1.80±0.34	3.78±0.20	–
19570	H_2	20.20±4.60	2.41±0.39	8.87±0.80	1.24±0.3	–	4.17±0.51	1.95±0.34	15.10±0.47
20332	H_2	4.94±0.57	1.13±0.10	3.67±0.56	–	1.14±0.3	1.81±0.34	0.95±0.14	5.10±0.44
20580	H_2	–	2.47±0.09	5.32±0.64	–	–	1.47±0.27	4.68±0.14	–
21218	H_2	10.00±1.26	2.40±0.18	6.91±0.72	0.6±0.08	2.37±0.4	3.61±0.25	0.84±0.12	13.70±0.25
21654	Brγ	–	6.67±0.19	16.60±0.71	–	–	5.88±0.27	6.98±0.07	1.40±0.33
22230	H_2	4.53±2.97	0.67±0.19	2.01±1.20	–	–	0.87±0.09	0.49±0.19	3.26±0.12
22470	H_2	1.47±0.37	0.83±0.12	1.18±0.12	–	–	0.72±0.10	0.29±0.04	1.51±0.14

(Ruschel-Dutra, in preparation). Using this simulated spectrum we defined the line limits and continuum band passes as illustrated in Fig. 3 and listed in Table 5.

We have measured the EWs for the most prominent absorption features using an updated PYTHON version of the PACCE code (Riffel & Borges Vale 2011). In this code version, the EW uncertainties are assumed to be the standard deviation of 1000 EWs measurements of simulated spectra created by perturbing each flux point by its uncertainty through a Monte Carlo approach. The line definitions used are listed in Table 5, and the measured values are in Tables 6 and 7. In order to have a sample of early type galaxies (ETG) to compare our results with, we have collected NIR spectra from the literature and measured the EW of the absorption features with the same definitions used for our sample. Tables B1 and B2 present the measurements for the sample of galaxies presented in Baldwin et al. (2017). For four of the galaxies we were able to find Sloan Digital Sky Survey data used to measure the optical EW, while for the remaining objects we collected the values of Fe5015, Mg_b and Fe5270 from McDermid et al. (2015). We also measured the values from the spectra presented by Dahmer-Hahn et al. (2018), which values are listed in Tab. B3.

4 DISCUSSION

4.1 Emission Lines

In order to compare the frequency of occurrence of the emission lines in our sample with what is seen in Seyfert galaxies, we show a histogram in Fig. 2 where the lines found here are compared to those of Riffel et al. (2006). What clearly emerges from this figure is that [S III], He I, and Paβ lines are less frequent in our sample (occurring in ~60% of the sources) than in Seyferts (present in almost all of the objects). On the other hand, we find a higher frequency of occurrence of lines of [C I] (~ 65%), [P II] (~ 40%) and [Fe II] (~ 65%) than in Sy 1 objects, and a similar rate as in Sy 2s. The remaining emission lines occur with similar frequencies in the present sample and in Seyferts (see also Lamperti et al. 2017). Lines that are less frequent in the present sample compared to AGNs are located in regions with strong stellar

Table 4. Continuation of Table 3

Line	Ion	UGC2982	NGC1797	NGC6814*	NGC6835	UGC12150	NGC7465	NGC7591	NGC7678
	C_{ext}	–	2.68±0.08	0.00	4.87±0.19	2.16±0.17	2.35±0.93	2.53±0.07	1.39±0.23
4861	Hβ	0.49±0.15	13.10±0.71	–	–	–	21.80±1.05	–	9.45±0.42
4959	[O III]	0.35±0.16	–	–	–	–	31.40±2.27	–	–
5007	[O III]	0.76±0.29	3.11±0.44	–	–	–	56.00±1.85	–	2.83±0.54
6548	[N II]	1.64±0.39	11.20±0.59	–	–	–	29.50±1.03	8.15±1.36	7.88±0.82
6563	Hα	13.90±0.40	88.70±0.74	–	–	–	122.00±0.89	21.10±1.00	53.40±1.00
6583	[N II]	5.62±0.39	46.40±0.76	–	–	–	71.10±0.98	18.60±1.04	27.60±1.00
6716	[S II]	2.77±0.45	10.80±0.41	–	–	–	39.70±1.17	4.87±1.94	9.23±0.97
6730	[S II]	2.66±0.75	10.30±0.46	–	–	–	34.10±1.22	3.46±1.94	10.30±1.37
9069	[S III]	–	5.80±0.59	23.70±0.49	–	5.16±0.27	18.00±1.43	–	6.59±0.64
9531	[S III]	–	12.10±0.59	55.50±0.58	–	5.22±0.20	38.20±0.78	10.00±0.32	15.60±0.64
9824	[C I]	–	1.71±0.16	–	–	–	2.41±0.76	0.98±0.15	0.82±0.09
9850	[C I]	–	1.67±0.16	–	–	2.49±0.17	3.32±0.76	2.58±0.15	1.74±0.09
10049	Paδ	–	–	–	–	–	–	3.85±0.44	–
10122	He II	–	–	–	–	–	–	3.28±0.23	–
10830	He I	–	7.72±1.08	–	–	8.40±1.23	25.60±1.52	8.41±0.88	9.47±0.77
10938	Paγ	–	3.98±1.08	–	–	2.57±0.57	8.07±1.20	3.02±0.47	4.08±0.55
11470	[P II]	–	1.30±0.37	–	–	1.17±0.14	–	2.50±0.87	–
11886	[P II]	–	1.80±0.37	3.83±1.08	–	1.46±0.14	–	4.98±0.87	–
12567	[Fe II]	–	5.04±0.25	4.64±0.52	2.06±0.23	4.73±0.33	11.80±0.66	6.80±0.21	3.28±0.49
12820	Paβ	–	12.10±0.26	3.53±0.57	4.86±0.19	7.86±0.30	9.57±2.61	9.74±0.21	9.20±0.51
12950	[Fe II]	–	1.18±0.42	–	–	–	–	–	–
13209	[Fe II]	–	2.94±0.42	–	–	–	5.60±0.34	–	–
15342	[Fe II]	–	–	–	–	–	–	–	–
16436	[Fe II]	–	4.65±0.47	5.53±0.48	3.24±0.08	3.56±0.18	9.20±0.28	6.05±0.60	3.09±0.21
16773	[Fe II]+Br11	–	–	–	–	–	–	–	–
17360	Br10	–	–	–	–	–	–	–	–
18750	Paα	4.70±0.18	60.40±0.46	82.50±3.49	32.60±0.29	34.30±0.17	31.60±3.36	36.70±0.67	23.30±0.32
19446	Brδ	–	2.12±0.39	–	2.36±0.22	–	–	–	1.05±0.10
19570	H_2	1.79±0.49	4.10±0.52	3.36±0.54	3.33±0.44	5.25±0.05	4.33±0.16	8.17±0.26	1.45±0.10
20332	H_2	0.61±0.08	1.48±0.30	1.25±0.20	0.86±0.05	1.65±0.07	2.36±0.39	2.46±0.20	2.03±0.20
20580	H_2	–	1.40±0.26	–	1.98±0.05	–	1.33±0.34	1.53±0.18	1.24±0.20
21218	H_2	0.60±0.02	3.21±0.28	2.14±0.20	1.34±0.21	4.00±0.13	3.92±0.27	4.80±0.36	0.88±0.14
21654	Brγ	0.80±0.04	5.33±0.09	0.52±0.32	4.66±0.25	2.88±0.13	3.75±0.69	4.07±0.05	2.56±0.15
22230	H_2	–	1.20±0.17	1.05±0.23	0.65±0.18	1.70±0.85	1.71±0.10	2.25±0.25	0.71±0.03
22470	H_2	–	1.18±0.16	0.61±0.13	–	0.55±0.12	0.49±0.06	1.30±0.26	0.32±0.14

features. Thus, it is possible that the absence of these features is because they are intrinsically weaker than in AGNs and/or diluted by the broad absorption features that dominate the $z + J$ band. Note though that for three objects (NGC 1055, NGC 6835 and NGC 520, see Fig 4), our spectral range excludes the [S III], He I, and [C I] emission lines. If present in these spectra, they would show up in ~80% of our sample.

It is worth mentioning that the kinematics of the [S III], [Fe II] and H_2 lines as well as the excitation mechanisms of the [Fe II] and H_2 lines of the galaxies of this sample were explored in Riffel et al. (2013b). However, the low-ionization forbidden lines of [C I] (i.e. λ 9850 Å) and [P II] (i.e. λ 11886 Å), also detected in our sample, were not yet analyzed. Although the [P II] line is stronger compared to [Fe II] λ 12570 Åin Sy 2s (Riffel et al. 2006) than in the other types of galaxies, the detection of [P II] lines is surprising here. This is because at Solar metallicity, Phosphorus is about 1000 times less abundant than Carbon (Ferguson et al. 1997) and 100 times less abundant than Iron (Oliva et al. 2001). Hence, if the P/C abundance is near to solar, the [P II] lines should not be present, unless other strong abundant elements are much more optically thick than they appear. A similar problem is found in some quasars for which broad absorption lines of P V $\lambda\lambda$1118,1128 Å are detected and extreme abundances ratios for P/C are found (Hamann 1998; Hamann et al. 2001; Borguet et al. 2012). According to Oliva et al. (2001) for a solar Fe/P ~ 100 abundance ratio, one expects that $\frac{[\mathrm{Fe\,II}]}{[\mathrm{P\,II}]} = 50$, similar to what is expected for supernova remnants. The NIR [P II] emission lines may probably help to set some constraints on the abundance of Phosphorus in galaxies.

As discussed in Oliva et al. (2001) bright [Fe II] lines can only be formed in regions where hydrogen is partially ionized. Such regions of hot, partially ionized gas can only be produced in an efficient way by shocks and/or photoionisation by soft X-rays. According to these authors, [Fe II]/[P II] can be used to distinguish between shocks (ratio $\gtrsim$20) and photoionisation (ratio $\lesssim$ 2). In order to test this hypothesis, we plotted in Fig. 4.1 [Fe II]/[P II] × [C I]/[P II] for our sample as well as the Seyfert galaxies of Riffel et al. (2006). As can be seen in this figure, there is a good correlation and no clear separation between the SFGs and the Seyferts, suggesting that the dominant excitation mechanism is the same for

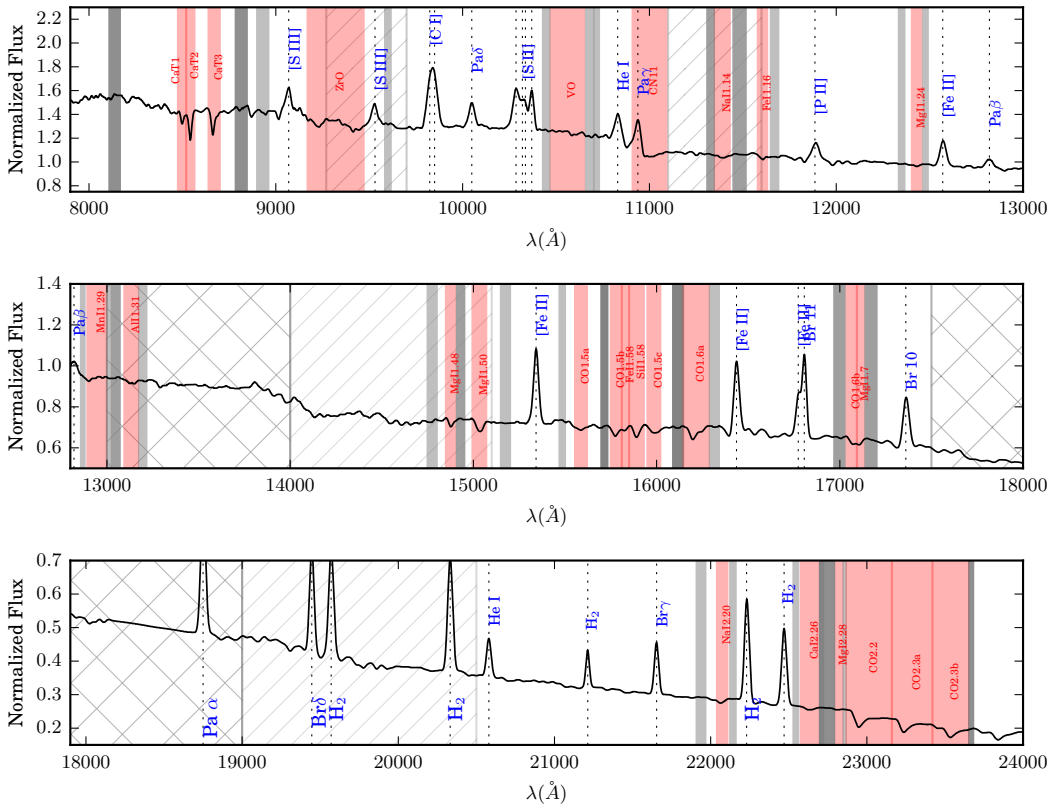

Figure 3. Simulated spectrum showing the NIR indices definitions. Blue and red continuum band passes are in grey and line limits in red. Regions of strong (transmission < 20%) telluric absorption are shaded with an "X" pattern, while regions of moderate (transmission <80%) telluric absorption are shaded with a line pattern. Emission lines and absorption features are labeled. See text for details.

the three ions. Furthermore, due to the low values derived for the [Fe II]/[P II] ratio, that excitation mechanism might be expected to be photoionisation based on the arguments of Oliva et al. (2001). To test this, we have computed photoionisation models using CLOUDY/C17.01[4] (Ferland et al. 2017) updated with the next release of collisional strengths for [P II] (taken from Tayal 2004) as well as with new transition probabilities[5] (private communication), however these models are not able to reproduce the observed line ratios, underestimating both (the models values for both ratios are nearly zero). This may be due to the fact that these lines are not in fact excited by photoionisation, but mostly driven by shocks.

4.2 Absorption Features

It is crucial to be able to derive ages and chemical composition in order to understand the dominant underlying unresolved stellar content of galaxies (Röck et al. 2017). So far, the NIR is lacking a clear procedure based on absorption-line strengths. The obvious choice to do this kind of study is using stellar clusters as probes, instead of the use of more complex star-forming objects. However, while observations of the integrated spectra of stellar clusters in the optical region have been available for almost 30 years (e.g. Bica 1988) in the NIR such observations are very difficult since the light emitted by the stars of the clusters in the NIR bands is dominated by a few very bright stellar phases making it difficult to get reliable integrated spectra of such objects in the NIR (e.g Lyubenova et al. 2010; Riffel et al. 2011c).

In order to have a more homogeneous data-set, in addition to the data-set we present here representing complex SFHs of SFGs (§ 2), we collected spectra of nearby ETGs (which tend to have less complex SFHs than our sample) observed similarly as those in the present work. Our final data set representing the older stellar population is composed of 12 ETG selected in order to span a wide range of ages (1-15 Gyr) at approximately solar metallicity and observed by Baldwin et al. (2017) using Gemini/GNIRS in the cross-dispersed mode ($\sim 0.8-2.5\mu m; R \sim 1700$; $\sigma \sim 75$ km s^{-1}) plus 6 ETG selected from the Calar Alto Legacy Integral Field Area Survey (CALIFA Sánchez et al. 2016) and observed by Dahmer-Hahn et al. (2018) using the TripleSpec spectro-

[4] Available at https://www.nublado.org.
[5] They are a combination of data taken from the MCHF/MCDHF Database at http://nlte.nist.gov/MCHF/ and data from the NIST Atomic Spectra Database at https://www.nist.gov/pml/atomic-spectra-database

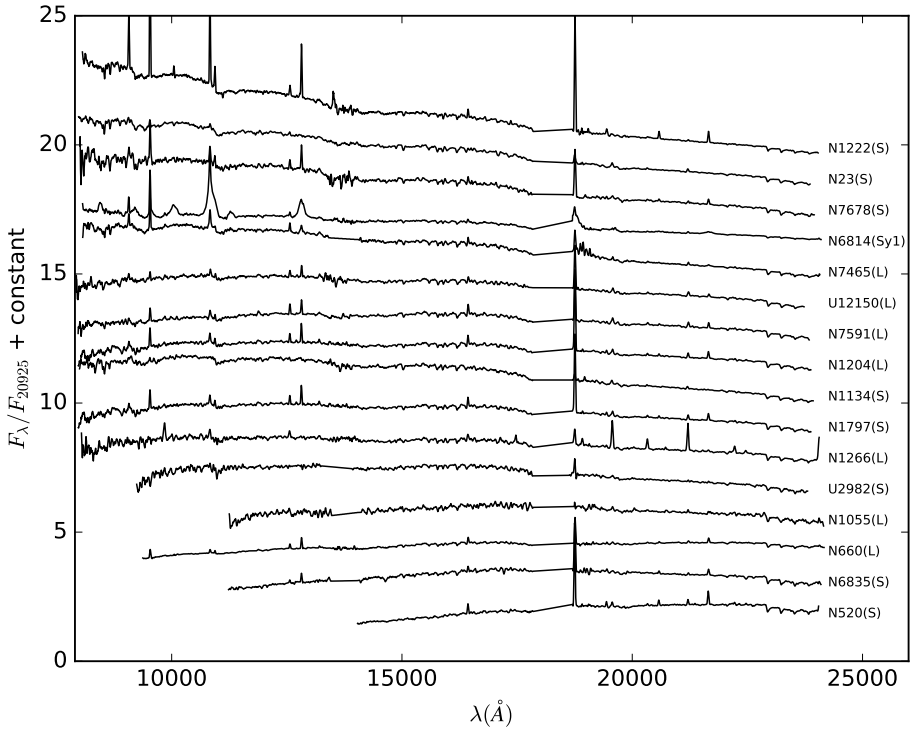

Figure 4. Near-infrared normalized spectra ordered according to their shapes from steeper (top) to flatter (bottom). The data were normalized at 20925Å. Activity types are listed (S = SFG and L=LINER).

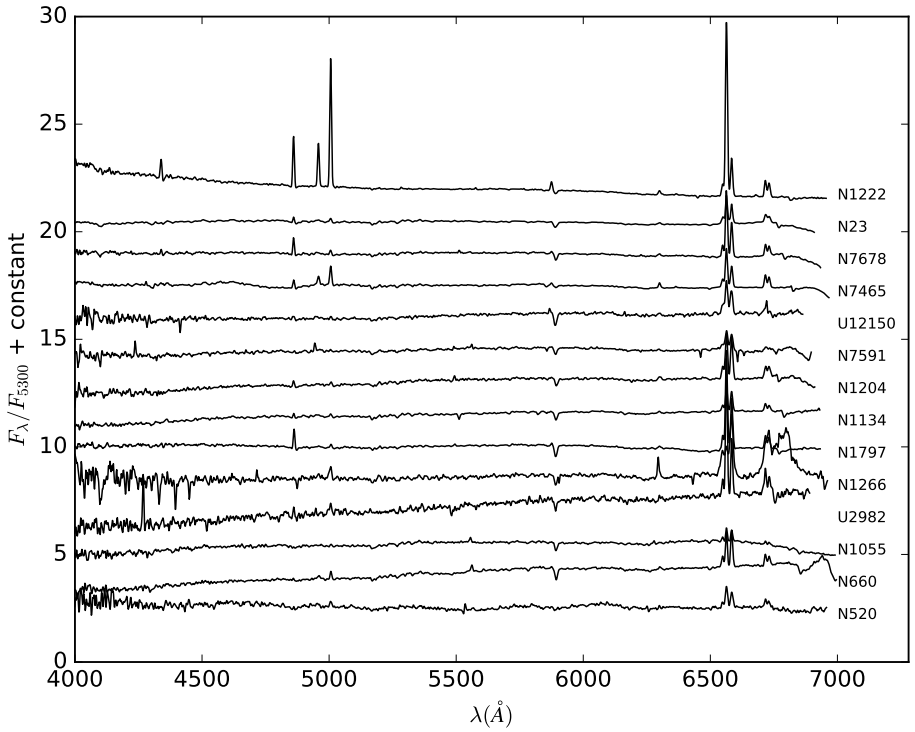

Figure 5. Same order as Figure 4, but for the optical spectral range. The data were normalized at 5300 Å.

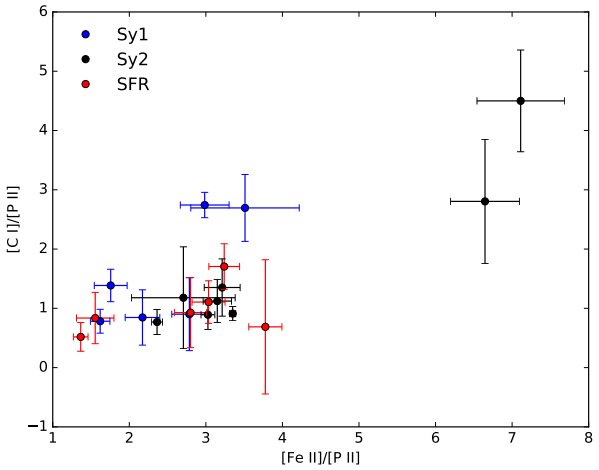

Figure 6. The correlation between the emission-line ratios of [C I] λ9850 Åand [Fe II] λ12570 Å

relative to [P II] λ11886 Å.

graph attached to the Astrophysical Research Consortium (ARC) 3.5-meter telescope ($\sim 0.95-2.45\mu m$; $R \sim 2000$; $\sigma \sim 64$ km s^{-1}). In addition to these NIR spectra, we also collected, when available, the optical spectra of the sources. In the case of Baldwin et al. (2017) galaxies, the optical spectra where taken from the Sloan Digital Sky Survey (Ahn et al. 2014), while for the sample of Dahmer-Hahn et al. (2018) we took the data from the (CALIFA Sánchez et al. 2016). The optical and NIR indices were measured by us using the definitions of Tab. 5 and are listed as online material in Tabs. B1, B2 and B3.

4.2.1 Previous NIR index - index correlations

Due to the lack of adequate data sets to test predictions of NIR data, compared to the optical (see Thomas et al. 2003, for example), there are only a few studies trying to understand the behaviour of NIR × NIR indices. For instance, Mármol-Queraltó et al. (2009) studied a sample of early type galaxies and found a strong correlation between $C_2$4668 and NaI2.20 indices. In Fig. 7a we show the Mármol-Queraltó et al. (2009) measurements (open diamonds) and the literature compilation presented by Röck et al. (plus symbols, 2017) together with our data (squares). Even though we only measured both indices for 4 sources, this correlation seems to still hold for SFGs, which populate the lower left end of the correlation (Fig. 7a).

Using a similar approach, Cesetti et al. (2009) reported a trend of correlation of the optical Mg_2 band with NIR indexes, such as NaI2.20, CaI2.26 and CO2.2 for early type galaxies. In Fig 7b,c and d we plotted our sample (filled squares), together with those of Cesetti et al. (2009, open diamonds) and Kotilainen et al. (open triangles 2012) for early type sources. Additionally we also added the inactive spirals (octagons, LTG-K12) of Kotilainen et al. (2012). From Fig. 7d we have excluded the two Seyfert galaxies (NGC 660 and NGC 6814) since the CO band can be very diluted in these kind of sources (Riffel et al. 2009; Burtscher et al. 2015).

From Fig. 7 it is clear that the trend seems to hold for NaI2.20 × Mg_2, while for CaI2.26 × Mg_2 there is no clear correlation, and in the case of CO2.2 × Mg_2 instead of a positive correlation there seems to be an inverse correlation. Additionally there seems to be a segregation between early and late-type galaxies in this plot (panel d). This indicates that CO is enhanced in younger stellar populations, in agreement with the predictions of the Maraston (2005) models as shown in Riffel et al. (2007).

To help in the interpretation of these results, on these index-index diagrams we have over-plotted the new optical-to-NIR IRTF-based stellar population synthesis models of the E-MILES team (Vazdekis et al. 2012, 2016; Röck et al. 2016). The models employed are those computed using the PADOVA isochrones (Girardi et al. 2000), with ages in the range 0.3 Gyr < t < 15.0 Gyr and metallicities within [Fe/H] = -0.40, [Fe/H] = 0.00 and [Fe/H] = 0.22 with two different spectral resolutions (σ=60km s^{-1} and σ=228km s^{-1}, the shaded area represents the differences caused by σ). We also plotted TP-AGB heavy (see Zibetti et al. 2013, for a comparison between TP-AGB heavy and light models), Pickles-based models of Maraston & Strömbäck (2011, M11 hereafter), which do have the same prescription than Maraston (2005) models but with a higher spectral resolution (R = 500) than the 2005 models, therefore making them more suitable for our comparisons. However, it is important to have in mind that M11 models do have a poorer spectral resolution than our data, the effects on the indices strengths by degrading the resolution to M11 models is within the uncertainties of our measurements. These models are shown as open brown stars and are only available for solar metalicity. What emerges from this exercise is that the models in general are not able to predict the NIR indices and that there is a segregation between early (open diamonds and plus markers) and late-type (filled squares and octagons) galaxies in these diagrams. The upper panels show significantly larger NaI2.20 index values than predicted by the models with standard IMF. Both the optical Mg and C dominated indices are stronger than the models for the most massive galaxies (i.e. the ones with the largest index values). In the case of the NaI2.20 index, Röck et al. (2017) concluded that for early-type sources the large values obtained for this index are due to a combination of a bottom-heavy initial mass function and the [Na/Fe] abundances. On the other hand, Alton et al. (2018) found that their sample of massive ETGs is consistent with having a Milky Way-like IMF, or at most a modestly bottom-heavy IMF, and suggested that their extreme abundance values for Na, in the cores of massive ETGs, may be explained by the metallicity-dependent nucleosynthetic yield of Na.

The lower panels of Fig. 7 show that the ETGs are in better agreement with the predicted values. However, about half of our SFGs sample show stronger CaI2.26 and CO2.2 values than predicted by the models. From these plots, we also can infer that the TP-AGB phase does not change substantially the CO index, once the solar metalicity M11 models are in agreement with the E-MILES ones for the younger ages ($t \lesssim 1$ Gyr), with a large discrepancy for the older ages. Besides age, metallicity appears as an additional discriminator for the measured strengths of CO bands, with low met-

alicity ([Fe/H] = -0.40) and intermediate ages (~350Myr) showing the largest values for the CO2.2 index. This is in agreement with the previous findings of Kotilainen et al. (2012), who found that the evolved red stars completely dominate the NIR spectra, and that in this age range, the hot, young stars contribution to the EWs is virtually nonexistent. So far, to fully access these younger stellar content of the galaxies it is necessary to fit the full spectrum, taking the continuum into account (see Baldwin et al. 2017; Dahmer-Hahn et al. 2018, for example). However, this is beyond the scope of the present paper and will be the subject of a future investigation (Riffel et al., *in preparation*). On the other hand, the lower values of the CO index presented by the ETGs are also not explained by the models, with M11 models underestimating and E-MILES models overestimating the main locus occupied by these sources.

4.2.2 New index - index correlations

Because we measured a large set of lines for our sample, we have tried to find new correlations among the different absorption features by plotting all the EWs listed in Tab. 6 and 7, as well as literature data (Tabs. B1 to B3) against each other. From these, we removed the correlations already discussed above (Fig. 7) as well as the optical × optical indices correlations since these are well studied [6]. Since the CaT lines are correlated (e.g. Cenarro et al. 2001), we only used CaT2 in our search for correlations. The final set of optical *versus* NIR and NIR *versus* NIR indices the correlations are shown in Figs. 8 and 9, together with a linear regression using the orthogonal distance regression (ODR) method that takes errors both in the x and y variables into account (Boggs & Rogers 1990). We note that when it was not possible to measure one of the indices used in the correlations, we have removed the galaxy from the plots and regression. In addition, we only considered the cases were both indices were measured at least for 6 sources. To help to understand these plots we have over-plotted the same model set as discussed above.

What emerges from Fig. 8 is that both model sets are able to predict well all the measured values for the optical indices. In the NIR, however, the models fail in their predictions, except for CO2.2 and ZrO, with E-MILES making better predictions of strengths than M11, especially in the case of atomic absorption features. In addition, there is a clear separation of the ETGs and SFGs on the G4300×MgI1.7, G4300×NaI2.20, Fe4531×MgI1.7 and Mg_1×NaI2.20 diagrams with ETGs in general showing higher values for both optical and NIR indices. A less evident separation of ETGs and SFGs is observed on the G4300×CO2.2 and Mg_b×NaI2.20 diagrams, while no separation is observed for the Fe5782×ZrO and TiO_1× CO2.2 diagrams.

The optical indices (G4300, Fe4531 and Mg_1) are not very sensitive to the α/Fe ratio while G4300 is mainly sensitive to the C and O abundances (Thomas et al. 2003). This

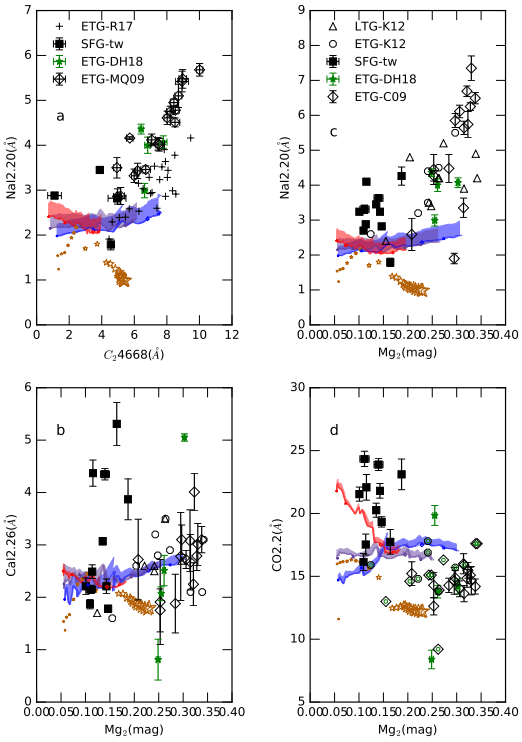

Figure 7. Index-index diagrams. Filled boxes are from this work. Plus markers indicate early-type objects indices presented in Röck et al. (2017, panel a, R17). Open diamonds are indices measured in early-type galaxies taken from Mármol-Queraltó et al. (panel a, ETG-MQ09 2009) and Cesetti et al. (panels b, c and d, ETG-C09 2009). Triangles and octagons represent, respectively, the late and early-type galaxies studied by Kotilainen et al. (2012, LTG-K12 and ETG-K12). Filled green stars represent our new measurements for the early-type galaxies of Dahmer-Hahn et al. (2018, ETG-DH18) in all panels. Note that the literature data may have different definitions between them selves and with the measurements we present here. Open brown stars represent Maraston & Strömbäck (2011) solar metalicity, Pickles-based models, with the size of the points scaling with ages (smallest points for 300Myr and largest for 15Gyr). The shaded areas represent IRTF-based EMILES models (Vazdekis et al. 2016; Röck 2015; Röck et al. 2016) with red, gray and blue indicating [Fe/H]=-0.40, [Fe/H]=0.00 and [Fe/H]=0.22, respectively. The shaded area represent models with a spectral resolution of σ=60 km/s (the lowest available) to σ=228 km/s. The age range used is between 0.3 Gyr and 15.0 Gyr, with arrows, triangles, diamonds and pentagons representing 0.3, 1, 5 and 10 Gyr, respectively. The E-MILES models with ages smaller than 1 Gyr should be taken with caution. For more details see text.

may indicate that the MgI1.7 and NaI2.20 indices are also sensitive to C and/or O abundances. This is also in agreement with the findings of Röck et al. (2017) who suggested that [C/Fe] enhancement might contribute to the values observed for NaI2.20 in ETGs. However, the good correlation of NaI with Mg_b may also indicate that this index is α/Fe dependent, since Mg_b is sensitive to changes in the α/Fe ratio (Thomas et al. 2003). red The CO2.2 index values

[6] The NaI2.20 and CO2.2 are well studied, however, we decided to keep them here for diagrams distinct from those presented in Fig. 7 because correlations with other lines may help to shed some light in the understanding of the mechanisms driving these lines.

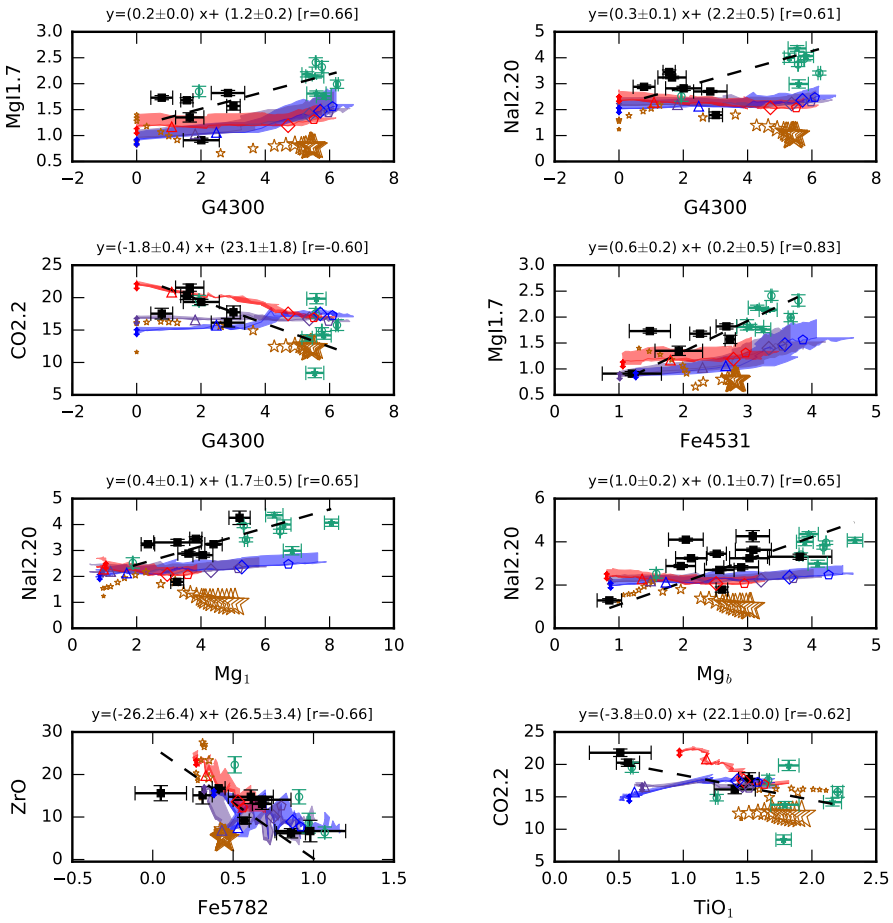

Figure 8. Index-index correlations. Black squares are the data points of the present work. Green diamonds are from Baldwin et al. (2017) and filled green stars are from Dahmer-Hahn et al. (2018). Open brown stars represent Maraston & Strömbäck (2011) solar metalicity, Pickles-based models, with the size of the points scaling with ages (smallest points for 300Myr and largest for 15Gyr). The shaded areas represent represent IRTF-based EMILES models (Vazdekis et al. 2016; Röck 2015; Röck et al. 2016) with red, gray and blue representing [Fe/H]=-0.40, [Fe/H]=0.00 and [Fe/H]=0.22, respectively. The shaded area represents models with a spectral resolution of σ=60 km/s (the lowest available) to σ=228 km/s. The age range used is between 0.3 Gyr and 15.0 Gyr, with arrows, triangles, diamonds and pentagons representing 0.3, 1, 5 and 10 Gyr, respectively. The models with ages smaller than 1 Gyr should be taken with caution. For more details see text.

are well described by the model predictions for both SFGs and ETGs, with an age-metallicity dependence for the SFGs and no evidence of strong changes on their strengths caused by the amount of TP-AGB stars (see above). This is additionally supported by the CO2.2 × TiO_1 diagram, where M11 models, independent of age, do populate the locus filled by the ETGs, while E-MILES models do not reproduce the larger TiO and smallest CO strengths. The CO and TiO_1 correlation is not unexpected since these absorptions depend on O being available. The models do show that ZrO is more metallicity dependent while TiO_1 seems to be age dependent. In addition, some ETG show TiO_1 values larger than the models (specially E-MILES models), which can be interpreted as an IMF effect (see La Barbera et al. 2013). In the case of the Mg-dominated indices (in the NIR and optical) the large values for these indices can be associated with the most massive ETGs, and can be explained by an [Mg/Fe] enhancement (e.g. Worthey et al. 1992; Martín-Navarro et al. 2018).

The correlations found from this exercise for the NIR indices are shown in Fig. 9. One particularly relevant correlation is CO1.6b×CN11, as the CN11 index is believed to be heavily dominated by the AGB evolutionary phase and particularly by C stars (Maraston 2005). Almost 50% of our SFG do show CN11$\gtrsim$10Å, with a mean value ~20% larger than in ETG (see Fig. 13) and are consistent with the intermediate age (0.3 - 2 Gyr) models. M11 models do cover better the space of values of the measurements, but all the older ages M11 models (t$\gtrsim$ 3 Gyr) do predict more or less constant values for CN11 (the same hapens for CO1.6b). The ETGs are more or less matched by SSP models with old ages and no indication of an intermediate age population is re-

quired to explain the absorption features of these sources, once, their strengths in some cases are smaller than those of the older E-MILES SSPs. The CO2.2 and CO2.3a,b (also CO1.5a and CO1.5b) indices are to some extent described by the models, with larger values predicted for intermediate age SSPs.The remaining strengths are not predicted by the models and no clear separation is found for SFGs and ETGs.

With the aim of understanding the behaviour of the NIR indices, we plotted them against the [MgFe]′ index of Thomas et al. (2003) defined as:

$$[MgFe]' \equiv \sqrt{Mgb(0.72 \times Fe5270 + 028 \times Fe5335)} \quad (1)$$

which, for this sample with a small range in metallicity, is basically an age-indicator and is completely independent of the α/Fe ratio. Assuming that the ETGs used here are objects with relatively normal old stellar populations, which is a valid assumption since their full spectra can be well fitted with SSP models (see Baldwin et al. 2017; Dahmer-Hahn et al. 2018, for details). This can also be seen in Figs. 10 to 12, where the ETGs do in general show less scatter in the [MgFe]′ index than the SFGs. This indicates a more complex SFH for the latter, most likely with a strong contribution from intermediate (∼1 Gyr) stellar populations. In order to test the effect of a more complex SFH on the NIR strengths, we show in Fig. 13 histograms comparing the strenght distributions between SFG and ETG. Except for a few indices (ZrO, MgI1.48, MgI1.50, CO1.5a, FeI1.58, CO1.5c, MgI1.7, NaI2.20), the mean value for SFG is larger than that for ETG. This more complex SFH can also explain why the CN and CO bands are in general stronger for the SFGs than the ETGs. These bands are enhanced by the short-lived younger red giant branch (RGB) and thermally pulsing asymptotic giant branch (TP-AGB) stars (Maraston 2005; Riffel et al. 2007, 2015). According to Maraston (1998), these stars can be responsible for up to 70 per cent of the total flux in the NIR. However, for the case of the NaI2.20 index, (Röck et al. 2017) constructed models using enhanced contribution from AGB stars and found that these stars have only a very limited effect on the model predictions and do not improve significantly the fit of the model NaI2.20 indices. They also show that small fractions (3 per cent) do have a similar impact on NaI2.20 than those with larger amounts of these stars. This result is consistent with our findings that NaI2.20 index has a mean value ∼20% larger in ETG than in SFG.

In general, the NIR line strengths are not well reproduced by any set of models, suggesting that the SFH of the galaxies cannot be recovered when only using NIR indices. Our results are in agreement with the finding of Baldwin et al. (2017) who have studied the SFH of a sample of ETG by fitting different SSP models and found that the SFH vary dramatically among the different EPS models when fitting NIR data, with higher spectral resolution models producing more consistent results. They also found variations in ages in the NIR tend to be small, and largely encoded in the shape of the continuum. This was also noticed in Riffel et al. (2015) who suggested that TP-AGB stars contribute noticeably to a mean stacked NIR spectrum made up with mostly late type galaxies hosting a low luminosity AGN, from the Palomar survey (Mason et al. 2015). This result was obtained by fitting a mix of individual IRTF stars to the mean galaxy spectrum. Nevertheless, in this same work we have shown that other evolved stars (red giants, C-R and E-AGB stars) can reproduce most of the absorption features detected, without having to resort to stars in the TP-AGB phase.

5 FINAL REMARKS

We analysed long-slit spectra spanning optical to near-infrared wavelengths of 16 infrared-luminous star-forming galaxies with the aim of offering the community a set of emission and absorption feature measurements that can be used to test the predictions of the forthcoming generations of stellar population models. The optical and NIR spectra were obtained at WIRO and at SpeX/IRTF, respectively. In addition to these, we collected literature spectra of early-type galaxies and performed the equivalent width measurements using a new homogeneous set of continuum and band pass definitions. The main findings can be summarized as follows:

- All our sources display H_2 emission, characteristic of the star-forming nature of our sample. In the optical they clearly display H I emission lines. However, NGC 1055 and NGC 1134 show a NIR spectrum free of H I emission lines. We interpret this latter result as the result of the low sensitivity of the NIR detector in this wavelength interval, thus the expected Brγ fluxes are below the detection limit.
- The continua are dominated by stellar absorption features. The most common features are due to Ca I, Ca II, Fe I, Na I, Mg I, plus prominent absorption bands of: TiO, VO, ZrO and CO. In most cases (70%) ,the stellar continua also show evidence of dust extinction.
- We present new definitions of continuum and line band passes for the NIR absorption lines. These definitions were made taking into account the position of the most common emission lines detected in this wavelength range.
- We report EW measurements for 45 indices, including both optical and NIR features. We also present measurements for most of these indices in spectra of ETGs taken from literature. To the best of our knowledge, they represent the most complete set of EW measurements reported in the literature to date, and can be used to test the predictions of stellar population models from the optical to the NIR.
- We looked for correlations among the different absorption features, presenting as the most robust ones those with a Pearson correlation coefficient r>0.6. In addition to the already-known correlations in the optical region, we propose here correlations between optical and NIR indices, as well as correlations between different NIR indices, and compare them with model predictions.
- While for the optical absorption features the new generation of models, with scaled-solar abundance ratios and standard IMF, share the same locus as the observed data points, they fail to predict the strengths of most of the NIR indices for the SFGs, while in the case of the early-type sources they roughly reproduce the observations. This may indicate more complex SFHs for the SFGs, which we interpreted as a strong contribution from the younger stellar populations, thus explaining the fact that the CN and CO bands are in general larger for the SFGs than the ETGs. These bands are enhanced in stars in the TP-AGB phase,

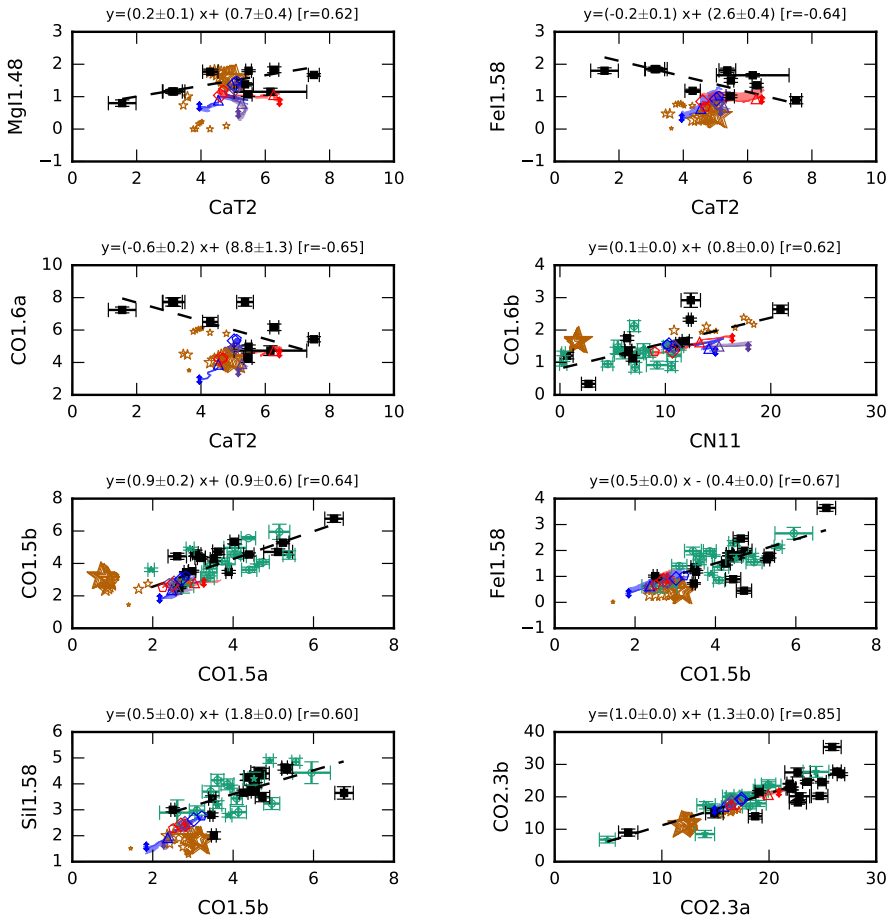

Figure 9. Same as Fig. 8 but for NIR *x* NIR indices.

however, they seems to have a limited impact on the indices of ETGs.

ACKNOWLEDGEMENTS

We are grateful to the referee for insight that has improved the quality of this paper. RR and RAR thank CNPq, CAPES and FAPERGS for financial support for this project and to Luis Colina for helpful discussions on this project. The authors are also grateful to Richard McDermid and Christina Baldwin for kindly offering information on the ETGs used in this work, as well as, to Jari Kotilainen for sharing information on his sample of objects. We also thank Peter van Hoof for providing the new collisional strengths for [P II] lines, which will be part of the new CLOUDY release, as well as for useful discussions. ARA thanks CNPq for financial support. RFP acknowledges financial support from the European Union's Horizon 2020 research and innovation program under the Marie Sklodowska-Curie grant agreement No. 721463 to the SUNDIAL ITN network. AV acknowledges support from grant AYA2016-77237-C3-1-P from the Spanish Ministry of Economy and Competitiveness (MINECO).

REFERENCES

Ahn C. P., et al., 2014, ApJS, 211, 17
Alton P. D., Smith R. J., Lucey J. R., 2018, MNRAS, 478, 4464
Baldwin C. M., McDermid R. M., Kuntschner H., Maraston C., Conroy C., 2017, preprint, (arXiv:1709.09300)
Balzano V. A., 1983, ApJ, 268, 602
Bica E., 1988, A&A, 195, 76
Bica E., Alloin D., 1987, A&A, 186, 49
Boggs P. T., Rogers J. E., 1990, Contemporary Mathematics: Statistical analysis of measurement error models and applications: proceedings of the AMS-IMS-SIAM joint summer research conference held June 10-16, 1989, 112, 186
Borguet B. C. J., Edmonds D., Arav N., Benn C., Chamberlain C., 2012, ApJ, 758, 69
Burtscher L., et al., 2015, A&A, 578, A47
Cardelli J. A., Clayton G. C., Mathis J. S., 1989, ApJ, 345, 245
Cenarro A. J., Cardiel N., Gorgas J., Peletier R. F., Vazdekis A., Prada F., 2001, MNRAS, 326, 959
Cesetti M., et al., 2009, A&A, 497, 41
Chen Y.-P., Trager S. C., Peletier R. F., Lançon A., Vazdekis A., Prugniel P., Silva D. R., Gonneau A., 2014, A&A, 565, A117
Chies-Santos A. L., Larsen S. S., Wehner E. M., Kuntschner H., Strader J., Brodie J. P., 2011a, A&A, 525, A19
Chies-Santos A. L., Larsen S. S., Kuntschner H., Anders P.,

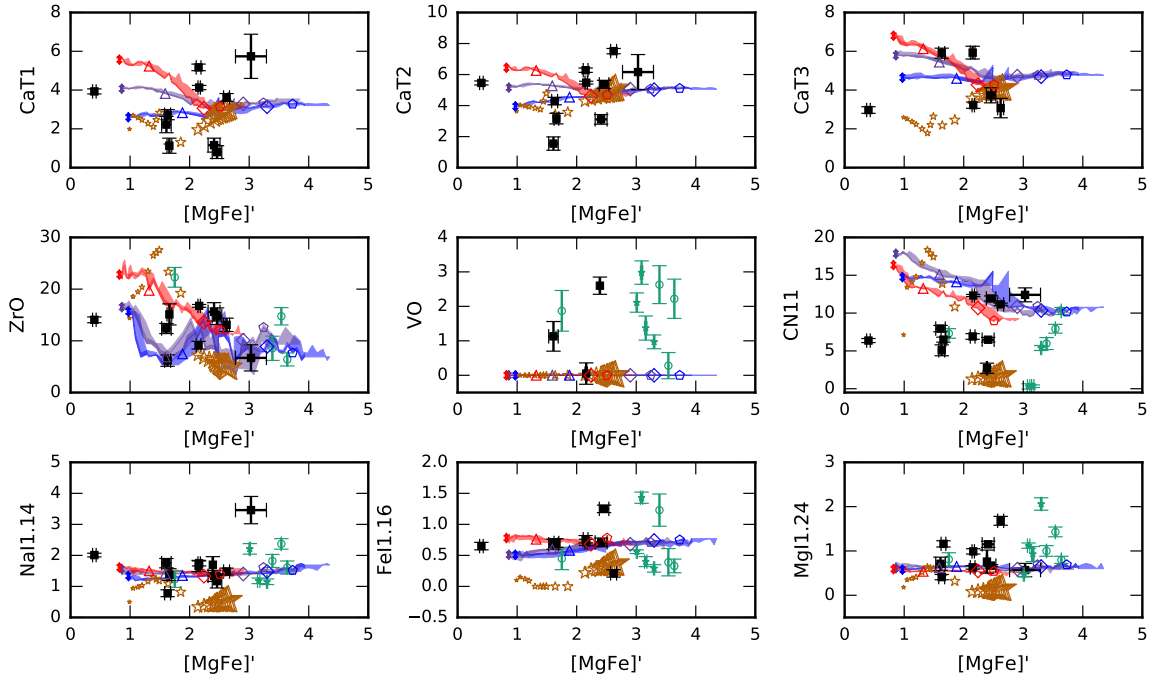

Figure 10. Comparison of NIR indices with [MgFe]'. The models are the same as Fig. 8.

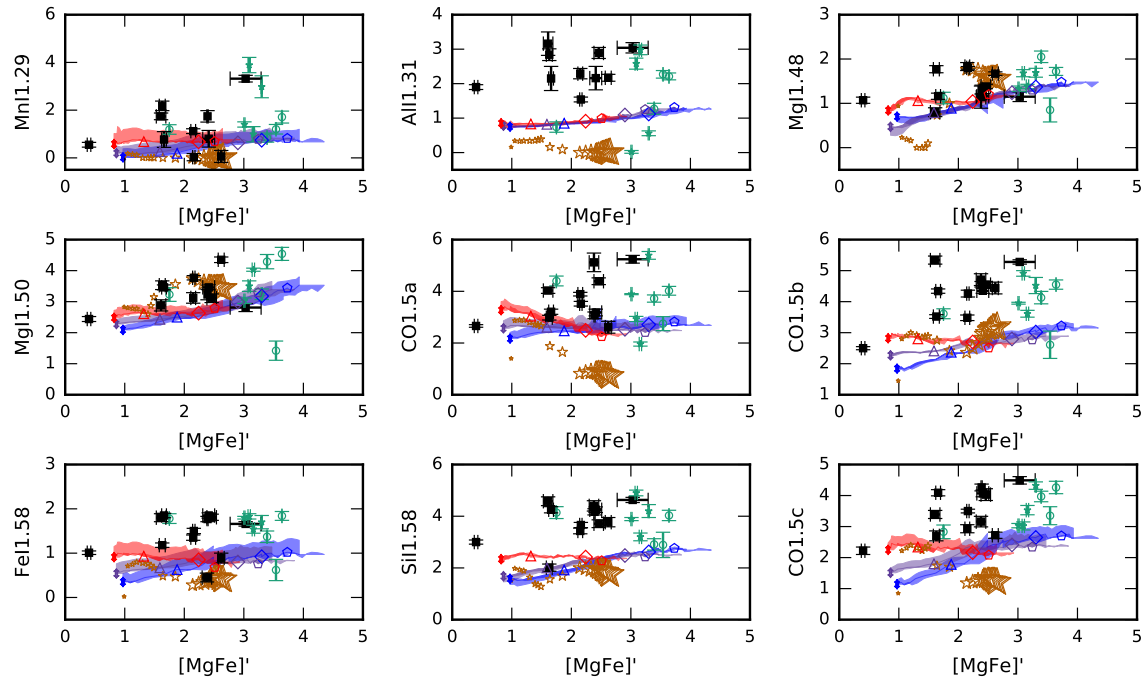

Figure 11. Comparison of NIR indices with [MgFe]'. The models are the same as Fig. 8.

Wehner E. M., Strader J., Brodie J. P., Santos J. F. C., 2011b, A&A, 525, A20

Condon J. J., Cotton W. D., Broderick J. J., 2002, AJ, 124, 675

Conroy C., van Dokkum P. G., 2012, ApJ, 760, 71

Cushing M. C., Vacca W. D., Rayner J. T., 2004, PASP, 116, 362

Dahmer-Hahn L. G., Riffel R., Rodríguez-Ardila A., Martins L. P., Kehrig C., Heckman T. M., Pastoriza M. G., Dametto N. Z., 2018, MNRAS, 476, 4459

Dahmer-Hahn L. G., et al., 2019, MNRAS, 482, 5211

Dametto N. Z., Riffel R., Pastoriza M. G., Rodríguez-Ardila A., Hernandez-Jimenez J. A., Carvalho E. A., 2014, MNRAS, 443, 1754

Dametto N. Z., et al., 2019, MNRAS, 482, 4437

Ferguson J. W., Korista K. T., Baldwin J. A., Ferland G. J., 1997, ApJ, 487, 122

Ferland G. J., et al., 2017, Rev. Mex. Astron. Astrofis., 53, 385

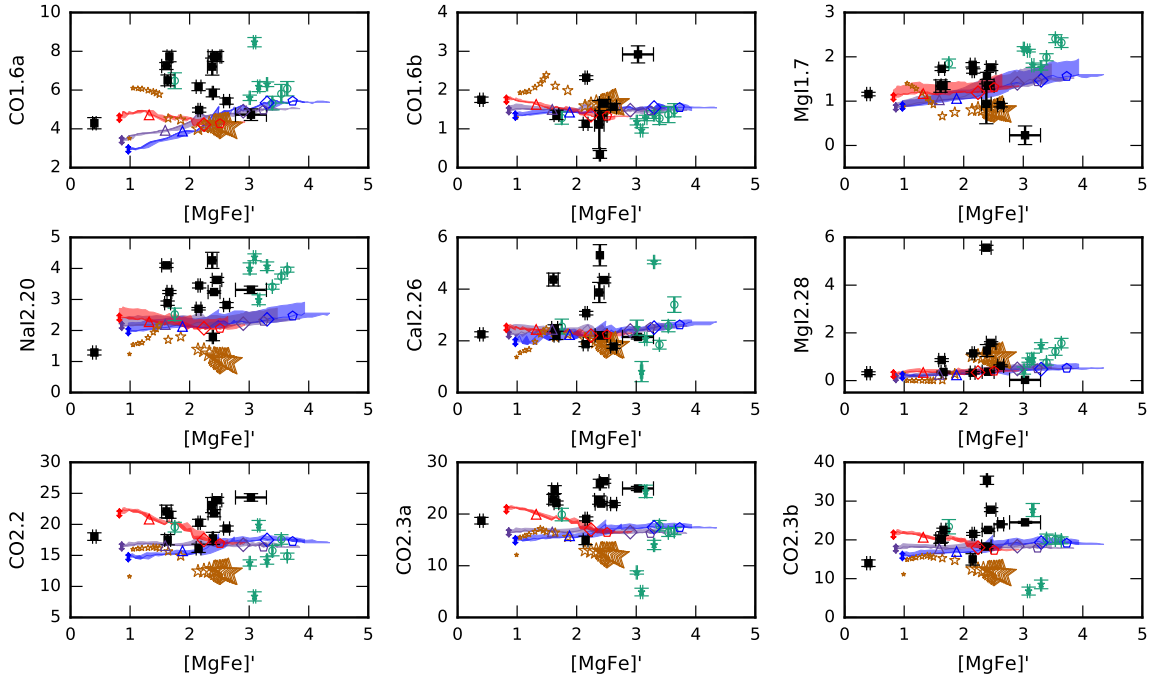

Figure 12. Comparison of NIR indices with [MgFe]'. The models are the same as Fig. 8.

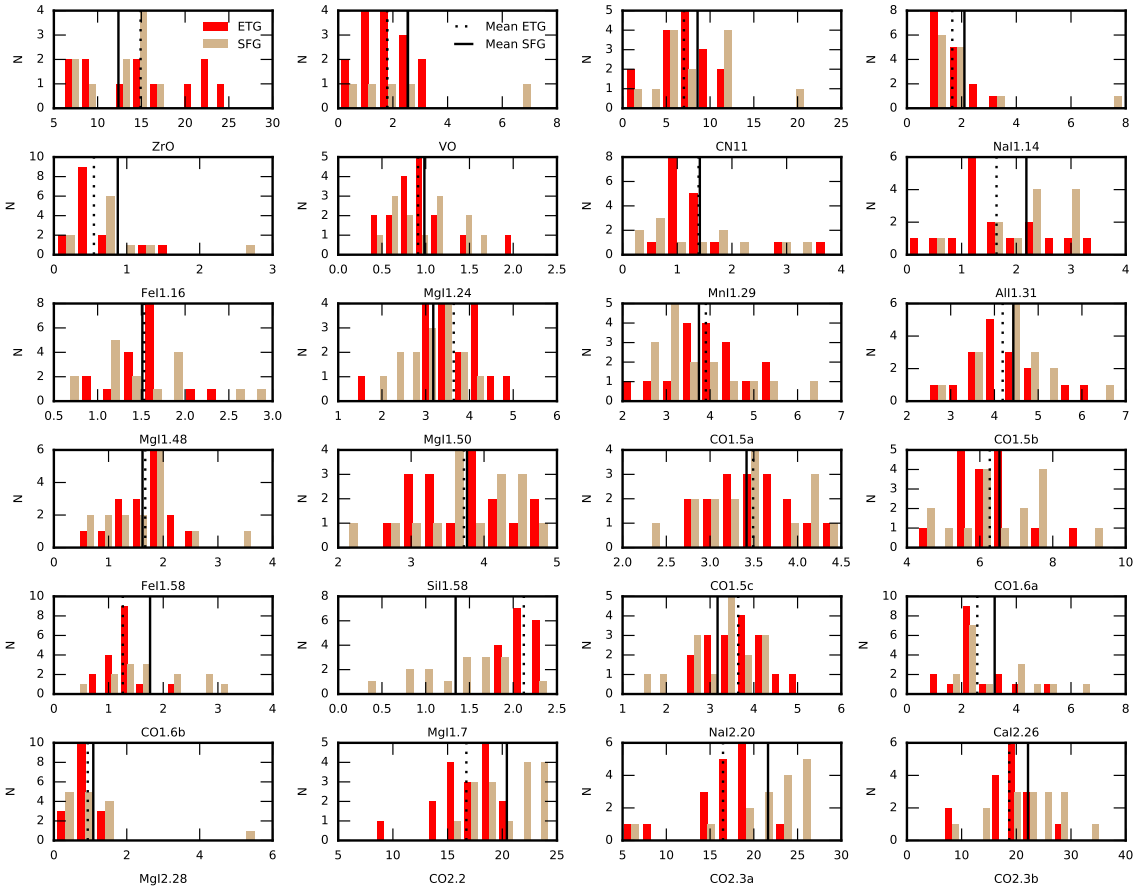

Figure 13. Comparison of NIR indices strengths between SFG and ETG.

Table 5. Line limits and continuum bandpasses.

Centre (Å)	Main Absorber	Index Name	Line Limits (Å)	Blue continuum (Å)	Red Continuum (Å)	Reference
4228.5	Ca I	Ca4227	4222.250 – 4234.750	4211.000 – 4219.750	4241.000 – 4251.000	Worthey et al. (1994)
4298.875	CH (G-Band)	G4300	4281.375 – 4316.375	4266.375 – 4282.625	4318.875 – 4335.125	Worthey et al. (1994)
4394.75	Fe I	Fe4383	4369.125 – 4420.375	4359.125 – 4370.375	4442.875 – 4455.375	Worthey et al. (1994)
4463.375	Ca I	Ca4455	4452.125 – 4474.625	4445.875 – 4454.625	4477.125 – 4492.125	Worthey et al. (1994)
4536.75	Fe I	Fe4531	4514.250 – 4559.250	4504.250 – 4514.250	4560.500 – 4579.250	Worthey et al. (1994)
4677.125	C_2	Fe4668	4634.000 – 4720.250	4611.500 – 4630.250	4742.750 – 4756.500	Worthey et al. (1994)
5015.875	Fe I	Fe5015	4977.750 – 5054.000	4946.500 – 4977.750	5054.000 – 5065.250	Worthey et al. (1994)
5101.625	MgH	Mg1	5069.125 – 5134.125	4895.125 – 4957.625	5301.125 – 5366.125	Worthey et al. (1994)
5175.375	MgH	Mg2	5154.125 – 5196.625	4895.125 – 4957.625	5301.125 – 5366.125	Worthey et al. (1994)
5176.375	Mg b	Mgb	5160.125 – 5192.625	5142.625 – 5161.375	5191.375 – 5206.375	Worthey et al. (1994)
5265.65	Fe I	Fe5270	5245.650 – 5285.650	5233.150 – 5248.150	5285.650 – 5318.150	Worthey et al. (1994)
5332.125	Fe I	Fe5335	5312.125 – 5352.125	5304.625 – 5315.875	5353.375 – 5363.375	Worthey et al. (1994)
5401.25	Fe I	Fe5406	5387.500 – 5415.000	5376.250 – 5387.500	5415.000 – 5425.000	Worthey et al. (1994)
5708.5	Fe I	Fe5709	5696.625 – 5720.375	5672.875 – 5696.625	5722.875 – 5736.625	Worthey et al. (1994)
5786.625	Fe I	Fe5782	5776.625 – 5796.625	5765.375 – 5775.375	5797.875 – 5811.625	Worthey et al. (1994)
5893.125	Na I	NaD	5876.875 – 5909.375	5860.625 – 5875.625	5922.125 – 5948.125	Worthey et al. (1994)
5965.375	TiO	TiO1	5936.625 – 5994.125	5816.625 – 5849.125	6038.625 – 6103.625	Worthey et al. (1994)
6230.875	TiO	TiO2	6189.625 – 6272.125	6066.625 – 6141.625	6372.625 – 6415.125	Worthey et al. (1994)
8498.0	Ca II	CaT1	8476.000 – 8520.000	8110.000 – 8165.000	8786.000 – 8844.000	Bica & Alloin (1987) (†)
8542.0	Ca II	CaT2	8520.000 – 8564.000	8110.000 – 8165.000	8786.000 – 8844.000	Bica & Alloin (1987) (†)
8670.0	Ca II	CaT3	8640.000 – 8700.000	8110.000 – 8165.000	8786.000 – 8844.000	Bica & Alloin (1987) (†)
9320.0	ZrO/TiO/CN	ZrO	9170.000 – 9470.000	8900.000 – 8960.000	9585.000 – 9615.000	New Definition (α)
10560.0	VO	VO	10470.000 – 10650.000	10430.000 – 10465.000	10660.000 – 10700.000	New Definition (α)
11000.0	CN	CN11	10910.000 – 11090.000	10705.000 – 10730.000	11310.000 – 11345.000	New Definition (β)
11390.0	Na I	NaI1.14	11350.000 – 11430.000	11310.000 – 11345.000	11450.000 – 11515.000	New Definition (β)
11605.0	Fe I	FeI1.16	11580.000 – 11630.000	11450.000 – 11515.000	11650.000 – 11690.000	Roeck (2015)
12430.0	Mg I	MgI1.24	12405.000 – 12455.000	12335.000 – 12365.000	12465.000 – 12490.000	Roeck (2015)
12944.0	Mn I	MnI1.29	12893.000 – 12995.000	12858.000 – 12878.000	13026.000 – 13068.000	New Definition
13132.5	Al I	AlI1.31	13095.000 – 13170.000	13000.000 – 13070.000	13175.000 – 13215.000	Roeck (2015)
14875.0	Mg I	MgI1.48	14850.000 – 14900.000	14750.000 – 14800.000	14910.000 – 14950.000	New Definition
15032.5	Mg I	MgI1.50	14995.000 – 15070.000	14910.000 – 14950.000	15150.000 – 15200.000	New Definition
15587.5	CO+Mg I	CO1.5a	15555.000 – 15620.000	15470.000 – 15500.000	15700.000 – 15730.000	New Definition (ϵ)
15780.0	CO+Mg I	CO1.5b	15750.000 – 15810.000	15700.000 – 15730.000	16095.000 – 16145.000	New Definition (ϵ)
15830.0	Fe I	FeI1.58	15810.000 – 15850.000	15700.000 – 15730.000	16090.000 – 16140.000	New Definition
15890.0	Si I + Mg I	SiI1.58	15850.000 – 15930.000	15700.000 – 15730.000	16090.000 – 16140.000	New Definition
15985.0	CO+Si I	CO1.5c	15950.000 – 16020.000	15700.000 – 15730.000	16090.000 – 16140.000	New Definition (ϵ)
16215.0	CO+Si I+Ca I	CO1.6a	16145.000 – 16285.000	16090.000 – 16140.000	16290.000 – 16340.000	New Definition (ϵ)
17064.0	CO + Fe I	CO1.6b	17035.000 – 17093.000	16970.000 – 17025.000	17140.000 – 17200.000	New Definition (ϵ)
17111.5	Mg I	MgI1.7	17093.000 – 17130.000	16970.000 – 17025.000	17140.000 – 17200.000	Roeck (2015)
22073.5	Na I	NaI2.20	22040.000 – 22107.000	21910.000 – 21966.000	22125.000 – 22160.000	Frogel et al. (2001)
22634.5	Ca I	CaI2.26	22577.000 – 22692.000	22530.000 – 22560.000	22700.000 – 22720.000	Frogel et al. (2001) (γ)
22820.0	Mg I	MgI2.28	22795.000 – 22845.000	22700.000 – 22720.000	22850.000 – 22865.000	New Definition (δ)
23015.0	CO	CO2.2	22870.000 – 23160.000	22700.000 – 22790.000	23655.000 – 23680.000	New Definition (ϵ)
23290.0	CO	CO2.3a	23160.000 – 23420.000	22700.000 – 22790.000	23655.000 – 23680.000	New Definition (ϵ)
23535.0	CO	CO2.3b	23420.000 – 23650.000	22700.000 – 22790.000	23655.000 – 23680.000	New Definition (ϵ)

Table Notes: The optical indices are those of the LICK observatory (Worthey et al. 1994, and references). The CaT indices are those of Bica & Alloin (1987) with a change in the blue continuum band passes in order to fit in our spectral region; α Based on Riffel et al. (2015) with small changes on the line limits; β New continuum limits with central bandpasses from Roeck (2015); ϵ adapted from Riffel et al. (2007) with fixed continuum band passes, with better identifications of the main absorbers as well as better constraints of the line limits; γ We made a small change on the blue continuum band pass to remove possible H_2 emission lines.; δ Adapted from Silva et al. (2008) in order to better accomodate the continuum regions for the CO lines.

Ferruit P., Wilson A. S., Mulchaey J., 2000, ApJS, 128, 139

Filho M. E., Fraternali F., Markoff S., Nagar N. M., Barthel P. D., Ho L. C., Yuan F., 2004, A&A, 418, 429

Francois P., Morelli L., Pizzella A., Ivanov V. D., Coccato L., Cesetti M., Corsini E. M., Dalla Bonta E., 2018, arXiv e-prints,

Frogel J. A., Stephens A., Ramírez S., DePoy D. L., 2001, AJ, 122, 1896

Genzel R., Tacconi L. J., Rigopoulou D., Lutz D., Tecza M., 2001, ApJ, 563, 527

Girardi L., Bressan A., Bertelli G., Chiosi C., 2000, A&AS, 141, 371

Goddard D., et al., 2017, MNRAS, 465, 688

Gonçalves A. C., Veron P., Veron-Cetty M.-P., 1998, A&AS, 127, 107

González Delgado R. M., et al., 2015, A&A, 581, A103

Hamann F., 1998, ApJ, 500, 798

Hamann F. W., Barlow T. A., Chaffee F. C., Foltz C. B., Weymann R. J., 2001, ApJ, 550, 142

Ho L. C., Filippenko A. V., Sargent W. L. W., 1997a, ApJS, 112, 315

Ho L. C., Filippenko A. V., Sargent W. L. W., Peng C. Y., 1997b, ApJS, 112, 391

Hummer D. G., Storey P. J., 1987, MNRAS, 224, 801

Kotilainen J. K., Hyvönen T., Reunanen J., Ivanov V. D., 2012, MNRAS, 425, 1057

La Barbera F., Ferreras I., Vazdekis A., de la Rosa I. G., de Carvalho R. R., Trevisan M., Falcón-Barroso J., Ricciardelli E., 2013, MNRAS, 433, 3017

Lamperti I., et al., 2017, MNRAS, 467, 540

Lançon A., Goldader J. D., Leitherer C., González Delgado R. M., 2001, ApJ, 552, 150

Lyubenova M., Kuntschner H., Rejkuba M., Silva D. R., Kissler-Patig M., Tacconi-Garman L. E., Larsen S. S., 2010, A&A,

Table 6. Absorption feature Equivalent Widths (in Å) .

Line	NGC23	NGC520	NGC660	NGC1055	NGC1134	NGC1204	NGC1222	NGC1266
Ca4227	0.36±0.06	–	0.53±0.61	–	1.14±0.16	–	–	–
G4300	1.56±0.19	–	5.18±1.62	–	2.01±0.56	–	–	–
Fe4383	1.67±0.22	–	7.23±0.68	–	3.84±1.05	–	–	7.53±2.22
Ca4455	0.49±0.1	3.22±0.47	2.01±0.3	–	0.28±0.22	–	–	–
Fe4531	2.26±0.16	–	–	–	1.2±0.46	–	–	–
$C_2$4668	3.88±0.2	–	–	–	4.94±0.55	–	–	–
Fe5015	–	–	–	–	–	–	–	–
Mg_1	3.84±0.19	–	5.26±0.3	5.2±0.33	4.06±0.31	4.39±0.27	–	3.27±0.74
Mg_2	4.98±0.13	–	6.46±0.21	6.73±0.2	5.36±0.18	5.24±0.18	–	4.14±0.37
Mg_b	2.52±0.15	–	2.71±0.25	3.08±0.26	2.9±0.27	3.03±0.31	0.85±0.19	3.81±0.5
Fe5270	1.91±0.12	–	2.53±0.35	1.92±0.32	2.44±0.2	2.09±0.3	–	2.43±0.45
Fe5335	1.73±0.12	–	2.02±0.24	1.64±0.34	2.17±0.2	1.48±0.33	0.66±0.28	2.38±0.67
Fe5406	0.95±0.04	–	1.0±0.15	0.57±0.27	1.25±0.14	0.68±0.3	0.09±0.1	2.33±0.32
Fe5709	0.64±0.04	–	0.77±0.1	0.72±0.13	0.79±0.07	0.75±0.14	0.45±0.04	0.74±0.4
Fe5782	0.41±0.04	–	1.11±0.08	–	0.68±0.06	0.05±0.16	0.68±0.18	0.98±0.22
NaD	4.25±0.08	1.91±0.25	5.07±0.19	4.02±0.27	4.71±0.12	3.56±0.21	–	6.37±0.23
TiO_1	0.57±0.09	–	–	–	–	0.51±0.24	–	–
TiO_2	3.82±0.11	–	5.79±0.2	7.96±0.28	6.13±0.2	6.07±0.27	3.87±0.19	8.34±0.51
CaT1	4.13±0.11	–	–	–	3.62±0.20	1.16±0.36	3.93±0.13	5.74±1.14
CaT2	5.48±0.09	–	–	–	7.51±0.17	3.11±0.31	5.46±0.13	6.16±1.13
CaT3	3.22±0.16	–	–	–	3.07±0.50	–	2.97±0.17	–
ZrO	16.76±0.27	–	–	–	13.09±1.29	15.60±1.78	14.06±0.56	6.70±2.53
VO	0.05±0.31	–	1.41±0.63	–	–	–	–	–
CN11	12.32±0.14	–	3.76±0.28	–	11.15±0.17	6.48±0.31	6.37±0.27	12.41±0.92
NaI1.14	1.74±0.08	–	2.43±0.18	–	1.48±0.11	1.34±0.18	2.01±0.06	3.46±0.44
FeI1.16	0.71±0.05	–	0.44±0.07	–	0.21±0.06	0.71±0.07	0.65±0.06	–
MgI1.24	0.99±0.06	–	0.74±0.05	–	1.68±0.10	1.15±0.07	–	0.57±0.15
MnI1.29	0.03±0.15	–	0.28±0.14	–	0.06±0.25	0.80±0.35	0.55±0.10	3.32±0.14
AlI1.31	1.54±0.07	–	1.93±0.57	–	2.17±0.10	2.16±0.34	1.90±0.07	3.04±0.15
MgI1.48	1.80±0.03	2.94±0.17	1.96±0.03	1.14±0.25	1.67±0.04	1.16±0.06	1.07±0.07	1.15±0.11
MgI1.50	3.77±0.07	3.28±0.30	2.43±0.10	–	4.35±0.09	3.46±0.08	2.44±0.08	2.81±0.13
CO1.5a	3.52±0.09	6.51±0.23	4.33±0.10	5.12±0.36	2.61±0.23	3.18±0.13	2.66±0.05	5.24±0.15
CO1.5b	4.26±0.11	6.76±0.23	4.94±0.10	4.71±0.19	4.44±0.19	4.35±0.08	2.50±0.05	5.28±0.07
FeI1.58	1.50±0.06	3.64±0.13	2.11±0.06	0.45±0.10	0.89±0.11	1.85±0.06	1.01±0.04	1.66±0.05
SiI1.58	3.66±0.10	3.65±0.24	4.03±0.13	4.40±0.20	3.77±0.18	4.25±0.11	3.00±0.08	4.63±0.10
CO1.5c	3.50±0.06	3.39±0.20	3.83±0.11	3.16±0.17	2.72±0.10	4.07±0.11	2.22±0.12	4.49±0.12
CO1.6a	4.97±0.11	7.60±0.39	6.70±0.15	7.21±0.44	5.43±0.16	7.73±0.25	4.29±0.29	4.73±0.30
CO1.6b	2.32±0.05	3.21±0.19	0.79±0.07	1.11±0.62	1.57±0.08	1.34±0.13	1.75±0.07	2.92±0.22
MgI1.7	1.68±0.05	0.76±0.21	1.37±0.04	0.94±0.45	0.91±0.04	1.35±0.08	1.16±0.04	0.23±0.21
NaI2.20	3.45±0.08	2.51±0.10	2.88±0.07	4.26±0.26	2.82±0.08	3.24±0.04	1.29±0.08	3.31±0.12
CaI2.26	3.07±0.07	4.07±0.12	2.40±0.18	3.87±0.39	1.78±0.07	2.21±0.14	2.25±0.10	2.15±0.08
MgI2.28	1.14±0.02	1.20±0.09	0.60±0.04	5.57±0.10	0.62±0.04	0.37±0.04	0.31±0.06	0.03±0.01
CO2.2	20.26±0.56	23.16±0.36	12.23±0.39	23.11±1.22	19.33±0.41	21.80±0.58	18.03±0.61	24.34±0.61
CO2.3a	19.07±0.38	26.71±0.35	12.45±0.66	22.69±0.80	21.93±0.26	22.02±0.43	18.71±0.64	24.94±0.40
CO2.3b	21.53±0.37	27.00±0.42	12.50±0.78	18.28±0.56	24.03±0.13	22.57±0.44	13.99±0.85	24.52±0.26

510, A19
Maraston C., 1998, MNRAS, 300, 872
Maraston C., 2005, MNRAS, 362, 799
Maraston C., Strömbäck G., 2011, MNRAS, 418, 2785
Marigo P., Girardi L., Bressan A., Groenewegen M. A. T., Silva L., Granato G. L., 2008, A&A, 482, 883
Mármol-Queraltó E., et al., 2009, ApJ, 705, L199
Martín-Navarro I., Vazdekis A., Falcón-Barroso J., La Barbera F., Yıldırım A., van de Ven G., 2018, MNRAS, 475, 3700
Martins L. P., Rodríguez-Ardila A., Diniz S., Gruenwald R., de Souza R., 2013a, MNRAS, 431, 1823
Martins L. P., Rodríguez-Ardila A., Diniz S., Riffel R., de Souza R., 2013b, MNRAS, 435, 2861
Mason R. E., et al., 2015, ApJS, 217, 13
McDermid R. M., et al., 2015, MNRAS, 448, 3484
Noël N. E. D., Greggio L., Renzini A., Carollo C. M., Maraston C., 2013, ApJ, 772, 58
Oliva E., et al., 2001, A&A, 369, L5
Origlia L., Moorwood A. F. M., Oliva E., 1993, A&A, 280, 536
Origlia L., Ferraro F. R., Fusi Pecci F., Oliva E., 1997, A&A, 321, 859
Pereira-Santaella M., Diamond-Stanic A. M., Alonso-Herrero A., Rieke G. H., 2010, ApJ, 725, 2270
Pogge R. W., Owen J., 1993, Ohio State University, Internal Report, 9301, 1
Rayner J. T., Toomey D. W., Onaka P. M., Denault A. J., Stahlberger W. E., Vacca W. D., Cushing M. C., Wang S., 2003, PASP, 115, 362
Rieke G. H., Lebofsky M. J., Thompson R. I., Low F. J., Tokunaga A. T., 1980, ApJ, 238, 24

Table 7. Absorption feature Equivalent Widths (in Å).

Line	UGC2982	NGC1797	NGC6814	NGC6835	UGC12150	NGC7465	NGC7591	NGC7678
Ca4227	–	0.91±0.12	–	–	–	0.47±0.1	–	–
G4300	–	1.65±0.44	–	–	–	2.84±0.52	–	0.78±0.34
Fe4383	–	–	–	–	–	2.77±0.27	–	2.24±0.4
Ca4455	–	–	–	–	–	0.53±0.16	–	1.11±0.12
Fe4531	–	1.93±0.37	–	–	–	2.67±0.16	–	1.48±0.32
$C_2$4668	–	–	–	–	–	–	–	1.1±0.42
Fe5015	–	–	–	–	–	–	–	–
Mg_1	–	2.35±0.21	–	–	–	–	–	3.61±0.33
Mg_2	–	3.77±0.13	–	–	4.28±0.26	4.07±0.24	5.14±0.36	4.23±0.16
Mg_b	–	2.12±0.24	–	–	2.04±0.27	2.56±0.23	3.09±0.28	1.96±0.23
Fe5270	–	1.32±0.19	–	–	1.34±0.28	1.78±0.17	1.82±0.29	1.31±0.16
Fe5335	–	1.22±0.13	–	–	1.11±0.37	1.85±0.15	2.32±0.3	1.5±0.29
Fe5406	–	0.87±0.11	–	–	0.44±0.2	0.78±0.15	1.31±0.21	1.04±0.12
Fe5709	–	0.35±0.06	–	–	0.64±0.1	0.7±0.06	1.14±0.17	0.78±0.11
Fe5782	–	0.31±0.06	–	–	–	0.57±0.03	0.61±0.14	0.86±0.09
NaD	4.78±0.37	6.27±0.19	–	–	7.47±0.52	1.67±0.27	3.86±0.19	4.17±0.25
TiO_1	–	–	–	–	–	1.4±0.16	–	–
TiO_2	–	2.08±0.23	–	–	4.88±0.52	4.63±0.15	3.4±0.25	4.6±0.21
CaT1	–	1.13±0.39	–	–	2.22±0.42	5.17±0.17	0.80±0.33	2.73±0.26
CaT2	–	3.16±0.34	0.36±0.19	–	1.55±0.43	6.28±0.14	5.37±0.26	4.29±0.24
CaT3	–	–	3.35±0.06	–	–	5.93±0.33	3.73±0.39	5.90±0.26
ZrO	–	15.11±2.04	1.20±1.74	–	12.38±0.98	9.16±0.75	14.76±1.61	6.18±1.10
VO	7.10±1.35	–	3.89±0.43	–	1.13±0.43	–	–	–
CN11	20.92±0.74	6.49±0.33	–	–	7.95±0.42	6.91±0.37	11.93±0.34	5.08±0.72
NaI1.14	–	1.38±0.19	3.99±0.13	7.92±0.83	1.75±0.15	1.66±0.18	1.17±0.22	0.78±0.11
FeI1.16	0.17±0.20	0.70±0.07	0.53±0.06	2.78±0.11	0.68±0.08	0.76±0.06	1.25±0.06	–
MgI1.24	1.40±0.06	1.16±0.07	0.76±0.05	1.49±0.06	0.71±0.15	0.63±0.04	0.67±0.02	0.41±0.06
MnI1.29	3.11±0.62	0.77±0.33	10.00±0.43	1.53±0.11	1.74±0.14	1.12±0.10	–	2.18±0.20
AlI1.31	0.46±0.26	2.15±0.35	1.33±0.11	–	3.16±0.34	2.29±0.15	2.89±0.16	2.84±0.17
MgI1.48	0.57±0.10	1.16±0.07	0.94±0.03	1.83±0.14	0.80±0.10	1.83±0.09	1.38±0.05	1.77±0.08
MgI1.50	2.41±0.10	3.46±0.08	2.07±0.07	1.82±0.25	2.88±0.18	3.12±0.17	3.11±0.14	3.53±0.14
CO1.5a	2.83±0.05	3.21±0.10	2.53±0.07	3.06±0.07	4.03±0.11	3.89±0.07	4.39±0.13	2.98±0.09
CO1.5b	3.46±0.04	4.34±0.07	3.10±0.05	4.63±0.19	5.34±0.13	3.48±0.09	4.55±0.10	3.52±0.06
FeI1.58	0.73±0.03	1.85±0.05	0.77±0.03	2.46±0.11	1.80±0.09	1.35±0.06	1.81±0.07	1.18±0.05
SiI1.58	2.81±0.07	4.25±0.12	2.57±0.07	4.45±0.19	4.58±0.17	3.43±0.11	3.71±0.15	2.01±0.14
CO1.5c	2.99±0.07	4.09±0.10	2.51±0.06	3.46±0.18	3.39±0.13	2.93±0.13	4.03±0.19	2.70±0.16
CO1.6a	6.02±0.19	7.73±0.27	4.26±0.20	9.42±0.45	7.24±0.18	6.17±0.20	7.73±0.26	6.50±0.28
CO1.6b	2.64±0.13	1.36±0.12	0.92±0.05	2.07±0.28	–	1.13±0.09	1.66±0.10	–
MgI1.7	0.85±0.11	1.35±0.09	1.11±0.03	2.21±0.29	1.34±0.14	1.82±0.05	1.76±0.07	1.73±0.04
NaI2.20	4.15±0.15	3.24±0.05	1.54±0.03	3.41±0.04	4.10±0.07	2.70±0.04	3.63±0.08	2.88±0.07
CaI2.26	6.74±0.13	2.21±0.16	1.04±0.04	2.43±0.04	4.37±0.25	1.87±0.09	4.35±0.11	2.49±0.13
MgI2.28	0.71±0.18	0.36±0.04	0.05±0.04	1.05±0.04	–	0.33±0.05	1.58±0.05	0.86±0.06
CO2.2	17.96±0.81	21.54±0.56	6.24±0.12	22.26±0.54	22.08±1.02	16.14±0.67	23.89±0.47	17.53±0.83
CO2.3a	22.66±1.19	22.13±0.39	2.96±0.16	23.54±0.41	22.84±0.95	14.90±0.82	26.34±0.40	24.72±0.77
CO2.3b	27.53±1.39	22.58±0.44	4.36±0.20	24.65±0.41	20.18±1.07	14.97±1.47	27.79±0.50	20.27±0.89

Riffel R., Borges Vale T., 2011, Ap&SS, 334, 351

Riffel R., Rodríguez-Ardila A., Pastoriza M. G., 2006, A&A, 457, 61

Riffel R., Pastoriza M. G., Rodríguez-Ardila A., Maraston C., 2007, ApJ, 659, L103

Riffel R., Pastoriza M. G., Rodríguez-Ardila A., Maraston C., 2008, MNRAS, 388, 803

Riffel R., Pastoriza M. G., Rodríguez-Ardila A., Bonatto C., 2009, MNRAS, 400, 273

Riffel R., Ruschel-Dutra D., Pastoriza M. G., Rodríguez-Ardila A., Santos Jr. J. F. C., Bonatto C. J., Ducati J. R., 2011a, MNRAS, 410, 2714

Riffel R., Bonatto C., Cid Fernandes R., Pastoriza M. G., Balbinot E., 2011b, MNRAS, 411, 1897

Riffel R., Riffel R. A., Ferrari F., Storchi-Bergmann T., 2011c, MNRAS, 416, 493

Riffel R. A., et al., 2013a, MNRAS, 429, 2587

Riffel R., Rodríguez-Ardila A., Aleman I., Brotherton M. S., Pastoriza M. G., Bonatto C., Dors O. L., 2013b, MNRAS, 430, 2002

Riffel R., et al., 2015, MNRAS, 450, 3069

Röck B., 2015, PhD thesis, Instituto de Astrofisica de Canarias <EMAIL>benny.roeck@gmail.com</EMAIL>

Röck B., Vazdekis A., Ricciardelli E., Peletier R. F., Knapen J. H., Falcón-Barroso J., 2016, A&A, 589, A73

Röck B., Vazdekis A., La Barbera F., Peletier R. F., Knapen J. H., Allende-Prieto C., Aguado D. S., 2017, MNRAS, 472, 361

Roeck B., 2015, PhD thesis, Instituto de Astrofisica de Canarias <EMAIL>benny.roeck@gmail.com</EMAIL>

Salaris M., Weiss A., Cassarà L. P., Piovan L., Chiosi C., 2014,

A&A, 565, A9
Sánchez-Blázquez P., Gorgas J., Cardiel N., González J. J., 2006, A&A, 457, 787
Sánchez S. F., et al., 2016, A&A, 594, A36
Sanders D. B., Mirabel I. F., 1996, ARA&A, 34, 749
Sanders D. B., Mazzarella J. M., Kim D.-C., Surace J. A., Soifer B. T., 2003, AJ, 126, 1607
Schmitt H. R., Calzetti D., Armus L., Giavalisco M., Heckman T. M., Kennicutt Jr. R. C., Leitherer C., Meurer G. R., 2006, ApJ, 643, 173
Silva D. R., Kuntschner H., Lyubenova M., 2008, ApJ, 674, 194
Sturm E., et al., 2006, ApJ, 653, L13
Tayal S. S., 2004, ApJS, 150, 465
Thomas D., Maraston C., Bender R., 2003, MNRAS, 339, 897
Trager S. C., Faber S. M., Worthey G., González J. J., 2000, AJ, 119, 1645
Vacca W. D., Cushing M. C., Rayner J. T., 2003, PASP, 115, 389
Vazdekis A., Ricciardelli E., Cenarro A. J., Rivero-González J. G., Díaz-García L. A., Falcón-Barroso J., 2012, MNRAS, 424, 157
Vazdekis A., Koleva M., Ricciardelli E., Röck B., Falcón-Barroso J., 2016, MNRAS, 463, 3409
Veilleux S., 2006, New Astron. Rev., 50, 701
Veilleux S., Kim D.-C., Sanders D. B., Mazzarella J. M., Soifer B. T., 1995, ApJS, 98, 171
Villaume A., Conroy C., Johnson B., Rayner J., Mann A. W., van Dokkum P., 2017, ApJS, 230, 23
Wang J. L., Xia X. Y., Mao S., Cao C., Wu H., Deng Z. G., 2006, ApJ, 649, 722
Worthey G., Faber S. M., Gonzalez J. J., 1992, ApJ, 398, 69
Worthey G., Faber S. M., Gonzalez J. J., Burstein D., 1994, ApJS, 94, 687
Zibetti S., Gallazzi A., Charlot S., Pierini D., Pasquali A., 2013, MNRAS, 428, 1479
van Dokkum P. G., Conroy C., 2012, ApJ, 760, 70

APPENDIX A: FINAL REDUCED SPECTRA

Final reduced and redshift-corrected spectra for the remaining sample. Available as online material.

APPENDIX B: LITERATURE DATA

Here we present the measurements using the index definitions listed in Tab. 5 for the literature data. The data used here are those of Dahmer-Hahn et al. (2018) and Baldwin et al. (2017). For the latter we found optical Sloan Digital Sky Survey data (Ahn et al. 2014) for four sources. For the remaining objects we collected the values of Fe5015, Mg_b and Fe5270 from McDermid et al. (2015), while for the sources of Dahmer-Hahn et al. (2018) the optical data were taken from the Calar Alto Legacy Integral Field Area Survey (CALIFA SÁNCHEZ ET AL. 2016) and we measured the EW of the optical lines.

This paper has been typeset from a TEX/LATEX file prepared by the author.

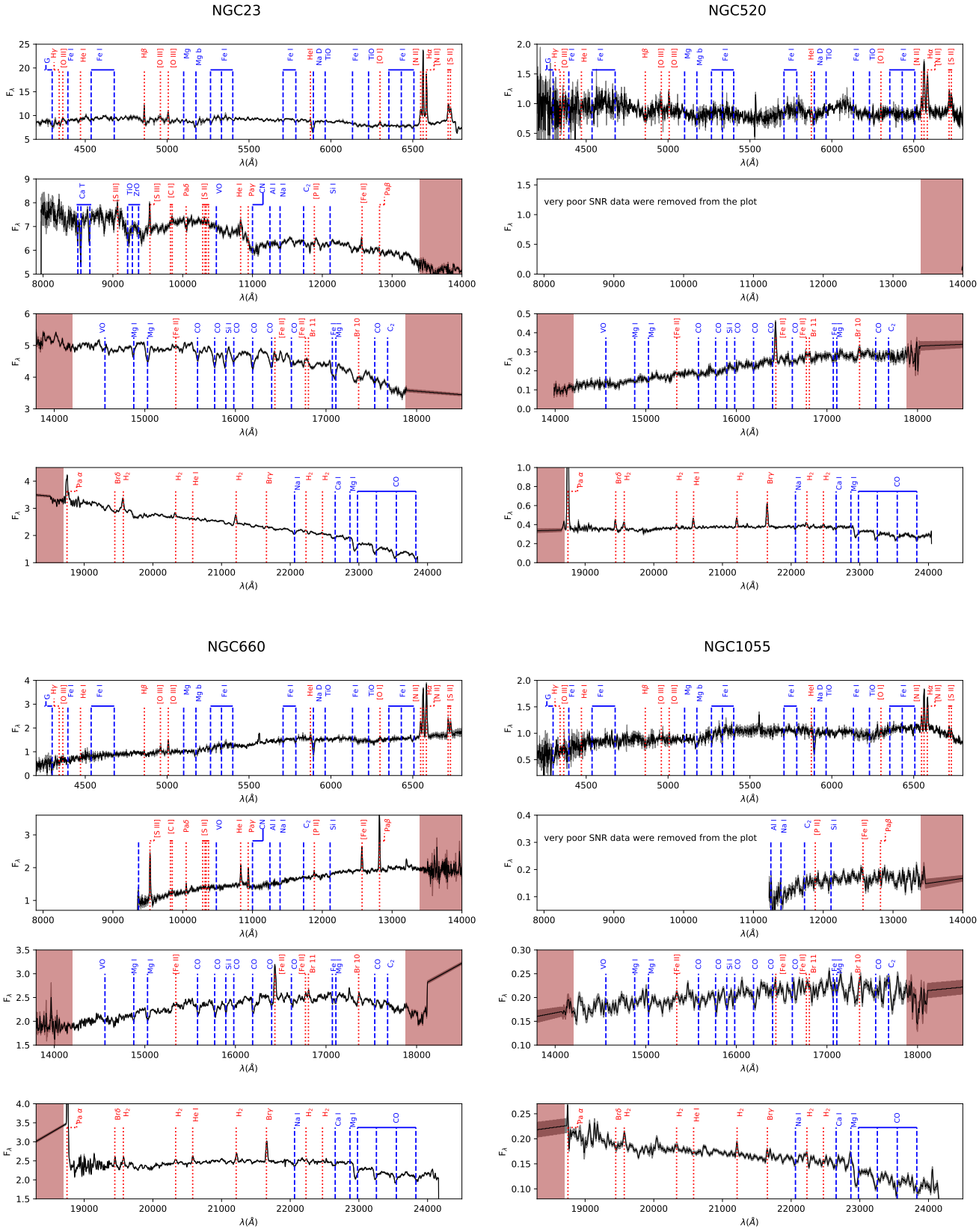

Figure A1. Final reduced spectra in the Earth's velocity frame, The sources are labeled. For each galaxy we show from top to bottom the optical, $z+J$, H, and K bands, respectively. The flux is in units of 10^{-15} erg cm^{-2} s^{-1}. The shaded grey area represents the uncertainties and the brown area shows the poor transmission region between different bands.

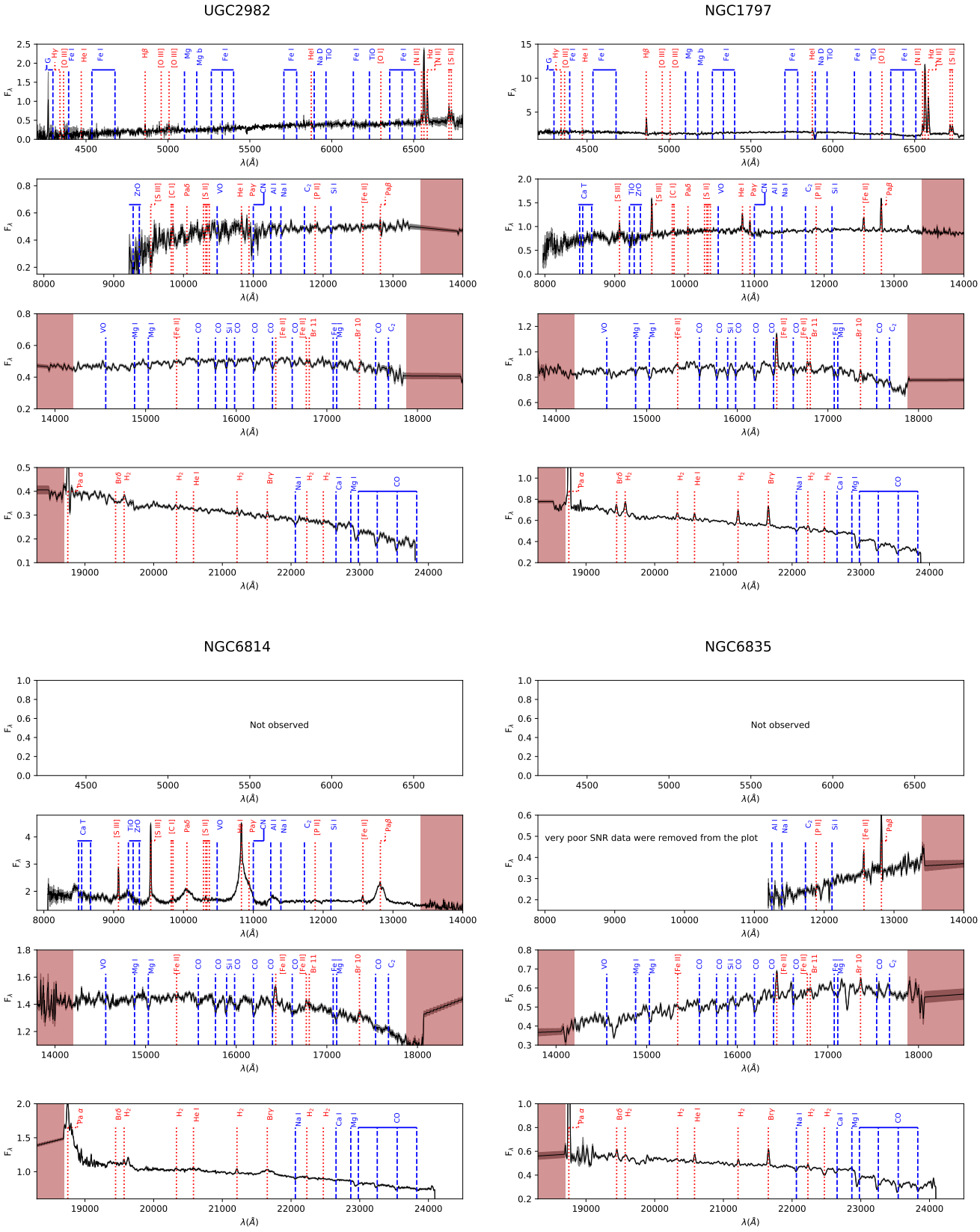

Figure A2. Final reduced spectra in the Earth's velocity frame. The sources are labeled. For each galaxy we show from top to bottom the optical, $z+J$, H , and K bands, respectively. The flux is in units of 10^{-15} erg cm^{-2} s^{-1}. The shaded grey area represents the uncertainties and the brown area shows the poor transmission region between different bands.

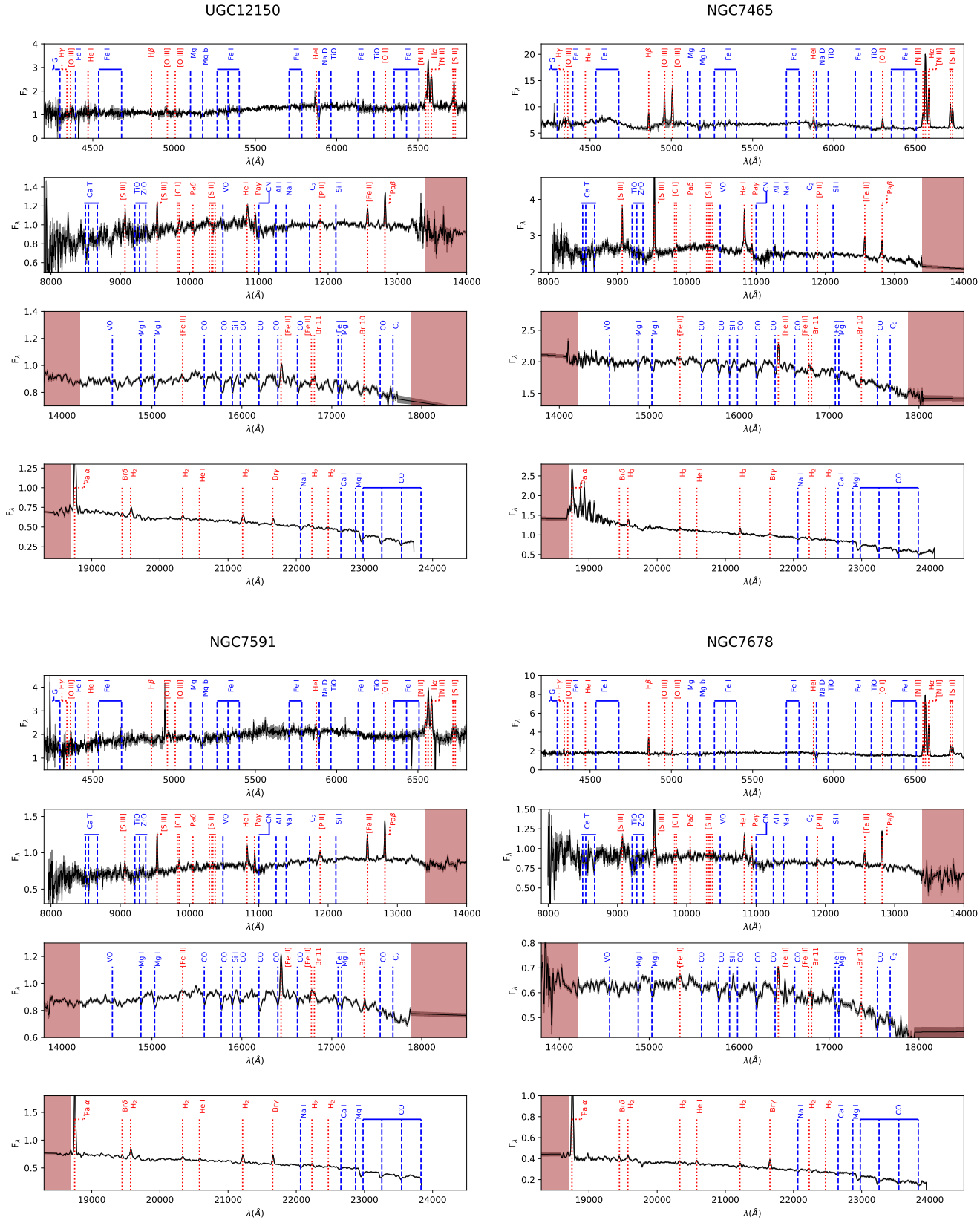

Figure A3. Final reduced spectra in the Earth's velocity frame. The sources are labeled. For each galaxy we show from top to bottom the optical, $z+J$, H , and K bands, respectively. The flux is in units of 10^{-15} erg cm^{-2} s^{-1}. The shaded grey area represents the uncertainties and the brown area shows the poor transmission region between different bands.

Table B1. Absorption feature Equivalent Widths (in Å) from the sample of Baldwin et al. (2017).

Line	IC0719	NGC3032	NGC3098	NGC3156	NGC3182	NGC3301
Ca4227	1.68±0.01	–	–	0.56±0.00	1.41±0.00	–
G4300	6.23±0.04	–	–	1.94±0.00	5.57±0.01	–
Fe4383	5.99±0.05	–	–	1.89±0.00	5.33±0.01	–
Ca4455	2.07±0.02	–	–	1.08±0.00	1.68±0.00	–
Fe4531	3.67±0.04	–	–	2.99±0.00	3.37±0.01	–
$C_2$4668	7.04±0.07	–	–	2.79±0.01	7.86±0.01	–
Fe5015	5.68±0.06	4.44±0.14	4.64±0.14	4.07±0.01	3.57±0.01	4.95±0.14
Mg_1	5.40±0.05	–	–	1.88±0.01	6.46±0.01	–
Mg_2	8.06±0.03	–	–	4.10±0.00	8.82±0.01	–
Mg_b	3.83±0.03	1.70±0.12	3.17±0.12	1.58±0.00	4.18±0.01	2.93±0.12
Fe5270	3.02±0.03	2.06±0.11	2.56±0.11	1.93±0.01	2.97±0.01	2.56±0.11
Fe5335	2.93±0.02	–	–	1.98±0.00	3.04±0.01	–
Fe5406	1.51±0.02	–	–	1.06±0.00	1.87±0.00	–
Fe5709	1.21±0.01	–	–	0.68±0.00	1.09±0.00	–
Fe5782	0.97±0.01	–	–	0.51±0.00	0.91±0.00	–
NaD	3.13±0.03	–	–	1.19±0.01	3.63±0.01	–
TiO_1	2.20±0.04	–	–	0.60±0.01	1.66±0.01	–
TiO_2	5.17±0.05	–	–	1.87±0.02	5.26±0.02	–
CaT1	–	–	–	–	–	–
CaT2	–	–	–	–	–	–
CaT3	–	–	–	–	–	–
ZrO	8.55±2.34	15.87±1.08	8.92±1.41	22.28±1.91	14.75±1.68	15.61±0.92
VO	2.63±0.55	–	0.32±0.51	1.87±0.59	0.28±0.38	1.45±0.39
CN11	5.97±0.79	10.58±0.37	11.35±0.39	7.31±0.64	7.93±0.58	8.47±0.36
NaI1.14	1.82±0.21	3.14±0.17	1.48±0.14	1.23±0.26	2.37±0.17	1.42±0.14
FeI1.16	1.23±0.26	–	0.61±0.10	0.45±0.18	0.39±0.22	0.03±0.05
MgI1.24	1.00±0.12	1.04±0.09	0.36±0.08	0.81±0.15	1.43±0.11	0.81±0.07
MnI1.29	0.85±0.19	1.06±0.09	1.20±0.13	1.19±0.20	1.20±0.20	1.26±0.18
AlI1.31	1.27±0.16	1.87±0.10	1.32±0.18	0.74±0.15	2.27±0.11	1.27±0.11
MgI1.48	2.05±0.13	1.62±0.11	1.71±0.08	1.12±0.13	0.85±0.27	1.55±0.09
MgI1.50	4.29±0.23	3.58±0.17	3.60±0.21	3.23±0.22	1.42±0.31	3.37±0.18
CO1.5a	3.72±0.14	4.74±0.16	4.05±0.28	4.40±0.19	2.75±0.27	4.38±0.18
CO1.5b	4.13±0.20	4.09±0.14	4.96±0.20	3.61±0.16	2.61±0.44	5.56±0.10
FeI1.58	1.37±0.13	0.85±0.11	1.55±0.11	1.78±0.11	0.62±0.24	2.14±0.07
SiI1.58	2.91±0.22	3.44±0.24	3.24±0.23	4.14±0.23	2.89±0.49	4.85±0.14
CO1.5c	3.97±0.17	3.56±0.24	3.20±0.16	2.83±0.22	3.35±0.29	3.98±0.16
CO1.6a	5.33±0.35	4.73±0.45	6.67±0.30	6.48±0.41	5.81±0.48	6.30±0.37
CO1.6b	1.27±0.16	0.89±0.14	1.51±0.13	1.28±0.16	1.37±0.21	1.31±0.15
MgI1.7	1.99±0.08	2.30±0.08	2.12±0.09	1.85±0.10	2.41±0.09	2.14±0.10
NaI2.20	3.41±0.08	5.15±0.14	2.84±0.13	2.52±0.20	3.74±0.08	2.77±0.19
CaI2.26	1.85±0.17	3.66±0.26	2.49±0.34	2.55±0.29	2.57±0.22	3.09±0.14
MgI2.28	0.76±0.11	0.94±0.12	1.05±0.09	–	1.22±0.16	0.94±0.04
CO2.2	15.76±0.83	20.43±0.68	14.80±0.70	19.55±0.78	17.57±0.77	19.47±0.58
CO2.3a	17.74±1.01	18.16±0.65	14.12±0.86	19.90±1.21	16.44±0.78	19.23±0.70
CO2.3b	20.23±1.27	17.06±0.78	17.40±1.13	23.39±1.85	20.04±1.15	21.83±0.98

Table Notes: The values of Fe5015, Mg_b and Fe5270 for NGC3032, NGC3098 and NGC3301 were taken from McDermid et al. (2015) for Re/8.

Table B2. Absorption feature Equivalent Widths (in Å) from the sample of Baldwin et al. (2017).

Line	NGC3489	NGC4379	NGC4578	NGC4608	NGC4710	NGC5475
Ca4227	–	–	–	–	–	1.32±0.00
G4300	–	–	–	–	–	5.76±0.01
Fe4383	–	–	–	–	–	5.43±0.01
Ca4455	–	–	–	–	–	1.87±0.00
Fe4531	–	–	–	–	–	3.79±0.01
$C_2$4668	–	–	–	–	–	7.12±0.01
Fe5015	4.84±0.14	5.41±0.14	5.24±0.14	4.64±0.14	4.46±0.15	5.09±0.01
Mg_1	–	–	–	–	–	5.33±0.01
Mg_2	–	–	–	–	–	8.28±0.00
Mg_b	2.80±0.12	3.66±0.12	3.88±0.12	3.78±0.12	3.05±0.1 2	4.22±0.00
Fe5270	2.58±0.11	2.85±0.12	2.90±0.11	2.59±0.11	2.44±0.15	3.10±0.00
Fe5335	–	–	–	–	–	3.24±0.00
Fe5406	–	–	–	–	–	1.96±0.00
Fe5709	–	–	–	–	–	1.09±0.00
Fe5782	–	–	–	–	–	1.07±0.00
NaD	–	–	–	–	–	3.58±0.00
TiO_1	–	–	–	–	–	1.26±0.01
TiO_2	–	–	–	–	–	4.73±0.01
CaT1	–	–	–	–	–	–
CaT2	–	–	–	–	–	–
CaT3	–	–	–	–	–	–
ZrO	12.10±0.68	25.45±0.64	22.91±0.98	19.96±1.62	6.11±1.51	6.40±1.26
VO	1.34±0.44	1.52±0.58	1.87±0.36	–	3.32±1.07	2.22±0.57
CN11	7.14±0.40	4.53±0.49	5.49±0.37	7.03±0.43	9.21±1.01	10.28±0.47
NaI1.14	1.35±0.20	1.47±0.19	1.63±0.16	1.69±0.21	1.22±0.25	1.61±0.21
FeI1.16	0.48±0.07	0.38±0.10	0.49±0.10	0.44±0.09	0.73±0.12	0.33±0.11
MgI1.24	0.60±0.04	0.88±0.06	0.99±0.07	0.94±0.07	0.71±0.15	0.80±0.08
MnI1.29	0.91±0.11	1.06±0.35	0.98±0.26	1.10±0.21	0.70±0.28	1.71±0.25
AlI1.31	1.19±0.10	1.35±0.18	1.65±0.12	1.65±0.09	1.38±0.15	2.21±0.10
MgI1.48	1.49±0.09	1.62±0.11	2.29±0.22	1.33±0.11	1.70±0.13	1.72±0.09
MgI1.50	3.13±0.13	4.07±0.18	5.10±0.35	3.86±0.15	4.02±0.19	4.54±0.21
CO1.5a	4.19±0.14	3.36±0.17	5.15±0.26	3.43±0.16	3.41±0.19	4.02±0.17
CO1.5b	4.46±0.13	3.10±0.19	5.95±0.47	3.86±0.16	3.44±0.21	4.55±0.15
FeI1.58	2.28±0.10	1.40±0.11	2.66±0.23	1.97±0.10	1.98±0.15	1.84±0.10
SiI1.58	3.75±0.18	2.97±0.18	4.43±0.42	3.98±0.21	3.70±0.22	4.03±0.20
CO1.5c	3.72±0.17	2.68±0.11	3.71±0.36	3.37±0.25	3.59±0.20	4.26±0.20
CO1.6a	6.74±0.29	5.51±0.29	6.64±0.54	6.78±0.37	5.59±0.34	6.07±0.37
CO1.6b	0.85±0.15	0.95±0.09	1.47±0.22	2.12±0.17	0.92±0.12	1.48±0.17
MgI1.7	1.94±0.06	2.25±0.06	2.27±0.10	2.33±0.08	2.13±0.06	2.32±0.11
NaI2.20	3.22±0.04	3.91±0.22	4.59±0.12	3.11±0.11	3.56±0.06	3.96±0.08
CaI2.26	2.38±0.09	0.88±0.42	2.10±0.15	2.09±0.30	2.41±0.28	3.40±0.30
MgI2.28	0.56±0.02	0.48±0.18	0.88±0.10	1.04±0.10	0.86±0.14	1.57±0.20
CO2.2	18.62±0.44	14.95±0.78	18.82±0.49	17.66±0.62	18.84±0.61	14.87±0.50
CO2.3a	17.39±0.53	14.74±0.81	19.96±0.67	16.66±0.75	18.11±0.63	16.69±0.68
CO2.3b	18.45±0.66	16.78±1.03	23.74±0.91	19.23±1.08	20.31±0.87	19.88±0.89

Table B3. Absorption feature Equivalent Widths (in Å) from the sample of Dahmer-Hahn et al. (2018).

Line	NGC4636	NGC5905	NGC5966	NGC6081	NGC6146	NGC6338	UGC08234
Ca4227	–	–	1.23±0.10	1.21±0.07	1.00±0.03	1.16±0.06	0.76±0.05
G4300	–	–	5.54±0.28	5.59±0.30	5.30±0.16	5.82±0.23	3.01±0.21
Fe4383	–	–	4.46±0.35	4.56±0.29	4.47±0.24	4.33±0.29	2.63±0.25
Ca4455	–	–	1.36±0.16	1.14±0.15	1.04±0.13	1.30±0.17	0.92±0.15
Fe4531	–	–	3.32±0.14	3.04±0.21	3.15±0.14	3.24±0.12	2.73±0.08
$C_2$4668	–	–	6.42±0.13	6.63±0.16	6.82±0.18	7.78±0.23	4.56±0.13
Fe5015	–	–	4.01±0.29	3.52±0.37	3.75±0.25	3.98±0.24	4.14±0.22
Mg_1	–	–	6.28±0.27	6.84±0.28	6.58±0.22	8.06±0.22	3.26±0.20
Mg_2	–	–	8.70±0.15	8.90±0.15	9.08±0.12	10.34±0.13	5.96±0.13
Mg_b	–	–	3.95±0.15	4.09±0.15	3.89±0.13	4.67±0.12	2.60±0.09
Fe5270	–	–	2.51±0.15	2.53±0.14	2.47±0.10	2.40±0.12	2.30±0.15
Fe5335	–	–	2.19±0.13	2.19±0.13	1.97±0.08	2.15±0.11	1.92±0.10
Fe5406	–	–	1.62±0.06	1.36±0.05	1.34±0.08	1.46±0.05	1.27±0.04
Fe5709	–	–	0.85±0.04	0.71±0.05	0.73±0.04	0.26±0.07	0.57±0.12
Fe5782	–	–	0.50±0.03	0.82±0.03	0.67±0.03	0.73±0.03	0.60±0.03
NaD	–	–	3.45±0.06	4.02±0.04	4.00±0.03	4.82±0.02	3.18±0.04
TiO_1	–	–	1.78±0.06	1.82±0.08	1.79±0.11	2.16±0.07	1.51±0.08
TiO_2	–	–	5.80±0.17	5.96±0.09	5.52±0.15	5.45±0.15	3.56±0.14
CaT1	–	–	–	–	–	–	–
CaT2	–	–	–	–	–	–	–
CaT3	–	–	–	–	–	–	–
ZrO	–	–	–	–	–	–	–
VO	2.61±0.20	1.86±0.46	2.98±0.34	1.37±0.35	2.11±0.28	0.97±0.20	2.60±0.25
CN11	10.82±0.68	0.68±0.57	0.31±0.35	0.34±0.17	–	5.39±0.33	2.71±0.67
NaI1.14	1.57±0.47	0.94±0.24	–	1.18±0.09	2.21±0.17	1.15±0.09	1.70±0.26
FeI1.16	–	1.02±0.07	1.43±0.09	0.40±0.08	0.56±0.03	0.29±0.06	–
MgI1.24	0.56±0.06	1.18±0.13	1.12±0.06	0.93±0.17	0.47±0.05	2.06±0.14	0.76±0.26
MnI1.29	1.15±0.14	–	3.89±0.32	0.99±0.32	1.40±0.11	2.98±0.46	1.74±0.24
AlI1.31	3.54±0.19	1.61±0.06	2.58±0.16	2.98±0.14	0.02±0.04	0.56±0.07	–
MgI1.48	0.92±0.14	2.60±0.07	1.68±0.08	1.38±0.05	1.33±0.06	1.69±0.10	1.31±0.10
MgI1.50	3.88±0.12	3.92±0.12	3.50±0.17	4.03±0.05	3.03±0.09	3.24±0.17	3.23±0.17
CO1.5a	4.59±0.06	3.63±0.14	2.93±0.10	1.96±0.08	3.89±0.02	5.39±0.15	3.07±0.13
CO1.5b	3.89±0.08	4.73±0.18	4.91±0.09	3.61±0.11	3.95±0.03	4.52±0.26	4.56±0.09
FeI1.58	1.10±0.05	1.99±0.09	1.83±0.06	1.54±0.09	1.80±0.03	1.70±0.15	1.77±0.06
SiI1.58	2.79±0.07	3.49±0.18	4.90±0.11	3.20±0.15	3.89±0.06	4.20±0.25	4.17±0.12
CO1.5c	3.24±0.04	3.27±0.15	3.02±0.13	3.53±0.15	3.03±0.07	4.32±0.12	4.26±0.11
CO1.6a	7.43±0.17	5.99±0.30	8.47±0.24	6.18±0.26	5.60±0.14	6.30±0.12	5.85±0.20
CO1.6b	1.22±0.04	1.21±0.10	0.96±0.07	1.28±0.07	1.18±0.08	1.37±0.10	0.34±0.10
MgI1.7	2.12±0.02	1.81±0.06	2.14±0.03	1.81±0.05	2.18±0.05	1.76±0.06	1.57±0.08
NaI2.20	3.73±0.06	3.96±0.07	4.36±0.11	2.99±0.16	4.00±0.18	4.07±0.14	1.79±0.12
CaI2.26	3.83±0.04	2.16±0.46	0.81±0.39	2.07±0.13	2.51±0.29	5.05±0.07	5.31±0.41
MgI2.28	0.92±0.08	0.83±0.12	0.86±0.09	0.91±0.24	0.42±0.15	1.46±0.13	1.26±0.25
CO2.2	16.65±0.38	17.53±0.66	8.39±0.74	19.84±0.79	13.78±0.50	14.18±0.60	17.74±0.98
CO2.3a	19.00±0.74	6.86±0.90	4.91±0.74	24.38±1.20	8.70±0.32	14.02±0.90	25.90±0.83
CO2.3b	17.96±0.93	8.97±1.09	6.80±1.03	27.70±1.68	–	8.52±1.12	35.37±1.07

Table Notes: The optical data where taken from CALIFA survey (Sánchez et al. 2016).